The road to the discovery of a Higgs boson in the $H \to WW^{(*)} \to \ell\nu\ell\nu$ channel

Magda Chelstowska

THE ROAD TO THE DISCOVERY OF A HIGGS BOSON IN THE $H \rightarrow WW^{(*)} \rightarrow \ell\nu\ell\nu$ CHANNEL

Proefschrift

ter verkrijging van de graad van doctor
aan de Radboud Universiteit Nijmegen
op gezag van de rector magnificus prof. mr. S.C.J.J. Kortmann,
volgens besluit van het College van Decanen
in het openbaar te verdedigen op woensdag 25 september 2013
om 15:30 uur.

door

Magda Chelstowska

geboren op 31 juli 1985
te Gdańsk, Polen

Contents

Chapter 1

Introduction

The Standard Model of particle physics explains and unifies three of the four fundamental forces of nature. It also describes all the known elementary particles. The electroweak symmetry in the Standard Model is spontaneously broken by a mechanism that predicts the existence of a new scalar particle. This particle, called the Higgs boson, is also responsible for giving masses to all the elementary particles. Searches for the Higgs boson have been conducted at LEP, the Tevatron and recently at the Large Hadron Collider.

Fits to electroweak precision results have set indirect limits on the Higgs boson mass of $m_H < 158$ GeV at 95% confidence level. Direct searches at LEP and the Tevatron have excluded at 95% confidence level the Higgs boson mass below 114.4 GeV and in the range 147 GeV $< m_H < 179$ GeV.

At the Large Hadron Collider, the main production mode of the Higgs boson is through gluon fusion ($gg \rightarrow H$), due to the large gluon density. The other production processes include vector boson fusion ($qq' \rightarrow qq'H$) and associated production with the W or Z bosons ($qq' \rightarrow WH, ZH$). The main decay channels of the Higgs boson include $H \rightarrow \gamma\gamma$, $H \rightarrow ZZ^{(*)}$, $H \rightarrow WW^{(*)}$, $H \rightarrow b\bar{b}$ and $H \rightarrow \tau\tau$. Searches for the Higgs particle decaying to a pair of bosons and fermions have been conducted both at the ATLAS and CMS experiments. The first direct evidence of its existence was presented at a seminar at CERN on July 4, 2012. The results were based on the analyses of data collected in 2011 at 7 TeV centre-of-mass energy and in 2012 at $\sqrt{s} = 8$ TeV. The ATLAS and CMS collaborations claimed the discovery of a new Higgs-like particle at a mass around 126 GeV, ATLAS with the local significance of 5σ and CMS with 4.9σ. Both collaborations continue to investigate whether the observed particle is a Standard Model Higgs boson through measurements of its properties.

The results presented by the ATLAS collaboration were later updated with the 2012 $H \rightarrow WW^{(*)} \rightarrow \ell\nu\ell\nu$ analysis and published at the end of July, 2012. The ATLAS experiment reported an excess of data events around 126 GeV with a local significance of 5.9σ. The analysis presented in this thesis is an extension of the published analysis. Not only does it use 7 fb^{-1} more data, but it also improves the sensitivity and the background rejection.

In the search for the Standard Model Higgs boson with a mass $\gtrsim 135$ GeV, the $H \rightarrow WW^{(*)} \rightarrow \ell\nu\ell\nu$ (where $\ell = e, \mu$) decay channel is the dominant one. It yields the highest sensitivity in the range 120 GeV $< m_H < 190$ GeV, which covers most of the region preferred by the global electroweak fits. The final state consists of two leptons, two neutrinos, and zero, one or two and more accompanying jets. Because of the existence of

the neutrinos, the mass of the Higgs particle cannot be fully reconstructed, which results in a poor mass resolution in this decay channel. Nevertheless, having the highest branching ratio and being the most sensitive in the mass range around 126 GeV, causes this channel to be of great importance and motivates the analysis presented in this thesis.

In this thesis, Chapter 2 describes the theoretical aspects of the Standard Model and the Higgs boson. The Large Hadron Collider and the ATLAS detector are presented in Chapter 3. The object and event reconstruction is outlined in Chapter 4 and is followed by a detailed description of the $H \to WW^{(*)} \to \ell\nu\ell\nu$ analysis in Chapter 5. The final results, based on a data sample corresponding to an integrated luminosity 13 fb^{-1} collected at $\sqrt{s} = 8$ TeV, are presented in Chapter 6. The combination of all the Higgs search channels in the ATLAS experiment that led to the discovery of the Higgs boson is also discussed. Chapter 7 gives the summary of this analysis and discusses its impact on the Higgs boson searches.

The $H \to WW^{(*)}$ analysis group is one of the six Higgs analyses working groups in the ATLAS experiment. I have been involved in the search for the Higgs boson in the $WW^{(*)} \to \ell\nu\ell\nu$ decay channel since the middle of 2010 when the LHC was colliding proton beams at 7 TeV centre-of-mass energy. Since then, the analysis has been updated with the 7 TeV 2011 and 8 TeV 2012 data and I have been involved in the continuous improvements and optimisations. Furthermore I was the main developer of the infrastructure framework that was designed to provide the analysis group with the event data structures used to obtain the official results. For the analysis presented in this thesis I have contributed in many activity areas but especially in the thorough understanding of the data to simulation comparisons. One of the main studies included the validation of the dominant background to the $H \to WW^{(*)} \to \ell\nu\ell\nu$ search: Standard Model WW continuum. It consisted of comparisons of different event generators, different definitions of the control regions and reweightings of the mismodelled variables. I am also the co-author of the newly developed estimation method of the $W\gamma$ background. It is based on the selection of the electrons coming from external photon conversions that can be clearly distinguished from the electron coming from the decays of W bosons. This method is documented in detail in this thesis but it has not been used in the official analysis since the obtained validation region is still statistically limited.

Chapter 2

Theory

The aim of this chapter is to outline the theoretical foundations of modern particle physics, especially the parts relevant to the topic of this thesis. The Standard Model (SM) of particle physics is introduced in the first section. It is followed by a description of the unification of electromagnetic and weak forces, and of electroweak symmetry breaking. The second part of this chapter explains how the SM Higgs boson fits in the electroweak theory and what the constraints on its mass are. The last part introduces the phenomenology of proton-proton collisions and the production of the Higgs boson at the Large Hadron Collider (LHC). A few details will be provided on the $H \to WW^{(*)} \to \ell\nu\ell\nu$ decay channel.

2.1 The Standard Model

2.1.1 Particles, forces and the SM

There are four fundamental forces that describe our universe. They include: the electromagnetic force which is responsible for the interactions between charged particles; the weak force which lies behind beta decay; the strong force which binds quarks together to form protons and neutrons; and the gravitational force. Gravity cannot be described in the framework of the SM and therefore it will not be addressed here. The forces are described by gauge theories, which will be explained later, and are mediated by particles with integer spin; so-called gauge bosons. The properties of the bosons and the force they carry are listed in Table 2.1. All of the bosons are spin-1 particles (apart from the postulated graviton which is supposed to be a massless spin-2 particle). Apart from the weak force carriers, they are massless and have no electric charge. Gluons carry a unit of colour which can be regarded as the "charge" of the strong interaction (in analogy to the electric charge in the electromagnetic interactions). Fermions are divided into two groups depending on the coupling to the strong force. Leptons are colourless and do not interact with the strong force. On the other hand, quarks carry colour and do interact strongly. Both leptons and quarks are spin-$^1/_2$ fermions. They are grouped in three generations (or families) with two quarks (up-type and down-type) and two leptons (charged and neutral) in each. They are listed in Table 2.2. Neutrinos are assumed to be weakly interacting massless particles, although recent experimental evidence of neutrino oscillations suggests that they have non-zero masses. Each of the fermions and bosons has an associated anti-particle with the same mass and spin, but with opposite electromagnetic charge. The photon, Z boson and gluons are identical to their anti-particles. All other known particles, apart from leptons, quarks and the gauge bosons, are composite. They are called hadrons and are made out of quarks.

Force	Name	Symbol	Charge	Spin	Mass
Electromagnetic	photon	γ	0	1	0
Weak	W boson	$W^{\pm}$	$\pm$	1	80.4
	Z boson	Z	0	1	91.2
Strong	gluon	g	0	1	0

Table 2.1: Fundamental forces and their gauge bosons. Charge is in units of the electron charge and mass is in GeV units. [1]

They are divided into baryons which are composed of three quarks (half-integer spin) and mesons which are composed of one quark and one anti-quark (integer spin).

Symmetries play a crucial role in particle physics. There is a symmetry S if a physical system is invariant under the transformation given by S. Based on the parameters defining the transformations, the symmetries can be classified into discrete (e.g. time-reversal, parity or charge conjugation) and continuous. The latter ones can be further divided into space-time or internal symmetries. Space-time symmetries, such as translations or rotations, act on the space-time coordinates. Internal symmetries, usually described by Lie groups, act on the internal quantum numbers and they transform one particle to another. Particle multiplets are the irreducible representations of the internal symmetries with the $SU(2)$ isospin symmetry as an example. The $SU(2)$ group is a set of 2×2 unitary matrices with three generators and the corresponding degenerate particle isospin multiplets are:

$$\left(\begin{array}{c} p \\ n \end{array} \right) \text{ isospin doublet } \quad \left(\begin{array}{c} \pi^+ \\ \pi^0 \\ \pi^- \end{array} \right) \text{ isospin triplet}$$

The above mentioned internal symmetries can be further divided in two important groups: global and local (gauge) symmetries. The isospin $SU(2)$ symmetry is a global one where the continuous parameters of the transformations do not depend on the space-time coordinates. The symmetries whose continuous parameters do depend on the space-time coordinates are local symmetries with $U(1)_{em}$ electromagnetic symmetry or $SU(2)_L$ weak isospin symmetry as two examples. The quantum field theories describing the electromagnetic, weak and strong interactions, are based on the gauge symmetries and they are called gauge theories.

The Lagrangian, $\mathcal{L}$, is a complete function that describes the dynamics of a system. It was first introduced in classical mechanics where it was defined as kinetic energy minus potential energy of the system, $T - V$. It is also commonly used in particle physics. The kinetic parts are general and depend on the spin of the particles. The potential energy parts are crucial as they describe the interactions. Gauge theories are described with a Lagrangian that is invariant under local transformations. There exist two principles that are relevant to the discussion here:

1. Noether's principle for global symmetries - if a Lagrangian of a physical system has a global symmetry, there must be a current and the associated charge that are conserved;

2. Gauge principle for gauge theories - when promoting a global symmetry, of a physical system ψ described by a Lagrangian $\mathcal{L}$, to a local symmetry, the theory transforms into an interacting theory. To keep the Lagrangian invariant under the local transformations, new vector boson fields (gauge fields) have to be introduced. The number of associated gauge fields equals the number of generators of the symmetry group.

type		I generation		II generation		III generation	charge	
up-type	u	$2.3^{+0.7}_{-0.5}$ MeV	c	1.275 ± 0.025 GeV	t	$173.5\pm0.6\pm0.8$ GeV	$+^2/_3$	quark
down-type	d	$4.8^{+0.7}_{-0.3}$ MeV	s	95 ± 5 MeV	b	4.18 ± 0.03 GeV	$-^1/_3$	
neutral	ν_e	~0	ν_μ	~0	ν_τ	~0	0	lepton
charged	e^-	$0.511\pm0.11\times10^{-7}$ MeV	μ^-	$105\pm35\times10^{-7}$ MeV	τ^-	1776.82 ± 0.16 MeV	-1	

Table 2.2: The properties of fermions. [1]

An example of the gauge principle will be given in the next section based on quantum electrodynamics (QED) but a generic case of $SU(N)$ symmetry has N^2-1 generators and therefore N^2-1 gauge bosons.

The Standard Model is a quantum field theory that is based on a gauge symmetry $SU(3)_C \times SU(2)_L \times U(1)_Y$. Quantum chromodynamics (QCD) is a theory that describes the strong interactions. It is based on the $SU(3)_C$ gauge symmetry. Here C refers to the colour as an additional quantum number and 3 refers to the number of possible colour states. The fundamental representation of this group are quarks and the interactions are mediated by the gauge bosons called gluons:

$$\text{quarks: } q_i, \, i = 1, 2, 3; \qquad \text{gluons: } g_\alpha, \, \alpha = 1, ..., 8$$

$SU(2)_L \times U(1)_Y$ is a symmetry group of electroweak interactions between the fermions. Here L denotes the left-handed fermions. Y is the generator of the $U(1)_Y$ group and its associated gauge boson mixes with the third component of the $SU(2)_L$ generator to give rise to a neutral Z boson. Y is a conserved quantum number and is called weak hypercharge. There exist 4 gauge bosons: γ, $W^\pm$ and Z, and only the γ, photon, is massless. The other bosons are massive which indicates that $SU(2)_L \times U(1)_Y$ is not a symmetry of the vacuum. Taking this one step further, the electroweak theory has a spontaneously broken symmetry which means that the Lagrangian describing the physical system is invariant under the symmetry transformations but the vacuum of the theory is not. The mechanism of spontaneous symmetry breaking was studied by Higgs, Englert, Brout, Guralnik, Hagen and Kibble [2–8]. Nowadays it is commonly referred to as the Higgs mechanism.

2.1.2 Electroweak unification

The idea of unification of electromagnetic and weak forces was first proposed by Glashow in 1961 [9] and then refined in 1967 by Weinberg and Salam (GWS model). The problem of different structures of electromagnetic (γ^μ) and weak vertex ($\gamma^\mu(1 - \gamma^5)$, V-A nature) factors was overcome by absorbing the axial vector part to the particle spinor. Here, γ^μ denotes the Dirac matrices. The only missing ingredient was the mechanism that would explain the massive $W^\pm$ and Z bosons. This section will use the Lagrange formalism to describe the electroweak interactions.

QED

The Dirac Lagrangian for spinor field with mass m and electric charge Qe, can be expressed as:

$$\mathcal{L} = \overline{\psi}(x)(i\gamma^\mu \partial_\mu - m)\psi(x), \tag{2.1}$$

where $\psi(x)$ is the fermion field and $\overline{\psi}(x) = \psi^\dagger \gamma^0$ is its adjoint). Applying the Euler-Lagrange equations yields the equation of motion for spin-$^1/_2$ particles (Dirac equation):

$$(i\gamma^\mu \partial_\mu - m)\psi(x) = 0. \tag{2.2}$$

7

This Lagrangian is invariant under the global $U(1)$ transformations:

$$\psi \to e^{iQ\theta}\psi; \ \overline{\psi} \to \overline{\psi}e^{-iQ\theta}; \ \partial_\mu\psi \to e^{iQ\theta}\partial_\mu\psi$$

where $Q\theta$ is the global phase and θ is the continuous parameter. Noether's theorem implies the conservation of the electromagnetic current, $J_\mu = \overline{\psi}\gamma_\mu eQ\psi$, and the electromagnetic charge, eQ. Requiring the symmetry to be local, changes the corresponding transformations and derivatives:

$$\psi \to e^{iQ\theta(x)}\psi; \ \overline{\psi} \to \overline{\psi}e^{-iQ\theta(x)}; \ \partial_\mu\psi \to e^{iQ\theta(x)}\partial_\mu\psi + iQ(\partial_\mu\theta(x))e^{iQ\theta(x)}\psi$$

According to the gauge principle, a new vector boson field has to be introduced so that the Lagrangian is invariant under the local transformations. The new photon field A_μ interacts with the fermionic field ψ and transforms as follows:

$$A_\mu \to A_\mu - \frac{1}{e}\partial_\mu\theta(x). \tag{2.3}$$

Substituting the normal derivative, ∂_μ, with the covariant derivative, D_μ:

$$D_\mu \to \partial_\mu - ieQA_\mu, \tag{2.4}$$

can be viewed as a recipe for local gauge invariance given the global gauge invariance, with the ψ field now transforming as:

$$D_\mu\psi \to e^{iQ\theta(x)}D_\mu\psi.$$

The Lagrangian thus obtained is locally invariant but it is not complete as it does not include the "free" term for the vector field. Introducing this term (according to the Proca Lagrangian), while keeping the Lagrangian invariant, requires the A_μ field to be massless. The final QED Lagrangian can be written as:

$$\mathcal{L}_{QED} = \overline{\psi}(x)(i\gamma^\mu D_\mu - m)\psi(x) - \frac{1}{4}F_{\mu\nu}F^{\mu\nu}, \tag{2.5}$$

where $F_{\mu\nu} = \partial_\mu A_\nu - \partial_\nu A_\mu$ is a field strength tensor. The interaction term between the photon and the fermion field is contained within the $\overline{\psi}i\gamma^\mu D_\mu\psi$ term, $\overline{\psi}eQA_\mu\gamma^\mu\psi$. The gauge transformations with a single phase belong to the unitary $U(1)_{em}$ group with one generator, Q and one parameter θ.

Yang-Mills theory

Suppose that there are two spin-$^1/_2$ fields ψ_1 and ψ_2. They can be composed in a doublet with its adjoint defined as:

$$\psi = \begin{pmatrix} \psi_1 \\ \psi_2 \end{pmatrix}, \quad \overline{\psi} = (\overline{\psi_1\psi_2}). \tag{2.6}$$

The free Lagrangian can be expressed in the same way as in Eq 2.1 but taking into account that ψ is now a field doublet and m is a 2×2 matrix with the masses of two particles on the diagonal. The gauge transformations, apart from already discussed phase transformations, acquire a new term which is responsible for ψ_1 and ψ_2 mixing. It has the form:

$$\psi \to e^{i\vec{\theta}\cdot\vec{\tau}}\psi, \tag{2.7}$$

where $\vec{\theta} \cdot \vec{\tau}$ is a Hermitian 2×2 matrix and τ_i (i =1,2,3) are the generators of $SU(2)$ symmetry group.[1] The τ_i do not commute:

$$[\tau_i, \tau_i] = i\epsilon_{ijk}\tau_k, \tag{2.8}$$

ϵ_{ijk} are called structure constants and the gauge group is said to be non-Abelian. In the fundamental representation of $SU(2)$, the τ_i are proportional to Pauli matrices, $\tau_i = \sigma_i/2$. To ensure the local invariance of the Lagrangian, and following the example of QED, the derivatives need to be substituted with covariant derivatives of the form:

$$D_\mu = \partial_\mu - ig\vec{W}_\mu \cdot \vec{\tau}, \tag{2.9}$$

where g is a coupling constant. This introduces three massless gauge fields W_μ^i (i =1,2,3) which transform, simultaneously with the ψ doublet, under $SU(2)$ as:

$$W_\mu^i \rightarrow W_\mu^i + \frac{1}{g}\partial_\mu\theta^i - \epsilon_{ijk}\theta^j W_\mu^k. \tag{2.10}$$

The transformation here is assumed to be infinitesimal. The last step is to choose a gauge invariant kinetic term for the vector fields W_μ^i. The full Lagrangian is then defined by:

$$\mathcal{L}_{YM} = \overline{\psi}(x)(i\gamma^\mu D_\mu - m)\psi(x) - \frac{1}{4}F_{\mu\nu}^i F_i^{\mu\nu}, \tag{2.11}$$

where $F_{\mu\nu}^i = \partial_\mu W_\nu^i - \partial_\nu W_\mu^i + g\epsilon_{ijk}W_\mu^j W_\nu^k$ accounts for the self-interactions of the non-Abelian fields. This $SU(2)$ Yang-Mills gauge model theory is a perfect candidate for the weak interactions as the vector field could give rise to the weak vector bosons via:

$$W^\pm = \frac{1}{\sqrt{2}}(W_\mu^1 \mp iW_\mu^2), \quad W_\mu^0 = W_\mu^3. \tag{2.12}$$

There are two complications. Firstly, the W_μ^i fields have to be massless to retain invariance and the weak vector bosons are experimentally confirmed to be massive. Secondly, the charged weak interactions are found to couple to left-handed fermions only. These two problems will be addressed in the following section.

Electroweak Symmetry Breaking

The unification of the electromagnetic and weak forces was made possible after the absorption of the axial vector coupling to the field spinor itself

$$\psi_L \equiv \frac{(1 - \gamma^5)}{2}\psi, \tag{2.13}$$

where L stands for left-handed and $\frac{(1-\gamma^5)}{2}$ is a projection operator picking out the chirality -1 component. Similarly one can define right-handed fields as:

$$\psi_R \equiv \frac{(1 + \gamma^5)}{2}\psi. \tag{2.14}$$

---

[1]In principle an $U(2)$ group could also be considered but it has been shown experimentally that the weak symmetry needs only three generators.

	T	T^3	Y	Q
ν_{eL}	$1/2$	$1/2$	-1	0
e_L	$1/2$	$-1/2$	-1	-1
u_L	$1/2$	$1/2$	$1/3$	$2/3$
d_L	$1/2$	$-1/2$	$1/3$	$-1/3$
e_R	0	0	-2	-1
u_R	0	0	$4/3$	$2/3$
d_R	0	0	$-2/3$	$-1/3$

Table 2.3: Quantum numbers.

These modified spinors are called chiral fermion states. The charged weak bosons couple only to left-handed particles (whereas the neutral weak and electromagnetic bosons couple to both right- and left-handed particles). Each left-handed neutrino and associated left-handed charged lepton form an isospin doublet:

$$\begin{pmatrix} \nu_l \\ l \end{pmatrix}, \tag{2.15}$$

which belongs to the $SU(2)_L$ symmetry. The conserved quantum number is called weak isospin, T. It is $1/2$ for left-handed fermions and 0 for right-handed fermions. The third component of isospin, T^3, is related to weak hypercharge and electric charge, by the Gell-Mann-Nishijima formula:

$$Q = T^3 + \frac{1}{2}Y \tag{2.16}$$

and a new gauge group $U(1)_Y$ is formulated with weak hypercharge as a conserved quantum number. Putting these two symmetries together, a $SU(2)_L \times U(1)_Y$ gauge invariant theory of electroweak interactions is formulated. The left-handed fermions transform as doublets under $SU(2)_L$, whereas the right-handed fermions transform as singlets i.e., they don't transform at all. The quantum numbers for the first generation of leptons and quarks are listed in Table 2.3. For a generic left-handed fermion field f, the covariant derivative for this gauge theory is:

$$D_\mu f = \left(\partial_\mu - ig\vec{W}_\mu \cdot \vec{\tau} - ig'\frac{1}{2}B_\mu Y \right) f, \tag{2.17}$$

where g and g' are the coupling constants. For a generic right-handed fermion field, the $-ig\vec{W}_\mu \cdot \vec{\tau}$ term should be omitted. According to the gauge principle, a massless field triplet W_μ^i is introduced for $SU(2)_L$ and a singlet B_μ for $U(1)_Y$. The full Lagrangian for the electroweak gauge theory is:

$$\mathcal{L}_{EW} = \overline{\psi}i\gamma^\mu D_\mu \psi - \frac{1}{4}W_{\mu\nu}^i W_i^{\mu\nu} - \frac{1}{4}B_{\mu\nu}B^{\mu\nu}, \tag{2.18}$$

and since fermion fields, ψ_L and ψ_R, transform in a different way under $SU(2)_L$, the fermionic component of the Lagrangian ($\overline{f}i\gamma^\mu D_\mu f$) is divided into two terms.

As in the previous case of QED, the gauge invariant electroweak interactions are generated from the $\overline{\psi}i\gamma^\mu D_\mu \psi$ term. This Lagrangian is invariant under local gauge transformations for $SU(2)_L$ and $U(1)_Y$ independently. The charged weak boson fields are obtained

following Eq. 2.12. Two neutral fields (A and Z) are constructed from the mixing of the third $\vec{W}_\mu$ component with B_μ:

$$A = B \cos \theta_W + W_3 \sin \theta_W, \quad Z = -B \sin \theta_W + W_3 \cos \theta_W. \tag{2.19}$$

θ_W is the weak mixing angle and it is a parameter in the electroweak theory. It can be expressed in terms of the g and g' coupling constants as $\cos \theta_W = \frac{g}{\sqrt{g'^2+g^2}}$. For given θ_W, the weak and electromagnetic interactions are unified and their couplings related:

$$g_Z = \frac{g_e}{\sin \theta_W \cos \theta_W}, \quad g_W = \frac{g_e}{\sin \theta_W}. \tag{2.20}$$

The generation of the masses of the bosons, while preserving the renormalisability of the gauge theory, is achieved by spontaneous symmetry breaking. The gauge symmetry of the Lagrangian remains, but is hidden by the appearance of the preferred direction in weak isospin space.

2.2 The Standard Model Higgs boson

So far, no mass terms were present in the Lagrangians mentioned in the previous sections. Adding the mass terms "by hand" to the Lagrangian ($m\psi\bar{\psi}$ for fermions and $\frac{1}{2}m^2V^\mu V_\mu$ for gauge bosons) will not work as it will break the gauge invariance and make the theory not renormalisable. In a proposed solution, called the Higgs mechanism, the universe is filled with a Higgs field, which is a doublet in $SU(2)$ space, has a non-zero $U(1)$ hypercharge and is a $SU(3)$ colour singlet. By interacting with this field, the gauge bosons and fermions acquire masses. States with a Higgs field are not orthogonal to the ground state (or vacuum state) which means that the $SU(2)$ and $U(1)$ quantum numbers of the vacuum are non-zero. The symmetry is still valid for the Langrangian but not for the vacuum state of the system. Such symmetry is called a spontaneously broken symmetry.

2.2.1 Higgs mechanism

Particles arise from the excitations of the fields around their value at the minimum - the vacuum state. In other words, to identify the mass term in the Lagrangian, one first has to locate the ground state (the field configuration for which the potential is a minimum), then rewrite the Lagrangian as a function of the deviation from the minimum. The coefficient of the squared term will be recognised as a mass of a particle. Consider a Lagrangian:

$$\mathcal{L} = T - V = \frac{1}{2}\partial_\mu \phi \partial^\mu \phi - \left(\frac{1}{2}\mu^2 \phi^2 + \frac{1}{4}\lambda\phi^4 \right), \tag{2.21}$$

where μ and λ are real constants. For $\mu^2 > 0$, the vacuum clearly corresponds to $\phi = 0$ but this is not the case for $\mu^2 < 0$. Here, the lowest value of the potential is for:

$$\phi = \pm\sqrt{\frac{-\mu^2}{\lambda}} \equiv \pm v, \tag{2.22}$$

where v is called the vacuum expectation value of ϕ and ϕ is called a Higgs field. Figure 2.1 shows the potential for these two cases of μ^2. In the following, the $\phi = +v$ choice is

considered. To obtain the particle spectrum, $\mathcal{L}$ has to be rewritten as a function of the fluctuations around the vacuum state:

$$\phi(x) = v + \eta(x), \tag{2.23}$$

which yields:

$$\mathcal{L} = \frac{1}{2}\partial_\mu\eta\partial^\mu\eta - \left(\lambda v^2\eta^2 + \lambda v\eta^3 + \frac{1}{4}\lambda\eta^4\right) + \text{constant}. \tag{2.24}$$

This Lagrangian describes a particle with squared mass $m_\eta^2 = 2\lambda v^2 = -2\mu^2$ with interactions of strength proportional to λ. The original $\mathcal{L}$ from Eq.2.21 was invariant under $\phi \to -\phi$ reflection but there is no symmetry in the newly obtained Lagrangian. It was broken when a specific vacuum state was chosen.

To arrive at the SM Lagrangian's $SU(2)_L \times U(1)_Y$ symmetry, let's first consider a
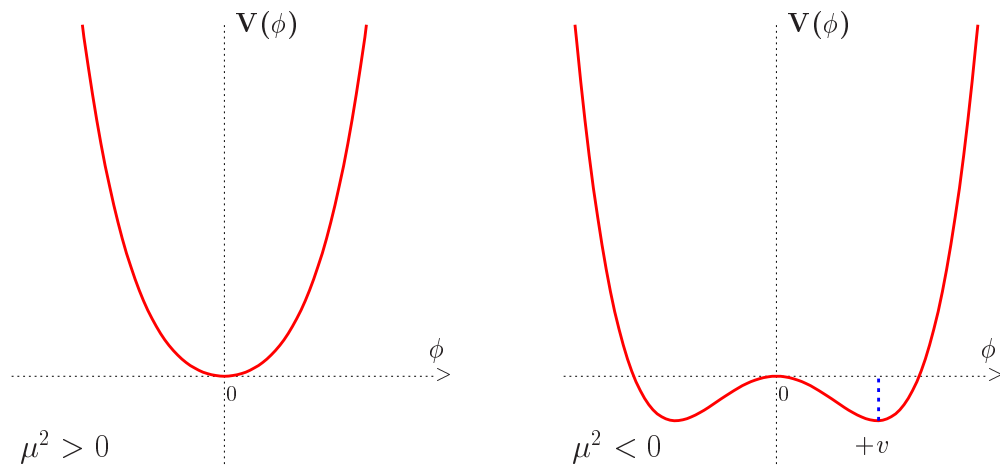
Figure 2.1: The potential V of the scalar field ϕ for $\mu^2 > 0$ (left) and $\mu^2 < 0$ (right). [10]

complex scalar field, $\phi = (\phi_1 + i\phi_2)/\sqrt{2}$, with a Lagrangian:

$$\mathcal{L} = (\partial_\mu\phi)^*(\partial^\mu\phi) - \mu^2\phi^*\phi - \lambda(\phi^*\phi)^2, \tag{2.25}$$

which is invariant under a global gauge transformation. For $\mu^2 < 0$, the minimum of the potential is along the circle of radius:

$$\phi_1^2 + \phi_2^2 = \frac{-\mu^2}{\lambda} = v^2. \tag{2.26}$$

Following the example of a real scalar field, the Lagrangian has to be expanded around $\phi_1^2 + \phi_2^2 = v^2$ which could be any point on the circle. Choosing one of them obviously breaks the global symmetry. Picking, $\phi_1 = v$, $\phi_2 = 0$, one can write:

$$\phi = \frac{(v + \eta(x) + i\xi(x))}{\sqrt{2}}, \tag{2.27}$$

with η and ξ real, and the Lagrangian can be expressed as:

$$\mathcal{L} = \frac{1}{2}(\partial_\mu\xi)^2 + \frac{1}{2}(\partial_\mu\eta)^2 + \mu^2\eta^2 - \lambda v(\eta\xi^2 + \eta^3) - \frac{\lambda}{2}\eta^2\xi^2 - \frac{\lambda}{4}\eta^4 - \frac{\lambda}{4}\xi^4 + \text{constant}. \tag{2.28}$$

The η field corresponds to a particle with a mass $m_\eta^2 = 2|\mu^2|$. The ξ^2 term has vanished implying that the ξ field particle is massless. The associated boson is called a Goldstone boson. Following the Goldstone theorem, a spin-0 massless boson appears whenever a continuous global symmetry is spontaneously broken. Requiring the Lagrangian from Eq. 2.25 to be gauge invariant implies a substitution of the partial derivative with the covariant derivative and the introduction of a massless vector field A_μ. In the result of expanding the Lagrangian around the vacuum state, the A_μ field became massive. The initial $\mathcal{L}$ had four degrees of freedom: two real scalars ϕ_1 and ϕ_2, and two transverse polarisations of the massless vector boson A_μ. The current $\mathcal{L}$ has five degrees of freedom, one for η, one for ξ, and three for the massive vector boson A_μ. This means that there must be a field which is not physical. It can be found in one of the bilinear terms of the $\mathcal{L}$ and it has to be eliminated. Rewriting the original field:

$$\phi = \frac{1}{\sqrt{2}}(v + \eta(x) + i\xi(x)) = \frac{1}{\sqrt{2}}(v + \eta(x))e^{i\xi(x)/v}, \tag{2.29}$$

profiting from the freedom of gauge transformations and making appropriate substitutions, all ξ terms disappear from the Lagrangian. This choice of gauge, for which only the physical particles are left, is called a unitary gauge.

The original $\phi(x)$ field expansion can be now written as:

$$\phi(x) = \frac{(v + h(x))}{\sqrt{2}}, \tag{2.30}$$

where h is a real scalar field and the resulting Lagrangian now has the form:

$$\mathcal{L} = \frac{1}{2}(\partial_\mu h)(\partial^\mu h) + \frac{1}{2}g^2 v^2 A_\mu A^\mu - \lambda v^2 h^2 - \lambda v h^3 - \frac{\lambda}{4}h^4 + g^2 v h A^\mu A_\mu + \frac{1}{2}g^2 h^2 A_\mu A^\mu - \frac{1}{4}F_{\mu\nu}F^{\mu\nu}. \tag{2.31}$$

The gauge boson indeed gains mass $M_A = gv$ that is non-zero only when the gauge symmetry is spontaneously broken by the Higgs field acquiring a vacuum expectation value. The previously introduced massless Goldstone boson has become the longitudinal polarisation of the new vector boson h, giving four degrees of freedom in the final state. The mechanism described is the so-called Higgs mechanism. As its consequence, a neutral, massive (with a mass $\sqrt{2\lambda v^2}$), spin-zero boson appears and is called a Higgs boson h. Its mass is not fixed but depends on the free parameter of the theory λ, that represents the Higgs self-coupling. The mass of the vector boson is fixed once g^2 and v are known.

To apply this mechanism to the Standard Model, one has to consider a Higgs field that is an $SU(2)$ doublet:

$$\phi = \begin{pmatrix} \phi^+ \\ \phi^0 \end{pmatrix}, \tag{2.32}$$

where ϕ^+ and ϕ^0 are complex fields:

$$\phi^+ = \frac{\phi_1 + i\phi_2}{\sqrt{2}} \quad \phi^0 = \frac{\phi_3 + i\phi_4}{\sqrt{2}}, \tag{2.33}$$

and the Lagrangian has the form:

$$\mathcal{L}_\phi = (\partial_\mu \phi)^\dagger (\partial^\mu \phi) - \mu^2 \phi^\dagger \phi - \lambda(\phi^\dagger \phi)^2. \tag{2.34}$$

The potential $\mu^2 \phi^\dagger \phi + \lambda(\phi^\dagger \phi)^2$ is invariant under the local gauge transformation:

$$\phi(x) \rightarrow e^{i\boldsymbol{\theta}(\boldsymbol{x})\cdot\boldsymbol{\tau}}\phi(x), \tag{2.35}$$

and the minimum of the potential for $\mu^2 < 0$ is at:

$$\phi^\dagger \phi = \frac{-\mu^2}{2\lambda} = \frac{v^2}{2}. \tag{2.36}$$

Choosing one of the possible vacuum states:

$$\phi_0 = \frac{1}{\sqrt{2}} \begin{pmatrix} 0 \\ v \end{pmatrix}, \tag{2.37}$$

corresponding to $\phi_3 = v$ and $\phi_1 = \phi_2 = \phi_4 = 0$, one can consider the following fluctuation around the ground state:

$$\phi(x) = \frac{1}{\sqrt{2}} \begin{pmatrix} 0 \\ v + H(x) \end{pmatrix}. \tag{2.38}$$

The other three components of ϕ are the needed would-be Goldstone bosons which in the end will become the longitudinal polarisation of the $W^\pm$ and Z bosons. Adding the $U(1)_Y$ symmetry, replacing ∂_μ with D_μ and picking the specific vacuum state of Eq. 2.37 gives the additional contribution to $\mathcal{L}$:

$$\frac{1}{8}v^2 g^2 \left((W_\mu^1)^2 + (W_\mu^2)^2\right) + \frac{1}{8}v^2 (g'B_\mu - gW_\mu^3). \tag{2.39}$$

Using the relations from Eq. 2.12, the first term can be rewritten as $(vg/2)^2 W_\mu^+ W_\mu^-$. The charged W bosons have acquired a mass $M_W = vg/2$! The combination of B_μ and W_μ^3 gives rise to the two neutral bosons Z_μ and A_μ with mass terms:

$$M_Z = \frac{1}{2}v\sqrt{g^2 + g'^2} \quad M_\gamma = 0. \tag{2.40}$$

One can also write:

$$M_W/M_Z = \cos\theta_W, \tag{2.41}$$

which links together the masses of the weak bosons through the electroweak mixing angle. It has been measured in various processes, yielding $\sim 30°$, and is consistent among them.

The full SM Lagrangian includes the previously defined EW term and additional terms appearing after accounting for the spontaneous symmetry breaking. These include the Higgs self-coupling and Yukawa coupling terms, with the latter one responsible for providing the fermion masses. As a result of the Higgs mechanism, the interactions of the Higgs field with fermions and gauge bosons are proportional to the gauge coupling and the corresponding particle masses:

$$f\bar{f}H \; : \; -i\frac{g}{2}\frac{m_f}{M_W} \; ; \quad W_\mu^+ W_\nu^- H \; : \; igM_W g_{\mu\nu} \; ; \quad Z_\mu Z_\nu H \; : \; \frac{ig}{\cos\theta_w}M_Z g_{\mu\nu}$$

The Higgs boson mass m_H and the Higgs self-coupling λ are free parameters of the SM and they are related by $\lambda = \frac{m_H^2}{2v^2}$.

Higgs mass constraints

All the parameters of the SM including the coupling constants, gauge boson and fermion masses, and quark mixing angles, have been determined experimentally, except for the Higgs boson mass. All of these parameters can be used to calculate any given physics
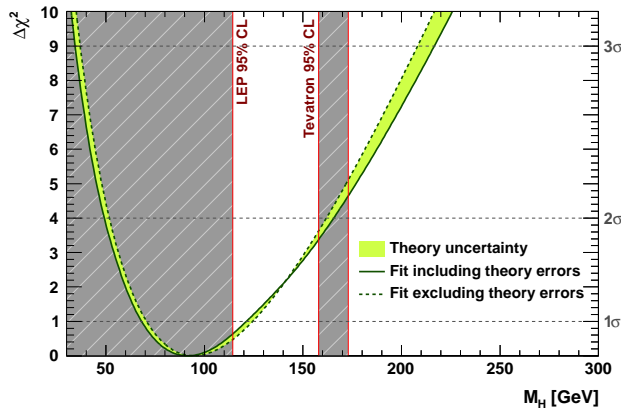
Figure 2.2: Indirect constraints on the Higgs mass using a $\Delta\chi^2$ fit [14].

observable and then compare the results with the experimental data. To have a more accurate description, higher order terms of the perturbative calculations are needed, so-called radiative corrections. Since the Higgs particle contributes to these radiative corrections to high-precision electroweak observables, constraints on its mass can be derived. Additionally direct constraints from the searches carried out by LEP [11, 12] or Tevatron [13] experiments can be used. Figure 2.2 shows the $\Delta\chi^2$ of the combined fit of the electroweak data as a function of m_H. The constraint on the Higgs mass is $m_{\mathrm{H}} = 91^{+30}_{-23}$ GeV with a 95% (99%) upper bound of 163 GeV (194 GeV).

2.3 The Higgs Boson at the LHC

2.3.1 Phenomenology of $p - p$ collisions

$p - p$ collisions are described by the interactions between the constituents of the protons, called partons. They include three valence quarks (uud), sea quarks and gluons, each of them carrying momentum fractions x_i. The hadronic interaction can be factorised into a hard scatter process (with high momentum transfer Q^2) and soft interactions between the proton remnants, defined by perturbative and non-perturbative QCD, respectively. The factorisation scale characterises the boundary between the hard and soft processes. The cross section of the $p - p$ interaction depends on the cross section of the hard scatter process which is calculable in pQCD. The rest is confined to universal and measurable parton density functions (PDFs) which are defined as the density for finding a particle with a certain longitudinal momentum fraction x_i at momentum transfer Q^2. Assuming a and b to be the constituents of the protons A and B, the hadronic interaction can be written as:

$$A + B \rightarrow c + X, \tag{2.42}$$

with the hard scatter process defined as $a + b \rightarrow c + X$. The resulting cross section is

$$\sigma_{A+B \rightarrow c+X} = \sum_{a,b} \int dx_a dx_b f_{a/A}(x_a, \mu_F) f_{b/B}(x_b, \mu_F) \hat{\sigma}_{a+b \rightarrow c+X}, \tag{2.43}$$

where the sum extends to all partonic processes leading to the production of particle c, and μ_F is the factorisation scale separating the hard and soft processes. $f_{a/A}, f_{b/B}$ denote
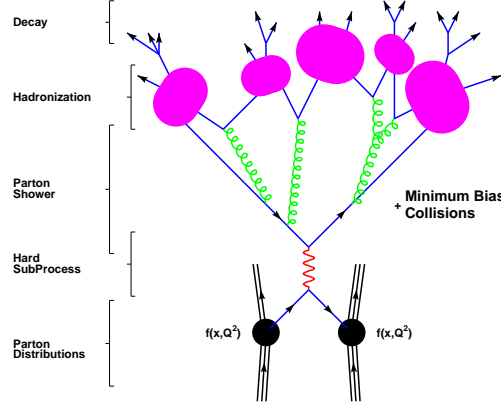
Figure 2.3: A graphical representation of a $p - p$ collision [15].

the PDFs which can be measured for example in deep inelastic scattering experiments at a given Q^2. The extrapolation to all values of Q^2 uses DGLAP evolution equations.

In the hard scattering, many quarks and gluons are produced. The quarks then radiate gluons which further radiate or create new $q\bar{q}$ pairs forming a parton shower (PS). Such parton showers can be also produced from the initial state partons which do not take part in the hard scatter process. The resulting coloured partons (quarks and gluons) cannot exist freely due to colour confinement. Instead they form colourless hadrons in a process called hadronisation. A narrow cone of such hadrons is called a jet. All contributions to the final state in a $p - p$ interaction not originating from the hard process are referred to as underlying event (UE). This also includes initial state and final state radiation, as well as interactions of the proton remnants. An example of a proton-proton collision is shown in Figure 2.3.

2.3.2 The Higgs boson at the LHC

The search for the Higgs boson is one of the main physics goals of the LHC and its two general-purpose experiments, ATLAS and CMS. This section summarises the production and decay modes of the Higgs boson in $p - p$ collisions at the LHC.

Production modes

The dominant production mechanism of the Higgs boson include: gluon-gluon fusion (ggF), vector boson fusion (VBF), associated production with W/Z bosons (W/ZH, also called Higgsstrahlung) and associated production with a pair of heavy quarks. The relevant processes are shown below and Figure 2.4 shows corresponding Feynman diagrams. Figure 2.5 shows the Standard Model Higgs boson production cross section for each of the production modes at $\sqrt{s} = 8$ TeV together with the corresponding theoretical uncertainties.

$$
\begin{aligned}
\text{gluon} - \text{gluon fusion}: \quad & gg \to H \\
\text{vector boson fusion}: \quad & qq \to qq + V^*V^* \to qq + H \\
\text{associated production with } W/Z: \quad & q\bar{q} \to V + H \\
\text{associated production with heavy quarks}: \quad & gg, q\bar{q} \to Q\bar{Q} + H
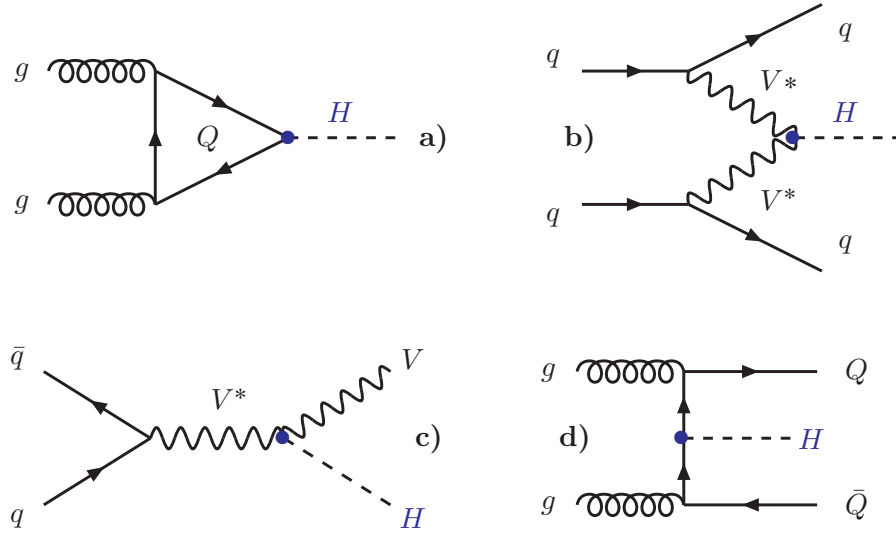\end{aligned}
\tag{2.44}
$$

Figure 2.4: Feynman diagrams describing Higgs production: a) ggF, b) VBF, c) W/Z H and d) QQH

The Higgs boson production cross sections and decay branching ratios as well as their uncertainties are compiled in Refs. [16, 17]. The gluon-gluon fusion process via a heavy quark loop is the most important process mainly because its cross section is the highest. Since the coupling of particles to the Higgs boson is proportional to their mass, it is enough to consider only top quark loops. The dynamics of this process is controlled by the strong interactions with the leading order (LO) contribution [18] proportional to α_s^2. The QCD radiative corrections at next-to-leading order (NLO) have been evaluated both for the large-m_t limit [19, 20] and maintaining the quark-mass dependence [21, 22]. They both increase the cross section by about 80-100%. The large-m_t limit is a very good approximation of the exact procedure and it was used in the next-to-next-to-leading order (NNLO) correction [19–21, 23–25] calculation, which further increases the cross section by about 25%. Soft-gluon resummations up to next-to-next-to-leading log (NNLL) [26] were also applied and they increase the cross section by 7-9%. The QCD corrections use the MSTW2008 PDF set [27] in the calculations. NLO electroweak (EW) radiative corrections are also applied [28, 29]. The results are compiled in Refs [30–32] assuming factorisation of QCD and EW corrections.

The second highest contribution arises from the vector boson fusion process where the SM Higgs is produced with two hard jets in the forward and backward regions of the detector. The cross sections are calculated with full NLO QCD and EW corrections [33–35], and approximate NNLO QCD corrections are applied [36]. The unique jet-production signature offers very good background suppression and allows for a clean signal selection following specifically designed VBF cuts. Recent studies show that only 4-5% of the ggF production contributes in the typical VBF selection [37].

The remaining contributions include the associated production with W/Z bosons, where the cross sections are calculated exactly at NLO [38] and at NNLO [39] in QCD, and NLO EW radiative corrections [40] are applied. The cross sections for associated Higgs production with a $t\bar{t}$ pair are calculated at NLO QCD [41–44].
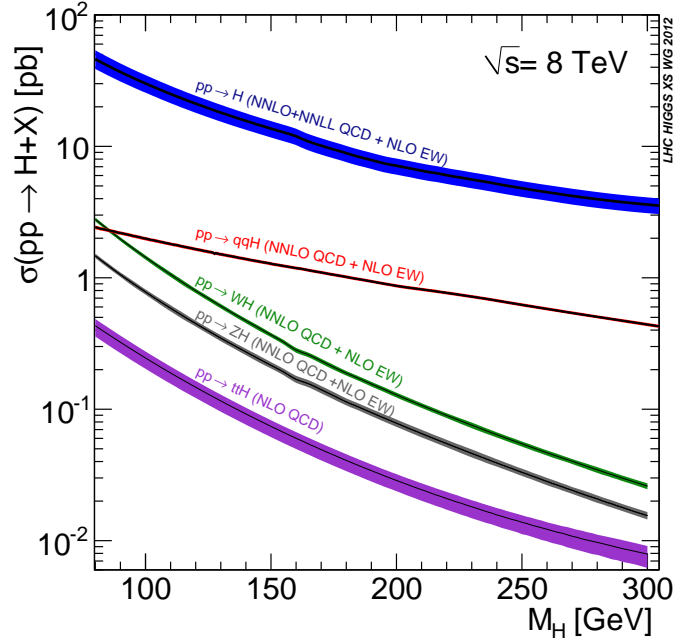
17

Figure 2.5: The Standard Model Higgs boson production cross section at $\sqrt{s} = 8$ TeV. The coloured bands indicate the total theoretical uncertainties. [16, 17].

Theoretical uncertainties

The uncertainties on the signal production cross sections include uncertainties on the QCD renormalisation and factorisation scales, on the PDF set used to evaluate the cross section and acceptance, and on the underlying event and parton shower model used [17]. Unaccounted for higher-order QCD radiative corrections are the major source of uncertainty. They are estimated by varying the QCD factorisation and renormalisation scales around a central value μ_0, which is in the order of the scale of the hard process. The scales are then independently varied in the range $0.5\mu_0 \leqslant \mu_F, \mu_R \leqslant 2\mu_0$ with a constraint $0.5 \leqslant \mu_F/\mu_R \leqslant 2$. The resulting QCD scale uncertainties, calculated for $m_H = 125$ GeV, are 8%, 20%, and 70% on the inclusive cross sections for events with $\geqslant 0$, $\geqslant 1$, and $\geqslant 2$ jets. Those uncertainties are assumed to be uncorrelated and are converted into uncertainties on the cross sections in exclusive jet multiplicity final states according to the prescription documented in Refs. [17, 45, 46]. The final uncertainties on the ggF production cross-section for $m_H = 125$ GeV are 17% for the $N_{\text{jet}} = 0$ and 36% for $N_{\text{jet}} = 1$ final states. The uncertainties on the PDF set used, on UE and PS are discussed in Chapter 5.

Decay modes

In the Standard Model, once the Higgs mass is fixed, the properties of the Higgs particle are uniquely determined. The Higgs couplings to gauge bosons and fermions are directly proportional to the masses of the particles and the Higgs boson will have the tendency to decay to the heaviest ones allowed kinematically. The main modes include decays into a pair of fermions or a pair of gauge bosons, and are represented by Feynman diagrams in Figure 2.6. Since photons and gluons are massless, they do not couple directly to the Higgs boson. Nevertheless, $\gamma\gamma$ or gg final states can be generated via loops involving massive
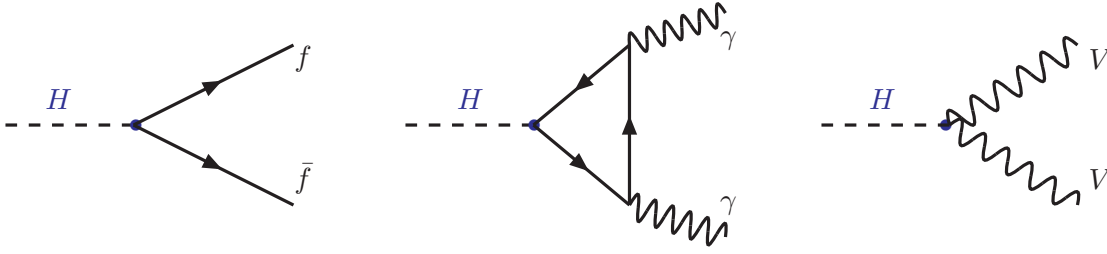
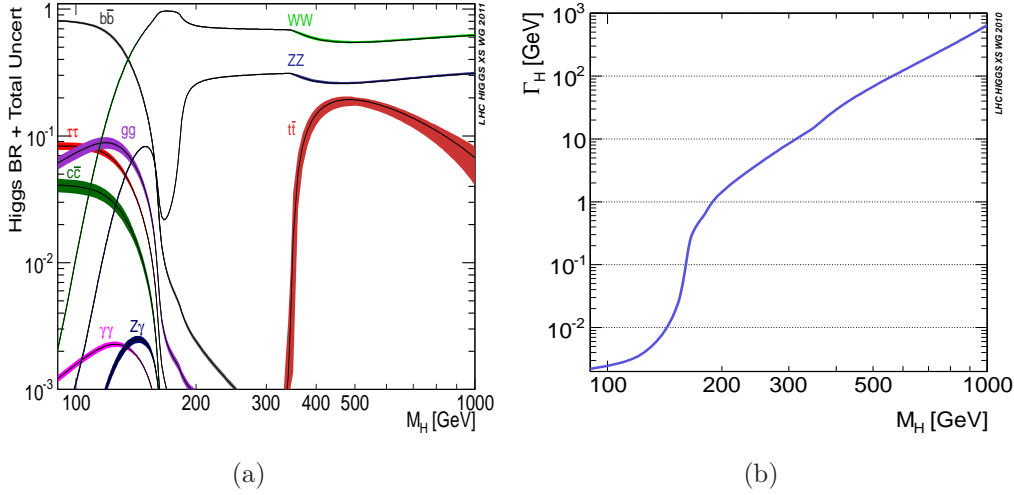Figure 2.6: Feynman diagrams of the Higgs boson decay modes.

(a)

(b)

Figure 2.7: SM Higgs boson decay branching ratios and total width [16, 17].

(charged or coloured) particles. In the mass range 130 GeV $< m_H$, the dominant decay is into $b\bar{b}$ with a branching ratio (BR) 60-90% depending on the Higgs mass. Decays into $\tau\bar{\tau}$, $c\bar{c}$ and gg follow with about 5% BR. $\gamma\gamma$ and $Z\gamma$ are very clean signals but are also very rare. In the mass range above 140 GeV, decays to WW and ZZ become dominant. Below the $2 \times m_V$ threshold, at least one of the gauge bosons must be virtual. Above 200 GeV, the ratio of WW and ZZ is fairly constant with WW decay being twice more frequent. The $t\bar{t}$ decay channel becomes relevant only for higher masses, with a BR up to 10%. The theoretical uncertainties on the Higgs branching ratios are well understood for the decays into a pair of gauge bosons. The decays into quarks and gluons are dominated by the uncertainties that are mainly due to the poor knowledge of the bottom and charm quark masses. In the low mass range, the Higgs is very narrow, with $\Gamma_H < 10$ MeV. At the ZZ threshold, the width reaches 1 GeV. For very large masses the decay width is at the level of the Higgs mass itself and the Higgs can hardly be considered a resonance. A summary of the branching ratios with the theoretical uncertainty and the total decay width of the Higgs boson is shown in Figure 2.7.

The detection potential of the Higgs boson in various decay channels depends on the understanding and the rate of the backgrounds. In order to efficiently suppress these, the kinematics and the unique signatures of the various decay channels have to be exploited. The production rate of different background and Higgs signal processes for both $p\bar{p}$ and pp collisions is shown in Figure 2.8. In the gluon-gluon fusion production process, the most promising discovery channels are $H \to \gamma\gamma$, $H \to ZZ^{(*)}$ and $H \to WW^{(*)}$.

proton - (anti)proton cross sections

σ_{tot}

Tevatron   LHC

σ_b

$\sigma_{jet}(E_T^{jet} > \sqrt{s}/20)$

σ_W

σ_Z

$\sigma_{jet}(E_T^{jet} > 100\ \text{GeV})$

σ_t

$\sigma_{jet}(E_T^{jet} > \sqrt{s}/4)$

$\sigma_{Higgs}(M_H = 120\ \text{GeV})$

200 GeV

500 GeV

WJS2009

σ (nb)

events / sec for $\mathcal{L} = 10^{33}\ \text{cm}^{-2}\text{s}^{-1}$

$\sqrt{s}$ (TeV)
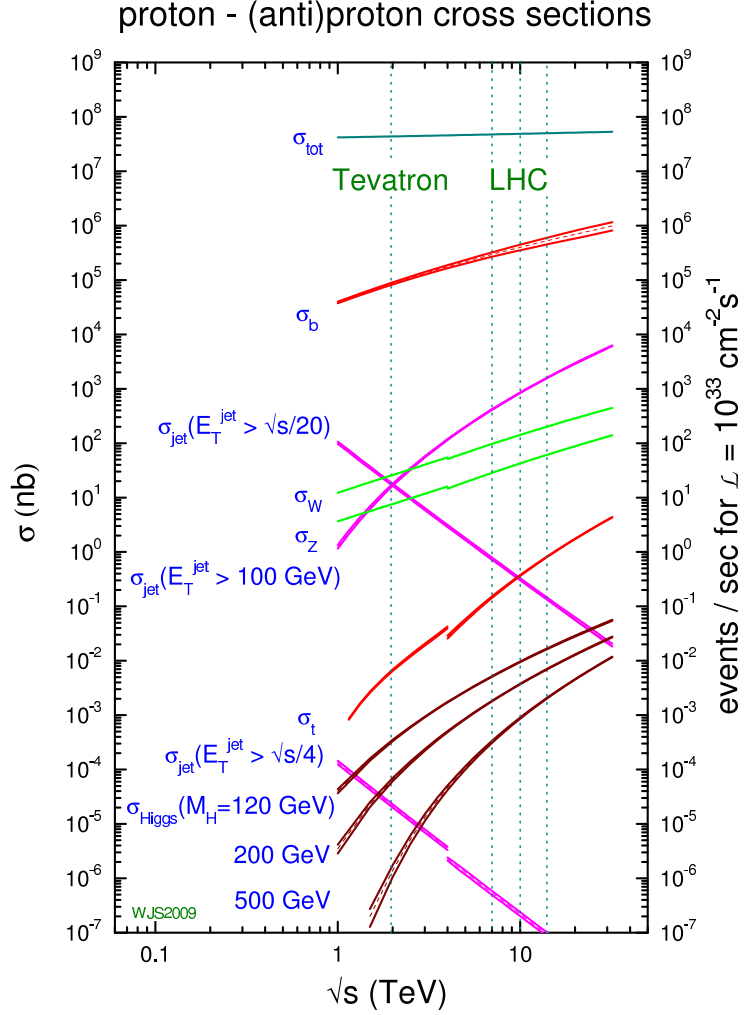
Figure 2.8: Production rates for signal and background processes at the Tevatron and LHC [47].

$H \rightarrow WW^{(*)}$ decay channel

This decay channel has a large rate across the full mass range and is the dominant one above 130 GeV. W bosons decay either leptonically or hadronically, giving rise to $\ell\nu\ell\nu$, $\ell\nu qq$ or $qqqq$ final states. In the case of the fully leptonic decay, which is the topic of this thesis, the mass of the Higgs boson cannot be fully reconstructed and a substitute in the form of a transverse mass variable has to be used. An explanation of this choice is given in Chapter 5. The major backgrounds include SM WW, $t\bar{t}$ and W+jets processes. One of the The most powerful separation from these backgrounds relies on the angular correlations between the leptons. Since the SM Higgs boson is a spin-zero particle the emerging W bosons have opposite spins, and since they couple to left-handed fermions only it means that the leptons tend to be emitted in the same direction. The signal sensitivity can also be improved by considering jet categories. The Feynman diagram describing this decay is shown in Figure 2.9.

Figure 2.9: Feynman diagram of the $H \to WW^{(*)} \to \ell\nu\ell\nu$ production and decay mode.

Chapter 3

The LHC and the ATLAS experiment

The Large Hadron Collider (LHC) is an accelerator located at CERN (European Organization for Nuclear Research) beneath the Franco-Swiss border near Geneva, Switzerland (see Figure 3.1). It was built from 1998 to 2008 in the o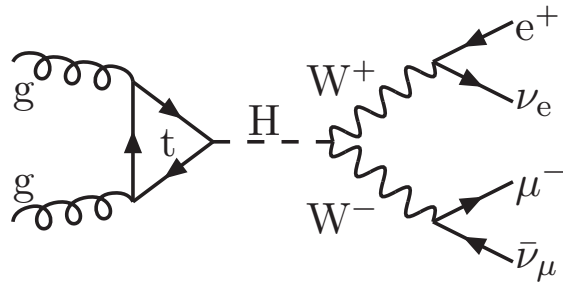ld tunnel occupied before by the Large Electron-Positron collider (LEP [48]). It has a circumference of 26.7 km and is located at a mean depth of 100 meters and at a gradient of 1.4%. Its depth varies between 175 meters (under the Jura mountain) to 50 meters (towards Lac Leman). The LHC is designed to collide both beams of protons and of heavy ions (Pb^{82+}). The beams interact with each other in four points along the LHC tunnel. These points mark the places of the collisions inside the detectors. There are two general-purpose detectors, ATLAS (A Toroidal LHC Apparatus) and CMS (Compact Muon Solenoid), and two specialised ones, LHCb (LHC-beauty) and ALICE (A Large Ion Collider Experiment). Since the original design three smaller detectors were installed at the LHC site: LHCf (LHC forward experiment), MoEDAL (Monopole and Exotics Detector at the LHC) and TOTEM (Total Cross Section, Elastic Scattering and Diffraction Dissociation at the LHC).

The physics program at the LHC is very broad and covers many areas of interest, but it is nevertheless possible to depict a few major points. Possibly the most important one is the confirmation (or exclusion) of the Higgs mechanism which is believed to complete the Standard Model of particle physics. Another main area of interest is probing the existence of SM extensions like Supersymmetry, which could also explain some of the questions on the dark matter and dark energy in our universe. The mystery of the matter-antimatter imbalance is another issue the LHC could shed light on. Last but not least, the heavy ion collisions are the perfect probe to the conditions of the early universe by creating and letting us study the quark-gluon plasma.

This chapter introduces the LHC complex in Section 3.1 followed by a brief description of its experiments. Section 3.2 concentrates specifically on the ATLAS detector, its performance and subdetectors.

3.1 The Large Hadron Collider

The first beams were circulated in the LHC tunnel on September 10th 2008. After an unfortunate accident 9 days later there was a requirement for a long technical intervention which lasted for over a year. The first collisions at the center-of-mass energy of 7 TeV
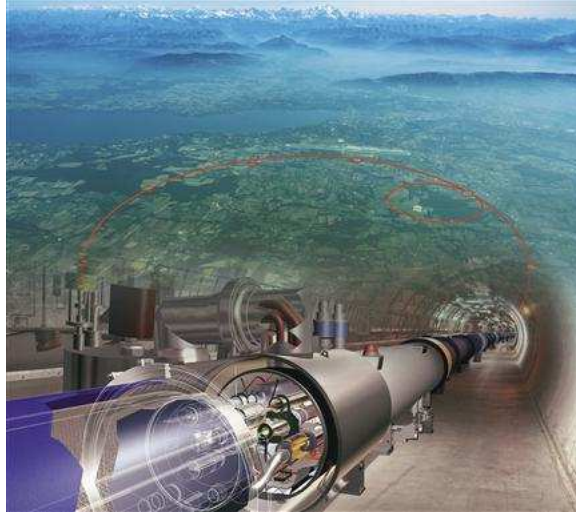
Figure 3.1: Aerial view of the LHC and the LHC tunnel with a dipole magnet [49].

were delivered and recorded in the beginning of 2010. This already exceeded the energy of the proton-anti-proton collisions ($\sqrt{s} = 1.96$ TeV) at Tevatron, Fermilab [50]. The LHC kept on running with 3.5 TeV energy per beam throughout 2010 and 2011, while increasing the instantaneous luminosity and the number of bunches per beam. In the following year, 2012, the energy was increased and the LHC started colliding protons at $\sqrt{s} = 8$ TeV. The design 14 TeV centre-of-mass energy and instantaneous luminosity of 10^{-34}cm^{-2}s^{-1} should be reached after a long shut down.

3.1.1 LHC accelerator complex and design

The schematic design of the LHC accelerator complex can be seen in Figure 3.2. It all starts with a bottle of hydrogen at the very beginning of the chain. To obtain protons, the hydrogen atoms are stripped of their orbiting electrons. The first acceleration to the energy of around 50 MeV is performed in LINAC2 (in the case of heavy ions LINAC3 is used). Then the protons are injected into the PS Booster (PSB) where the first bunches are formed and the energy is further increased to 1.4 GeV. The goal of the PSB is also to squeeze the newly formed bunches. The beam then is transferred through the TT1 transfer line to the Proton Synchrotron (PS) and Super Proton Synchrotron (SPS) which sequentially accelerate the beam to 25 GeV and 450 GeV. The final stage consists of injecting the beams of proton bunches to the LHC, where they reach their designated energy.

The procedure for obtaining the lead ion beams is to some extent similar to the proton beam case. The major difference is in the way the ions are prepared. The process starts with the ionised lead vapour (heated to around 550°C). Pb^{29+} ions are selected and accelerated to 4.2 MeV/u (per nucleon energy) in LINAC3. Then, after passing through a carbon foil, a Pb^{54+} beam is accumulated, further accelerated to 72 MeV/u in the Low Energy Ion Ring (LEIR) and transferred to the PS after preparing the first bunch structure. In the PS the beam gets a boost to 5.9 GeV/u and is then sent through another stripping foil which selects the final sample of the Pb^{82+} lead ions. The SPS accelerates the beam to 177 GeV/u before passing it on to the LHC, which accelerates it to the final energy of 2.76 TeV/u.
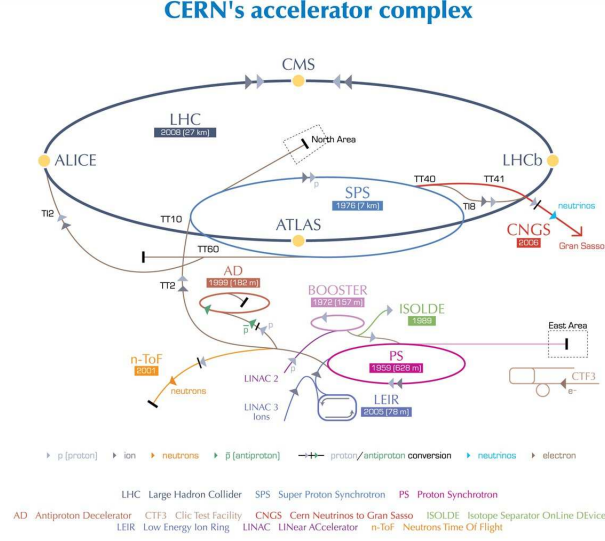
Figure 3.2: The full complex of CERN accelerators [51].

The following paragraphs explain in more detail the principles of the LHC operation and describe the collisions (bunches, number of interactions, luminosity). As can be seen from Table 3.1, which shows the basic parameters of the LHC, the number of magnets is quite substantial. They are mainly used for bending and focusing the beams. The most notable ones (and at the same time, the biggest and the heaviest; each is 14.3 m long and weighs $\sim$ 35 tonnes) are the main dipoles. They use the technology of Nb-Ti (niobium-titanium) cables which become superconductive below 10 K. To increase the performance of the superconductivity (for example Tevatron used the Nb-Ti magnets, cooled down using helium, which produced a magnetic field of 5 T), the magnets are cooled down to 1.9 K. This in turn enables them to run the high current 11 700 A and produce the magnetic field of 8.4 T. The magnets have two apertures, one for each of the counter-rotating beams, which makes them coupled both magnetically and mechanically. Apart from the dipole magnets, there are also 858 quadrupole magnets whose aim is to focus the beams. The focusing allows the beams' width and height to be constrained in the vacuum tube. Typically the focusing and de-focusing magnets are combined together and they keep the beams oscillating around the nominal orbit. It was measured that the magnetic coupling between the two apertures is negligible. The quadrupole magnets are also kept in a superconducting state with the help of superfluid helium. The acceleration of the bunches is performed using the electric fields in the RF (radio frequency) cavities. Each of the eight cavities per beam delivers 2MV (using an accelerating field of 5MV/m) at 400 MHz. They operate at 4.5K and are grouped in the cryomodules.

To ensure that the particles always see an accelerating voltage, the RF frequency must be an integer multiple of the revolution frequency:

$$h = \frac{f_{RF}}{f_{rev}}, \tag{3.1}$$

where $f_{rev} = \frac{\beta c}{2\pi R}$. In the LHC, the harmonic number h can be at most 35640. The segments of the circumference centred on these virtual points are called buckets. A particle with

Parameter	Number
Circumference	26.7 km
Dipole operating temperature	1.9 K
Number of magnets	9593
Number of main dipoles	1232
Number of main quadrupoles	392
Number of RF cavities	8 per beam
Nominal energy, protons	7 TeV
Nominal energy, ions	2.76 TeV/u
Peak magnetic dipole field	8.33 T
Min. distance between bunches	~7 m
Design luminosity	$10^{34} \text{cm}^{-2}\text{s}^{-1}$
No. of bunches per proton beam	2808
No. of protons per bunch (injection)	1.1×10^{11}
Number of turns per second	11 245
Number of collisions per second	600 million

Table 3.1: The design parameters of the LHC operating at $\sqrt{s} = 14$ TeV.

h=1 will keep a constant energy as it will be synchronised with the cavity's frequency and will not be accelerated at all. All the other particles will oscillate longitudinally around the synchronous particle under the influence of the RF system and will form a bunch. A bunch will be contained inside a bucket but it is useful to note that not all the buckets have to be filled with bunches. The configuration of the buckets will determine the collision points in the LHC, where the maximum number of the occupied buckets can be 2808.

The beam emittance, ϵ, is determined in the process of bunch preparation and it defines the area of the phase space volume occupied by the beam. The amplitude function, β, is determined by the accelerator magnet configuration and it describes the width of the beam squared divided by the emittance ($\beta = \pi\sigma^2/\epsilon$, when σ is the cross sectional size of the beam). The smaller the β the narrower (more squeezed) the beam is. β^* is the value of the β function at the collision point. In 2012, the LHC has been running with 1380 bunches, 50 ns bunch spacing and β^* of 0.6 m.

An important parameter of every accelerator is the luminosity, which is a measure of the number of collisions per cm^2 and per second. It can be determined directly from the beam parameters using the following formula:

$$L = \frac{n_{b_1} n_{b_2} N_1 N_2 f_{rev} \gamma}{4\pi\epsilon\beta^*} F, \qquad (3.2)$$

where n_{b_1} and n_{b_2} are the numbers of bunches in each beam, N_1 and N_2 are the number of protons per bunch in the beams, f is the revolution frequency, γ is the relativistic factor and F is a geometric luminosity reduction factor ($\leqslant 1$), due to the crossing angle at the interaction point (ϵ and β^* were defined previously). This formula expresses the instantaneous luminosity which obviously decreases with time as we have fewer protons with every collision. The beams can in principle collide for multiple hours. Production rates are proportional to the integrated luminosity defined as:
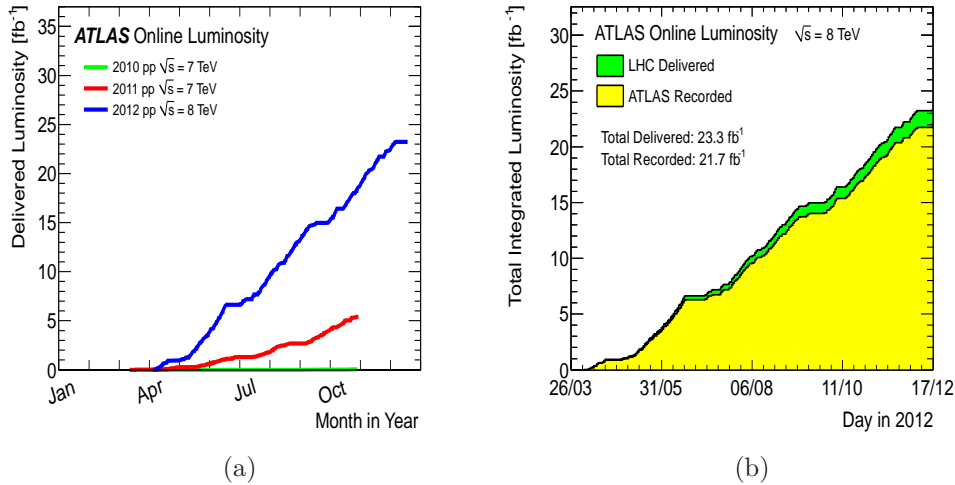
$$\mathscr{L} = \int L dt \qquad (3.3)$$

Figure 3.3: Delivered luminosity to ATLAS over the last years of p-p collisions (a) and the integrated luminosity in 2012 only (b) [51].

This parameter is expressed in units of inverse barns, where $1b = 1 \times 10^{-28} \mathrm{m}^2$. In 2010 the ATLAS detector recorded 45.0 pb^{-1} at 7 TeV centre-of-mass energy. This value was significantly increased in 2011 data taking and yielded 5.25 fb^{-1}. In the 2012 data-taking period, the ATLAS detector recorded 21.7 fb^{-1} at $\sqrt{s} = 8$ TeV. Figure 3.3a shows the delivered luminosity to ATLAS during stable beams for $p - p$ collisions in 2010, 2011 and 2012. Figure 3.3b shows the delivered and recorded integrated luminosity by ATLAS in 2012. Data collected in 2012 until September were used in the analysis presented in this thesis.

Related to the instantaneous luminosity is the mean number of interactions per crossing, referred to as pile-up events, defined by the relation:

$$\mu = \frac{L\sigma_{inel}}{n_b f_{rev}}, \tag{3.4}$$

where σ_{inel} is the inelastic cross section taken to be 71.5 mb for 7 TeV collisions and 73.0 mb for 8 TeV collisions. Figure 3.4 shows the luminosity-weighted distribution of the mean number of interactions per crossing for the 2011 and 2012 datasets. The average number of interactions per crossing increased from 10 to 20 across the years.

3.1.2 Experiments at the LHC

As was mentioned before, the LHC delivers $p - p$ and heavy ion collisions to 4 major experiments. Two of them, ATLAS and CMS, are general-purpose ones which have a very broad physics programme. ALICE was specifically designed to provide an insight into heavy ion collisions and the quark-gluon plasma. The last of the major experiments is LHCb; it is a forward detector whose main focus is the study of rare B decays and the asymmetry between matter and antimatter present in interactions of B-particles (containing b quarks).

There are three additional experiments at the LHC. TOTEM is located near the collision point of the CMS detector; it measures the total $p - p$ cross section and studies elastic scattering and diffractive dissociation at the LHC. LHCf consists of two calorimeters placed
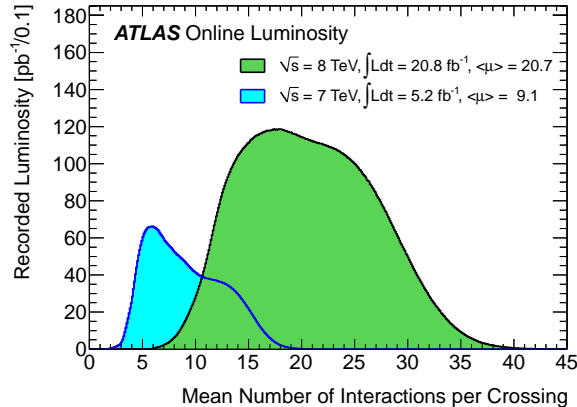
Figure 3.4: Average number of interactions per crossing in 2011 and 2012 data [51].

140m away from the ATLAS interation point. Their purpose is to study forward produc-tion of neutral particles in $p - p$ collisions. The MoEDAL detector is located in the LHCb cavern and it was designed to search for magnetic monopoles and other highly ionising stable massive particles (SMPs).

3.2   The ATLAS detector

The ATLAS detector is a general-purpose detector, which means that it was designed to cover a wide range of physics searches and measurements. It is 25 m high, 25 m wide and 46 m long, which makes it the largest experiment at the LHC. Its weight is approximately 7000 tonnes and it comprises a complex magnet system. The detector and physics perfor-mance is described in detail in the Technical Design Report (TDR) [52, 53] and later in the ATLAS technical paper [54]. Here only an overview of the main components of the ATLAS experiment and their performance is given.

As depicted in Figure 3.5, the ATLAS experiment is composed of different sub-detectors: Inner Detector (ID), calorimeters (Liquid Argon and Tile) and Muon Spectrom-eter (MS). Different particles leave different signatures in the sub-detectors. Figure 3.6 shows the trajectories and the detection points of the final state particles that are observed in the ATLAS detector. The closest to the IP is the set of trackers: the pixel detector, the semiconductor tracker (SCT) and the transition radiation tracker (TRT). Having them immersed in the solenoid field enables a measurement of the momenta of the charged parti-cles such as electrons, muons and pions. The energy measurement is based on the deposits in the electromagnetic and hadronic calorimeters. The final set consists of the muon de-tectors and toroid magnets which provide the momentum and position measurements of the muons. Neutrinos are almost massless, neutral and weakly interacting particles, which allows them to escape the detector without leaving any trace. They will manifest their existence in the form of apparent missing momentum. The required resolution and $|\eta|$ coverage for the different sub-systems of ATLAS is listed in Table 3.2.

ATLAS uses a coordinate system with the origin at the IP in the centre of the detector, and the z-axis along the beam line, with the side-A of the detector defined as that with the positive z. The $x - y$ plane is orthogonal to the beam axis, with the positive x axis pointing from the detector to the center of the LHC ring and the positive y axis pointing
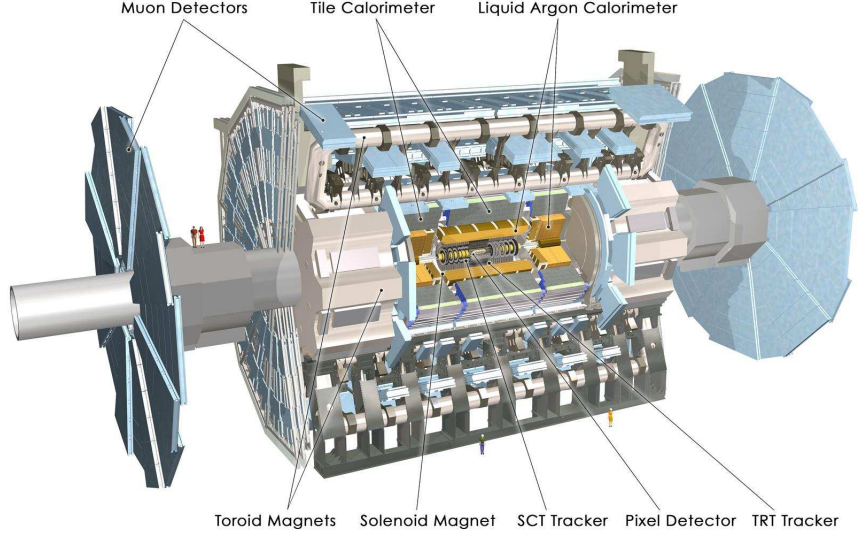
Figure 3.5: The ATLAS detector [51].

Detector component	Resolution	$\|\eta\|$ coverage	
		Measurement	Trigger
Tracking	$\sigma_{p_T}/p_T = 0.05\%\ p_T \otimes 1\%$	$\pm\ 2.5$	
EM Calorimetry	$\sigma_E/E = 10\%/\sqrt{E} \otimes 0.7\%$	$\pm\ 3.2$	$\pm\ 2.5$
Hadronic Calorimetry(jets)			
barrel and end-cap	$\sigma_E/E = 50\%/\sqrt{E} \otimes 3\%$	$\pm\ 3.2$	$\pm\ 3.2$
forward	$\sigma_E/E = 100\%/\sqrt{E} \otimes 10\%$	$3.1 < \|\eta\| < 4.9$	$3.1 < \|\eta\| < 4.9$
Muon Spectrometer	$\sigma_{p_T}/p_T = 10\%$ at $p_T = 1\text{TeV}$	$\pm\ 2.7$	$\pm\ 2.4$

Table 3.2: General performance goals of the ATLAS detector. The units are in GeV. [54]

upwards towards the surface. The azimuthal angle ϕ is measured around the beam axis, and the polar angle θ is the angle from the positive z axis towards the y axis. The rapidity is a very important quantity and is defined as:

$$y = \frac{1}{2}\ln(\frac{E + p_z}{E - p_z}), \qquad (3.5)$$

where E is the energy of the particle and p_z is the particle's momentum component in the z direction. Rapidity differences are invariant under boosts along the beam direction. Because masses of the particles cannot be measured, more common usage has the pseudorapidity $\eta = -\ln(\tan(\frac{\theta}{2}))$, which is actually the limit of y when setting the masses to zero. The value of $\eta = 0$ is at $\theta = \pi/2$. The distance ΔR in $\eta - \phi$ plane is defined as $\Delta R = \sqrt{\Delta^2\eta + \Delta^2\phi}$.

The momentum of each particle in the collision can be decomposed into a component parallel (longitudinal, along the z axis) and perpendicular (transverse, in the $x - y$ plane) to the beam. The transverse momentum p_T is defined as:

$$p_T = p\sin(\theta), \qquad (3.6)$$

and is also Lorentz invariant under longitudinal boosts. In hadron colliders, the incoming particles collide head-on and have negligible transverse momentum before the hard scattering. This means that the final state particles have approximately zero total transverse momentum. In the case of processes involving neutrinos in the final state, there will be missing transverse momentum observed. The momentum along the beam line (p_z) is usually associated to the underlying event.
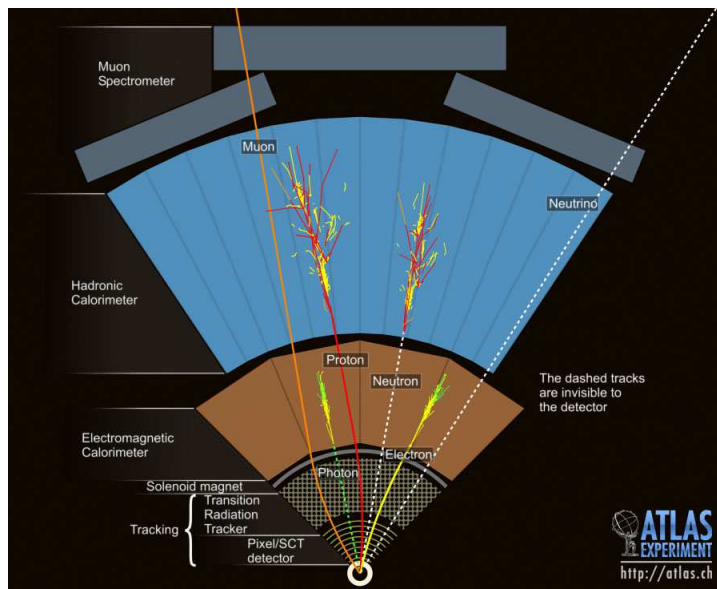
Figure 3.6: An illustration of the signatures of different particles in the ATLAS detector [51].

3.2.1 Inner Detector

The ID is the closest detector located directly around the beam pipe. It is contained within a cylinder of length 7 m and a radius of 1.15 m, limited by the solenoid magnet and LAr electromagnetic calorimeter. The whole inner detector is immersed in a solenoidal magnetic field of 2 T. It consists of three highly granular sub-systems: pixel detector, SCT layers and TRT straws. Pattern recognition, momentum and vertex measurements are achieved with a combination of the inner tracking detectors. The outer part has the capability of measuring the transition radiation produced by ultra-relativistic charged particles, which contributes to the particle identification process and is mainly used to help distinguish $e^\pm$ from $\pi^\pm$. The layout of the ATLAS ID provides full tracking coverage for $|\eta| \leqslant 2.5$ and is presented in Figure 3.7. In the barrel region, the high-precision detector layers are arranged on concentric cylinders around the beam axis, while the end-cap detectors are mounted on disks perpendicular to the beam axis. Each track of a charged particle can be fully identified by five parameters which are measured at the point of closest approach to the nominal beam axis ($x = 0$ and $y = 0$). They include:

- q/p - charged curvature

- d_0, z_0 - impact parameters in $x - y$ and $r - z$ planes respectively

- ϕ, θ - azimuthal and polar angles.
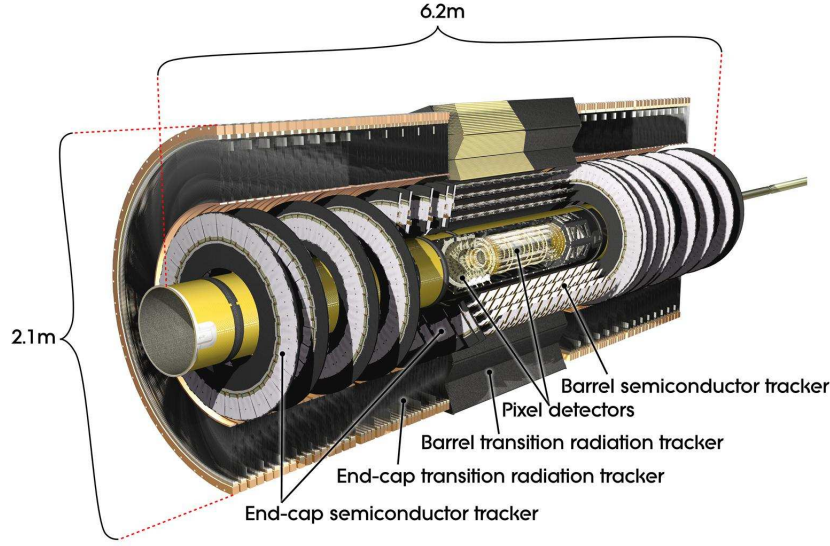
Figure 3.7: The layout of the ATLAS inner detector [51].

Typically for each track the pixel detector contributes three and the strip layers four space points. At larger radii approximately 36 tracking points are provided by the TRT straws (see Figure 3.8). The relative precision of the measurement is well matched, so that no single measurement dominates the momentum resolution.

The pixel detector is designed to provide a very high-precision set of measurements as close to the interaction point as possible. Its primary goal is to determine the interaction point, the impact parameter resolution and to provide the identification of short-lived particles such as b hadrons or τ leptons. The system consists of three barrels at average radii of 5 cm, 9 cm, and 12 cm, and three disks on each side, between radii of 9 and 15 cm, and reaching until $|z| = 65$ cm, which complete the angular coverage. The pixel barrel layers are segmented in $r - \phi$ and z whereas the end-cap elements are located in planes perpendicular to the beam axis. There are around 80 million pixel elements with dimensions of 50×400 μm^2. They are contained in 1744 (1456 in the barrel and 288 in the end-caps) identical rectangular modules whereas each module includes 16 chips that are read out with binary electronics. A precision of 10 μm in the transverse direction ($r - \phi$) and 115 μm in the longitudinal direction (z for the barrel and r for the end-caps) is achieved.

The SCT is the second innermost detector in ATLAS, located between the pixel and the TRT detectors. It is designed to provide eight precision measurements per track in the intermediate radial range, contributing to the measurement of momentum, impact parameter and vertex position. The barrel SCT uses four layers of silicon micro-strip detectors to provide precision points in the $r - \phi$ and z coordinates, using a small (40 mrad) stereo angle to obtain the z measurement. Each silicon detector is 6.36×6.40 cm^2 with 780 readout strips. The barrel modules are mounted on carbon-fibre cylinders at radii of 30.0, 37.3, 44.7, and 52.0 cm. The end-cap modules are mounted onto nine wheels, which are interconnected by a space-frame. The spatial resolution is 16 μm in the $r - \phi$ plane and 580 μm in the longitudinal direction (z for the barrel and r for the end-caps), per module containing one $r - \phi$ and one stereo measurement.
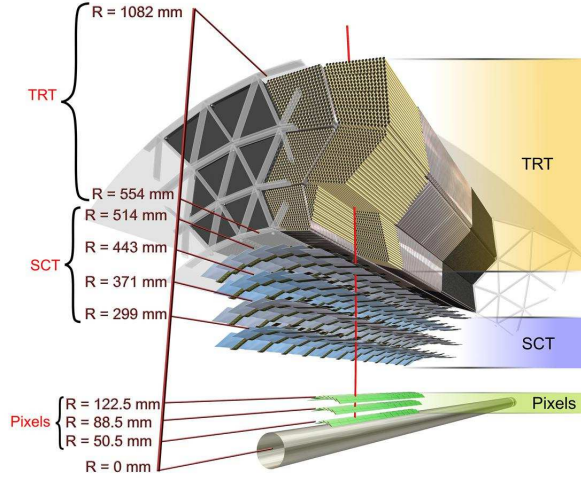
Figure 3.8: The sensors and structural elements traversed by a charged track of 10 GeV p_T in the barrel ID [54].

The TRT is a gaseous straw detector providing on average 36 hits per track in the barrel. Its main goals are to enhance the tracking capability of the silicon detectors and to provide particle identification, in particular by distinguishing electrons from pions and other charged particles. The TRT detector can operate at very high rates thanks to the small diameter and the isolation of the sense wires within individual gas volumes. Each straw is about 150 cm long, 4 mm in diameter and equipped with a 30 μm diameter gold-plated W-Re wire. There are in total 370 000 straws, located axially in the barrel and radially in the end-caps. In the barrel, the detector is divided into 32 modules creating three rings and in each end-cap 20 wheels are assembled together. The transition radiation is produced by highly relativistic particles when they cross the boundary between two media of different dielectric constants (polypropylene foils in the TRT). The total energy loss of a charged particle (in the form of emitted photons) depends on the γ factor and is used to discriminate between electrons and hadrons. The TRT is operated with a non-flammable gas mixture of 70% Xe, 27% CO_2 and 3% O_2, with a total volume of 3 m^3.

3.2.2 Calorimeters

After the particles have travelled through the ID and the solenoid, they enter the highly granular ATLAS calorimetry system. Here, the electrons, photons and hadrons shower and therefore deposit their energy, which is then measured. Electrons and photons interact with matter electromagnetically, while hadrons (mainly charged pions) mostly interact hadronically. Because of the different nature of these two interactions, there is a need for two sets of calorimeters: electromagnetic (EM) and hadronic. The EM calorimeter covers the pseudorapidity range $|\eta| < 3.2$ and the hadronic one covers the region $|\eta| < 4.9$. For an illustrative view of the different calorimeter components, see Figure 3.9.

The EM calorimeter consists of a barrel ($|\eta| < 1.475$) and two end-cap components ($1.375 < |\eta| < 3.2$), with a transition region at $1.37 < |\eta| < 1.52$. It uses lead as an

Figure 3.9: The calorimeters of ATLAS [51].

absorbing medium and liquid argon (LAr) as a detection medium. An accordion geometry of the electrodes has been chosen to pr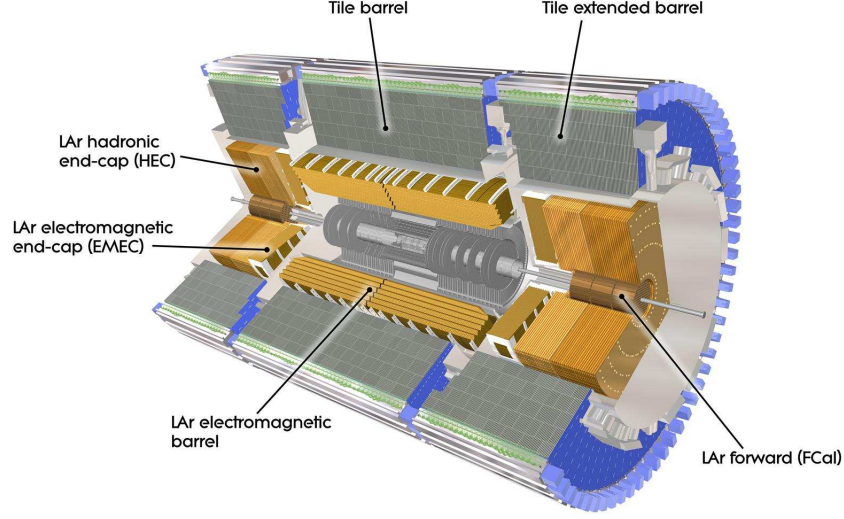ovide full azimuthal coverage and LAr was chosen for its radiation hardness and the speed of the electronic read-out. In the region $|\eta| <$ 2.5, the calorimeter modules are divided into three sections (strip, middle and back; see Figure 3.10). The strip section, which has a thickness of 4.3 radiation lengths (X_0), acts as a "pre-shower" detector. It contributes to the particle identification and precise position measurement. The middle section ($\sim$16 X_0 thick) is transversely segmented into $\Delta\eta \times \Delta\phi$ towers of 0.025$\times$0.025 and it contains most of the shower energy. The back section ($\sim$2 X_0) is coarsely segmented and it is designed to check the confinement of the electromagnetic shower. Before ending up in the calorimeter, the particles traverse up to $\sim$2 X_0 in the ID (see Figure 3.11). The total thickness of a module in the barrel is at least 22 X_0, increasing from 22 X_0 to 30 X_0 between $|\eta| = 0$ and $|\eta| = 0.8$ and from 24 X_0 to 33 X_0 between $|\eta| = 0.8$ and $|\eta| = 1.3$. The energy loss upstream of the calorimeter, for $|\eta| < 1.8$ is determined by a presampler detector. It consists of an active LAr layer of thickness 1.1 cm (0.5 cm) in the barrel (end-cap) region and is placed in front of the inner surface of the EM calorimeter. In the end-cap the total active thickness is greater than 24 X_0 except for $|\eta| < 1.475$. The thickness increases from 24 X_0 to 38 X_0 as $|\eta|$ increases from 1.475 to 2.5 (outer wheel) and from 26 X_0 to 36 X_0 as $|\eta|$ increases from 2.5 to 3.2 (inner wheel).

The hadronic calorimeter was designed to measure the energy of the hadronic particles and to contain their showers. In the barrel, $|\eta| < 1.7$, it consists of the Tile Calorimeter (TileCal) and of LAr end-cap (HEC) and forward calorimeters (FCal). The two latter were constructed following the same technique as the EM LAr calorimeter and they all share the same cryostat. The hadronic calorimeter is also very thick (maximum 11 interaction lengths λ including the outer support) because it has to reduce the punch-through into the muon system, which means that it has to contain all final state particles apart from the muons and the non-interacting ones. It was shown by the simulation that 10λ is enough to provide good resolution for high energy jets which, together with the full $|\eta|$-coverage, will guarantee a good missing transverse energy measurement. The TileCal is a sampling

Figure 3.10: An illustration of the EM calorimeter barrel modules [52, 53].

Figure 3.11: Cumulative amounts of material, in units of radiation length X_0, separately for the barrel (a) and end-cap (b) EM calorimeter [52, 53].

calorimeter using low-carbon steel (iron) as the absorber and plastic scintillating tiles as the active material. It consists of a long barrel and two extended barrels, which are divided azimuthally into 64 modules in ϕ. Radially, each module is further segmented into three layers and the overall granularity yields $\Delta\eta \times \Delta\phi =$0.1×0.1 (0.2×0.1 in the third layer) [55]. The total TileCal thickness at the outer edge is 9.7λ at $\eta = 0$. Each of the LAr HEC moduls consists of two independent wheels, located directly behind the end-cap electromagnetic calorimeter. They are built out of 32 identical wedge-shaped modules and cover the region until $|\eta| = 3.2$. The FCal extends the $|\eta|$ coverage to 4.9 and it consists of three layers: one copper plate and two tungsten absorbers.

3.2.3 Muon Spectrometer

The Muon Spectrometer (MS, see Figure 3.12) forms the outermost part of the ATLAS detector. The muon tracks bend in the magnetic field of the air-core toroid magnets and their momentum is measured in the range $|\eta| < 2.7$ (with a resolution of 10% for 1 TeV tracks). The MS is instrumented with a set of four different kinds of chambers: two for high

precision tracking and two others for triggering purposes. Whereas the tracking chambers provide a precision measurement of the track coordinates in the bending plane ($r - z$ plane) of the magnetic field, the trigger chambers have three functions:

- bunch-crossing identification,
- triggering on well defined p_T thresholds,
- measurement of the muon coordinate in a direction orthogonal to that measured by the tracking chambers.

In the barrel, over the range $|\eta| < 1.4$, the bending is provided by the large barrel toroid magnet; the range $1.6 < |\eta| < 2.7$ is covered by two end-cap magnets inserted into the ends of the barrel toroid. The gap between $|\eta| > 1.4$ and $|\eta| < 1.6$ is called a transition region and there, the magnetic deflection is provided by the combination of the barrel and end-cap magnets. Each of the three toroids consists of eight coils assembled radially and symmetrically around the beam axis. The performance of the magnets is often characterised by their bending power which is a field integral $\int$Bdl, where B is the azimuthal field component and the integral is taken on a straight line trajectory between the inner and the outer muon chamber planes. The barrel toroid provides 1.5-5.5 Tm bending power and the end-cap toroids approximately 1-7.5 Tm. The four sub-detectors of the MS are described in the following paragraphs and their parameters are presented in Table 3.3.

The precision measurement of the muon tracks is made in the $r - z$ projection (the
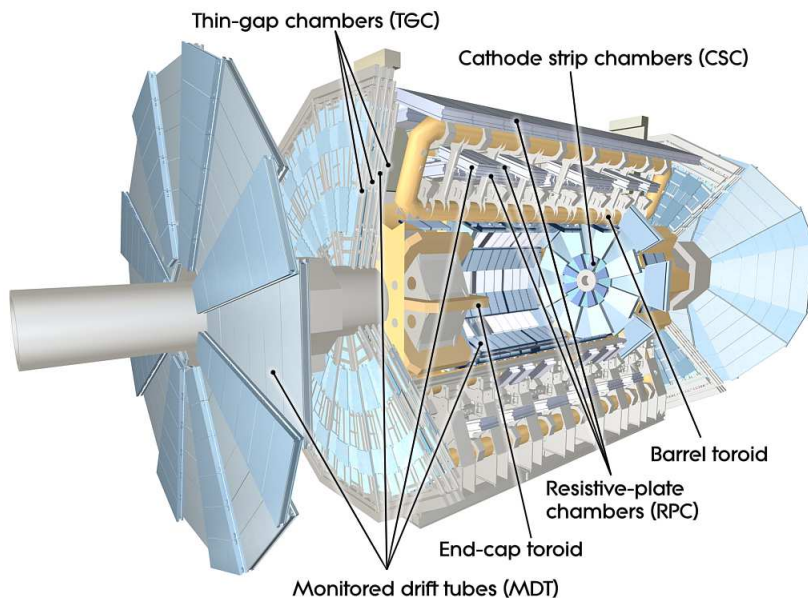
Figure 3.12: Cut-away view of the ATLAS muon system [51].

axial coordinate (z) is measured in the barrel and the radial coordinate (r) in the transition and end-cap regions) using two types of chambers: Monitored Drift Tubes (MDT) and Cathode Strip Chambers (CSC). In the barrel region, the chambers are arranged in cylindrical layers around the beam axis and in the transition and end-cap regions, they are installed in planes perpendicular to the beam. The MDTs are made out of aluminium tubes with a 50 µm diameter W-Re wire and filled with a gas mixture of 93% Ar and 7

% CO_2. They consist of three to eight layers of drift tubes, covering the region of $|\eta| <$ 2.7 and providing an average resolution of 80 μm per tube ($\sim$35 μm per chamber). In the forward tracking layer ($2.0 < |\eta| < 2.7$), the CSCs are used due to their higher rate capability and time resolution. These are multiwire proportional chambers with cathode planes segmented into strips in the orthogonal direction and filled with a gas mixture of 30% Ar, 50% CO_2 and 20% CF_4. The chambers are able to measure the position in both coordinates and they achieve a resolution of 40 μm in the bending plane and 5 mm in the transverse plane.

The purpose of the calorimeters is to contain all the electromagnetic and hadronic

Type	Function	Resolution			Coverage
		z/r	ϕ	time	η
MDT	tracking	35 μm (z)	-	-	$|\eta| < 2.7$
CSC	tracking	40 μm (r)	5 mm	7 s	$2.0 < |\eta| < 2.7$
RPC	trigger	10 mm (z)	10 mm	1.5 s	$|\eta| < 1.05$
TGC	trigger	2-6 mm (r)	3-7 mm	3-7 s	$1.05 < |\eta| < 2.4$

Table 3.3: Main parameters and functions of the ATLAS Muon Spectrometer.

showers, so that the only particles that are left largely untouched are the minimum interacting muons. This gives a great opportunity to trigger on these objects and is exploited in the trigger chambers. The Resistive Plate Chambers (RPC) cover the barrel region ($|\eta| <$ 1.05) and the Thin Gap Chambers (TGC) provide a measurement in the end-cap (1.05 $< |\eta| < 2.7$, with $|\eta| < 2.4$ for triggering). The RPCs consist of parallel electrode-plates, kept at a distance of 2 mm. They form three cylindrical layers around the beam axis, referred to as trigger stations, and deliver the track information with a resolution of 10 mm. The TGCs operate on the same principle as the multiwire proportional chambers but they are smaller in size and they provide good time resolution and high rate capability. The details on the triggering in ATLAS are presented in Section 3.2.4.

3.2.4 Trigger and data acquisition

The ATLAS trigger system is of crucial importance to the physics analyses. Its main goal is to select interesting events from the vast number of collisions. The bunch-crossing rate is $\sim$20 MHz. The rate needs to be reduced to about 300 Hz for permanent storage. This requires a very fast selection algorithm together with an efficient recording system of the collected data. The ATLAS trigger design consists of three levels and each of them significantly reduces the acceptance rate. The data acquisition (DAQ) system then records the selected events. Figure 3.13 shows a simplified block diagram of the TDAQ system.

The Level-1 (L1) trigger performs an initial event selection based on the reduced-granularity information from the calorimeters and the muon detectors. Objects that the calorimeter trigger is searching for are, for example high-p_T, e/γ objects, jets, as well as the total transverse energy. Muons are identified by the trigger chambers: RPCs in the barrel and TGCs in the end-cap. The location where one of these objects is registered is then defined as a region of interest (RoI). The RoIs extend as a cone from the interaction point to the outer parts of the ATLAS detector. The L1 trigger decision is based on a coincidence or a veto of the combination of the required objects. It is hardware based and has programmable thresholds that can be adjusted according to luminosity and physics
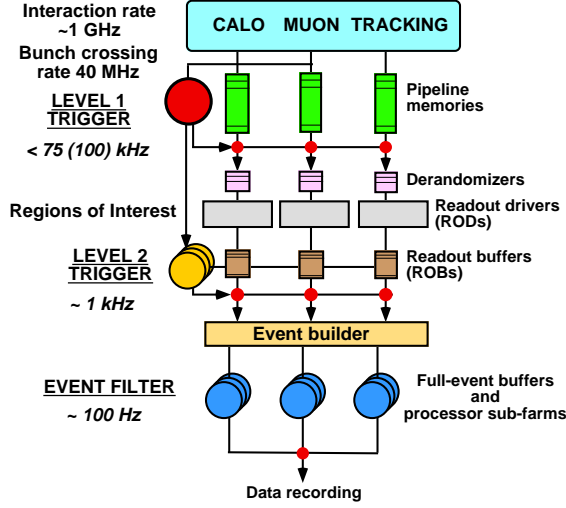
Figure 3.13: Block diagram of the TDAQ system as taken from the TDR [52, 53].

requirements. Most of the physics requirements can be met already by using the criteria of the first level trigger. The time taken to form and distribute the L1 trigger decision is required to be less than $2.5\mu s$. During this time the data from the sub-detectors are initially stored in "pipeline" memories.

All the data selected by L1 trigger are held in read-out buffers (ROBs) until they are processed by the Level-2 (L2) trigger. Then they can be either discarded or accepted, in which case they are transferred by the DAQ system to the storage system for the next level of triggering. The L2 makes use of the full data in the RoIs that are provided by the L1 trigger. This includes the information on the position (η and ϕ) and p_T of the candidate objects. L2 selections use, at full granularity and precision, all the available detector data within the RoIs (approximately 2% of the total event data). The L2 menus are designed to reduce the trigger rate to approximately 3.5 kHz, with an event processing time of about 40 ms.

The data accepted by the L2 trigger systems are further passed on to the Event Builder (EB), which performs a full reconstruction of the event. At the next step, the events are processed by the last stage of the trigger system, the Event Filter (EF). The EF uses offline algorithms and methods, adapted to the online environment, and uses the most up to date calibration and alignment information and the magnetic field map. The EF will make a final selection of the physics events which will be written to the mass storage for offline physics analysis. The output rate from EF should be around 300 Hz.

The L1 muon trigger, used in this thesis, is based on the measurement of the muon trajectories in three different stations. The angle of deflection of the muons in the toroid field depends on their momentum and the field integral along the trajectory. The L1 muon-trigger scheme is shown in Figure 3.14. The trigger plane farthest from the interaction point in the end-cap, and in the middle in the barrel, is called the pivot plane. The muon triggering is based on the predefined p_T thresholds. Each hit found in station RPC1 (TGC3) is extrapolated to station RPC2 (TGC2) along a straight line through the nominal interaction point. Then a coincidence window, depending on the p_T threshold, is defined around that point. The low-p_T trigger condition is then satisfied if, for both projections, there is at least one hit within the coincidence window, and at least one of the two low-p_T

stations has hits in both trigger planes. In the high-p_T trigger procedure, the pivot plane together with RPC3 (TGC1) is used. The high-p_T trigger is satisfied if the track passes the low-p_T criteria, and additionally in the barrel at least one hit in the two trigger planes of RPC3 are in coincidence, and in the end-cap if at least two of the three planes of TGC1 in the η view, and one of the two planes of TGC1 in the $r-\phi$ view are within the appropriate coincidence window. The L2 muon trigger is used for the identification of the muon tracks, the accurate calculation of the position and transverse momentum in the MS, and the extrapolation to the ID and calorimeter [52].

The L1 electron triggers are based on the trigger towers of granularity 0.1×0.1 in
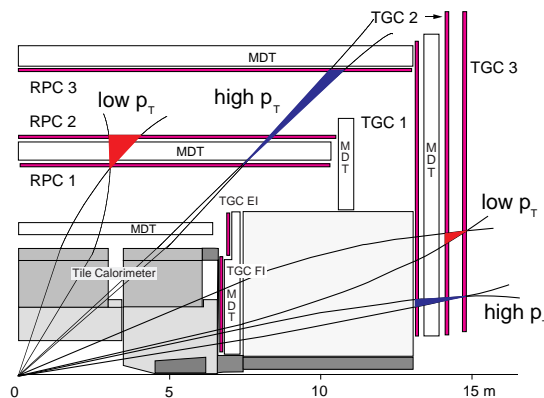

Figure 3.14: Scheme of the L1 muon trigger [52, 53].

$\Delta\eta \times \Delta\phi$, see Figure 3.15. The selection algorithms use a window of 4×4 towers in the EM and hadronic calorimeters in the region $|\eta| < 2.5$. They consist of four elements:

- a 2×2-tower EM cluster, used to identify the position of candidate RoIs;

- a 2×1 or 1×2-tower EM cluster, used to measure the E_T of EM showers, where the energy measurement is converted to E_T assuming the nominal interaction point;

- a ring of 12 electromagnetic towers surrounding the clusters, which is used to require isolation in the EM calorimeter;

- and the 16 hadronic towers behind the EM clusters and isolation ring, which are used for an isolation requirement in the hadronic calorimeters.

Single-electron triggers, which are used in this thesis, are satisfied if at least one signal above the E_T threshold is detected. The L2 electron selection takes as input the RoIs selected by the L1 EM trigger and refines the cluster energy and position measurements by using the full calorimeter granularity. In the EF this information is used to build shower-shape variables which, together with E_T, discriminate electrons from jets which also passed the L1 EM trigger selection. More details on the specific variables used can be found in Ref. [52].

3.3   Monte Carlo simulation

The comparison of the collected data events with theoretical expectations is done with the help of simulated events. They are used not only to confirm the expected signatures of different particles but also to test the performance of the ATLAS detector. The understanding
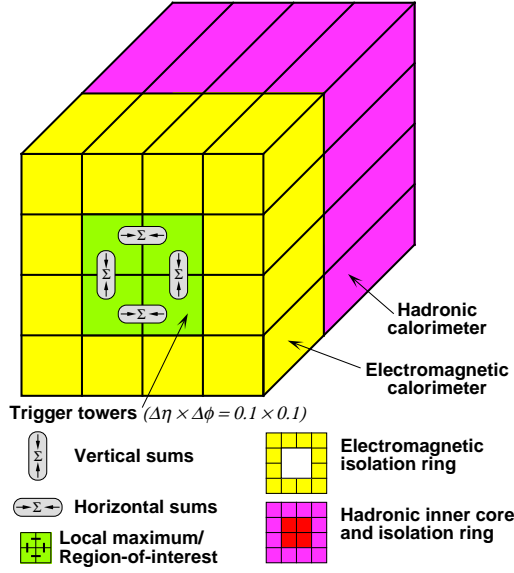
Figure 3.15: Calorimeter towers [52,53].

of the response of the detector is of the highest importance in any physics analysis. The simulation of the ATLAS experiment can be divided in four different steps: event generation, detector simulation, digitisation and event reconstruction. They are briefly described in the following.

The first step consists of the generation of the proton-proton interactions. The whole process includes the hard scatter between the proton constituents, parton showering, hadronisation and the underlying event. The event generator programs use Monte Carlo (MC) methods to randomly generate the initial hard interactions according to the differential cross section of the process under consideration. Two main challenges include the calculation of the matrix element (ME) and the parton distribution functions (PDFs), which describe the momentum distribution of the incoming quarks and gluons in the protons. The ME is relatively well understood and the uncertainty on the PDFs is caused mainly by the uncertainty on the distributions of the incoming gluons. Most event generators used by ATLAS calculate the ME at the leading order (LO). The next to leading order (NLO) real and virtual corrections to the cross section calculation are accounted for by a so-called k-factor. The k-factor is the ratio of the cross section between NLO and LO calculation and it can depend on the event kinematics. The PDFs are not calculated in the event generator but rather serve as an input. The differences in the cross section calculations using different PDF sets are considered as uncertainties on the MC predictions due to the PDFs.

After the generation of the hard scattering, the initial partons and the produced particles radiate gluons, which can in turn split into additional gluons or quark-anti-quark pairs. This radiation is called parton showering and is followed by a process of hadronisation (quarks or gluons grouping into tight cones of particles - jets). The uncertainty on the modelling of the parton showers is reflected in the final parton distribution of the jets, and this modelling is often tuned to the jet distribution in data.

The event generator programs are used by many experiments as they do not depend on detector specifics. There are many different generators available and they can be grouped according to the level of detail of the calculations. Herwig [56], Pythia [57,58] or Sherpa [59]

use the ME calculation along with the parton showering, hadronisation and decay. They include the calculation of 2→1 and 2→2 hard scatter processes. There are other generators that are able to calculate the ME for 2→n processes but they require interfacing to other LO generators for the parton shower modelling. The commonly used ones are Alpgen [60] or MadGraph [61, 62]. The last group consists of event generators that calculate the ME at the NLO level with both real and virtual corrections. They include the commonly used MC@NLO [63] and Powheg [64] (with interfacing to other generators for showering and hadronisation).

The event generators provide a list of outgoing semi-stable particles and their properties. In the next stage the propagation of these particles through the ATLAS detector is simulated [65]. The interactions of the particles with the detector material are simulated using the GEANT4 [66] package. Later on the process of translating the interactions between the particles and the detector to the detector signals is performed. This step is called digitisation and is followed by the event reconstruction. At this stage a fair comparison can be made between the simulated data and the real collision data.

Chapter 4

Event and object reconstruction

This chapter summarises the reconstruction and identification of the objects used in the analysis presented in this thesis. The description of tracking and vertex reconstruction is followed by a detailed summary of the leptons' identification and reconstruction performance. Subsequent sections treat jets, with one section dedicated to the b-tagging algorithm, and the missing transverse energy.

4.1 Tracking and vertex reconstruction

As already mentioned in Chapter 3, a track is characterised by a set of five parameters: curvature q/p, impact parameters in the transverse and $r - z$ planes d_0, z_0, and the azimuthal and polar angles ϕ and θ. Tracks are reconstructed within the full Inner Detector acceptance ($|\eta| < 2.5$). In the first stage of track reconstruction, the raw data from the pixel, SCT and TRT detectors are interpreted and translated into clusters and space-points. The search for track candidates starts by forming track seeds from a combination of space-points in three pixel layers and the first SCT layer. Then these seeds are extended through the remaining layers of the SCT in search for further hits. A hit that reduces the fit quality is called an outlier and if there was no hit found (where expected) it is called a hole. A set of quality cuts is then placed on the number of good hits, outliers and holes. In the next stages, the ambiguities between the tracks are resolved (by placing a score on the track quality [67]) and more refined fitting is performed. It includes global-χ^2 and Kalman-fitting techniques. In the final stage a track is extended with the TRT hits. This track-finding algorithm is called inside-out tracking. There also exists outside-in tracking (also called back-tracking) which starts from the TRT seeds and extends them back to the inner layers of SCT and pixel detectors. It is mainly used to efficiently reconstruct tracks from secondary interactions. Figure 4.1a shows the number of track candidates, comparing data to MC, as a function of η at different stages in the ambiguity solver. All reconstructed tracks (black) are compared to the ones rejected because they are assigned a track score of zero (blue), rejected because of quality cuts (red) and accepted as resolved tracks (green) [67]. The high pile-up environment substantially increases the detector occupancy which influences the number of fake tracks (track segments not assigned to primary or secondary particles). It has been shown that more robust quality cuts (on the silicon hits and holes) minimise the number of fakes. The track reconstruction efficiency changes within 1% with increasing pile-up conditions but more robust track requirements decrease the efficiency by around 5% [68]. Figure 4.1b shows the change in the track reconstruction
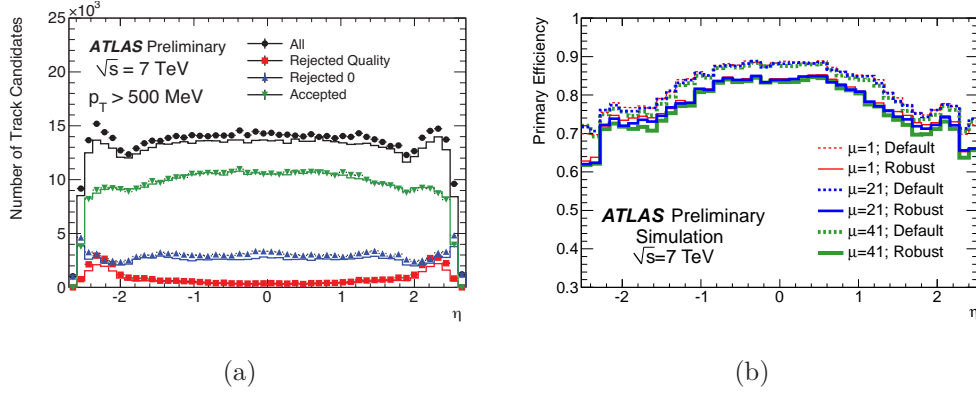
(a) (b)

Figure 4.1: The number of track candidates at the different stages in the ambiguity solver algorithm (a) [67] and the track reconstruction efficiency in different pile-up conditions (b) [68].
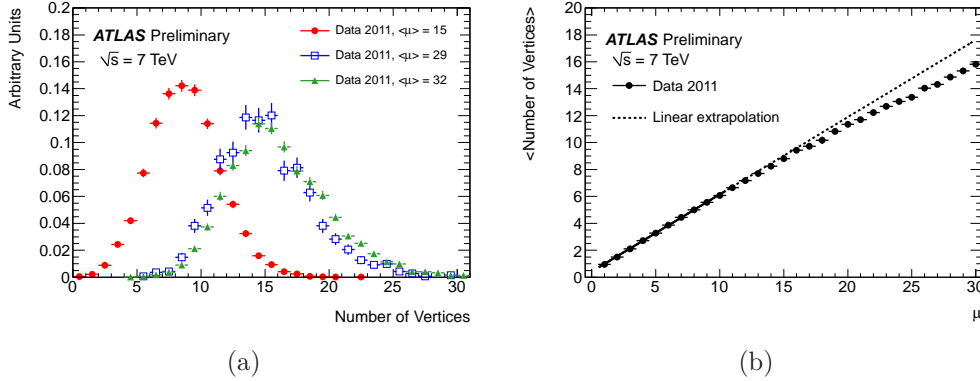

(a) (b)

Figure 4.2: The number of primary vertices in data containing different amount of pile-up (a) and the correlation between the average number of vertices and the average number of interactions per bunch crossing (b) [68].

efficiency for different track quality cuts and as a function of pile-up multiplicity μ.

The tracks thus obtained are then used to reconstruct the interaction points (the primary vertices) and the secondary vertices from particle decays. The reconstruction of the vertices consists of a vertex finding algorithm designed to associate the tracks to vertex candidates, and a vertex fitting algorithm dedicated to reconstructing the vertex parameters [69]. The iterative primary vertex finding algorithm first selects the reconstructed tracks which are compatible with originating from the interaction region. Then a vertex seed is selected based on a global maximum in the z distribution of the tracks. In the final stage the vertex position is determined by a robust χ^2-based fitting algorithm [70]. Unaccounted for tracks are used to seed a new vertex and the whole procedure is repeated until no unassociated tracks are left. If there is more than one vertex in the event, the one with the highest sum of $p_T{}^2$ of the associated tracks is selected as the one corresponding to the interesting interaction and in the following will be referred to as the primary vertex (PV). The beam-spot parameters are used both in the vertex finding and fitting algorithms. The vertex reconstruction efficiency decreases with higher pile-up conditions because of an increased number of fake tracks and so-called shadowing of the nearby interactions (where vertices
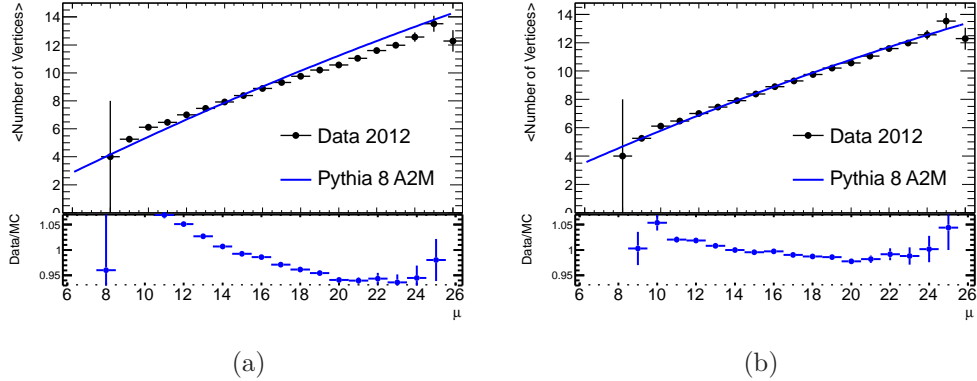
Figure 4.3: The differences in data and MC of the number of primary vertices as a function of the average number of interactions per bunch crossing before (a) and after (b) the μ-rescaling [72].

are merged) which results in less accurate reconstruction of the position of the vertices [68].

The number of reconstructed vertices is correlated with the number of interactions per bunch crossing. Figure 4.2 shows the number of primary vertices in data containing different amounts of pile-up and the correlation between the average number of vertices and the average number of interactions per bunch crossing [68]. A degradation of the reconstruction efficiency can be seen in data for $\mu \gtrsim 15$. This study was performed on the data taken in 2011 at $\sqrt{s} = 7$ TeV. The comparison of 2012 data with the default MC simulation at $\sqrt{s} = 8$ TeV showed a disagreement in the minimum bias vertex multiplicity. This can be attributed to the differences in the minimum bias visible cross section between the data and the Monte Carlo simulation [71]. To recover a reasonable agreement between data and MC, the average number of interactions per bunch crossing in MC has to be multiplied by 1.11±0.03. Figure 4.3 shows the impact of μ-rescaling on the agreement between the number of primary vertices and the average number of interactions per bunch crossing.

4.2 Leptons

This section describes the reconstruction and identification of electrons and muons. The comparison of the performance of the algorithms between data and MC is shown. Since no τ leptons are used in this analysis, they are not described here; the performance of their reconstruction and identification is described in Refs. [73, 74].

4.2.1 Electrons

The reconstruction and identification of electron candidates starts from the clusters of energy deposits in the EM calorimeter. These are found by a *sliding-window* algorithm [75, 76] which is based on summing energy deposits in cells within a fixed-size rectangular window (3×5 in units of 0.025×0.025 in $\eta \times \phi$ space) in search for a local transverse energy maximum. Then these energy deposits become seed clusters which are matched to the tracks, which are extrapolated from their last measurement point. This matching of tracks to the cluster seeds is very loose as it has to account for the radiative energy losses (bremsstrahlung) of high-energy electrons. These losses can substantially change the electrons' trajectories and hence the track parameters when they traverse the magnetic field. In the ATLAS

analyses in 2010 and 2011, the track fitting procedure was the same for every charged particle (with a pion particle hypothesis to estimate the material effects), which proved to be inefficient in the case of electrons. In the 2012 data taking a new track refitting approach, the Gaussian Sum Filter (GSF) algorithm [77], was used for electron reconstruction. In the absence of bremsstrahlung, the distribution of $p_{\text{true}}/p_{\text{reco}}$ should be a Gaussian but with the bremsstrahlung present this is not the case. The GSF algorithm takes into account the non-Gaussian noise by modelling it as a weighted sum of Gaussian components. An improvement in reconstructed track parameters is obtained [78]. All electron candidate tracks, found by the algorithms explained in the previous section, with $p_{\text{T}} > 400$ MeV and $|\eta| < 2.5$ can be refitted. The re-defined track parameters are then again used in the matching to the calorimeter clusters and in the electron four-momentum computation. This procedure improves both the reconstruction and identification efficiencies. The final cluster energy is determined [78] by summing four different contributions: (1) the estimated energy deposited in the material in front of the EM calorimeter, (2) the measured energy deposited in the cluster, (3) the estimated external energy deposited outside the cluster (lateral leakage), and (4) the estimated energy deposited beyond the EM calorimeter (longitudinal leakage).

Electron identification in the central region $|\eta| < 2.47$ follows a cut-based selection approach using calorimeter, tracking and combined variables. There are three sets of cuts which define *loose*, *medium* and *tight* quality electrons. The cuts are optimised in bins of η and E_{T}. They are arranged according to decreasing signal electron efficiency and increasing background rejection. The *loose* selection uses the shower shape variables of the EM calorimeter middle layer and hadronic leakage variables. On top of the above mentioned criteria the variables from the EM calorimeter strip layer, track quality requirements and track-cluster matching are added to the *medium* selection. The *tight* quality selection includes all the previously listed criteria and adds E/p (where E is the energy measurement in the calorimeter and p the momentum measured in the tracking detectors), particle identification using the TRT, and discrimination against photon conversions [76]. Electrons used in the analysis presented in this thesis were selected based on the *tight* identification criteria that were optimised with respect to the original ones to cope with the higher level of pile-up.

On top of the identification criteria, a set of cuts on the calorimeter and track isolation should be placed. In the 2012 data analysis, the calorimeter isolation energy is calculated from the so-called topological clusters which was found to be more efficient in noise suppression and in higher pile-up conditions. Topological clusters are found inside a $\Delta R = 0.3$ cone around the cluster seed and are built from clusters of calorimeter cells whose energy is above a threshold depending on the expected noise. The total topological isolation energy is a sum of thus defined topological clusters [75].

The reconstruction, identification and isolation efficiency measurements are based on the tag-and-probe (T&P) method on $Z \rightarrow ee$ events (in some cases aided by $W \rightarrow e\nu$ or $J/\psi \rightarrow ee$ events) [76]. The basic idea is to select one lepton (tag) with the standard cuts, look for a second candidate (probe) with looser cuts and see how often it passes the nominal selection criteria. Figure 4.4a shows the reconstruction efficiency as a function of η_{cluster} for data and MC. It shows also the comparison of the reconstruction algorithms used for 2011 and 2012 data analyses. A higher and more uniform reconstruction efficiency is obtained for the 2012 analysis where a GSF algorithm is used. Figure 4.4b shows the reconstruction efficiency as a function of the transverse energy, again for the 2011 and 2012 reconstruction algorithms. The identification efficiency for different electron quality

43
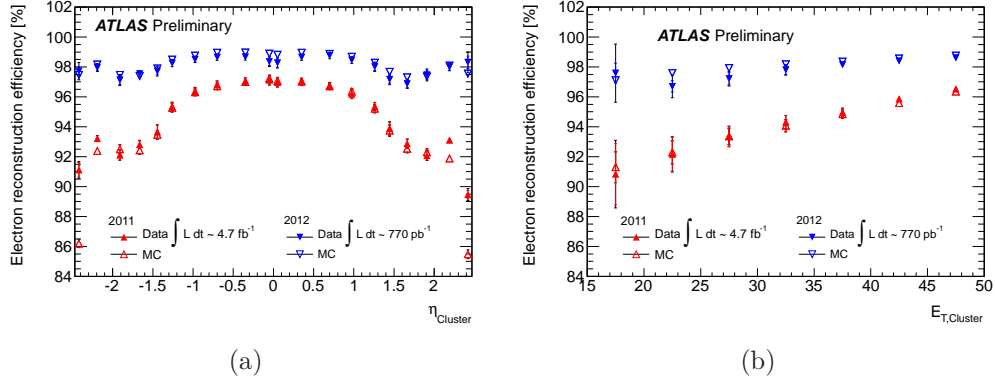
Figure 4.4: The reconstruction efficiency as a function of η_{cluster} for electrons with E_T between 30 and 50 GeV, and as a function of E_T, for data and MC for 2011 and 2012 data analyses [79].
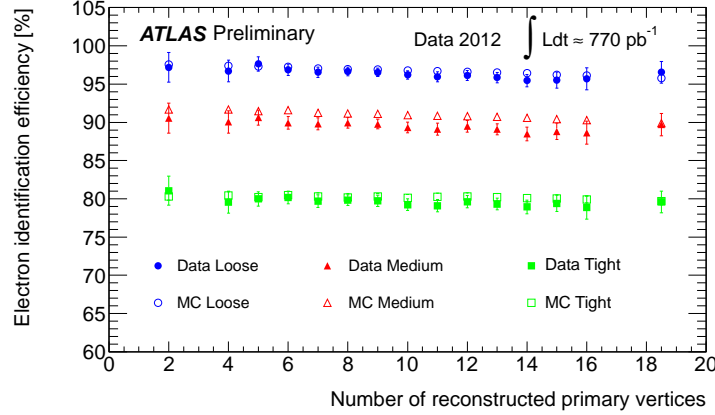
Figure 4.5: The identification efficiency a function of the number of primary vertices for *loose*, *medium* and *tight* quality electrons in the 2012 data taking [79].

definitions was measured using the first part of the 2012 data. Figure 4.5 shows the identification efficiency as a function of the number of primary vertices for *loose*, *medium* and *tight* quality electrons. In 2012 data taking, the electron particle identification (PID) menu was further optimised to diminish the efficiency degradation at high pile-up conditions and to cope with the high trigger rate induced by the higher instantaneous luminosity and by the increased centre-of-mass energy with respect to the 2011 data taking conditions. The isolation efficiency was measured for electrons passing the selection criteria used in this thesis, and the results, as a function of E_T, are shown in Figure 4.6.

The differences in the measured efficiencies between data and MC can be observed for all of the above outlined properties: reconstruction, identification and isolation. At the analysis level it results in application of a scale factor (SF) which corrects the MC simulation for what is actually observed in data.
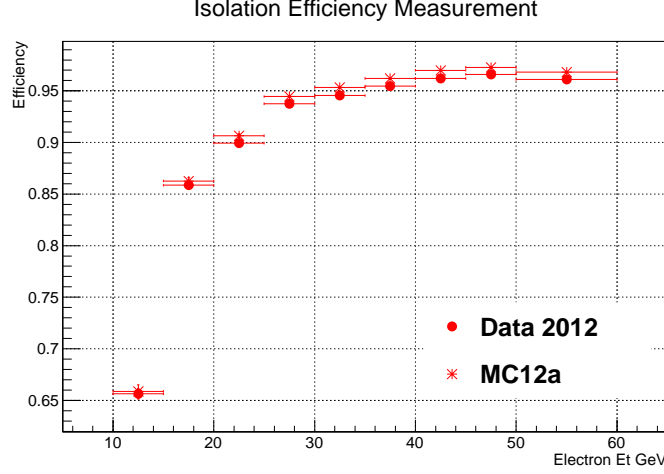
Figure 4.6: The electron isolation efficiency as a function of E_T determined in data and MC for the isolation criteria used in the analysis presented in this thesis [80].

4.2.2 Muons

The Muon Spectrometer (described in Section 3.2.3) is the primary means of identification and reconstruction of high-p_T muons. There are four types of muons that can be used in the physics analysis: stand-alone, segment-tagged, combined and calorimeter-tagged, and there exist two reconstruction algorithms for each type of muons. They are grouped in two families, and both the muon collections and the families are named after the combination algorithm. They are called Staco [81] and Muid [82]. Three types of muons, that are relevant to the analysis presented in this thesis, are briefly described below. The calorimeter-tagged muons, used in combination with other identification and reconstruction algorithms, help to recover inefficiencies in the regions where muon spectrometer coverage is limited or when dealing with low-p_T muons.

- Stand-alone (SA) muon tracks are tracks reconstructed in the Muon Spectrometer and then extrapolated to the beam line. First a region of activity (ROA) is identified using the trigger chambers, then a track segment is found in each of the muon stations in the ROA. In the next step, a muon track candidate is formed from a combination of these track segments and finally a global fit of the muon track candidate is performed. The extrapolation to the beam line must account for the multiple scattering and energy loss in the calorimeter; this extrapolation is made using the average energy loss based on the material crossed in the calorimeter. The reconstruction can be performed up to $|\eta| < 2.7$ and the muon momentum is measured in the MS.

- Combined muons (CB) are found by matching stand-alone muons and inner detector tracks which are reconstructed as described in the previous section. The combination is based on the match χ^2, defined as the difference between outer and inner track parameters weighted by their combined covariance matrix. It provides a quality measure and is used to decide which track pairs are kept. The muon's momentum is then defined as a weighted combination of the MS and the ID p_T measurements. The reconstruction of combined muons is limited to $|\eta| < 2.5$ by the ID coverage.

- Segment-tagged (ST) muons are found by extrapolating the ID track to the first
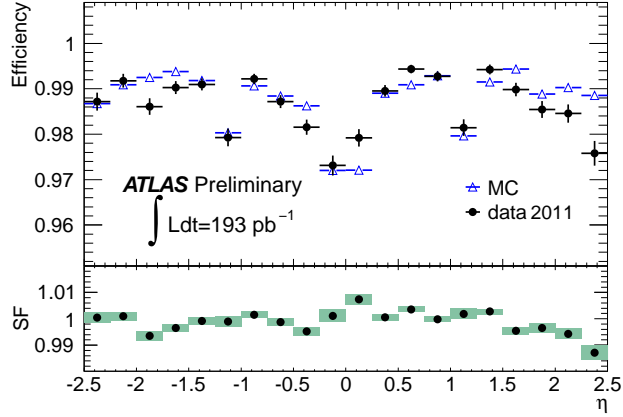
Figure 4.7: Comparison of the measured ID muon reconstruction efficiency as a function of η with the Monte Carlo prediction. [51].

station of the Muon Spectrometer. The match quality is then defined as a tag χ^2 using the difference between the MS track segment and the prediction from the extrapolated ID track. The algorithm was designed to improve the reconstruction of low-p_{T} muons which do not penetrate the outer layers of the MS. It uses only the ID tracks and the MS segments that have not been identified as a muon candidate by the Staco combination algorithm. Segment-tagged muon momenta are measured by the ID and the reconstruction coverage is $|\eta| < 2.5$.

The reconstruction efficiency of the combined muons is influenced by the reconstruction of the MS tracks, which varies with η and ϕ. There are two regions in η with decreased reconstruction efficiency of the combined muons: a region around $\eta \sim 0$, which is not fully equipped with muon chambers to allow maintenance works, and a transition region around $|\eta| \sim 1.2$, where only one muon chamber is used in the track reconstruction. The efficiency of the muon reconstruction is calculated using the T&P (described in the previous section) method. Both tag and probe candidates have to pass a set of quality requirements on the ID tracks (for example, on the number of hits and outliers). Figure 4.7 compares the ID muon efficiency as a function of η for the data taken in 2011 at $\sqrt{7} =$ TeV and the MC. The small efficiency drops around $\eta \sim 0$ and $\eta \sim 1$ can be explained by the ID hit requirements. No dependence on ϕ or p_{T} is observed [54]. Figure 4.8a shows the reconstruction efficiency for combined muons as a function of η [51]. The bottom parts of the plots show the ratio of the efficiencies observed in data to the expected MC efficiency. As in the case of electrons, the differences are used to correct the MC prediction to reflect the efficiency in data. Overall the scale factors are consistent with 1 but for the transition region. This can be attributed to inconsistencies in the magnetic field strength distribution between the MC simulation and the reconstructed data. Addition of the segment-tagged muons recovers this drop in efficiency, as shown in Figure 4.8b.

A study of the pile-up dependence of the reconstruction efficiency was performed using the data collected in 2011 [83]. The full dataset of 4.7 fb^{-1} was split into a few data taking periods with different levels of pile-up (due to different LHC running conditions). Figure 4.9 shows the CB+ST muon reconstruction efficiency as a function of η with a mean pile-up of 5.50 (4.9a) and 11.25 (4.9b). It can be seen that the reconstruction efficiency is independent of the level of pile-up. Figure 4.10 shows the comparison of the reconstruction
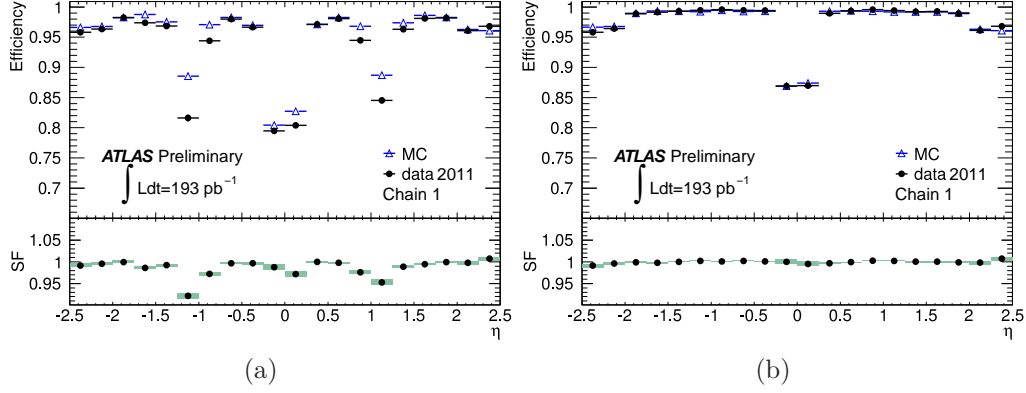
Figure 4.8: The reconstruction efficiencies and scale factors for CB (a) and CB+ST (b) muons as a function of η [51].
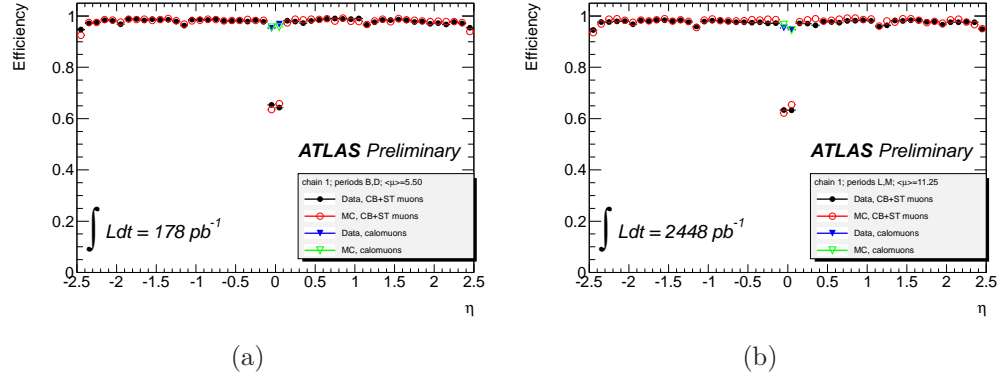
Figure 4.9: The reconstruction efficiency for CB+ST muons as a function of η in periods of different level of pile-up: 5.50 (a) and 11.25 (b) average interactions [83].

efficiencies between the full 2011 dataset and the MC simulation, as a function of η and p_T.

The selected muons are also required to be well isolated. Requirements on track and calorimeter isolation are applied. The calorimeter isolation energy is defined as the energy deposited in the calorimeter towers in a $\Delta R = 0.3$ cone around the muon's trajectory. The track isolation energy is calculated as a sum of the transverse momenta of the tracks in $\Delta R = 0.3$ around the muon's ID track. The efficiency for muons to pass the isolation criteria was measured as a number of primary vertices in the event on a full dataset collected in 2011. The calorimeter isolation efficiency was also measured and it shows a non-linear dependence on the number of primary vertices. Therefore a quadratic correction as a function of the number of primary vertices was applied to the measured isolation energy. It recovers the drop in efficiency at a high number of primary vertices. Figure 4.11 shows the calorimeter isolation efficiency before and after the pile-up correction. As in the case of the muon reconstruction efficiency, the differences in the isolation efficiencies between data and MC, used in the analysis described in Chapter 5, are accounted for by the scale factors.

(a)   (b)

Figure 4.10: The reconstruction efficiency for CB+ST muons as a function of η and p_T for the full 2011 dataset [83].

(a)   (b)

Figure 4.11: The calorimeter isolation efficiency as a function of primary vertex multiplicity, before and after the pile-up correction is applied [83].

4.3 Jets

Jets can be defined as composite objects contained in narrow cones in $\eta - \phi$ space. One can distinguish calorimeter jets, track jets or particle jets, with calorimeter jets being relevant to the analysis presented in this thesis. Calorimeter jets are composed of calorime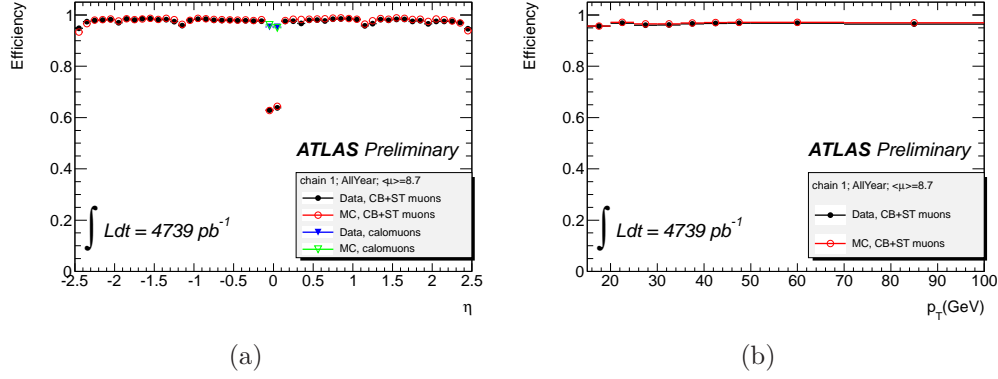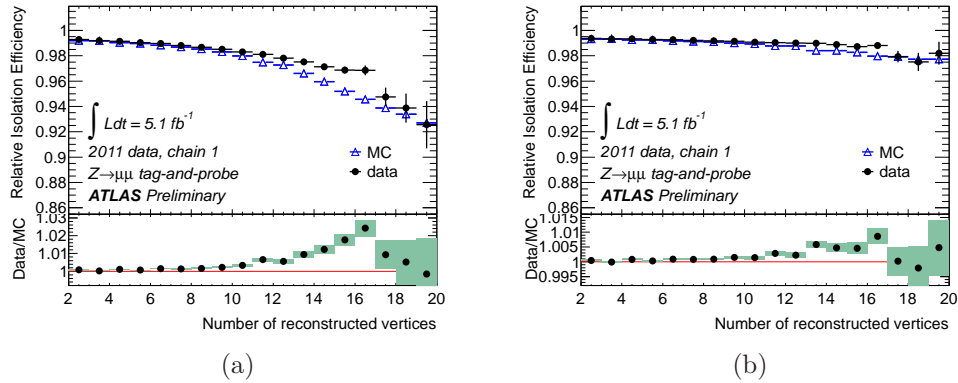tric signal objects. The combination scheme of the basic calorimeter cells (both electromagnetic and hadronic) is based on the topological cell clusters, defined previously in Section 4.2.1. Such topological clusters serve as inputs to the jet finding algorithms. It is important to notice that these algorithms do not find jets, they define them. There are theoretical and experimental guidelines that the jet finding algorithms have to follow. The main ones are infrared (any soft particle should not affect the number of jets found) and collinear safety (it should not matter if a certain amount of transverse momentum is carried by one particle or if it is split among several collinear particles) [78]. Experimental guidelines include detector technology and environment independence.

The early implementation of jet finding algorithms included fixed-cone algorithms. First the input objects are ordered in p_T and if the highest one passes a pre-defined threshold, it is used a seed. Then all objects within a $\Delta R < R_{\text{cone}}$ are collected and the direction of the cone is updated based on the four-momenta of the objects inside. A jet is considered stable, if a continuous process or recombination does not further change the direction of the centre of the cone. This algorithm was found to be infrared unsafe and a new set of algorithms was defined based on the sequential recombination of the input objects based on a distance between them, d_{ij}, and a distance between the beam and the object, d_{iB}:

$$d_{ij} = \min(k_{iT}^{2p}, k_{jT}^{2p})\frac{\Delta R_{ij}^2}{R^2}, \tag{4.1}$$

$$d_{iB} = k_{iT}^{2p}, \tag{4.2}$$

where k_{iT} is a transverse momentum of object i. A list of all the d values is compiled and if d_{ij} is the smallest one then the objects i and j are combined and a list is recalculated. If, on the other hand, d_{iB} is found to be smaller then the object is considered stable and is defined as a jet. The variable R is a parameter and three types of algorithms can be defined based on the value of p:

- $k_\perp$ (also called k_t) [84], with $p =1$, which first merges objects with low relative k_T. The final merge will involve the hardest object and this can be used to study the structure of a jet. Also if the k_T with respect to the beam is smaller then with respect to any other object, then the object will not be merged. This means that soft objects will not be combined into a jet.

- Cambridge/Aachen [85], with $p =0$, where the transverse momentum is irrelevant and the only information used is the ΔR distance between the objects. The closest objects will be merged first and this feature can as well be used to study the jet structure or to improve the jet resolution by removing the smallest and furthest objects.

- anti-$k_\perp$ (also called anti-k_t) [86], with $p =-1$, where clustering will be strictly centered around the highest p_T objects. Soft particles will be included in the hard objects long before the distance between two soft particles will be even considered. If a hard particle is isolated from other hard particles within a $2R$ distance, then such formed jet will gather all soft particles in a cone of radius R. If there are two hard particles

within a $2R$ distance (but $\Delta R_{12} > R$) then two jets are formed. If $\Delta R_{12} < R$ then two hard particles will cluster to form one single jet. In this algorithm, the soft particles do not change the shape of the jet which makes it soft-radiation resilient. The jets used in the analysis presented in this thesis are identified using the anti-k_t algorithm with a parameter $R = 0.4$.

Jet energy calibration

Jets are formed from the calorimetric energy deposits reconstructed at the electromagnetic energy scale (EM). The EM energy scale provides an energy calibration for electromagnetically interacting particles and was determined using test-beam measurements for electrons. The correction for the lower response to hadrons is based on the topology of the energy deposits observed in the calorimeter [87]. The next step includes the calibration of the jet energy and pseudorapidity to the particle jet scale. This correction (so-called jet energy scale, JES, correction) is obtained from the study of the calorimeter response to truth jets in the Monte Carlo simulation. The truth jets are formed from stable particles and are reconstructed using the same jet finding algorithm. Residual corrections derived from the *in-situ* techniques are also applied. They are meant to correct for any differences in the calibration of the JES using MC [88]. Jets used in the analysis presented in this thesis were calibrated using the EM+JES calibration scheme. Other calibration schemes use cluster-by-cluster (local cell weighting, LCW) or jet-by-jet (global cell weighting, GCW) information to reduce some of the fluctuations in the energy response [54].

The EM+JES calibration scheme consists of three steps which are designed to correct the jet's energy and direction. In the first step, the average energy due to pile-up interactions is subtracted from the energy measured at the EM scale. Then the direction of the jet is corrected such that it originates from the primary vertex rather than from the ATLAS geometrical centre. The last step consists of applying the JES corrections derived from the MC simulation as a function of the energy and direction of the jet. Systematic uncertainties are evaluated and applied according to the recommendations. They include four baseline uncertainties:

- the baseline jet energy calibration which represents the overall knowledge of the JES from the *in-situ* analyses;

- the forward JES uncertainty which relates the calibration of jets from the central to the forward region (so-called η-intercalibration);

- the in-time event pile-up uncertainty applied as a function of the number of primary vertices;

- the out-of-time event pile-up uncertainty applied as a function of the average number of pile-up interactions;

and three additional sourced of uncertainties related to the jet flavour composition and event topology:

- close-by-jet uncertainty showing the extent to which the MC simulation described the response of non-isolated jets;

- flavour composition and response uncertainties which arise from the fact that quark-initiated and gluon-initiated jets have different responses;
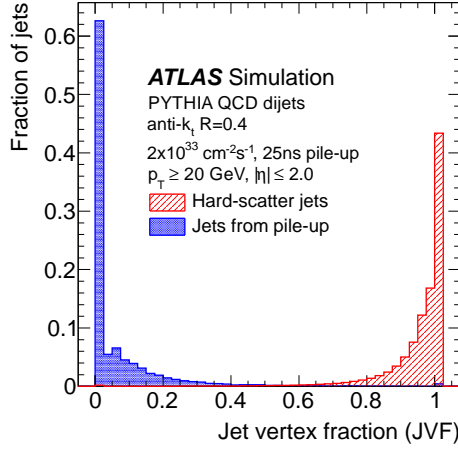
Figure 4.12: The JVF distribution in the MC QCD events [83].

- b-jet energy scale uncertainty.

The impact of these seven sources of uncertainties on the analysis presented in this thesis is summarised in Chapter 5.

One of the solutions to cope with the additional jets produced in the high pile-up conditions, is to use a jet vertex fraction (JVF) algorithm which is used to quantify the amount of energy coming from the pile-up events. The JVF variable is defined, per jet, as a scalar summed transverse momentum of tracks associated to the primary vertex divided by the summed transverse momentum of tracks associated to all the vertices in the event. Three distinct regions can be identified: JVF = 1: jets with little or no direct contribution from pile-up, JVF < 1: jets with additional tracks orginating from the primary interactions (other than the selected hard-scattering interaction), and JVF = 0: jets with all charged tracks originating from the pile-up interactions. JVF = -1 is assigned to jets without matched tracks (mainly forward jets). Figure 4.12 shows the JVF distribution in the MC QCD events corresponding to moderate instantaneous luminosity and pile-up conditions. Hard scatter jets can be distinguished from the pile-up jets with the help of the JVF variable. A study of the dependence of the jet multiplicity on the number of reconstructed primary vertices has been performed on the 2012 data using the $Z \rightarrow \mu\mu$ event selection. Figure 4.13 shows the ratio of $Z \rightarrow \mu\mu + 1$ jet events to all $Z \rightarrow \mu\mu$ events as a function of the number of reconstructed primary vertices, with and without applying the JVF requirement. The selection used, $|JVF| > 0.5$ has been found to be robust against pile-up.

4.3.1 b-tagging

The efficient identification and reconstruction of jets originating from b-quarks (b-jets) is crucial as it is used in the rejection of $t\bar{t}$ and single-top ($tW/tb/tqb$) backgrounds, where a top quark decays to a bottom quark and a W boson. This section briefly summarises the b-tagging algorithms and the methods used to measure the b-tagging efficiency. All of the algorithms heavily depend on the tracking (especially on the impact parameters' determination) and displaced vertex reconstruction [90]. The IP3D algorithm uses the transverse impact parameter significance (d_0/σ_{d_0}) and the longitudinal impact parameter significance (z_0/σ_{z_0}) [91] of all the tracks in a jet. The secondary vertex-based algorithms [92] use the

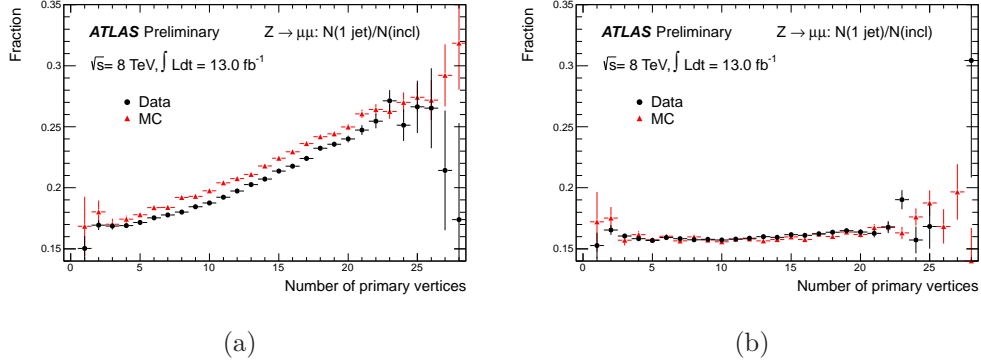Figure 4.13: Ratio of $Z\to\mu\mu$ + 1 jet events to all $Z\to\mu\mu$ events as a function of the number of reconstructed primary vertices, before (a) and after (b) applying the $|JVF| > 0.5$ requirement [89].

decay length significance ($L_{3D}/\sigma_{L_{3D}}$) measured in 3D and signed with respect to the jet direction (SV0) and additionally some of the vertex properties (SV1). The JetFitter algorithm [93] exploits the topological structure of weak b- and c-hadron decays inside a jet. All of the algorithms mentioned above (apart from SV0 which only uses the decay length significance) use the likelihood ratio method where the measured value S_i of a discriminating variable is compared to the distributions for both the b- and light jet hypotheses, $b(S_i)$ and $u(S_i)$, determined in simulated events. The ratio of probabilities $b(S_i)/u(S_i)$ defines a track/vertex weight which can be combined to a global jet weight. In this thesis, the MV1 b-tagging algorithm is used, which is based on a neural network using the output jet weights of the JetFitter+IP3D, IP3D and SV1 algorithms as input.

A cut on the discriminating variable output (weight) defines the operating point of a b-tagging algorithm. Different operating points provide different b-tagging efficiencies and light-jet rejection. Figure 4.14 shows the expected performance of the various b-tagging algorithms in jets from a simulated $t\bar{t}$ sample [94]. The high-performance algorithms are expected to have lower mistagging rates (light jets tagged as b-jets) than their earlier versions, for the same b-tagging efficiency point. The calibration results are presented in a form of a p_T and $|\eta|$ dependent scale factor which is defined as a ratio of the b-tagging efficiency in data to that in the simulation (generator level parton matching). In the analysis presented in this thesis the p_T^{rel} [95] method was used to measure the b-jet efficiency in data. It is based on a sample of jets containing a reconstructed muon. The p_T^{rel} variable is defined as the momentum of the muon transverse to the combined muon plus jet axis. Muons originating from b-quarks have a harder p_T^{rel} spectrum of this variable than muons in light or c-jets. The p_T^{rel} muon spectrum in data is fit to the template spectra to obtain a fraction of b-jets before and after requiring a b-tag. Then the total number of jets and a fraction of b-jets in the pre-tagged and tagged samples can be used to obtain a b-tagging efficiency in data. Other b-tagging efficiency calibration method include the system8 [96] or $t\bar{t}$-based methods [97]. The former one was designed to measure the b-tagging efficiency with a reduced dependence on the MC simulation. This method uses two data samples with different b-jet fractions and two uncorrelated tagging algorithms. Then a system of 8 non-linear equations, with 8 known (for example the number of b-jets tagged by the first algorithm) and 8 unknown quantities (among which the b-tagging efficiency), can be written down and solved. The methods based on $t\bar{t}$ selections provide the measurements in
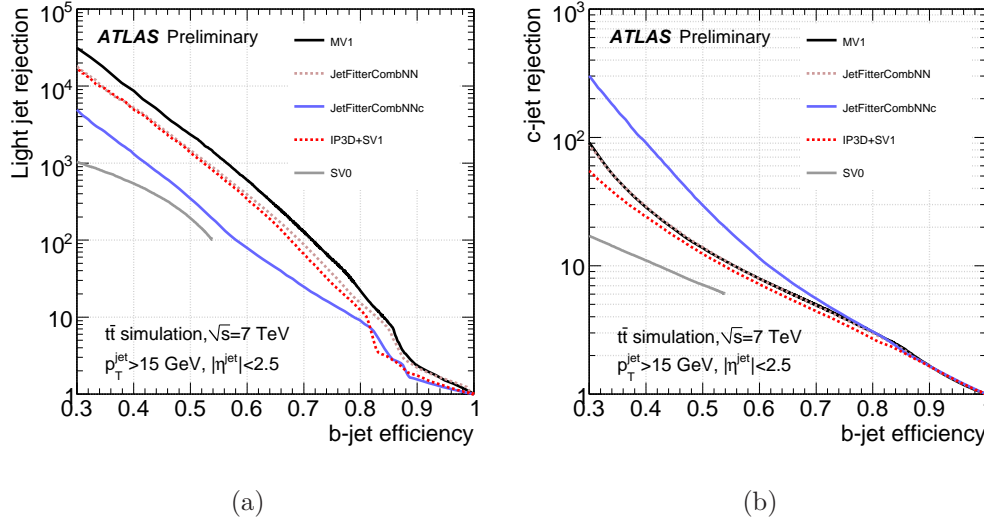
Figure 4.14: Light and c-jet rejection as a function of the b-tagging efficiency based on a simulated $t\bar{t}$ sample [94].

an inclusive b-jet sample and allow to extend the calibrated p_T range. Figure 4.15a shows the MV1 85% b-tagging efficiency in 5fb^{-1} of 2011 data and MC simulation for the p_T^{rel} and system8 methods [94]. This is the b-tagging operating point used in the analysis of this thesis. Additionally, Figure 4.16 shows the MV1 70% b-tagging efficiency in 4.7fb^{-1} of 2011 data as obtained with different calibration methods. The results are consistent within the uncertainties.

4.4 Missing $\mathbf{E}_T$

The missing transverse momentum, $\mathbf{E}_T^{miss}$, is regarded as the event momentum imbalance in the transverse plane. This is due to momentum conservation and the fact that before the hard scatter there is hardly any momentum in the transverse plane. The $\mathbf{E}_T^{miss}$ is obtained as a negative sum of the transverse momenta of all particles in the final state. The magnitude of $\mathbf{E}_T^{miss}$ is denoted as E_T^{miss}. Since neutrinos interact weakly with matter and escape the ATLAS experiment undetected, they will be a source of real E_T^{miss}. Mis-reconstructed objects, imperfect resolution or detector inefficiencies lead to fake E_T^{miss} which degrades the overall E_T^{miss} performance. Understanding of the E_T^{miss} is crucial for the analyses which expect it in the final states, such as the analysis presented in this thesis, $H \to WW^{(*)} \to \ell\nu\ell\nu$.

The E_T^{miss} is reconstructed from the energy deposits in the calorimeters and from the muon tracks in the Muon Spectrometer [98]. Low-p_T tracks that do not enter the calorimeter and ID muon tracks that are not matched to the MS segments are also accounted for. The E_T^{miss} components, defined as a sum of the calorimeter and muon terms, can be written as:

$$E_{x(y)}^{miss} = E_{x(y)}^{miss,calo} + E_{x(y)}^{miss,\mu}. \tag{4.3}$$

Calorimeter term

Calorimetric cells, used in the reconstruction of the $\mathbf{E}_T^{miss}$, are associated with the reconstructed and identified parent objects. They include: electrons, photons, hadronically
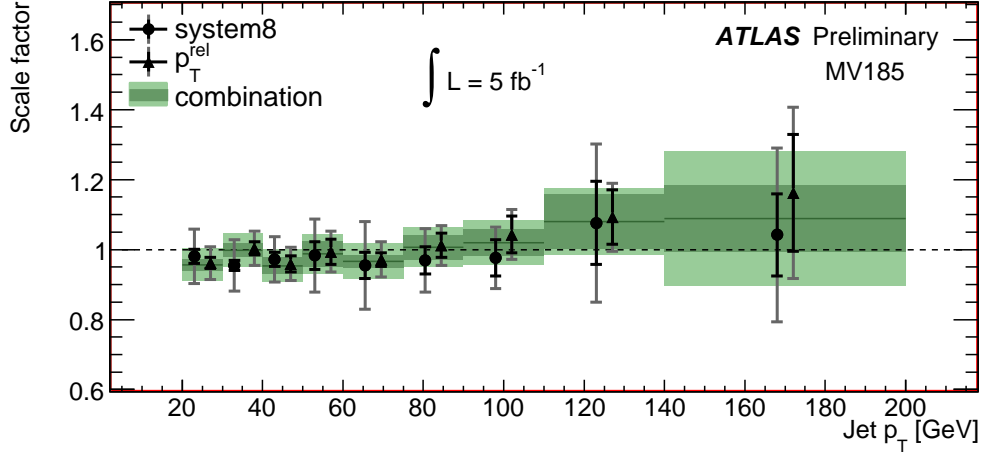
Figure 4.15: The *b*-tagging efficiency for the p_T^{rel} and system8 methods in data and MC simulation [94].

Figure 4.16: The MV1 70% *b*-tagging efficiency comparing different calibration methods [51].

decaying τ leptons and jets. The cells that are not included in the definition of any of these objects are also accounted for in an additional term, $E_{x(y)}^{\mathrm{miss,CellOut}}$. The final calorimeter term is calculated as

$$E_{x(y)}^{\mathrm{miss,calo}} = E_{x(y)}^{\mathrm{miss,e}} + E_{x(y)}^{\mathrm{miss,\gamma}} + E_{x(y)}^{\mathrm{miss,\tau}} + E_{x(y)}^{\mathrm{miss,jets}} + E_{x(y)}^{\mathrm{miss,soft-jets}} + E_{x(y)}^{\mathrm{miss,CellOut}}, \quad (4.4)$$
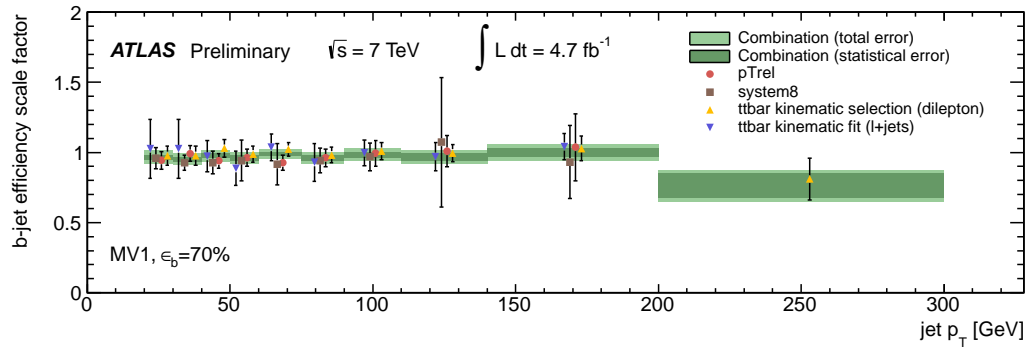
where each of the terms is defined as a negative sum of cell energies inside the given objects (in the range $|\eta| < 4.5$). The calibration of the cells follows the default calibration of the associated objects:

- $E_{x(y)}^{\mathrm{miss,e}}$- default calibration for the medium quality electrons with $p_{\mathrm{T}} > 10$ GeV;

- $E_{x(y)}^{\mathrm{miss,\gamma}}$- EM scale calibration for the tight quality photons with $p_{\mathrm{T}} > 10$ GeV;

- $E_{x(y)}^{\mathrm{miss,\tau}}$- LCW scale calibration for the τ-jets, reconstructed with the *tight τ* identification criteria, with $p_{\mathrm{T}} > 10$ GeV;

- $E_{x(y)}^{\mathrm{miss,jets}}$- LCW+JES scale calibration for the anti-k_{T} jets with $p_{\mathrm{T}} > 20$ GeV;

- $E_{x(y)}^{\mathrm{miss,soft-jets}}$- LCW scale calibration for the anti-k_{T} jets with $7 < p_{\mathrm{T}} < 20$ GeV;

- $E_{x(y)}^{\mathrm{miss,CellOut}}$- LCW scale calibration for the topological clusters outside reconstructed objects and for low-p_{T} reconstructed tracks.

Muon term

The muon term is defined as the negative sum of the momenta of muon tracks with $|\eta| < 2.7$. In the region covered by the ID ($|\eta| < 2.5$), the tracks of the combined muons are used and outside of this region only SA muons are taken into account. In the inactive regions of the MS, the ST muons are used. Since the muons lose a fraction of their energy in the calorimeter, it has to be accounted for in the calculation of the $E_{\mathrm{T}}^{\mathrm{miss}}$. The procedure is different if the muon is identified as being isolated or not isolated ($\Delta R < 0.3$ from a reconstructed jet) [98]. If a muon is isolated then the energy lost by the muon in the calorimeter is already taken into account and is included in the $E_{x(y)}^{\mathrm{miss,calo}}$ term. This is not the case if a muon is not isolated.

The $E_{\mathrm{T}}^{\mathrm{miss}}$ performance can be studied in $Z \rightarrow \ell\ell$ or $W \rightarrow \ell\nu$ events where the observed $E_{\mathrm{T}}^{\mathrm{miss}}$ is mainly coming from fake or real sources, respectively. The distributions of the $E_{\mathrm{T}}^{\mathrm{miss}}$ reconstructed as explained above are shown in Figure 4.17a for $Z \rightarrow \mu\mu$ events in 4.2 fb^{-1} data at $\sqrt{s} = 7$ TeV and compared to the MC simulation [99]. A good agreement is observed between the data and MC distributions. Figure 4.17b shows the $E_{\mathrm{T}}^{\mathrm{miss}}$ distribution in the $W \rightarrow e\nu$ events in 4.2 fb^{-1} of data at $\sqrt{s} = 7$ TeV and compared to the MC simulation [99]. A degradation of the performance of the $E_{\mathrm{T}}^{\mathrm{miss}}$ with higher pile-up conditions can be especially seen in the soft-jets and CellOut terms. They are combined together to form the $E_{x(y)}^{\mathrm{miss,SoftTerm}}$ term. Several pile-up supression methods have been developed to counter this degradation but only one, the soft term vertex fraction method (STVF), is quoted here [99]. This method scales the $E_{x(y)}^{\mathrm{miss,SoftTerm}}$ with the STVF quantity, defined as a fraction of soft tracks (not matched to physics objects) associated with the primary vertex. The improvement in the $E_{x(y)}^{\mathrm{miss}}$ resolution as a function of the number of primary vertices in $Z \rightarrow \mu\mu$ events without jets with $p_{\mathrm{T}} > 20$ GeV is shown in Figure 4.18.
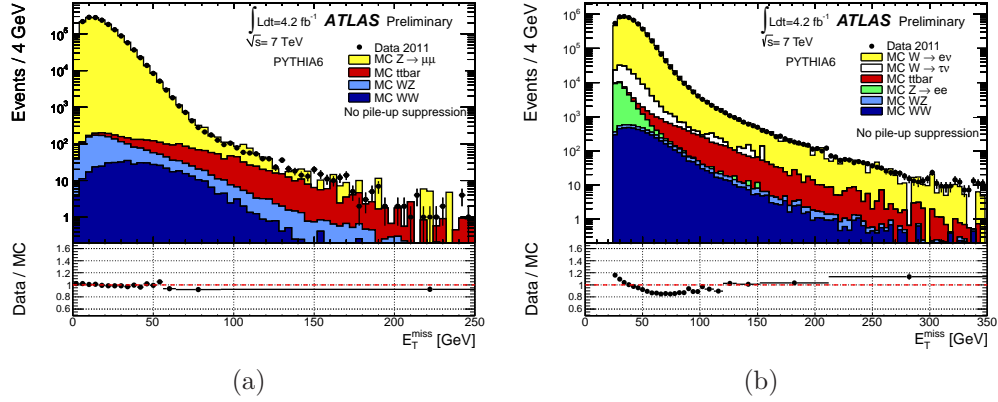
Figure 4.17: The E_T^{miss} distributions in the $Z \to \mu\mu$ (a) and $W \to e\nu$ (b) events, comparing the 4.2fb^{-1} data at $\sqrt{s} = 7$ TeV with the MC simulation [99].
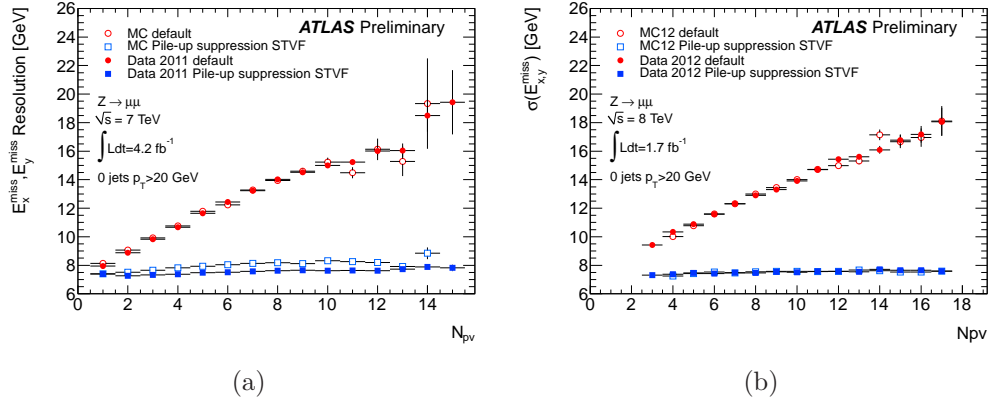
Figure 4.18: The $E_{x(y)}^{\mathrm{miss}}$ resolution as a function of the number of primary vertices in the $Z \to \mu\mu$ events without jets with $p_T > 20$ GeV, comparing the 4.2fb^{-1} data at $\sqrt{s} = 7$ TeV (a) and 1.7 fb^{-1} data at $\sqrt{s} = 8$ TeV (b) [99].

The comparison shows the effect of the STVF pile-up suppression method in 4.2 fb^{-1} of $\sqrt{s} = 7$ TeV events (4.18a) and 1.7 fb^{-1} of $\sqrt{s} = 8$ TeV events (4.18b).

Chapter 5

$H \to WW^{(*)} \to \ell\nu\ell\nu$ physics analysis

5.1 Introduction

The $H \to WW^{(*)} \to \ell\nu\ell\nu$ channel (where $\ell = e, \mu$) is one of the main channels where the search for the SM Higgs Boson has been performed. It is one of the most sensitive channels in the region preferred by the global electroweak fits and because of the high production cross section via ggF and high branching fraction of $H \to WW^{(*)}$ decay it is an important channel in the low mass Higgs searches. The final state of this decay channel consists of two high-p_T isolated leptons and large E_T^{miss}, defined previously in Chapter 4. In this channel, the mass of the Higgs boson cannot be fully reconstructed because of the neutrinos in the final state. To get a handle on the Higgs boson's mass, a transverse mass variable is used. As the name suggests it uses information only from the transverse plane. It nevertheless is somewhat sensitive to the mass of the Higgs boson but unfortunately it will result in a poor mass resolution. Thus this channel suffers from larger backgrounds as compared to other multi-lepton channels. The backgrounds considered include (listed according to their decreasing contribution in this analysis):

- irreducible SM WW with W bosons decaying leptonically,

- $t\bar{t}$ where each of the top quarks decays to a W boson and a bottom quark. If two W bosons decay leptonically then the final state consists of 2 leptons, E_T^{miss} and b-quarks,

- $tW/tb/tqb$ with Wt contributing the most where the top quark decays to a W boson and as bottom quark, and two W bosons decaying leptonically,

- W+jets background where the second lepton is a product of a heavy flavour decay or a jet is misreconstructed as an electron,

- $W\gamma^{(*)}$ where a photon gives rise to the conversion electron (or μ/τ in case of a virtual photon),

- Z/γ^*+jets where two leptons come from the decay of a virtual photon, γ^*, or a Z boson and fake E_T^{miss} is present,

- $WZ^{(*)}/Z^{(*)}Z^{(*)}$ backgrounds with the W and Z bosons decaying leptonically and with real or fake $E_\mathrm{T}^\mathrm{miss}$.

The combination of the Higgs searches with the ATLAS detector based on the full 2011 dataset taken at $\sqrt{s} = 7$ TeV reported an excess of observed events over the background prediction [100]. It corresponded to 3.5σ significance around 126 GeV. No significant excess was observed in the $H \to WW^{(*)} \to \ell\nu\ell\nu$ channel alone [101]. The strategy for the 2012 data analysis was to focus on the region around $m_H = 125$ GeV. In the first stage, the kinematic region designed to select the SM Higgs boson with $110 < m_H < 140$ GeV was excluded from the analysis. This region was unblinded only after a satisfactory agreement between data and MC was reached in the specifically designed background control regions and signal region side-bands.

In this analysis of the 2012 8 TeV data, because of the difficulty of understanding of the fake $E_\mathrm{T}^\mathrm{miss}$ in Z/γ^*+jets events, which dominates the same flavour channels ($ee + \mu\mu$), only the different flavour channels were used ($e\mu + \mu e$). The data collected in the period between April and September 2012 were used in the analysis presented in this thesis. The data were recorded by the ATLAS experiment at a centre-of-mass of energy 8 TeV and correspond to 13 fb^{-1}.

This chapter presents the MC samples used in the analysis and describes in detail the selection of good quality objects and events. Later on, a description of the background estimation is provided along with a treatment of the theoretical and experimental systematic uncertainties. The last part focuses on the statistical model used to test the hypothesis of the SM Higgs boson. The 2012 results, together with the full ATLAS combination, are presented in Chapter 6.

5.2   MC samples

The MC generators used to simulate the signal and background processes are summarised in Table 5.1. The table quotes the final cross section derived at $\sqrt{s} = 8$ TeV and $m_H = 125$ GeV for the signal processes. The signal contributions considered here include the dominant gluon fusion production process ($gg \to H$, ggF), the vector-boson fusion production process ($qq' \to qq'H$, VBF) and the associated production processes ($qq' \to WH, ZH, WH/ZH$). The details on the Higgs production and decay were already covered in Chapter 2. The signal cross section is computed to next-to-next-to-leading order (NNLO) [19–21, 23–25] in QCD for the ggF process using the MSTW2008 PDF set [27]. The ggF Higgs boson p_T spectrum in POWHEG [17] is reweighted to agree with the prediction from HqT [105]. The calculation of the cross section for VBF signal production uses the approximate NNLO QCD corrections [36] and full NLO QCD and EW corrections [33–35]. The cross sections of the associated WH/ZH production processes are calculated up to NNLO QCD corrections [38, 39] and NLO EW corrections [40]. Only the $H \to WW^{(*)} \to \ell\nu\ell\nu$ (with $\ell = e\,\mu$) channels are considered, which include the small contributions from leptonic τ decays. The branching fraction for this decay as a function of m_H is calculated using the PROPHECY4F [106, 107] program, with HDECAY also used in calculating the total width [108].

As described in Chapter 3, different event generators are used to simulate the hard scattering process and to model the parton showering, hadronisation, and the underlying event. For the latter three steps, PYTHIA6 [57], PYTHIA8 [58] or HERWIG [56] (interfaced to JIMMY [109] for the UE modelling) are used both in signal and background processes. In

Process	Generator	$\sigma \cdot \mathcal{B}$ (pb)
ggF	POWHEG [64]+PYTHIA8 [58]	0.441
VBF	POWHEG+PYTHIA8	$35 \cdot 10^{-3}$
WH/ZH	PYTHIA8	$127 \cdot 10^{-3}$
$q\bar{q}/g \to WW$	POWHEG+PYTHIA8	5.68
$gg \to WW$	GG2WW [102]+HERWIG [56]	0.16
$t\bar{t}$	MC@NLO+HERWIG	238.1
tW/tb	MC@NLO+HERWIG	28
tqb	AcerMC [103]+PYTHIA6	88
inclusive W	ALPGEN [60]+HERWIG	$37 \cdot 10^{3}$
inclusive Z/γ^*	ALPGEN+HERWIG	$16 \cdot 10^{3}$
$Z^{(*)}Z^{(*)} \to 4l$	POWHEG+PYTHIA8	0.73
$W(Z/\gamma^*)(m_{(Z/\gamma^*)} > 7$ GeV$)$	POWHEG+PYTHIA8	0.825
$W(Z/\gamma^*)(m_{(Z/\gamma^*)} < 7$ GeV$)$	MADGRAPH [61, 62, 104]+PYTHIA6	11.0
$W\gamma$	ALPGEN+HERWIG	369

Table 5.1: MC generators used to model the signal and background processes, and the corresponding cross sections at $\sqrt{s} = 8$ TeV (given for $m_H = 125$ GeV in the case of the signal processes). Leptonic decays of W and Z are assummed with the exception of the WH/ZH processes, which include all W and Z decays [89].

the background processes that use the Alpgen [60] LO ME calculator for multi-partonic final states for the hard scattering, the MLM matching scheme [110] is used to avoid double counting of contributions present in both ME and PS computations. These backgrounds include W+jets, Z/γ^*+jets and $W\gamma$ processes. The CT10 PDF set [111] is used for the POWHEG and MC@NLO samples, and CTEQ6L1 [112] is used for the ALPGEN, Mad-Graph, and PYTHIA8 samples. The simulation of both signal and background processes incorporates a model of the pile-up conditions in the 2012 data. These were discussed in Chapter 3.

Leptonic decays of W and Z are assummed with the exception of the WH/ZH processes, which include all W and Z decays. The quoted cross sections include the branching ratios and are summed over lepton flavours. The exception is top quark production, for which inclusive cross sections are quoted. In the generation of some of the MC background processes a set of kinematic criteria was applied. The Z/γ^*+jets process was generated with a dilepton invariant mass greater than 10 GeV. The $W\gamma$ process simulated with ALP-GEN only includes events where the photon has p_{T} greater than 8 GeV and is separated from the charged lepton by $\Delta R = \sqrt{(\Delta\eta^2) + (\Delta\phi^2)} > 0.25$. In the case of $W\gamma^*$ background (with $m_{(Z/\gamma^*)} < 7$ GeV), a set of kinematic cuts is placed on the leptons (p_{T} greater than 5 GeVand $|\eta| < 3$ for the ee and $\mu\mu$ case and $|\eta| < 5$ for the $\tau\tau$ case) and on their invariant mass, $m_{\ell\ell} > 2m_e$. The $WZ^{(*)}$ process covering higher $m_{(Z/\gamma^*)}$ masses is simulated with POWHEG. The phase-space overlap between the POWHEG and MadGraph samples is removed by requiring $m_{\ell\ell} > 7$ GeV for the POWHEG samples. A filter at the generation stage requiring at least two charged leptons with $p_{\mathrm{T}} > 5$ GeV and $|\eta| < 2.8$ is applied. The $Z^{(*)}Z^{(*)}$ background samples are generated with an invariant mass cut of $m_{\ell\ell} > 4$ GeV. It applies to any opposite-sign lepton pair. The $t\bar{t}$ process was generated with a dilepton filter.

	k	$f_i(\text{Sherpa})/f_i(\text{MG})$	C_i
0 jets	2.01±0.16	0.69±0.11	1.4±0.2
1 jets	2.01±0.16	1.4±0.4	2.9±0.8
⩾ 2 jets	2.01±0.16	4.1±1.3	8±3

Table 5.2: The correction factors applied to the $W\gamma^*$ sample, including the global normalisation and the jet multiplicity dependent k-factors [114].

The LO cross sections for the $W\gamma$ and $W\gamma^*$ processes are normalised to the MCFM [113] NLO predictions. In order to determine the normalisation, it is important to replicate the same generation parameters across different MC samples. All of the requirements used to generate the ALPGEN $W\gamma$ sample were applied in the generation of events with MCFM. The inclusive cross section has been calculated using MCFM and it yields 122.5 pb at $\sqrt{s} = 8$ TeV (for the $W \rightarrow e\nu$ decay only). ALPGEN provides a cross section summed over all lepton flavours which, for one lepton flavour decay, is equal to 106.9 pb at $\sqrt{s} = 8$ TeV. The k-factor for the $W\gamma$ samples is then 1.15. The MadGraph generator was chosen to simulate $W\gamma^*$ process because it is able to perform the generation down to very low $m_{\gamma*}$ masses of $2m_e$. The MCFM integration is unstable for $m_{\gamma*} < 0.5$ GeV. The cross sections from MadGraph and MCFM are therefore compared in the region 0.5 GeV $< m_{\gamma*} < 7$ GeV and an extrapolation to lower photon masses is performed. MadGraph uses PYTHIA for the parton showering and hadronisation, which is known to underestimate the jet multiplicities. Therefore the jet multiplicity distributions were compared to the ones obtained from the multi-leg SHERPA generator. In summary, a global cross section normalisation k-factor is applied together with a jet multiplicity dependent k-factor. The final correction factors are applied according to the Eq. 5.1 (f_i are the fractions of events with i jets) and the numerical values are presented in Table 5.2. During the course of the analysis, a problem was found in the generated MadGraph samples which affected the events with $m_{\gamma*} < 3$ MeV. To remedy this situation, the problematic events were removed and a reweighting factor was applied to preserve the cross section [114].

$$C_i = \frac{\sigma_{\geqslant 0 \text{ jets}}(\text{MCFM})}{\sigma_{\geqslant 0 \text{ jets}}(\text{MG})} \times \frac{f_i(\text{Sherpa})}{f_i(\text{MG})} \tag{5.1}$$

5.3   Object selection

The final state events consist of three categories of objects: leptons (e, μ), jets and $E_{\text{T}}^{\text{miss}}$. Understanding of the reconstruction, identification and selection of the various objects is therefore crucial to this analysis (see Chapter 4). In this section, the selection of the good quality objects is summarised (for details refer to [80, 115]).

Electrons

Electrons are selected by using a set of tight identification criteria which use a combination of tracking and calorimeter information ($tight++$ in the ATLAS electron particle identification, PID, nomenclature). Bad quality clusters or fake clusters originating from calorimeter problems are rejected with the help of object quality flags. The range $|\eta| <$

2.47, with the excluded region $1.37 < |\eta| < 1.52$, corresponding to the boundary between the barrel and the end-cap calorimeters, is used and the transverse energy is required to be greater than 15 GeV. In the 2012 data analysis, calorimeter isolation is based on topological clusters which reduces the pile-up dependence (as explained in Chapter 4). In addition, lateral leakage (an electron will leak some of its energy outside of the central core) and pile-up noise corrections are applied to the topological isolation energy. Also the track isolation performance is improved in terms of the background rejection efficiency thanks to lowering a threshold of the tracks which are used in the calculation of the track isolation (from 900 MeV in 2011 to 400 MeV in 2012). The track isolation uses the scalar sum of the transverse momenta of all tracks within a $\Delta R = 0.3$ cone around the electron normalised to the electron p_{T}. Similarly, the calorimeter isolation uses the scalar sum of the topological clusters' transverse energies within a $\Delta R = 0.3$ cone around the electron normalised to the electron p_{T}. The exact values differ between the track and calorimeter-based criteria and depend on the electron p_{T}. To guarantee that the electrons emerge from the primary vertex, cuts on the impact parameters are applied. It is required that the electron track points back to the primary vertex with transverse impact parameter significance less than 3 and that the distance in z with respect to the primary vertex ($|z_0| = |z - z_{\mathrm{PV}}|$) is less than 0.4 mm. In the 2012 data analysis, the cut on $|z_0|$ was changed to $|z_0 \sin\theta|$ to take into account the fact that forward tracks have a longer projection on the z-axis and thus a larger uncertainty. If there are two reconstructed electrons found within a $\Delta R = 0.1$ cone, the one with higher p_{T} is kept in the analysis. Similarly, if an electron is found in the proximity ($\Delta R = 0.1$) of a muon, selected with the criteria described in the next section, it is removed from the event.

Muons

Muon candidates are identified by matching tracks reconstructed in the inner detector and in the muon spectrometer, where the reconstruction of a full track in the MS drives the identification. Each of the components (pixel, SCT and TRT) of the associated inner detector track is required to pass a set of quality cuts, which provide good background rejection, particularly against pion/kaon decays-in-flight. Muons are selected in the $|\eta| < 2.5$ range and the transverse momentum is required to be greater than 15 GeV. To select muons from W decays, a requirement on the pile-up corrected calorimeter isolation is applied. Additionally, any muon candidates that overlap with selected jets ($\Delta R = 0.3$) are removed. Similarly to the electrons, requirements on the calorimeter and track isolation within a $\Delta R = 0.3$ cone are applied as a function of muon p_{T}. To select muons that come from the primary vertex, the transverse impact parameter significance should be less than 3. Additionally it is required that $|z_0 \sin\theta|$ is less than 1 mm.

Jets

Jets are reconstructed using the anti-k_{t} algorithm with distance parameter $R = 0.4$, as explained in Section 4.3. Only jets with $p_{\mathrm{T}} > 25$ GeV and $|\eta| < 4.5$ are considered. The jet p_{T} threshold is increased to 30 GeV in the forward region $2.5 < |\eta| < 4.5$ to reduce the contribution from jets produced by pile-up events. In order to reject jets that are produced in the central part of the detector by pile-up interactions, a selection criterion is applied to each jet with $|\eta| < 2.5$ on a quantity called the jet vertex fraction (JVF). The JVF is defined, using the charged-particle tracks associated with a given jet (based on the ΔR

distance), to be the p_T sum of the tracks originating from the primary vertex divided by the p_T sum of all of the tracks. Jets are required to have $|\mathrm{JVF}| > 0.5$. Every electron is also reconstructed as a jet, and to avoid double counting any jet that is within a $\Delta R = 0.3$ cone around an electron candidate is removed from the event.

Missing transverse energy

The missing transverse energy, $E_\mathrm{T}^\mathrm{miss}$, is the magnitude of $\mathbf{E}_\mathrm{T}^\mathrm{miss}$, the opposite of the vector sum of the transverse momenta of the reconstructed objects, including muons, electrons, photons, jets, and clusters of calorimeter cells not associated with these objects. The calculation of the $E_\mathrm{T}^\mathrm{miss}$ is contained within $|\eta| < 4.9$ ($|\eta| < 2.7$ for the muon tracks) and it is described in Section 4.4. In this analysis a variable called relative missing energy is used, $E_\mathrm{T,rel}^\mathrm{miss}$. It is defined as:

$$E_\mathrm{T,rel}^\mathrm{miss} = \begin{cases} E_\mathrm{T}^\mathrm{miss} & \text{if } \Delta\phi \geqslant \pi/2 \\ E_\mathrm{T}^\mathrm{miss} \cdot \sin \Delta\phi & \text{if } \Delta\phi < \pi/2 \end{cases}, \tag{5.2}$$

where $\Delta\phi$ is the minimum azimuthal angle between $\mathbf{E}_\mathrm{T}^\mathrm{miss}$ and any of the selected leptons or jets. Compared to $E_\mathrm{T}^\mathrm{miss}$, the use of $E_\mathrm{T,rel}^\mathrm{miss}$ increases the rejection of events with significant mismeasurement of a jet or a lepton (referred to as fake $E_\mathrm{T}^\mathrm{miss}$), since in such events the direction in ϕ of the $\mathbf{E}_\mathrm{T}^\mathrm{miss}$ is correlated with the direction of the mismeasured object. Z/γ^*+jets is the major background that involves substantial amounts of fake $E_\mathrm{T}^\mathrm{miss}$. Figure 5.1 shows the differences between the $E_\mathrm{T}^\mathrm{miss}$ (left) and $E_\mathrm{T,rel}^\mathrm{miss}$ (right) distributions.
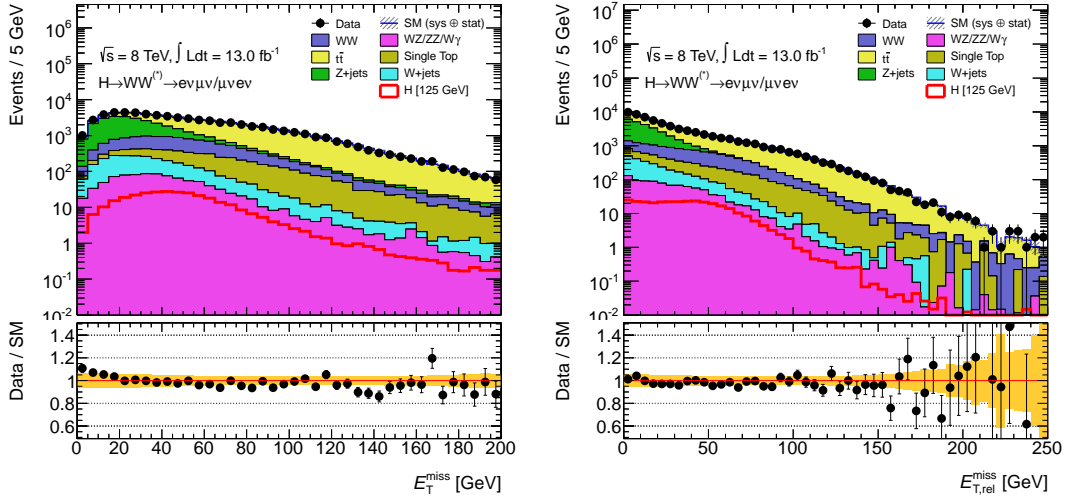
Figure 5.1: The $E_\mathrm{T}^\mathrm{miss}$ (left) and $E_\mathrm{T,rel}^\mathrm{miss}$ (right) distributions for the $e\mu + \mu e$ channels. The shaded area represents the uncertainty on the background yields from statistical, experimental, and theoretical sources. The lower part of each plot shows the ratio between the data and the expectation from MC, with the yellow band representing the uncertainty on the normalisation of the various background components. The signal is shown for $m_H = 125$ GeV and is overlaid as a red curve.

5.4 Event selection

Optimal data-taking conditions for the detector system are required for an event to be accepted by the offline analysis. This is guaranteed by applying the Data Quality (DQ) status flags which ensure that all the sub-detectors, triggers and reconstruction algorithms were properly operating. The μ-rescaling procedure has been applied to the MC simulation, as described in Section 4.1. Events are required to have a primary vertex consistent with the beam spot position, with at least three associated tracks with $p_T > 400$ MeV. The data used for this analysis were collected using inclusive single-muon and single-electron triggers. The two main triggers require the p_T of the leptons to be greater than 24 GeV and that the leptons are isolated. The lepton trigger efficiencies are measured as a function of p_T and η using Z events. The efficiencies are approximately 90% for electrons, and 90% (70%) for muons in the endcap (barrel). Overall cleaning criteria are applied to events in order to suppress non-collision backgrounds such as cosmic-ray muons, beam-related backgrounds, or noise in the calorimeters. The following sections provide the details on the selection of the events optimised to maximise the background rejection efficiency while keeping the Higgs signal efficiency at a high level.

5.4.1 Pre-selection

The events are selected if there are exactly two good quality leptons with $p_T > 15$ GeV (passing the criteria outlined in the previous section) present. Only final states with the different flavour leptons ($e\mu + \mu e$) are considered. The leptons are required to be oppositely charged and the leading one has to have p_T greater than 25 GeV. The Drell-Yan (DY) process (Z/γ^*+jets, di-lepton production from the $q\bar{q}$ annihilation via the exchange of the Z boson or a virtual photon, γ^*) is suppressed by the cuts on the lepton p_T and the invariant mass, $m_{\ell\ell} > 10$ GeV. Further reduction of the Z/γ^*+jets (mainly $Z/\gamma^* \to \tau\tau$ decays with a small contribution from $Z/\gamma^* \to \mu\mu$) and QCD multijets backgrounds is obtained by the requirements on the $E_{T,rel}^{miss} > 25$ GeV. The different flavour channels are separated into two categories depending on the flavour of the higher p_T lepton, i.e., $e\mu$ has a leading p_T electron whereas in the μe channel, a muon is the leading one. The $m_{\ell\ell}$ and $E_{T,rel}^{miss}$ distributions for the $e\mu$ and μe channels separately are shown in Figures 5.2 and 5.3 after imposing the minimum $m_{\ell\ell}$ cut.

Figure 5.4 shows the distribution of the jet multiplicity after the requirement on $E_{T,rel}^{miss}$. It can be clearly seen that the background rate and composition vary as a function of the number of jets. The events without any accompanying jets are dominated by the irreducible SM WW continuum and the DY background. Lower in rate but also important are W+jets and non-WW diboson backgrounds. In the case of one jet present in the event, the top ($t\bar{t}$ and $tW/tb/tqb$) background dominates. The estimation of all the relevant backgrounds to the Higgs boson search is described in Section 5.5, with a more detailed description of the $W\gamma$ estimate. Due to different background compositions in different jet bins, the analysis is split into two parts and the specific event selection is described below. Tables 5.3 and 5.4 show the impact of the pre-selection cuts (up to and including the $E_{T,rel}^{miss}$ cut) on the observed and expected number of events for $e\mu$ and μe channels separately. The agreement between the observed and expected numbers of events is very good.

Common to the different jet multiplicities' selections are the cuts exploiting the topology and the kinematic features of the $H \to WW^{(*)} \to \ell\nu\ell\nu$ decay mode. Due to the spin-0 nature of the Higgs boson, one can exploit the spin correlations in the $WW^{(*)}$ system. The W
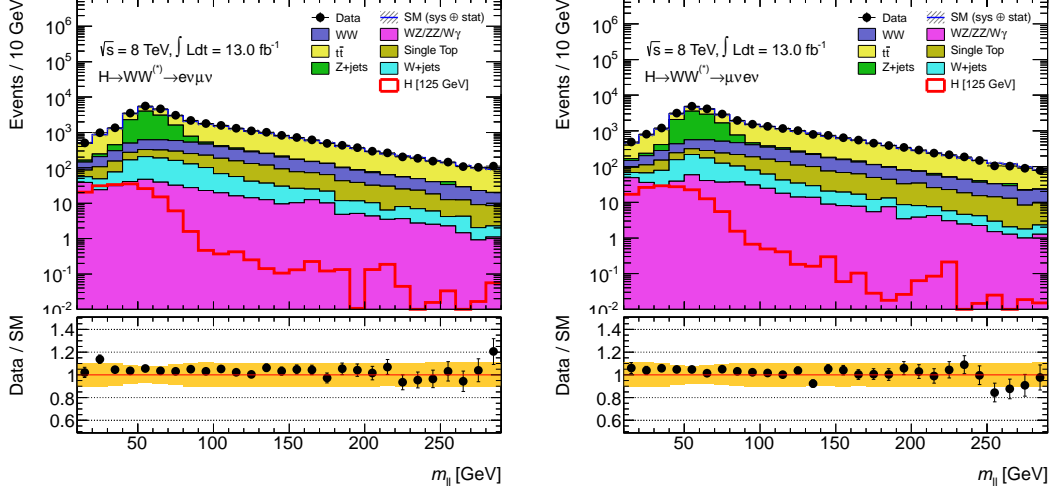
Figure 5.2: The dilepton invariant mass distribution for the $e\mu$ (left) and μe (right) channels with the minimum lepton $p_{\rm T}$ and $m_{\ell\ell}$ requirements applied. Statistical and systematic uncertainties are included. The signal is shown for $m_H = 125$ GeV and is overlaid as a red curve.

	Signal	WW	$WZ/ZZ/W\gamma$	$t\bar{t}$	$tW/tb/tqb$	$Z+$jets	$W+$jets	Total Bkg.	Observed
all events	214 ± 2	3583 ± 12	1170 ± 21	18031 ± 55	1844 ± 23	11803 ± 49	1694 ± 16	38126 ± 83	39980
lepton $p_{\rm T}$	180 ± 1	3385 ± 12	964 ± 19	17044 ± 54	1745 ± 23	9388 ± 44	1694 ± 16	34218 ± 78	35485
OS leptons	173 ± 1	3374 ± 12	475 ± 14	16995 ± 54	1730 ± 22	9263 ± 41	1083 ± 13	32920 ± 75	34253
$m_{\ell\ell}>10$ GeV	172 ± 1	3371 ± 12	467 ± 14	16983 ± 54	1729 ± 22	9260 ± 41	1080 ± 13	32890 ± 75	34220
$E_{\rm T,rel}^{\rm miss}>25$ GeV	111 ± 1	2383 ± 11	241 ± 11	10503 ± 43	1160 ± 19	1188 ± 14	330 ± 8	15804 ± 52	15708

Table 5.3: Observed and expected number of events at the pre-selection stage in the $e\mu$ channel. The $W+$jets background is determined entirely from data. The other background processes are taken from MC with WW, top and $Z/\gamma^* \to \tau\tau$ predictions corrected by the normalisation factors, described in Section 5.5. Only statistical uncertainties are reported here.

bosons have opposite spins and because the W coupling to fermions is purely left handed, the leptons tend to emerge in the same direction from the interaction point. This allows to place cuts on the invariant mass of the leptons and on the azimuthal opening angle between them. The exact cut values are $m_{\ell\ell} < 50$ GeV and $\Delta\phi_{\ell\ell} < 1.8$ radians. Another very important variable used in this analysis to test for the presence of the signal, is called a transverse mass, $m_{\rm T}$ [116, 117], and is defined as:

$$m_{\rm T} = \sqrt{(E_{\rm T}^{\ell\ell} + E_{\rm T}^{\rm miss})^2 - |\mathbf{p}_{\rm T}^{\ell\ell} + \mathbf{E}_{\rm T}^{\rm miss}|^2},$$

where $E_{\rm T}^{\ell\ell} = \sqrt{|\mathbf{p}_{\rm T}^{\ell\ell}|^2 + m_{\ell\ell}^2}$ and $\mathbf{p}_{\rm T}^{\ell\ell} = \mathbf{p}_{\rm T}^{\ell1} + \mathbf{p}_{\rm T}^{\ell2}$. The neutrinos in the final state escape the detector and only the sum of their transverse momenta can be inferred from the $E_{\rm T}^{\rm miss}$ in the event. This means that the mass of the Higgs boson cannot be fully reconstructed because the only variables that one has access to are in the transverse plane. Nevertheless, the $m_{\rm T}$ observable is sensitive to the Higgs boson mass and is used to distinguish the signal events from the background events.
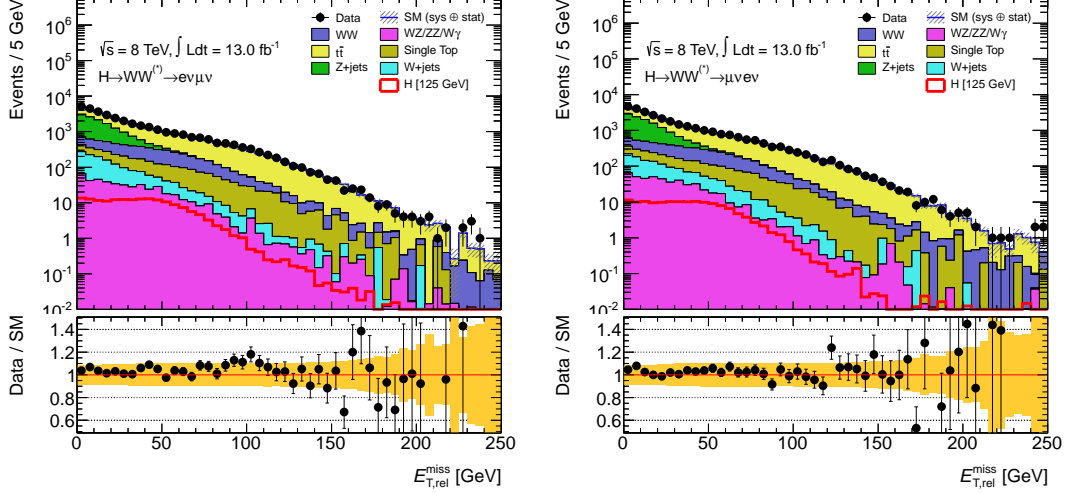
Figure 5.3: The $E_{\mathrm{T,rel}}^{\mathrm{miss}}$ distribution for the $e\mu$ (left) and μe (right) channels with the minimum lepton p_{T} and $m_{\ell\ell}$ requirements applied. Statistical and systematic uncertainties are included. The signal is shown for $m_H = 125$ GeV and is overlaid as a red curve.

	Signal	WW	$WZ/ZZ/W\gamma$	$t\bar{t}$	$tW/tb/tqb$	Z + jets	W + jets	Total Bkg.	Observed
all events	181 ± 1	3254 ± 12	1398 ± 22	15776 ± 52	1632 ± 22	11383 ± 63	1306 ± 11	34749 ± 89	36691
lepton p_{T}	152 ± 1	3084 ± 11	1033 ± 20	15000 ± 50	1544 ± 21	9020 ± 59	1306 ± 11	30986 ± 84	31987
OS leptons	145 ± 1	3077 ± 11	508 ± 13	14973 ± 50	1526 ± 21	8823 ± 55	882 ± 10	29789 ± 80	30721
$m_{\ell\ell} > 10$ GeV	144 ± 1	3074 ± 11	496 ± 13	14960 ± 50	1525 ± 21	8819 ± 55	880 ± 10	29755 ± 80	30679
$E_{\mathrm{T,rel}}^{\mathrm{miss}} > 25$ GeV	92.88 ± 0.98	2172 ± 10	240 ± 8	9192 ± 41	1007 ± 18	1116 ± 19	335 ± 6	14061 ± 50	13796

Table 5.4: Observed and expected number of events at the pre-selection stage in the μe channel. The W+jets background is determined entirely from data. The other background processes are taken from MC with WW, top and $Z/\gamma^* \to \tau\tau$ predictions corrected by the normalisation factors, described in Section 5.5. Only statistical uncertainties are included at this stage.

5.4.2 $N_{\mathrm{jet}} = 0$ channel

In the case of events without accompanying jets, the background is dominated by the irreducible WW continuum and the remaining Z/γ^*+jets background (mainly in the $\tau\tau$ decay mode). In the 2012 data analysis, an additional cut on the opening angle between the dilepton system and the $E_{\mathrm{T}}^{\mathrm{miss}}$ was placed. It removes pathological events with highly mismeasured leptons or jets and it is 99% efficient for signal events. Figure 5.5 shows the distribution of the opening angle between the dilepton system and the $E_{\mathrm{T}}^{\mathrm{miss}}$. As expected, cutting on $\Delta\phi_{\ell\ell, E_{\mathrm{T}}^{\mathrm{miss}}} > \frac{\pi}{2}$ mainly rejects the processes with fake $E_{\mathrm{T}}^{\mathrm{miss}}$ which are dominated by Z/γ^*+jets events. Further reduction of the DY background can be achieved by placing a cut on the magnitude $p_{\mathrm{T}}^{\ell\ell}$ of the transverse momentum of the dilepton system. At the last stage, the two topological cuts, defined earlier in this section, are applied. Figure 5.6a shows the $p_{\mathrm{T}}^{\ell\ell}$ distribution after the 0 jet requirement, for the $e\mu$ and μe channels separately. The Z/γ^*+jets background contribution is substantially reduced by requiring $p_{\mathrm{T}}^{\ell\ell} > 30$ GeV. The invariant mass distribution after the $p_{\mathrm{T}}^{\ell\ell}$ requirement and the opening angle between the leptons after the $m_{\ell\ell}$ cut are shown in Figure 5.6b and Figure 5.6c, respectively. The $N_{\mathrm{jet}} = 0$ selection is summarised below:
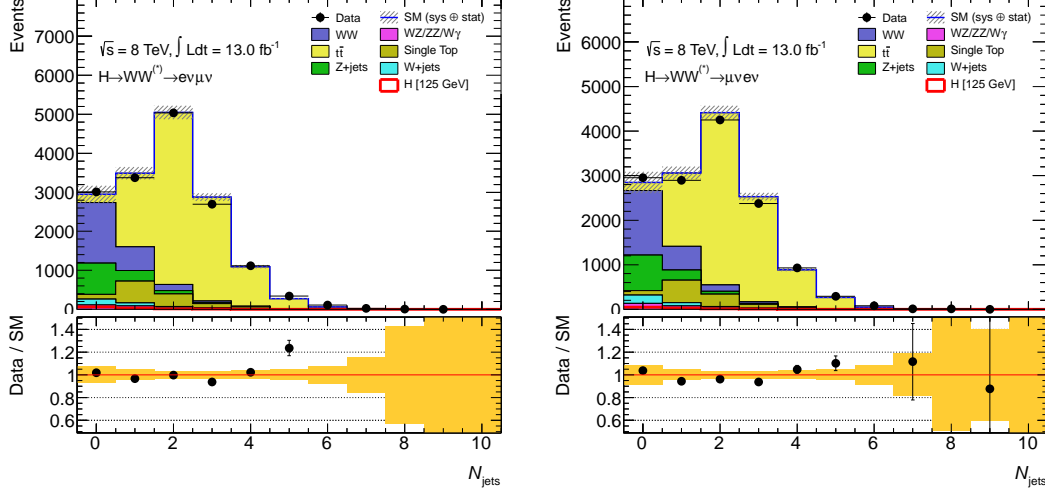
Figure 5.4: Multiplicity of jets after the cut on $E_{\mathrm{T,rel}}^{\mathrm{miss}}$ for the individual $e\mu$ (left) and μe (right) channels. Statistical and systematic uncertainties are included. The signal is shown for $m_H = 125$ GeV and is overlaid as a red curve.

- $\Delta\phi_{\ell\ell,E_{\mathrm{T}}^{\mathrm{miss}}} > \frac{\pi}{2}$

- $p_{\mathrm{T}}^{\ell\ell} > 30$ GeV

- $m_{\ell\ell} < 50$ GeV

- $\Delta\phi_{\ell\ell} < 1.8$ radians

and the impact of these cuts is presented in Tables 5.5 and 5.6 for the $e\mu$ and μe channels separately. A clear excess of the observed data events over the expected background events is present in both lepton flavour channels. The m_{T} distribution (Figure 5.7) after the requirement on $\Delta\phi_{\ell\ell}$ is fit using a binned likelihood in the statistical analysis of the candidate data. The exact procedure is detailed in Section 5.7.
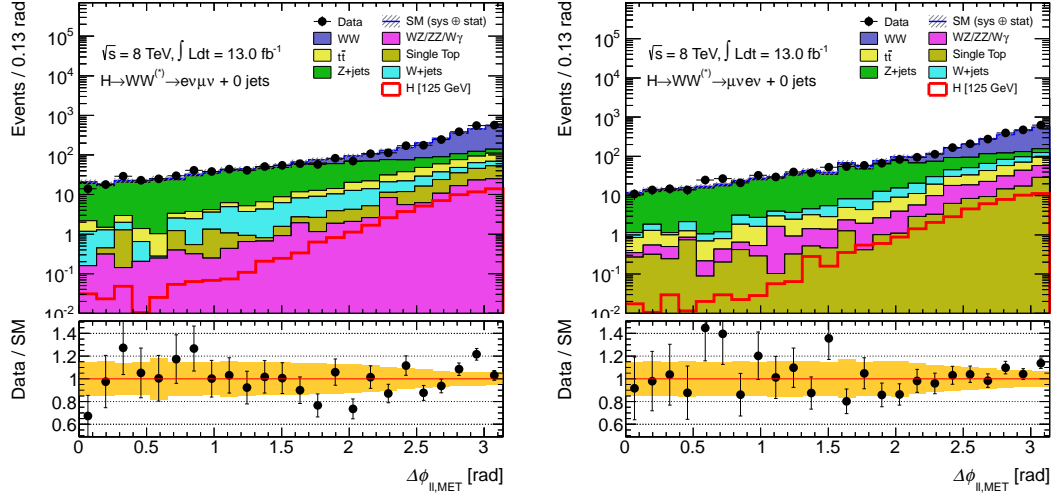
Figure 5.5: Opening angle between the dilepton system and the E_T^{miss} after the 0 jet requirement for the individual $e\mu$ (left) and μe (right) channels. Statistical and systematic uncertainties are included. The signal is shown for $m_H = 125$ GeV and is overlaid as a red curve.
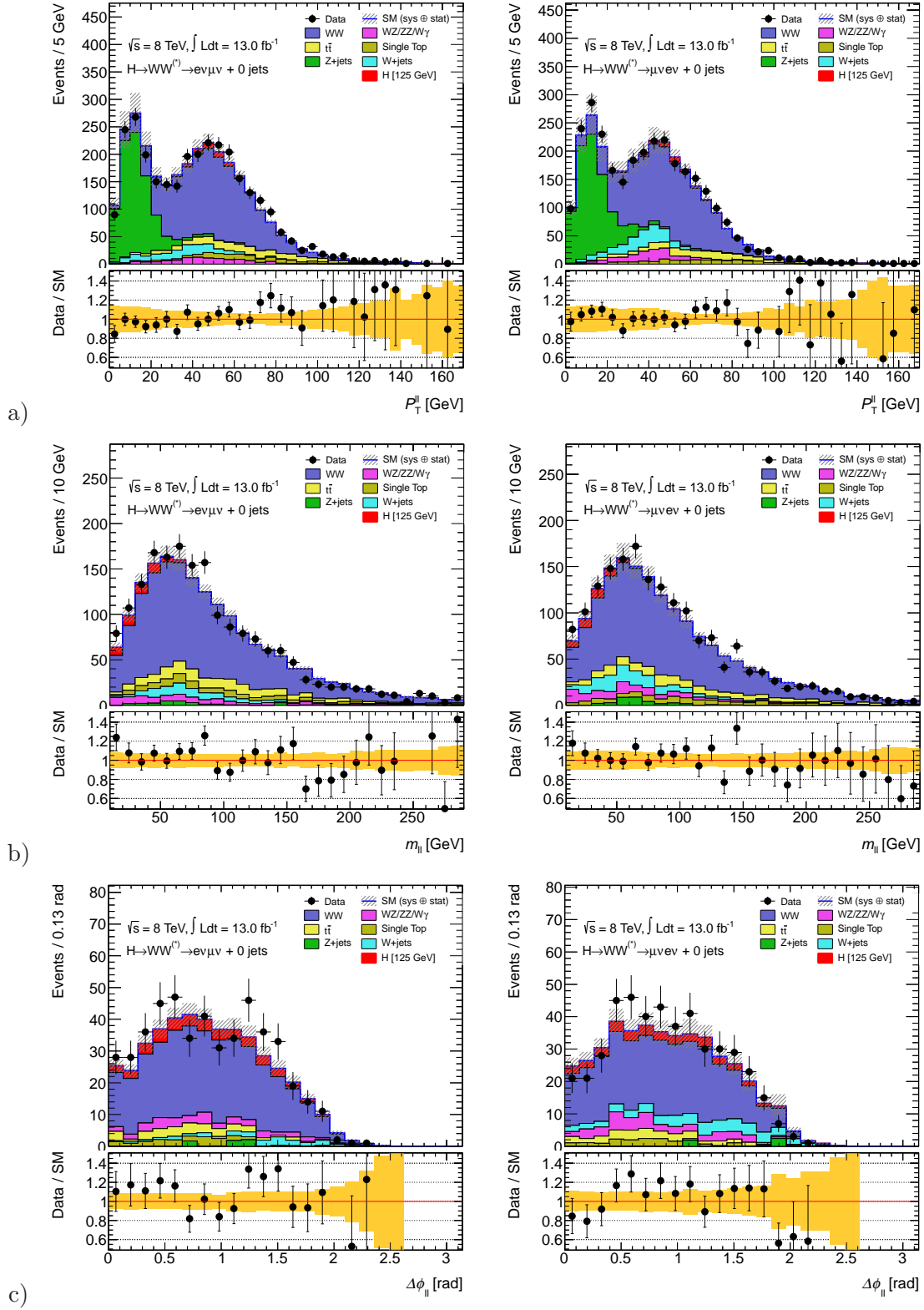
Figure 5.6: Kinematic distributions in the $N_{\text{jet}} = 0$ channel for the individual $e\mu$ (left) and μe (right) channels. The plots show: a) the $p_T^{\ell\ell}$ distribution after the 0 jet requirement, b) the $m_{\ell\ell}$ distribution after the $p_T^{\ell\ell}$ requirement and c) the $\Delta\phi_{\ell\ell}$ distribution after the $m_{\ell\ell}$ requirement. Statistical and systematic uncertainties are included. The signal is shown for $m_H = 125$ GeV and is stacked on top of the background.

	Signal	WW	$WZ/ZZ/W\gamma$	$t\bar{t}$	$tW/tb/tqb$	$Z+\text{jets}$	$W+\text{jets}$	Total Bkg.	Observed
jet veto	59.9 ± 0.8	1556 ± 9	111 ± 6	208 ± 6	115 ± 6	791 ± 10	152 ± 4	2933 ± 17	3007
$\Delta\phi_{\ell\ell,E_{\mathrm{T}}^{\mathrm{miss}}}>\pi/2$	58.9 ± 0.8	1519 ± 9	106 ± 6	194 ± 6	110 ± 6	559 ± 10	129 ± 4	2617 ± 17	2598
$p_{\mathrm{T},\ell\ell}>30$ GeV	54.1 ± 0.7	1271 ± 8	88 ± 5	178 ± 5	105 ± 6	24 ± 4	89 ± 3	1756 ± 13	1868
$m_{\ell\ell}<50$ GeV	43.3 ± 0.6	309 ± 4	30 ± 3	28 ± 2	18 ± 2	6 ± 3	19 ± 1	411 ± 7	487
$\Delta\phi_{\ell\ell}<1.8$	41.8 ± 0.6	296 ± 4	29 ± 3	28 ± 2	18 ± 2	6 ± 3	16 ± 1	392 ± 7	469

Table 5.5: Observed and expected number of events in the $N_{\mathrm{jet}}=0$ $e\mu$ channel. The W+jets background is determined entirely from data. The other background processes are taken from MC with WW, top and $Z/\gamma^*\to\tau\tau$ predictions corrected by the normalisation factors, described in Section 5.5. Only statistical uncertainties are reported here.

	Signal	WW	$WZ/ZZ/W\gamma$	$t\bar{t}$	$tW/tb/tqb$	$Z+\text{jets}$	$W+\text{jets}$	Total Bkg.	Observed
jet veto	49.9 ± 0.7	1448 ± 8	131 ± 6	179 ± 6	99 ± 5	784 ± 17	188 ± 3	2830 ± 22	2953
$\Delta\phi_{\ell\ell,E_{\mathrm{T}}^{\mathrm{miss}}}>\pi/2$	49.2 ± 0.7	1422 ± 8	126 ± 6	167 ± 5	95 ± 5	642 ± 19	177 ± 3	2629 ± 23	2632
$p_{\mathrm{T},\ell\ell}>30$ GeV	44.4 ± 0.7	1171 ± 7	101 ± 5	152 ± 5	88 ± 5	33 ± 7	132 ± 2	1677 ± 14	1762
$m_{\ell\ell}<50$ GeV	35.2 ± 0.6	270 ± 4	39 ± 3	27 ± 2	16 ± 2	5 ± 3	46 ± 1	403 ± 6	460
$\Delta\phi_{\ell\ell}<1.8$	33.8 ± 0.5	260 ± 4	38 ± 3	26 ± 2	16 ± 2	2 ± 2	39.78 ± 0.97	382 ± 6	448

Table 5.6: Observed and expected number of events in the $N_{\mathrm{jet}}=0$ μe channel. The W+jets background is determined entirely from data. The other background processes are taken from MC with WW, top and $Z/\gamma^*\to\tau\tau$ predictions corrected by the normalisation factors, described in Section 5.5. Only statistical uncertainties are reported here.

5.4.3 $N_{\mathrm{jet}}=1$

In the $N_{\mathrm{jet}}=1$ channel, the top contribution (which includes $t\bar{t}$ and single top processes) dominates the background composition at the beginning of the selection. Top quarks decay to W bosons and b-quarks which means that $t\bar{t}$ and tW backgrounds will have overlapping signatures with the $H\to WW^{(*)}\to\ell\nu\ell\nu$ signal region. These backgrounds are substantially suppressed by rejecting events containing a jet identified as being consistent with originating from a b-quark using a b-tagging algorithm, as described in Section 4.3.1. In 2011 and in the earlier 2012 data analyses, a cut on the total transverse momentum, $p_{\mathrm{T}}^{\mathrm{tot}}$ was applied to suppress the top backgrounds that have additional low-p_{T} jets. This requirement was also removing $\sim40\%$ of the signal and after careful studies it was decided to remove this cut from the analysis. Dropping this requirement increased the expected signal significance by $\sim10\%$ but it also slightly increased the predicted WW and top backgrounds. Suppression of the $Z/\gamma^*\to\tau\tau$ background can be obtained using the $\tau\tau$ invariant mass reconstruction within the collinear approximation [118]. Assuming that the τ directions are given by the directions of the visible τ decay products and that the ν from τ decays are the only source of the $E_{\mathrm{T}}^{\mathrm{miss}}$, the τ momenta can be reconstructed. If the energy fractions x_{τ_1} and x_{τ_2} carried by the visible decay products are positive (the collinear approximation does not always yield good solutions) and the invariant mass of the hypothetical $\tau\tau$ system ($m_{\tau\tau}=m_{\ell\ell}/\sqrt{x_{\tau_1}x_{\tau_2}}$) satisfies $|m_{\tau\tau}-m_Z|<25$ GeV, the event is rejected. The $N_{\mathrm{jet}}=1$ selection is summarised below:

- b-jet veto

- $Z\to\tau\tau$ veto

- $m_{\ell\ell}<50$ GeV

- $\Delta\phi_{\ell\ell}<1.8$ radians

Figure 5.7: Transverse mass, m_T, distribution after all the selection cuts in the $N_{jet} = 0$ channel for the individual $e\mu$ (left) and μe (right) channels. Statistical and systematic uncertainties are included. The signal is shown for $m_H = 125$ GeV and is stacked on top of the background.
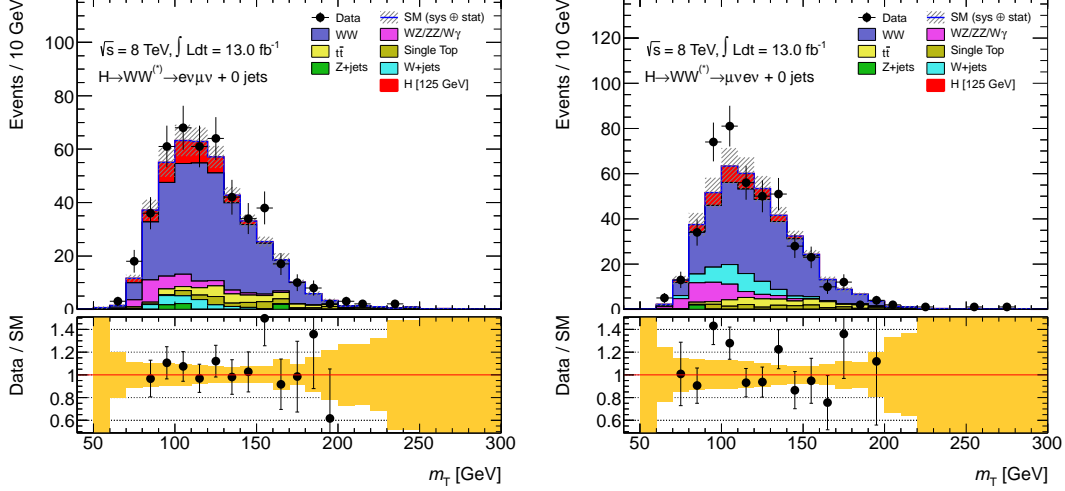
	Signal	WW	$WZ/ZZ/W\gamma$	$t\bar{t}$	$tW/tb/tqb$	Z + jets	W + jets	Total Bkg.	Observed
one jet	32.2 ± 0.6	453 ± 4	83 ± 6	1841 ± 18	545 ± 13	273 ± 7	82 ± 4	3278 ± 24	3371
b-jet veto	27.2 ± 0.5	387 ± 4	66 ± 3	454 ± 9	143 ± 7	232 ± 6	66 ± 3	1349 ± 14	1408
$Z \to \tau\tau$ veto	27.1 ± 0.5	376 ± 4	63 ± 3	435 ± 9	135 ± 7	197 ± 6	64 ± 3	1270 ± 14	1339
$m_{\ell\ell} < 50$ GeV	20.5 ± 0.4	70 ± 2	19 ± 1	75 ± 4	28 ± 3	54 ± 3	13 ± 1	259 ± 6	286
$\Delta\phi_{\ell\ell} < 1.8$	18.9 ± 0.4	63 ± 1	17 ± 1	71 ± 4	26 ± 3	14 ± 2	11 ± 1	202 ± 6	226

Table 5.7: Observed and expected number of events in the $N_{jet} = 1$ $e\mu$ channel. The W+jets background is determined entirely from data. The other background processes are taken from MC with WW, top and $Z/\gamma^* \to \tau\tau$ predictions corrected by the normalisation factors, described in Section 5.5. Only statistical uncertainties are reported here.

and the impact of these cuts is presented in Tables 5.7 and 5.8 for the $e\mu$ and μe channels separately. An excess of observed events over the MC prediction is also seen in the $N_{jet} = 1$ channel but it is less significant than the excess in the $N_{jet} = 0$ case. Kinematic distributions of the relevant quantities are shown in Figure 5.8 and the final transverse mass distribution used in the fit is shown in Figure 5.9.

5.5 Background estimation

The SM backgrounds that have the same signature as the $H \to WW^{(*)} \to \ell\nu\ell\nu$ signal include WW and top ($t\bar{t}$ and $tW/tb/tqb$) processes. They all produce two high-p_T isolated leptons along with the E_T^{miss} (there are additional b-jets in the top background). Together with the small contribution from $Z/\gamma^* \to \tau\tau$ background, they are normalised to the observed rates in data in specifically chosen control regions (CRs) which are dominated by the relevant background source. The W+jets background estimation follows a fully data-driven method. It will become clear in the next section that the dominant systematic uncertainties come from theoretical sources, with the WW cross section normalisation in the first place. To reduce the impact of the theoretical uncertainties on the sensitivity of the analysis,
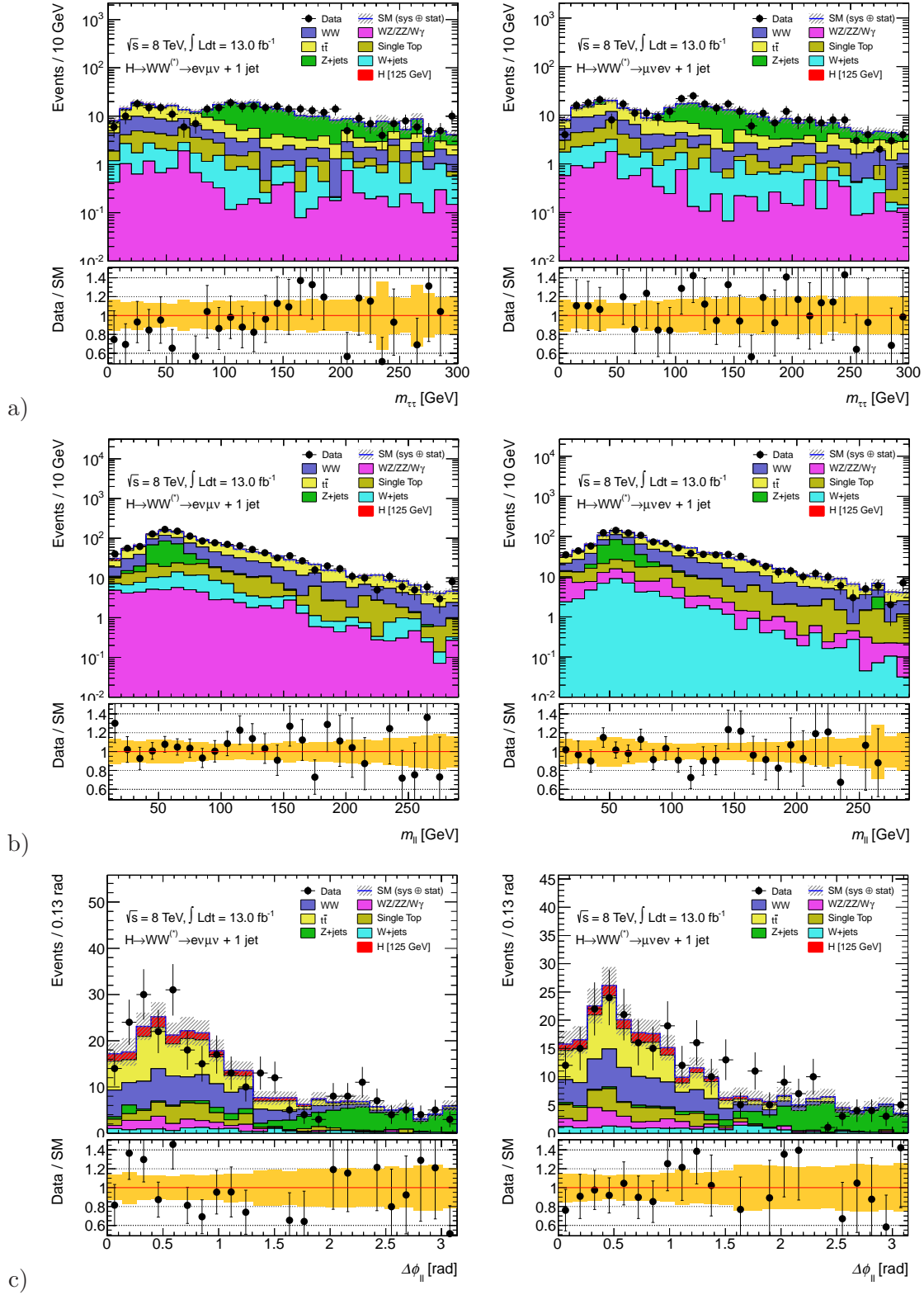
Figure 5.8: Kinematic distributions in the $N_{\text{jet}} = 1$ channel for the individual $e\mu$ (left) and μe (right) channels. The plots show: a) the $m_{\tau\tau}$ distribution after the b-jet veto requirement, b) the $m_{\ell\ell}$ distribution after the $Z \to \tau\tau$ veto and c) the $\Delta\phi_{\ell\ell}$ distribution after the $m_{\ell\ell}$ requirement. Statistical and systematic uncertainties are included. The signal is shown for $m_H = 125$ GeV and is stacked on top of the background.

	Signal	WW	$WZ/ZZ/W\gamma$	$t\bar{t}$	$tW/tb/tqb$	Z + jets	W + jets	Total Bkg.	Observed
one jet	27.4 ± 0.5	396 ± 4	74 ± 5	1610 ± 17	493 ± 12	231 ± 6	72 ± 3	2877 ± 22	2893
b-jet veto	23.2 ± 0.5	341 ± 3	61 ± 4	408 ± 9	140 ± 7	196 ± 6	60 ± 2	1207 ± 14	1247
$Z \to \tau\tau$ veto	23 ± 0.5	332 ± 3	59 ± 4	388 ± 9	134 ± 7	170 ± 6	58 ± 2	1141 ± 13	1172
$m_{\ell\ell} < 50$ GeV	17.2 ± 0.4	60 ± 1	20 ± 2	67 ± 4	27 ± 3	45 ± 2	17 ± 1	236 ± 6	262
$\Delta\phi_{\ell\ell} < 1.8$	16 ± 0.4	55 ± 1	18 ± 2	62 ± 4	27 ± 3	8.07 ± 0.75	13.38 ± 0.95	184 ± 5	207

Table 5.8: Observed and expected number of events in the $N_{\text{jet}} = 1$ μe channel. The W+jets background is determined entirely from data. The other background processes are taken from MC with WW, top and $Z/\gamma^* \to \tau\tau$ predictions corrected by the normalisation factors, described in Section 5.5. Only statistical uncertainties are reported here.

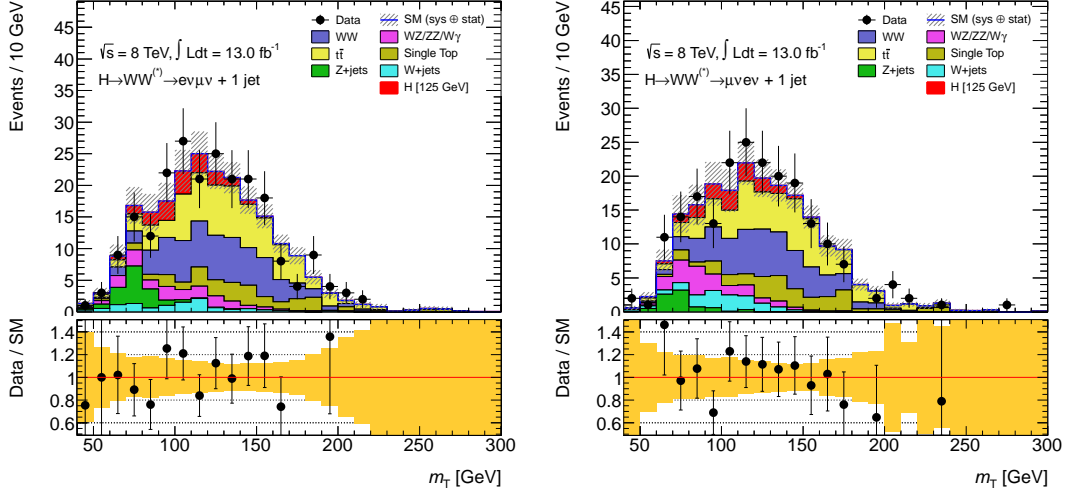Figure 5.9: Transverse mass, m_{T}, distribution after all the selection cuts in the $N_{\text{jet}} = 1$ channel for the individual $e\mu$ (left) and μe (right) channels. Statistical and systematic uncertainties are included. The signal is shown for m_H = 125 GeV and is stacked on top of the background.

it is important to normalise the backgrounds using data-driven methods. The remaining backgrounds which include non-WW diboson processes ($W\gamma^{(*)}$,$WZ^{(*)}$,$Z^{(*)}Z^{(*)}$) are estimated using Monte Carlo simulation. They are however checked, together with W+jets, in a validation region (VR, as opposed to CR, which is used to directly normalise the corresponding backgrounds) constructed from a sample of two leptons with the same charge. The $W\gamma$ background is a very important background, with a small rate but kinematically close to the signal region. Therefore an additional validation region has been built; it is described in detail in Section 5.5.5. In the following sections, each background estimate is described after any others on which it depends. Because of this, the largest background (WW) is described last and is only followed by the non-WW diboson validation regions. The correlations introduced among the backgrounds by the presence of other processes in the CRs are fully incorporated in the statistical procedure, as described in Section 5.7. Table 5.9 summarises the treatment of the backgrounds in the $H{\to}WW^{(*)}{\to}\ell\nu\ell\nu$ analysis.

Channel	WW	Top	$Z/\gamma^*{\to}\tau\tau$	$Z/\gamma^*{\to}ee/\mu\mu$	W+jets	$WZ/ZZ/W\gamma$
$N_{\rm jet}=0$	CR	CR	CR	MC	Data	MC + VR
$N_{\rm jet}=1$	CR	CR	CR	MC	Data	MC + VR

Table 5.9: The estimation procedures for various background processes are given in four categories: normalised using a control region (CR); data-driven estimate (Data); normalised using the MC (MC), and normalised using the MC, but validated in a validation region (MC + VR).

5.5.1 W+jets background

The contribution from W+jets production comes from events in which a jet is the origin of a second reconstructed lepton (the first one coming from the leptonic decay of the W boson). This lepton can be either a true electron or a muon from the decay of a heavy quark or a product of jet fragmentation incorrectly reconstructed as an isolated electron candidate (this process is commonly called as a jet faking an electron). A control region is then built from a dilepton sample where one of the leptons satisfies the identification criteria of a signal lepton (as described in Section 5.3) and the second one does not. They are referred to as "identified" and "anti-identified" leptons, respectively. The specific criteria that the anti-identified lepton is required to pass, are listed in Table 5.10 separately for electrons and muons. In this way, a control sample is divided into two types of events depending on which of the lepton flavours is the anti-identified one. The purity of W+jets events is about 90% in the electron channel and 80% in the muon channel.

Fake factor

The W+jets background in the signal region is obtained by scaling the number of events in the data control sample by a so-called fake factor. The fake factor is defined as the ratio of the number of identified leptons to the number that are anti-identified. It is estimated as a function of anti-identified lepton $p_{\rm T}$ using a di-jet data sample, after subtracting the contributions from real leptons arising from leptonic W and Z decays. The small remaining lepton contamination, which includes $W\gamma^{(*)}$ events, is subtracted using MC simulation. The fake factor uncertainty is the main uncertainty on the W+jets background

Electron	Muon
Electron Candidate	Muon Candidate
$|z_0 \sin \theta| < 0.4$ mm	$|z_0 \sin \theta| < 1$ mm
$|d_0|/\sigma_{d_0} < 3$	$|d_0|/\sigma_{d_0}$ requirement removed
calorimeter iso.	calorimeter iso.
track iso.	—
fails medium++	fails the muon SR selection

Table 5.10: The definition of the anti-identified leptons.
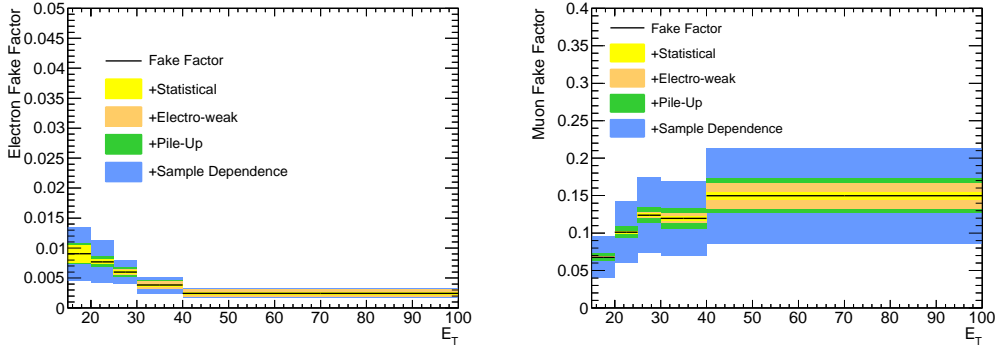
Figure 5.10: The fake factor as a function of p_{T} including the total systematic uncertainty for electrons (left) and muons (right) [119].

contribution. This uncertainty is dominated by the differences in jet properties between di-jet and W+jets samples evaluated with simulated events, with smaller contributions originating from trigger effects, pile-up dependence and the EW subtraction (subtraction of the W/Z events). The relative total uncertainty on the fake factor is estimated to be approximately 50% [119]. The breakdown of the uncertainties on the fake factor is summarised in Table 5.11. Only the uncertainties contributing to the lowest bin in p_{T} are shown since the W+jets background is the most relevant in this p_{T} bin. Much smaller statistical uncertainty on the muon fake factor is due to different trigger requirement in the di-jet selection between electrons and muons. The low threshold electron trigger is highly pre-scaled. Figure 5.10 shows the resulting fake factors, together with the uncertainties, for electrons and muons obtained with 13 fb^{-1} of data.

Source	Electron	Muon
Sample Dependence	45%	40%
Statistical Error	16%	0.9%
Pile-Up Error	10%	7%
EW-Contamination	2.9%	0.7%
Total Uncertainty	49%	41%

Table 5.11: Fake factor uncertainties in the 15 - 20 GeV bin for electron and muons.

5.5.2 Z+jets

In the different lepton flavour channels ($e\mu + \mu e$) the majority of the Z/γ^*+jets background comes from the $Z/\gamma^* \to \tau\tau$ decay channel (with a small, few %, contamination from $Z/\gamma^* \to \mu\mu$ decays where one muon is not reconstructed and a jet or a photon fakes an electron). The Z/γ^*+jets contribution is much smaller than in the ee and $\mu\mu$ channels but it was found to be mismodelled in the current MC samples. A control region has been selected and defined as events passing the full pre-selection (including the $E_{\mathrm{T,rel}}^{\mathrm{miss}}$ requirement) and additionally with $m_{\ell\ell} < 80$ GeV and $\Delta\phi_{\ell\ell} > 2.8$ radians. Figure 5.11 shows the $\Delta\phi_{\ell\ell}$ distribution just before making the final cut on this variable. The normalisation factors (NFs) for the Z/γ^*+jets background to be applied in the $H \to WW^{(*)} \to e\nu\mu\nu$ analysis are derived from the ratio of the background subtracted event yields in data (taking data-driven W+jets and other processes from the simulation prediction), divided by the expected Z/γ^*+jets event yield from MC. As was mentioned before, the Z/γ^*+jets composition is dominated by $Z/\gamma^* \to \tau\tau$ decays and the $Z/\gamma^* \to \mu\mu$ decay contribution is included in the calculation of the NF. No significant difference is observed between the $e\mu$ and μe channels, therefore the combined $e\mu + \mu e$ channel is used to derive the final NF that is applied to both final states. The NF obtained from the CR without any accompanying jets is applied in the $N_{\mathrm{jet}} = 0$ analysis, whereas the NF for the $N_{\mathrm{jet}} = 1$ channel is derived from a CR without any jet multiplicity requirement. The normalisation factor obtained in an exclusive 1 jet bin is consistent with the one derived when not making any jet multiplicity requirement, but the relative statistical uncertainty is 17% compared to 4%. Purities of about 94% and 73% are reached for the zero jet and jet inclusive control regions, respectively. Table 5.12 shows the event yields in the $Z/\gamma^* \to \tau\tau$ control regions. The final normalisation factors are 0.85 ± 0.03 (stat) for the $N_{\mathrm{jet}} = 0$ channel and 0.87 ± 0.03 (stat) for the $N_{\mathrm{jet}} = 1$ channel. The systematic uncertainties on these ratios are estimated as the difference from unity, which amounts to 15% and 13%, respectively. The total uncertainty on the $Z/\gamma^* \to \tau\tau$ estimate in the $N_{\mathrm{jet}} = 0$ signal region is however dominated by the large statistical uncertainty of the MC sample.

	$Z/\gamma^* \to \tau\tau$ CR	$Z/\gamma^* \to \tau\tau$ CR 0 jet
Z/γ^*+jets	1571 ± 20	1408 ± 19
W+jets	63 ± 3	41 ± 3
WW	85 ± 2	44 ± 1
$WZ/ZZ/W\gamma$	16 ± 2	9 ± 1
$t\bar{t}$	363 ± 8	4 ± 1
$tW/tb/tqb$	30 ± 3	1.3 ± 0.6
Total Bkg.	2127 ± 22	1508 ± 20
Signal [125 GeV]	5.1 ± 0.2	2.0 ± 0.1
Observed	1916	1300

Table 5.12: Expected and observed event yields in the $Z/\gamma^* \to \tau\tau$ control regions for the combined $e\mu + \mu e$ channels. The inclusive jet multiplicity bin is used to derive the normalisation factor to be applied in the $N_{\mathrm{jet}} = 1$ channel and the exclusive 0 jet multiplicity bin is used to derive the normalisation factor to be applied in the $N_{\mathrm{jet}} = 0$ channel. Only statistical uncertainties are reported here.
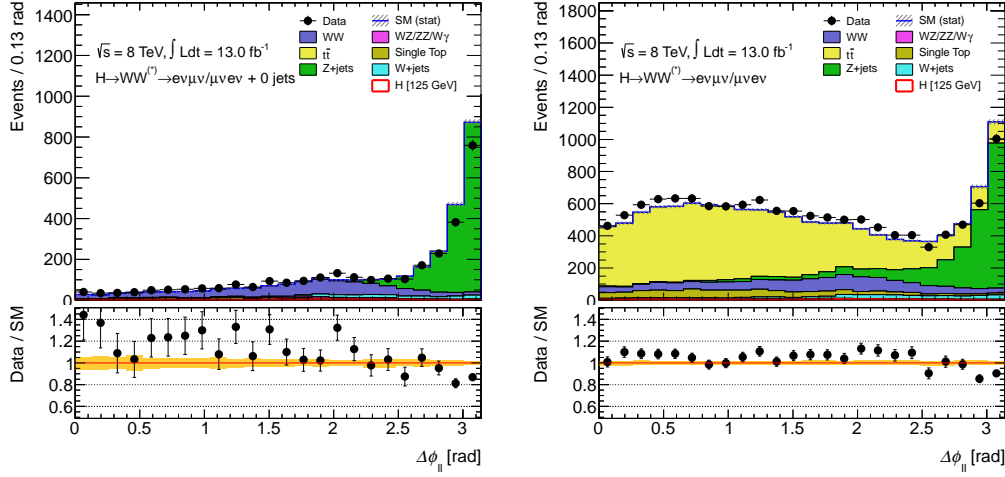
Figure 5.11: The $\Delta\phi_{\ell\ell}$ distribution in the $Z/\gamma^*\to\tau\tau$ CR before the requirement on the $\Delta\phi_{\ell\ell}$ itself. The plots show the data/MC comparison in the 0 jet exclusive sample (left) and the jet inclusive one (right). Only statistical uncertainties are included.

5.5.3   Top background

Top quark events, especially $t\bar{t}$ and the single top Wt processes, are the leading backgrounds to the $H\to WW^{(*)}\to\ell\nu\ell\nu$ analysis. The majority of them have one or more jets present because of the decay of top quark to a b-quark and a W boson. The contribution in the $N_{\text{jet}}=0$ channel (about 12% of the total background) is not negligible though. The following section summarises the estimation of the top background in the $N_{\text{jet}}=0$ and $=1$ final states. Both estimates are partially data-driven methods and each of them results in a single normalisation factor used to scale the MC prediction in the signal region.

$N_{\text{jet}}=0$ estimate

The full jet veto survival probability method (JVSP) [120] is used to estimate the top background contribution in the $N_{\text{jet}}=0$ channel. It relies on a data-driven assessment of the fraction of top events passing the jet veto requirement, $f_{0-\text{jet}}^{\text{data}}$, estimated as

$$f_{0-\text{jet}}^{\text{data}} = f_{0-\text{jet}}^{\text{MC}} \times \left(\frac{p_{\text{data}}^{\text{btag}}}{p_{\text{MC}}^{\text{btag}}}\right)^2. \qquad (5.3)$$

where $f_{0-\text{jet}}^{\text{MC}}$ is the fraction of top MC events passing the jet veto cut and p^{btag} defines a jet veto efficiency in a b-tagged sample. It is calculated, both in data and MC, as the ratio of events containing at least one b-jet and no additional jets to the number of events containing at least one b-jet. Then the estimated number of top events in the $N_{\text{jet}}=0$ channel can be expressed with the formula:

$$N_{\text{top}}^{\text{est}}(\ell\ell + E_{\text{T}}^{\text{miss}}, 0j) = N_{\text{top}}^{\text{data}}(\ell\ell + E_{\text{T}}^{\text{miss}}) \times f_{0-\text{jet}}^{\text{data}}, \qquad (5.4)$$

where $N_{\text{top}}^{\text{data}}(\ell\ell + E_{\text{T}}^{\text{miss}})$ is the number of top events observed in data after the pre-selection cuts. The non-top background contributions are subtracted using the data-driven W+jets

76

estimate and MC simulation for all other processes. The resulting normalisation factor is calculated as a ratio of the estimated number of top background events to the number of MC top background events in the $N_{\text{jet}} = 0$ signal region and yields 1.04 ± 0.05(stat.). Table 5.13 summarises the numerical values of the components used in the top background estimation. The total uncertainty including statistical and systematic contributions is 13%. Section 5.6 gives more details on the systematic uncertainty evaluation.

quantity	value
$p_{\text{data}}^{\text{btag}}$	0.218 ± 0.004
$p_{\text{MC}}^{\text{btag}}$	0.219 ± 0.002
$f_{0-\text{jet}}^{\text{MC}}(\times 10^{-2})$	2.79 ± 0.05
$f_{0-\text{jet}}^{\text{data}}(\times 10^{-2})$	2.77 ± 0.12
$N^{\text{data}}(\ell\ell + E_T^{\text{miss}})$	29504 ± 172
$N_{\text{non-top}}(\ell\ell + E_T^{\text{miss}})$	7846 ± 34
$N_{\text{top}}^{\text{est}}(\ell\ell + E_T^{\text{miss}}, 0j)$	601 ± 27
$N_{\text{top}}^{\text{MC}}(\ell\ell + E_T^{\text{miss}}, 0j)$	578 ± 11
Ratio (NF)	1.04 ± 0.05

Table 5.13: Top 0 jet normalisation factor calculation.

$N_{\text{jet}} = 1$ estimate

The top background in the $N_{\text{jet}} = 1$ signal region is normalised to data in a control region defined by reversing the b-jet veto. Also the requirements on $m_{\ell\ell}$ and $\Delta\phi_{\ell\ell}$ are dropped to gain statistics. The sample thus obtained contains mostly top events ($\sim 90\%$) and the remaining backgrounds are estimated with the data-driven method for W+jets and MC simulation for the other processes. Figure 5.12 shows the relevant kinematic distributions in the top CR. A good agreement is observed between data and MC and the resulting normalisation factor for the $N_{\text{jet}} = 1$ analysis is 1.03 ± 0.02(stat.). The total uncertainty including statistical and systematic uncertainties is 37%. Section 5.6 gives more details on the systematic uncertainty evaluation.

5.5.4 WW background

The SM WW background is the leading background in the $H \rightarrow WW^{(*)} \rightarrow \ell\nu\ell\nu$ analysis. It accounts for about 70% and 30% of the total background expectation in the $N_{\text{jet}} = 0$ and $= 1$ channels, respectively. Apart from the MC@NLO generator, which was used in the 2011 and previous 2012 analyses, there exist other choices of generators that could be used in the simulation of the WW process. A compatibility test of the data with the MC@NLO and POWHEG generators in the WW control region has been performed based on the $m_{\ell\ell}$, $\Delta\phi_{\ell\ell}$ and m_{T} distributions. It was based on a likelihood with one parameter of interest describing the preferred model in the data. Test results showed that POWHEG is preferred to MC@NLO at 99% CL. More details can be found in Ref. [114].

The topology of the low mass spin-0 Higgs boson decaying to a pair of W bosons prefers the leptons to be emitted in the same direction, which in turn results in small invariant mass values. This property is exploited in building a signal-free WW control
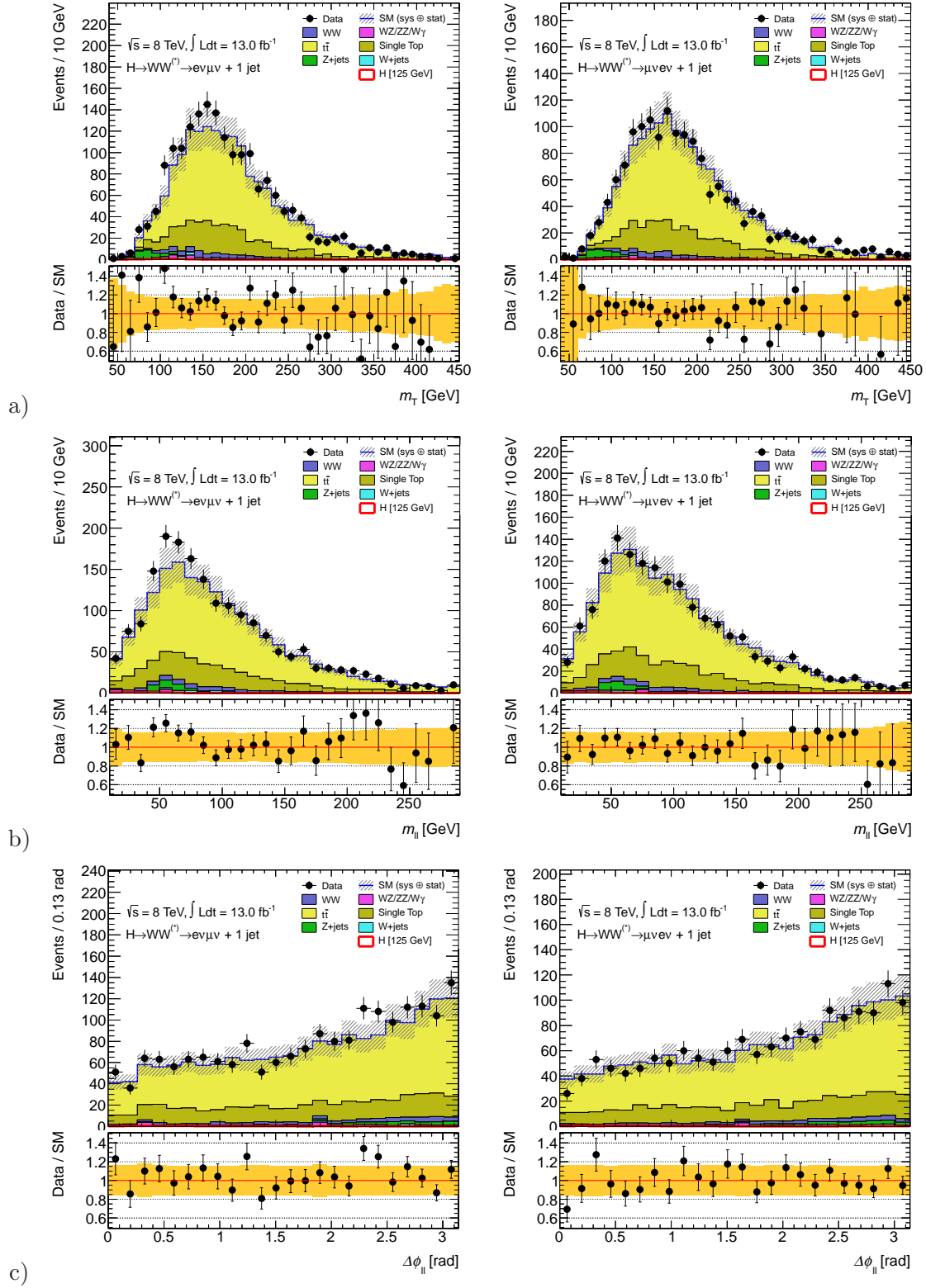
Figure 5.12: Kinematic distributions in the top CR in the $N_{\text{jet}} = 1$ channel for the individual $e\mu$ (left) and μe (right) channels. The plots show: a) the m_{T} distribution, b) the $m_{\ell\ell}$ distribution and c) the $\Delta\phi_{\ell\ell}$ distribution. Statistical and systematic uncertainties are included.

78

region. It is based on a sample passing the signal region criteria except that the $\Delta\phi_{\ell\ell}$ cut is not applied and the dilepton invariant mass $m_{\ell\ell}$ is required to be greater than 80 GeV. The expected and observed number of events are shown in Table 5.14. Here, the top and $Z/\gamma^*\to\tau\tau$ NFs were applied to the relevant backgrounds. The purity of the CR is about 70% and 40% in the $N_{\rm jet}=0$ and $N_{\rm jet}=1$ cases for the $e\mu$ and μe channels combined. The contamination in the $N_{\rm jet}=1$ WW CR comes primarily from the top background. The normalisation issues can be seen from the comparison of the number of data and MC events in the WW CRs. The resulting NF for the $e\mu$ and μe channels combined is $1.13\pm0.04({\rm stat.})$ and $0.84\pm0.08({\rm stat.})$ for the $N_{\rm jet}=0$ and $N_{\rm jet}=1$ channel, respectively. These normalisation factors are not used in the final results but instead, in the statistical analysis, the data control regions are used directly to constrain the WW contribution. The differences in the normalisation factors between the jet bins can be partially explained by the inability of the POWHEG generator to model correctly the jet bin migrations. This does not however pose any problems since the modelling is accounted for independently in the exclusive jet multiplicity bins. Figure 5.13 shows the distributions of the key variables in the WW $N_{\rm jet}=0$ CR, here the normalisation factors were already applied to the top, $Z/\gamma^*\to\tau\tau$ and WW contributions. Figure 5.14 shows the same distributions in the WW $N_{\rm jet}=1$ CR. The shapes of the kinematic distributions appear to be fairly well modelled. The most discrepant distribution seems to be that of $\Delta\phi_{\ell\ell}$ in the $e\mu$ $N_{\rm jet}=0$ channel. The corresponding disrtibution in the μe channel does not show the same mismodelling features. Multiple studies have been performed to understand if the nature of this discrepancy could be due to the detector or simulation issues, mismodelling of specific variables or simply if some of the backgrounds have not been accounted for. None of the studies was able to point directly to one obvious source of the problem which hints that it is a complex effect or simply a statistical fluctuation. Generator modelling has been checked by comparing the sensitive distributions among different generators: POWHEG, MC@NLO, MCFM and Sherpa. The discrepancies can be seen both in the high $\Delta\phi_{\ell\ell}$ region in the WW control region and in for low $m_{\rm T}$ values in the signal region. These differences are accounted for in the form of the $m_{\rm T}$ shape systematic uncertainties as described in Section 5.6.

	Signal [125 GeV]	WW	$WZ/ZZ/W\gamma$	$t\bar{t}$	Single top	Z+jets	W+jets	Total Bkg.	Observed
0j: WW CR ($e\mu$)	0.54 ± 0.13	568 ± 5	38 ± 4	109 ± 4	60 ± 4	6 ± 3	38 ± 2	820 ± 9	889
0j: WW CR (μe)	0.61 ± 0.17	534 ± 5	33 ± 3	98 ± 4	55 ± 4	7 ± 3	40 ± 1	768 ± 8	836
1j: WW CR ($e\mu$)	0.65 ± 0.16	247 ± 3	29 ± 2	255 ± 7	77 ± 5	11 ± 2	30 ± 2	649 ± 10	623
1j: WW CR (μe)	0.53 ± 0.15	219 ± 3	23 ± 3	236 ± 6	75 ± 5	11 ± 3	21 ± 1	585 ± 9	537

Table 5.14: Observed and expected number of events in the WW CR in the $N_{\rm jet}=0$ and $=1$ channels. Only statistical errors are included.

5.5.5 Non-WW diboson backgrounds

The diboson backgrounds, other than the SM WW continuum, consist of $W\gamma^{(*)}$,$WZ^{(*)}$ and $Z^{(*)}Z^{(*)}$ processes. These backgrounds add up to about 10% of the total estimated background in the $N_{\rm jet}=0$ and $=1$ channels and are of the same magnitude as the signal. The most dominant of these backgrounds are $W\gamma$, $W\gamma^*$ and $WZ^{(*)}$.

Figure 5.13: Kinematic distributions in the WW CR in the $N_{\text{jet}} = 0$ channel for the individual $e\mu$ (left) and μe (right) channels. The plots show: a) the m_{T} distribution, b) the $m_{\ell\ell}$ distribution and c) the $\Delta\phi_{\ell\ell}$ distribution. Statistical and systematic uncertainties are included.
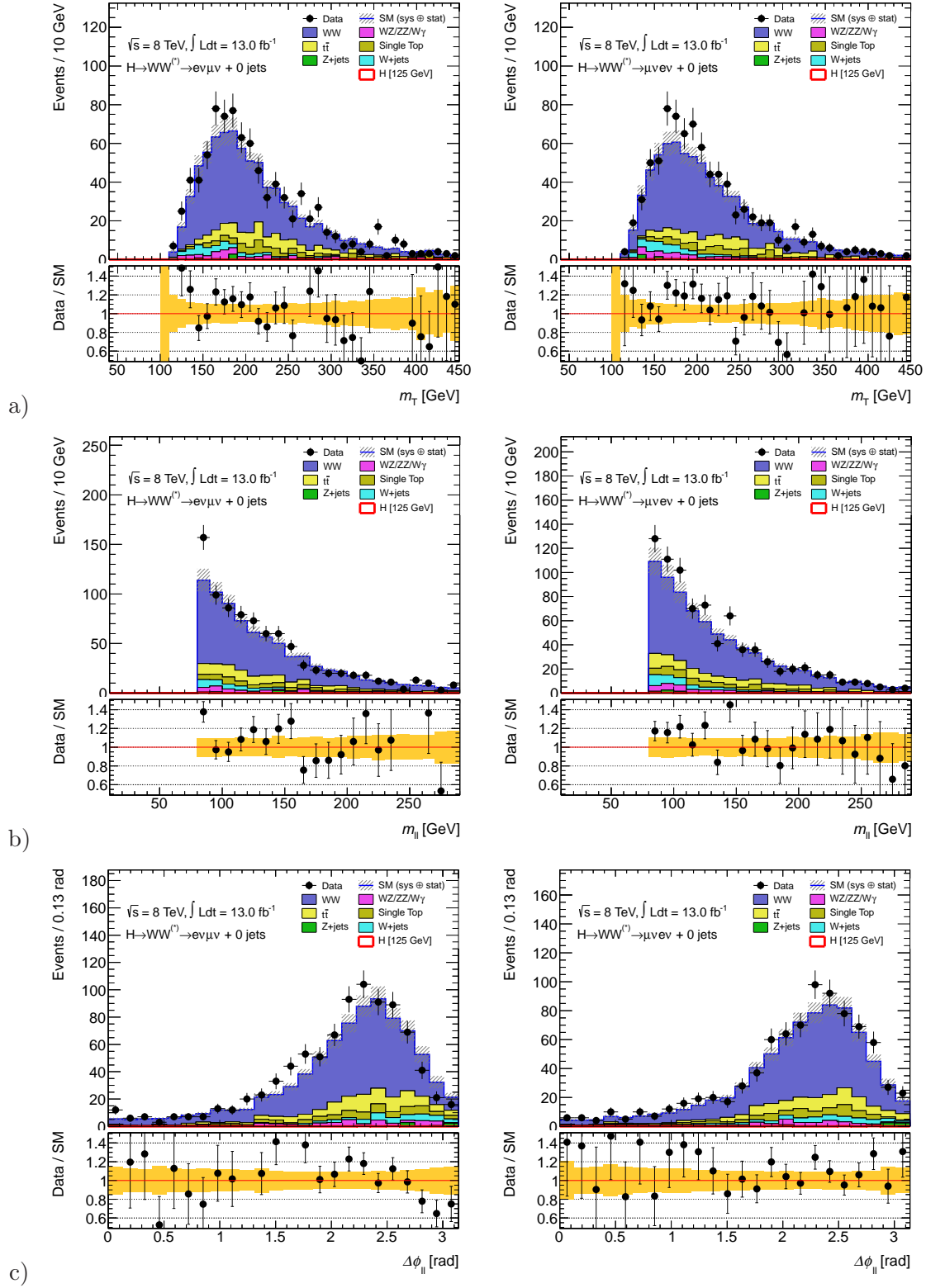
Figure 5.14: Kinematic distributions in the WW CR in the $N_{\text{jet}} = 1$ channel for the individual $e\mu$ (left) and μe (right) channels. The plots show: a) the m_{T} distribution, b) the $m_{\ell\ell}$ distribution and c) the $\Delta\phi_{\ell\ell}$ distribution. Statistical and systematic uncertainties are included.
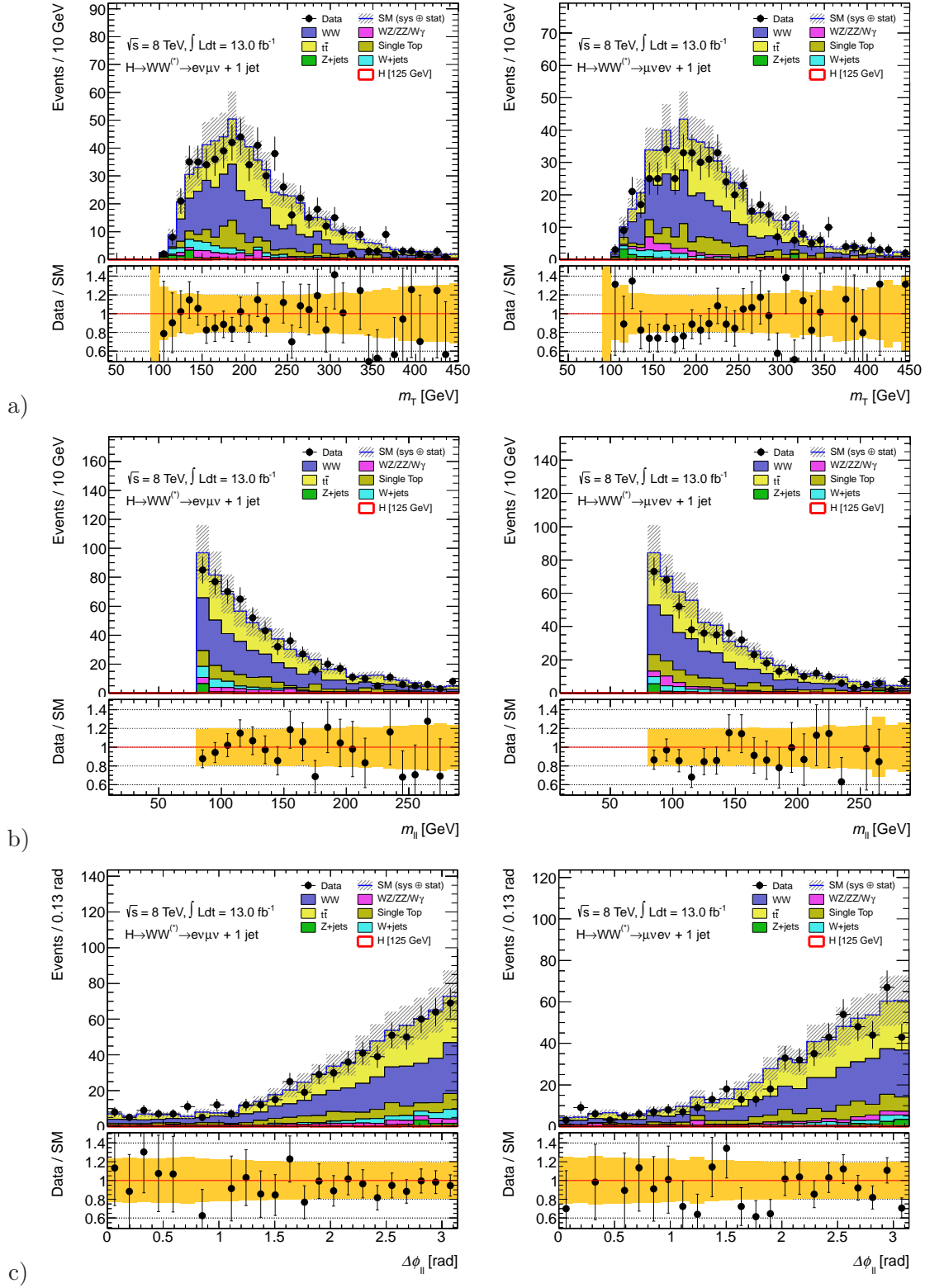
The $W\gamma$ background and data validation region

A data-driven estimation of the $W\gamma$ background has been suggested. Its application in the analysis instead of the purely MC based approach could result in smaller systematic uncertainties. It is a newly developed method and it still needs further studies. Nonetheless, the $W\gamma$ background and the proposed method, are discussed in the following.

The $W\gamma$ process is an important background in the search for the low mass Higgs in the $H \rightarrow WW^{(*)} \rightarrow \ell\nu\ell\nu$ channel as it is similar kinematically and in size to the signal after full selection. Here, one lepton is a product of the W boson decay and the second one (an electron) comes from the photon conversion in the tracking detector. The available simulated $W\gamma$ statistics for the 2011 analysis was very limited - of the same order as the 2011 data. The m_T shape and thus the 2011 limits were shown to be very sensitive to statistical fluctuations in the $W\gamma$ MC predictions. The increased $W\gamma$ MC statistics for the 2012 analysis is thus a large improvement alone to the analysis. In addition a $W\gamma$ validation region has been defined, where the MC modelling of this background is scrutinised. The $W\gamma$ validation region uses loosened electron identification criteria, in order to select the conversion electrons. The validation region is used together with a conversion fake factor to derive normalisation factors for the $N_{\mathrm{jet}} = 0$ and $= 1$ bins.

Another improvement for 2012 is the tightened electron impact parameter and isolation requirements with respect to 2011. Although these improvements were primarily designed to reduce the W+jets background, they have been shown to decrease the $W\gamma$ background in 2012.

$W\gamma$ validation region definition

The $W\gamma$ background contributes to the ee and $e\mu + \mu e$ final states where the photon can fake an electron if it converts to an electron-positron pair. Truth studies show that the photon conversion is mostly asymmetric and that it is highly unlikely for the lower p_T electron to be reconstructed. The method presented here focuses on the $e\mu$ and μe channels, also showing the VR distributions for the combination of the two channels to reduce the large statistical error. A first attempt to estimate the $W\gamma$ background in the ee channel is presented in Appendix A.

To select events with electrons from photon conversions, the following two identification criteria (or *bits* taken as the arguments to the electron identification determination) are relaxed: the conversion bit and the b-layer bit, which indicates whether the electron is matched to a conversion and if it has a hit in the inner detector layer closest to the interaction point. To reduce contamination from other backgrounds, only same sign events are chosen. Studying the m_T shape of the $W\gamma$ MC after the lepton selection shows that loosening the electron identification criteria and including same sign events does not introduce any bias. For the final $W\gamma$ validation region, only events for which at least one of the identification criteria mentioned above was not satisfied are selected. In this manner a more pure $W\gamma$ VR is obtained.

The majority of the $W\gamma$ events in the $N_{\mathrm{jet}} = 1$ channel lie in the low $E_{\mathrm{T,rel}}^{\mathrm{miss}}$ phase-space. Therefore the $E_{\mathrm{T,rel}}^{\mathrm{miss}}$ cut is dropped in the $N_{\mathrm{jet}} = 1$ channel, while the cut is still applied in the $N_{\mathrm{jet}} = 1$ channel. Figure 5.15 shows the *Tight Bit Electron* for same-sign events with the $E_{\mathrm{T,rel}}^{\mathrm{miss}}$ cut not applied in case of the $N_{\mathrm{jet}} = 1$ channel. The Tight Bit is defined as 1 if an electron fails both the b-layer and the conversion bits requirement, 2 if an electron fails either of those two bits and 3 if an electron passes both bits, which is the case for

the signal region electron selection. Tight Bit 1 has a high purity of $W\gamma$ events, and here a satisfactory agreement is obtained for the normalisation between data and MC within the statistical uncertainties. Both the Tight Bits 1 and 2 are used for the $W\gamma$ validation region to increase the statistics of the $W\gamma$ sample.

The $W\gamma$ $e\mu + \mu e$ validation region selection is summarised below:

- only events with two leptons of same sign are considered,

- the electron must fail at least one of the b-layer and conversion electron identification requirements,

- in the $N_{\mathrm{jet}} = 1$ channel, the $E_{\mathrm{T,rel}}^{\mathrm{miss}}$ cut is dropped.

The resulting data and MC events in the $W\gamma$ zero and one jet validation regions at the final cut stage ($\Delta\phi_{\ell\ell} < 1.8$) are summarised in Table 5.15. The purity of $W\gamma$ events in the validation regions reaches 77% in the $N_{\mathrm{jet}} = 0$ channel and 76% in the $N_{\mathrm{jet}} = 1$ channel. The remaining other backgrounds in the $W\gamma$ VR predominantly consist of W+jets and Z/γ^*+jets events. The W+jets MC does not model the data well so this background is therefore estimated using the data driven fake factor method. The W+jets fake factor is evaluated based on a dijet data control sample (see Section 5.5.1). The modified W+jets electron fake factor for the $W\gamma$ VR, with the conversion and b-layer bits relaxed in the numerator, is shown in Figure 5.16. The muon fake factor is the same as for the nominal W+jets data-driven estimate. The Z/γ^*+jets contribution in the $W\gamma$ $e\mu + \mu e$ VR mainly originates from $Z \rightarrow \mu\mu\gamma$ decays where one muon fails either the reconstruction or the identification criteria and the photon converts into an electron-positron pair. For this type of event the requirement of having same sign leptons and reverting the electron identification criteria does not reject the background. Figures 5.17 and 5.18 show the $E_{\mathrm{T,rel}}^{\mathrm{miss}}$ and m_{T} distributions for data and MC events for the $W\gamma$ $N_{\mathrm{jet}} = 0$ and $= 1$ validation regions defined above. The histograms indicate a good agreement between the data and the MC within the uncertainties. Note that the $E_{\mathrm{T,rel}}^{\mathrm{miss}}$ distributions in the $N_{\mathrm{jet}} = 1$ channel show a very good compatibility between data and MC, indicating that the $N_{\mathrm{jet}} = 1$ VR without a $E_{\mathrm{T,rel}}^{\mathrm{miss}}$ cut can be used for later determining a normalisation factor. Although the 2012 $W\gamma$ MC now contains much improved statistics compared to 2011, the VR still suffers from poor statistics in the data and in the $Z\gamma$ MC.

	$WZ/ZZ/W\gamma$	$W\gamma$	$W\gamma^*$	$Z\gamma$	WZ	ZZ	Z+jets	W+jets	Total Bkg.	Observed
$W\gamma$ $e\mu + \mu e$ 0 jet	201 ± 9	176 ± 5	2.4 ± 1.3	22 ± 7	0.17 ± 0.07	0.04 ± 0.01	0.15 ± 0.11	26 ± 1	228 ± 9	202
$W\gamma$ $e\mu + \mu e$ 1 jet	200 ± 9	168 ± 4	3.0 ± 2.2	29 ± 8	0.41 ± 0.11	0.18 ± 0.03	2.03 ± 0.51	18 ± 1	221 ± 9	228

Table 5.15: Observed and expected number events in the $W\gamma$ $N_{\mathrm{jet}} = 0$ and $= 1$ VR at the final cut stage ($\Delta\phi_{\ell\ell} < 1.8$) for 13 fb^{-1}. Only statistical errors are included.

$W\gamma$ with the full 2012 dataset

To be able to have a fully data-driven method for the $W\gamma$ background, a fake factor for the conversion and b-layer bits, estimated from $Z \rightarrow \mu\mu\gamma$ FSR events, is going to be applied to the $W\gamma$ validation region. This is however beyond the scope of the current dataset, and can be used when the $W\gamma$ validation region is no longer statistically limited in data.
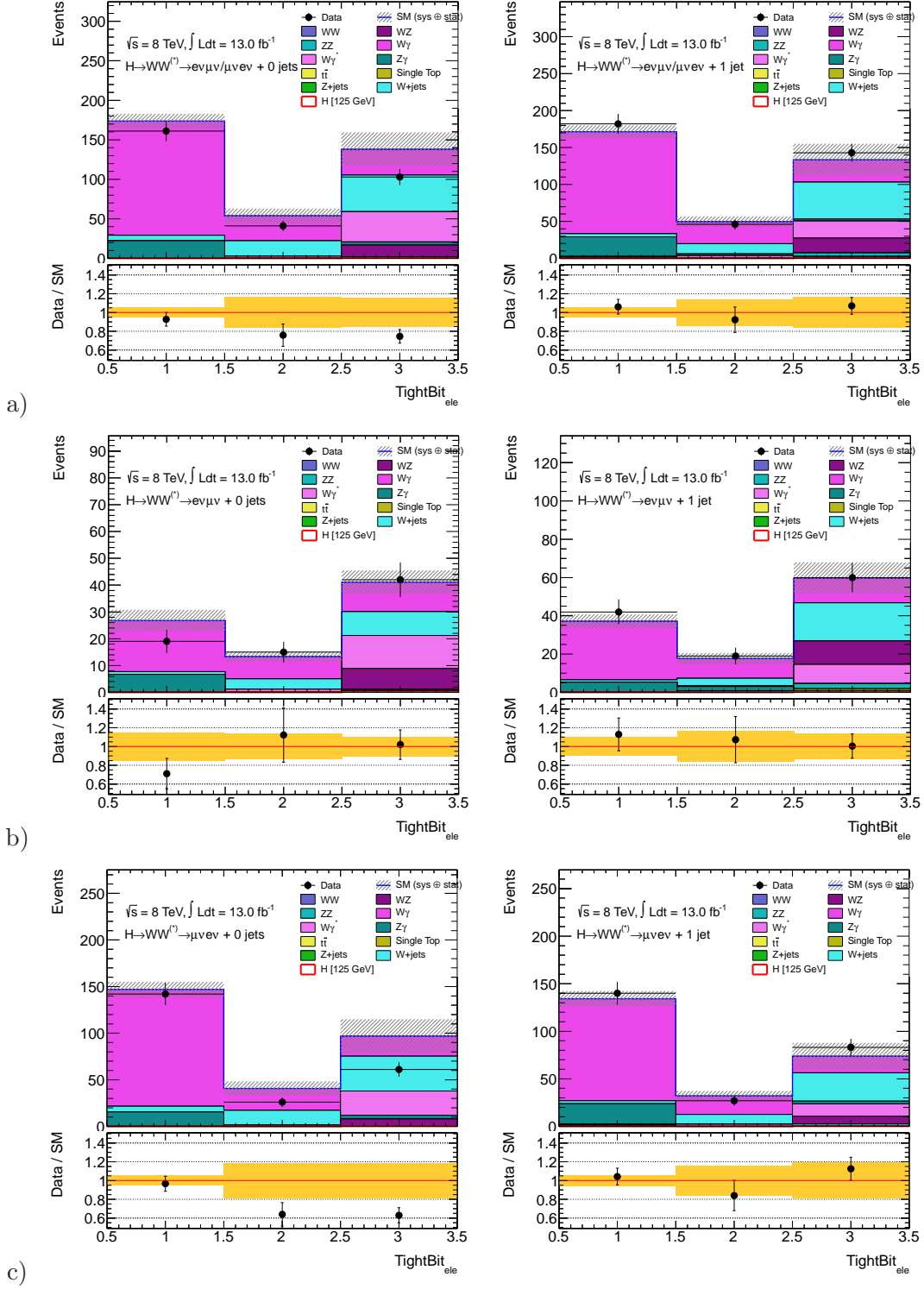
Figure 5.15: The Tight Bit (conversion and b-layer electron bits), where bits 1 and 2 constitute the $W\gamma$ VR and bit 3 the standard same-sign selection. The plots show a) $e\mu + \mu e$, b) $e\mu$ and c) μe and $N_{\text{jet}} = 0$ (left) and $N_{\text{jet}} = 1$ (right). Statistical and systematic uncertainties are included.
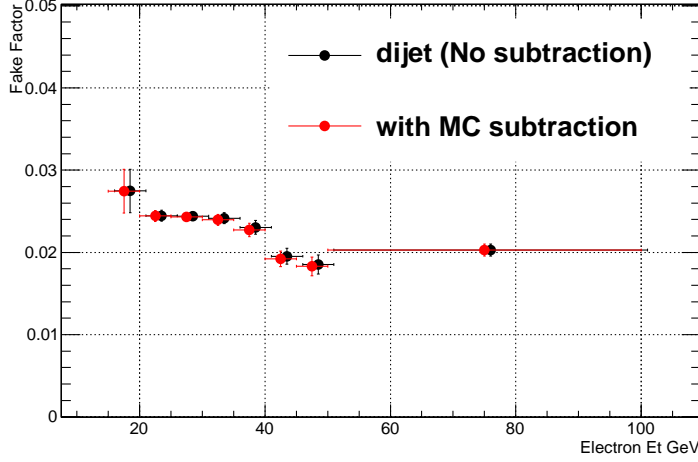
Figure 5.16: The customised W+jets fake factor, with the electron b-layer and conversion bits relaxed in the numerator, used to estimate the W+jets background in the $W\gamma$ validation region.

The preliminary NF results are however documented below. For the 13 fb^{-1} analysis, the $W\gamma$ background is taken from MC. It is however visible from the figures above that this background is well modelled by the Monte Carlo.

$W\gamma$ normalisation factors

The $W\gamma$ data/MC NFs for the $e\mu + \mu e$ $N_{\text{jet}} = 0$ and $= 1$ analyses are estimated through the following steps:

- the data and MC event yields are estimated in the $W\gamma$ $N_{\text{jet}} = 0$ validation regions, following the selection described above;

- the non-$W\gamma$ components in these validation regions are subtracted from the data. These contributions are mainly dominated by $Z\gamma$, which is taken from MC, and W+jets, which is estimated in data with a modified fake factor for the $W\gamma$ VR. A small contribution from $W\gamma^*$ and $WZ^{(*)}$ backgrounds is also present. The statistical and systematic uncertainties on these subtracted backgrounds are properly accounted for in the total uncertainty on the NF;

- the normalisation ratio between the non-$W\gamma$ background subtracted data (data_{sub}) and the $W\gamma$ MC estimate is evaluated in the $W\gamma$ validation region;

Since the lepton selection in the $W\gamma$ VR and the SR is not the same, one needs to account for these differences. This can be achieved via a comparison of the so-called conversion fake factor (convFF). It is evaluated using $Z \rightarrow \mu\mu\gamma$ final state radiation (FSR) event selection in data, and defined as the ratio of number of events passing the full electron SR selection to the number of events passing the loosened electron selection. It yields 0.206 ± 0.033 in data, where the error is statistical only. The corresponding MC value is taken as a ratio of the $W\gamma$ SR events to the $W\gamma$ VR events. The final NF, to be applied to correct the $W\gamma$ in the SR, is the product of the NF in the $W\gamma$ VR and the ratio between the
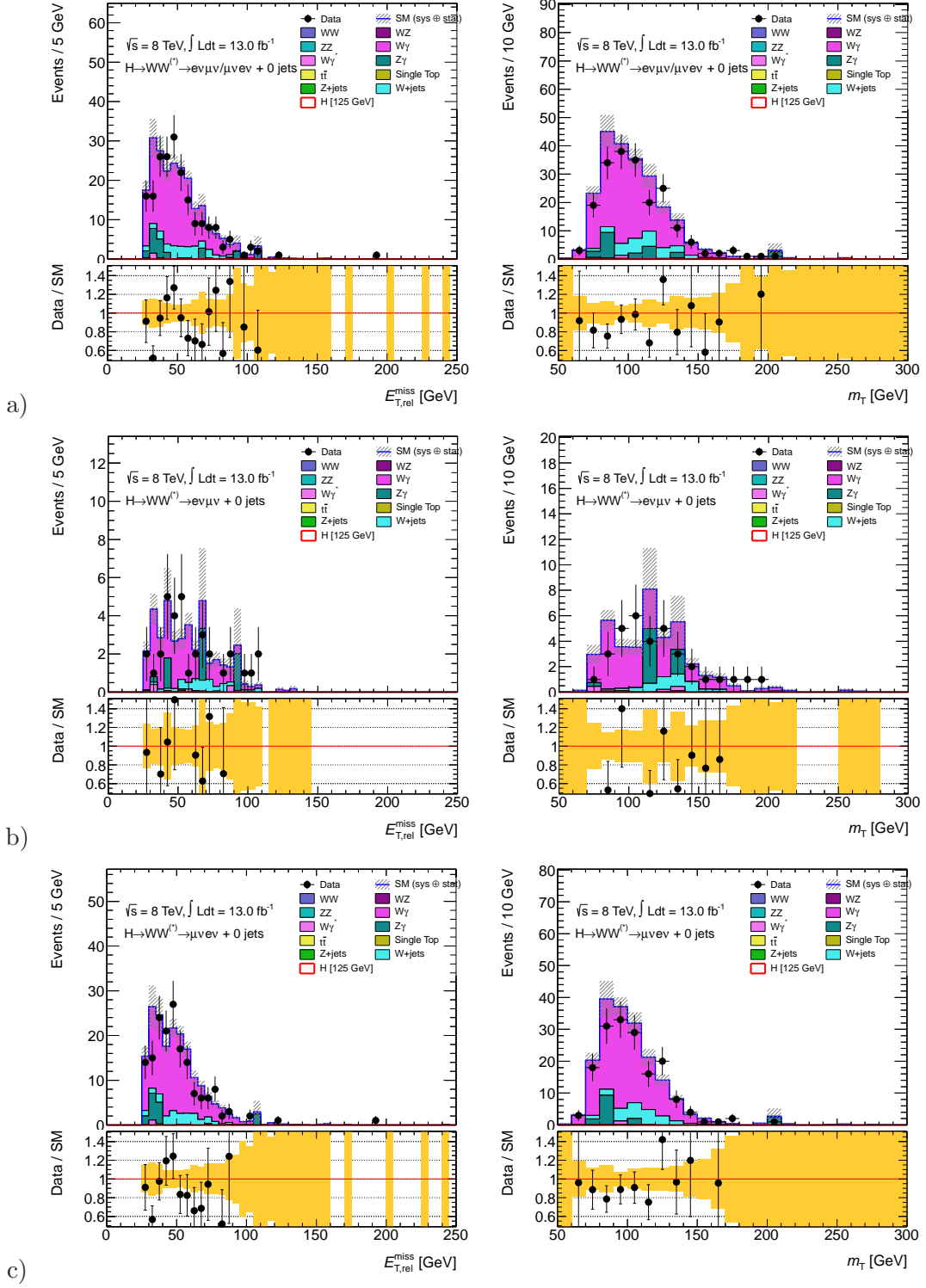
Figure 5.17: The $E_{\mathrm{T,rel}}^{\mathrm{miss}}$ and m_{T} distributions in the $W\gamma$ 0 jet VR for the a) $e\mu + \mu e$, b) $e\mu$ and c) μe channels. Only events passing the $E_{\mathrm{T,rel}}^{\mathrm{miss}} > 25$ GeV are considered in the $N_{\mathrm{jet}} = 0$ $W\gamma$ VR. Statistical and systematic uncertainties are included.
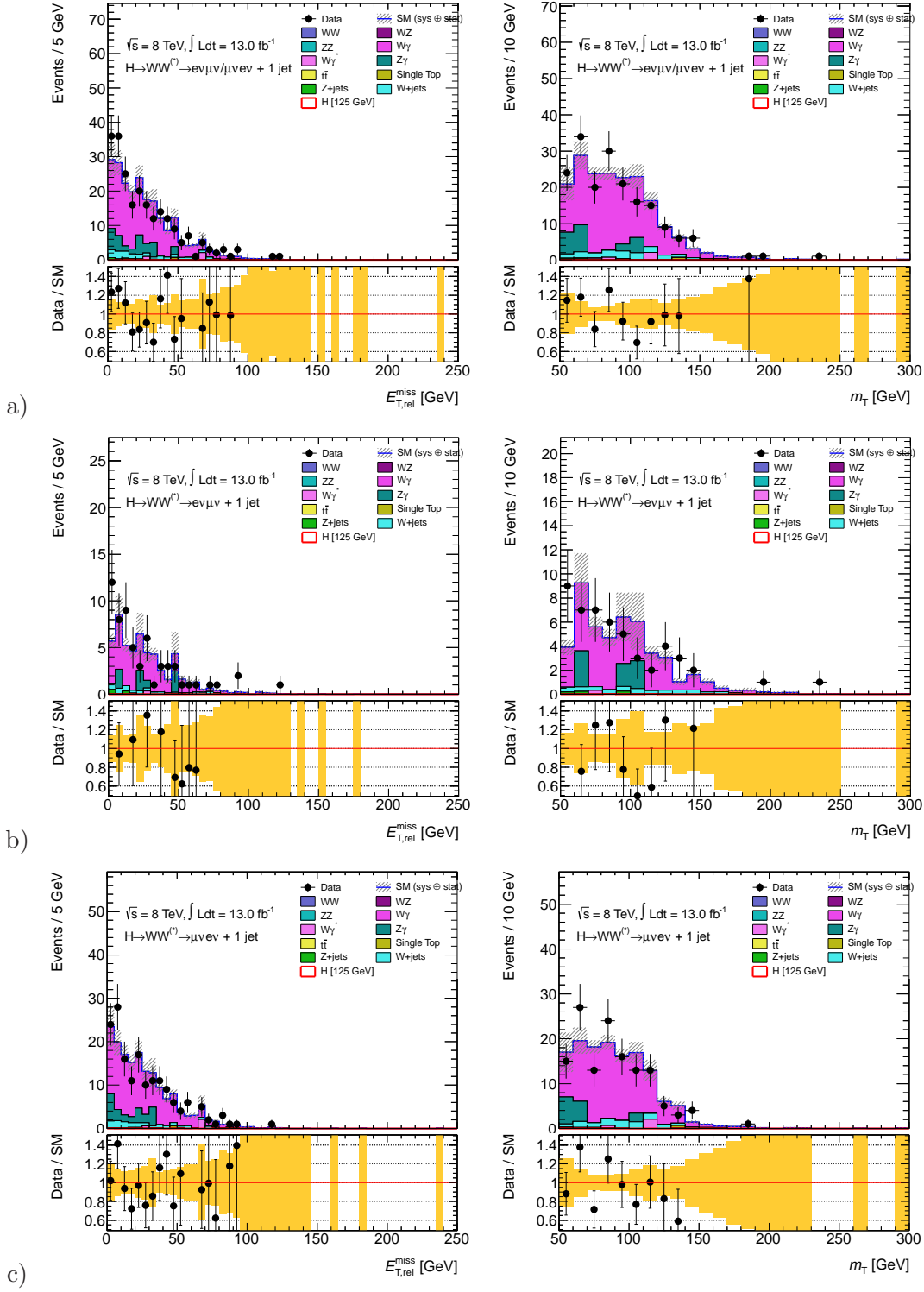
Figure 5.18: The $E_{\mathrm{T,rel}}^{\mathrm{miss}}$ and m_{T} distributions in the $W\gamma$ $N_{\mathrm{jet}}=1$ VR for the a) $e\mu + \mu e$, b) $e\mu$ and c) μe channels. No $E_{\mathrm{T,rel}}^{\mathrm{miss}}$ cut is applied for the $N_{\mathrm{jet}}=1$ $W\gamma$ VR. Statistical and systematic uncertainties are included.

conversion fake factor determined in data and the equivalent factor from the $W\gamma$ MC. In this manner the value and uncertainty of the $W\gamma$ MC in the VR cancels in the different ratios. What remains in the calculations are the non-$W\gamma$ background subtracted data, the conversion fake factor and the $W\gamma$ MC in the signal region. A caveat here is that the removal of the $E_{\mathrm{T,rel}}^{\mathrm{miss}}$ cut for the 1 jet VR is not accounted for. However, investigating the VR distributions show that the $E_{\mathrm{T,rel}}^{\mathrm{miss}}$ shape in data is very well modelled by the MC. The different inputs and the resulting $W\gamma$ NFs are summarised in Table 5.16. The final NFs $0.95 \pm 0.19 \pm 0.10$ for 0 jet and $1.19 \pm 0.23 \pm 0.10$ for the 1 jet channel, are compatible with unity within the uncertainties, which are dominated by the statistical components.

	0 jet	1 jet
$W\gamma$	$176 \pm 5 \pm 12$	$168 \pm 4 \pm 7$
data	$202 \pm 14 \pm 0$	$228 \pm 15 \pm 0$
$W\gamma^*$	$2.4 \pm 1.3 \pm 6$	$3 \pm 2 \pm 5$
$Z\gamma$	$22 \pm 7 \pm 7$	$29 \pm 8 \pm 7$
WZ	$0.04 \pm 0.01 \pm 0.01$	$0.17 \pm 0.03 \pm 0.01$
ZZ	$0.16 \pm 0.07 \pm 0.04$	$0.41 \pm 0.11 \pm 0.11$
$W+$jets	$27 \pm 1 \pm 10$	$18 \pm 1 \pm 6$
WW	0.5 ± 0.1	0.3 ± 0.1
$t\bar{t}$	0.1 ± 0.1	0.0 ± 0.2
single top	0	0.5 ± 0.5
$Z+$jets	0.2 ± 0.1	2 ± 0.5
data$_{sub}$	$150 \pm 16 \pm 14$	$175 \pm 17 \pm 11$
$W\gamma_{MC}^{SR}$	$33 \pm 2 \pm 2$	$30 \pm 2 \pm 2$
convFF^{data}	0.206 ± 0.033	0.206 ± 0.033
NF	$0.95 \pm 0.19 \pm 0.10$	$1.19 \pm 0.23 \pm 0.10$

Table 5.16: Different components that enter the $W\gamma$ NF calculations (central value $\pm$ stat $\pm$ syst).

$W\gamma$ summary

A validation region for $W\gamma$ background events has been defined and scrutinised. It reaches a purity of about 80% for the different channels ($e\mu + \mu e$ in $N_{\mathrm{jet}} = 0$ and $= 1$). The relevant distributions in the validation region indicate that the $W\gamma$ background is well modelled by the MC. The uncertainties in the validation region are however still large due to the relatively poor statistics in the data. This background is thus extracted from MC for the current analysis, although preliminary NFs can be found in Section 5.5.5, obtained by combining the $W\gamma$ VR and a conversion fake factor. The validation of the $W\gamma$ background in the ee lepton flavour channel is presented in Appendix A.

In the analysis presented in this thesis, the $W\gamma$ background is taken from the MC simulation. A k-factor normalising the cross section to the NLO prediction is applied and it yields 1.15 with a scale uncertainty of 11% in the $N_{\mathrm{jet}} = 0$ channel and 53% in the $N_{\mathrm{jet}} = 1$ channel. For more details on the theoretical derivation of the normalisation see Section 5.2 and Ref. [114].

$W\gamma^*$ and WZ/γ^* normalisations

The $W\gamma^*$ and $WZ^{(*)}$ normalisations were already discussed at the beginning of this chapter. In summary, $W\gamma^*$ background originates from the associated production of a W boson

with a virtual photon, γ^*, where the photon internally converts to a pair of charged leptons. Unlike the external conversion case, $\gamma^* \to \mu\mu$ and $\gamma^* \to \tau\tau$ can occur, although the latter production is negligible. The $W\gamma^*$ background is generated with the MadGraph program and its cross section is normalised to the MCFM NLO prediction. The $WZ^{(*)}$ process is simulated with the POWHEG generator which is already an NLO generator, therefore no normalisation factor is needed. Both the $W\gamma^*$ and $WZ^{(*)}$ backgrounds are most significant in the 0 jet bin where they contribute a few percent to the total background, equivalent to about 25% of the size of the signal. The kinematics of the electron-positron pairs were investigated with truth studies. The feasibility of reconstructing the track of the third lepton was assessed. The $W\gamma^* \to e\nu\mu\mu$ background is not investigated here, since only a handfull of such events are expected in the current dataset.

For the $W\gamma$ background, a control region could be identified since the electron from the conversion usually fails the conversion and b-layer identification requirements. The photon from $W\gamma^*$, on the other hand, converts internally and the reconstructed electron usually passes these identification requirements. An investigation was instead made whether it is feasible to reconstruct, at least the track, of the second electron to select $W\gamma^*$ events and reject other types of background. Figure 5.19 shows the true p_T of the sub-leading electron from the γ^*, which is well above the limit for electron reconstruction. Figure 5.20 shows the distance between the electron and the positron from the γ^* and it is clear from the plot that the particles are very close together. In fact, the two electrons are only both reconstructed in about a percent of the selected events and two separate tracks can be only be found in about 7% of the events. It is therefore not possible to pursue a data-driven method for $W\gamma^*$ through selecting the two tracks originating from the γ^*.
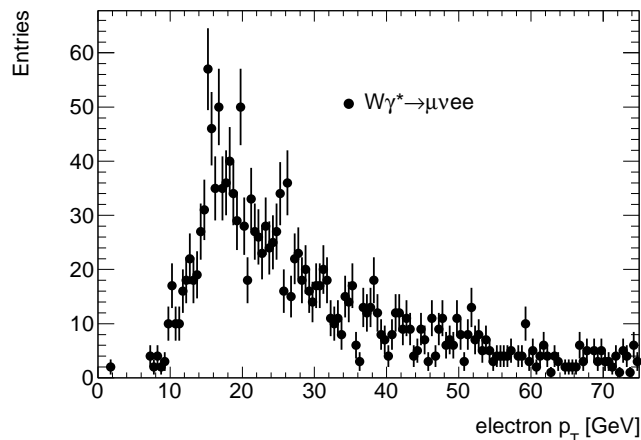
Figure 5.19: The p_T of the sub-leading electron from the γ^* calculated from the MC truth, for $W\gamma^* \to \mu\nu ee$ events passing the $e\mu + \mu e$ channel selections up to the $E_{T,rel}^{miss}$ cut.

Even though there is no explicit $W\gamma^*$ validation region, the most pure phase-space, in comparison with other backgrounds, is obtained for same-sign leptons at the cut stages of $p_T^{\ell\ell}$ for 0 jets and the b-jet veto for the $N_{jet} = 1$ channel, where the $W\gamma$ background is less dominant. The resulting purity is around 50%, reaching up to 66% for the $N_{jet} = 0$ channel. Figures 5.21 and 5.22 show different variables at the mentioned cut stages as a validation of these backgrounds in the $e\mu$ and μe channels. Data and MC agree well within the total uncertainties.
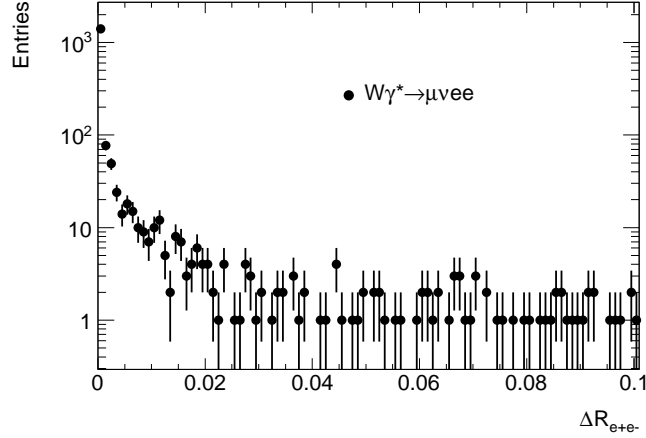
Figure 5.20: The distance between the electron and positron from the photon calculated in the MC truth, for $W\gamma^* \to \mu\nu ee$ events passing the $e\mu + \mu e$ channel selection cuts up to the $E_{\mathrm{T,rel}}^{\mathrm{miss}}$ cut.

The $Z^{(*)}Z^{(*)}$ background

The remaining non-WW diboson background originates from the $Z^{(*)}Z^{(*)}$ processes. This background contributes a small fraction to the total predicted background and is estimated using Monte Carlo predictions.

Summary

To summarise this section concerning the non-WW diboson backgrounds, the final yield at the end of the selection in the zero and one jet same sign lepton selection is presented in Table 5.17. The contributions from $W\gamma$, $W\gamma^*$, $WZ^{(*)}$ and $Z^{(*)}Z^{(*)}$ are shown separately.

	$WZ/ZZ/W\gamma^{(*)}$	$W\gamma$	$W\gamma^*$	WZ^*	ZZ
$e\mu$ 0j:	31.4 ± 2.8	11.01 ± 1.15	12.35 ± 2.48	7.69 ± 0.49	0.32 ± 0.04
μe 0j:	55.1 ± 4.6	21.59 ± 1.61	25.94 ± 4.32	7.19 ± 0.48	0.38 ± 0.04
$e\mu$ 1j: $\Delta\phi_{\ell\ell} < 1.8$	19.0 ± 1.9	6.12 ± 0.80	4.72 ± 1.75	7.67 ± 0.51	0.51 ± 0.04
μe 1j: $\Delta\phi_{\ell\ell} < 1.8$	20.4 ± 2.5	7.63 ± 0.89	7.47 ± 2.28	4.91 ± 0.40	0.42 ± 0.04

Table 5.17: The event yield for the non-WW diboson processes in the same-sign selection in the zero and one jet bin for 13 fb^{-1} after all cuts. Only statistical errors are included.

5.5.6 Summary

This section presented a summary of the background estimation methods in the $H \to WW^{(*)}$ analysis. One can divide the methods into three groups depending on the way the backgrounds are normalised: fully data-driven, partially data-driven and purely MC based. The W+jets background belongs to the first category and it is estimated using a fake factor method. WW, $t\bar{t}$, $tW/tb/tqb$ and Z/γ^*+jets backgrounds are normalised using dedicated

Figure 5.21: $W\gamma^*$ validation plots for $N_{\text{jet}} = 0$ same-sign lepton selection at the $p_T^{\ell\ell}$ cut stage. The plots show a) $e\mu + \mu e$, b) $e\mu$ and c) μe and $m_{\ell\ell}$ (left) and $\Delta\phi_{\ell\ell}$ (right). Statistical and systematic uncertainties are included.
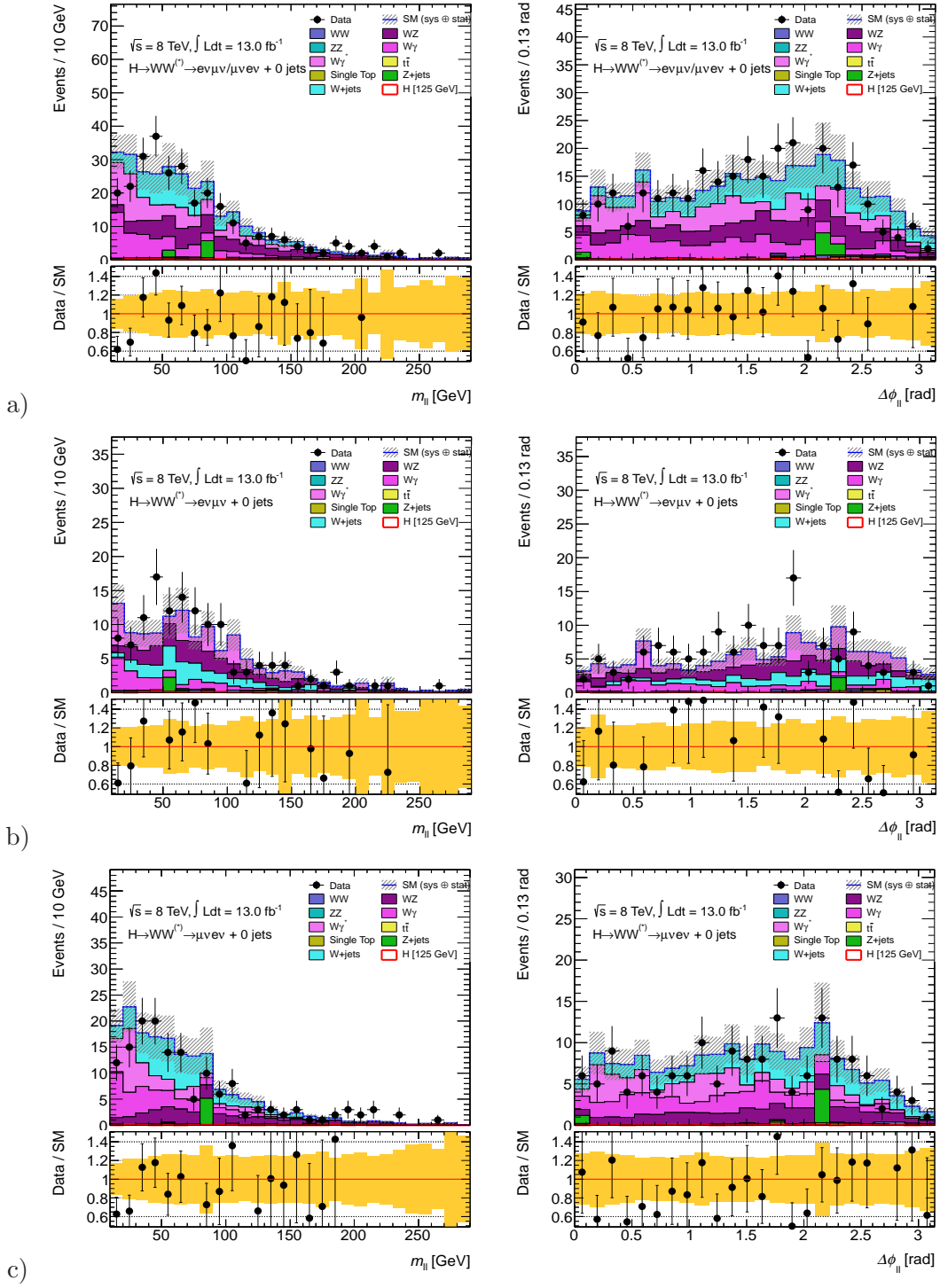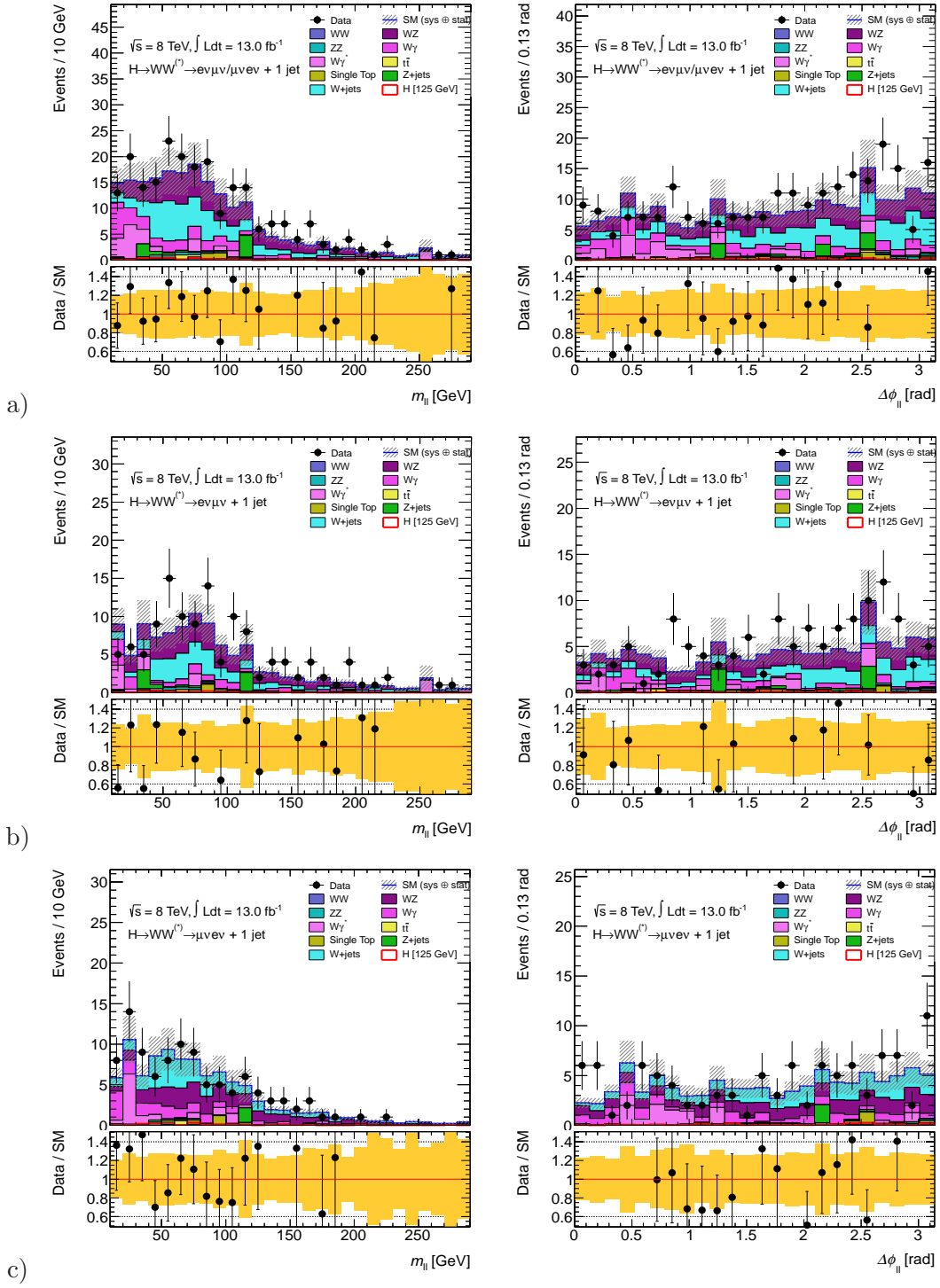
Figure 5.22: $W\gamma^*$ validation plots for $N_{\text{jet}} = 1$ same-sign lepton selection at the b-veto cut stage. The plots show a) $e\mu + \mu e$, b) $e\mu$ and c) μe and $m_{\ell\ell}$ (left) and $\Delta\phi_{\ell\ell}$ (right). Statistical and systematic uncertainties are included.

Composition of main control regions									
	Signal	WW	$WZ/ZZ/W\gamma$	$t\bar{t}$	$tW/tb/tqb$	$Z/\gamma^* + \mathrm{jets}$	$W + \mathrm{jets}$	Total Bkg.	Obs.
WW 0-jet	1.2 ± 0.2	1102 ± 7	71 ± 5	208 ± 6	115 ± 6	13 ± 4	78 ± 2	1587 ± 13	1725
WW 1-jet	1.2 ± 0.2	466 ± 4	52 ± 3	492 ± 9	152 ± 7	22 ± 3	51 ± 2	1235 ± 13	1160
Top 1-jet	7.8 ± 0.3	117 ± 2	27 ± 6	2405 ± 20	699 ± 14	55 ± 2	29 ± 3	3332 ± 25	3431

Table 5.18: Observed and expected number of events in the WW and top $N_{\mathrm{jet}} = 1$ control regions. W+jets contribution is taken from the data-driven method and the only normalisation factor applied is the top background estimate in the WW $N_{\mathrm{jet}} = 0$ and $= 1$ control regions. Only statistical errors are shown [89].

control regions in data. The non-WW diboson backgrounds including $W\gamma^{(*)}$, $WZ^{(*)}$ and $Z^{(*)}Z^{(*)}$ are taken from the Monte Carlo simulation. The $W\gamma$ background prediction was proposed to be estimated from a validation region. In the presented analysis it is nevertheless taken from the MC as there is not enough data statistics for the normalisation to be precise. The composition of the main control regions is shown in Table 5.18. Here the W+jets contribution is taken from the data-driven method and the only normalisation factor applied is the top background estimate in the WW $N_{\mathrm{jet}} = 0$ and $= 1$ control regions.

5.6 Systematic uncertainties

This section summarises the systematic uncertainties on the signal and background processes. The theoretical uncertainties are first described and are followed by a discussion of the experimental uncertainties.

5.6.1 Theoretical uncertainties

ggF signal process

The impact of the uncertainties on the QCD renormalisation and factorisation scales on the signal production cross section has been discussed in Chapter 2. The final QCD uncertainties on the ggF production cross section for $m_H = 125$ GeV, including the anti-correlations caused by migrations of events between different jet multiplicities, are 17% for the $N_{\mathrm{jet}} = 0$ and 36% for $N_{\mathrm{jet}} = 1$ final states. This includes an additional contribution of about 4%, corresponding to the QCD scale uncertainty on the acceptance alone, which is correlated between the $N_{\mathrm{jet}} = 0$ and $N_{\mathrm{jet}} = 1$ analyses. Taking into account other production contributions to the total signal cross-section, mainly the VBF production, reduces the uncertainty in the $N_{\mathrm{jet}} = 1$ analysis to 30%.

PDF uncertainties on the signal cross section and acceptance are evaluated using the envelopes of error sets as well as different PDF sets, applied separately to quark-quark, quark-gluon, and gluon-gluon initiated processes [27, 111, 121, 122]. For $m_H = 125$ GeV, the relative PDF uncertainty is 8% for the ggF process. Uncertainties on the POWHEG+PYTHIA8 modelling of the signal processes, particularly the sensitivity to the underlying event and parton shower model, are estimated by comparison to the MC@NLO+HERWIG generator. The resulting uncertainties are 3% for the $N_{\mathrm{jet}} = 0$ signal

	Scale	PDFs	PS/UE
$N_{\text{jet}} = 0$	17%	8%	3%
$N_{\text{jet}} = 1$	36%	8%	10%

Table 5.19: QCD scale, PDF and parton-shower/underlying event (PS/UE) modelling uncertainties on the ggF signal production cross section [89].

and 10% for the $N_{\text{jet}} = 1$ signal, anti-correlated between the jet multiplicity bins. A summary of the theoretical uncertainties on the ggF signal production cross-section is shown in Table 5.19.

Background processes

The treatment of the uncertainties on the backgrounds estimated by the partially data-driven methods differs from the backgrounds estimated fully from the Monte Carlo simulation. The former ones include the WW and top backgrounds which use the MC prediction corrected by the data/MC agreement in signal-depleted control regions. The estimated number of background events in the signal region is calculated using the extrapolation parameter, α, and the number of observed events in the control region:

$$\alpha \times N_{\text{data}}^{\text{CR}},$$

where $\alpha = N_{\text{MC}}^{\text{SR}}/N_{\text{MC}}^{\text{CR}}$ and $N_{\text{data}}^{\text{CR}}$ is corrected for contributions of other backgrounds in the control region. The uncertainty on the extrapolation parameter is evaluated by varying the different sources of theoretical uncertainties on the background prediction and comparing the resulting ratio with the nominal one. In the case of the WW background, extrapolation parameters α_{WW}^{0j} and α_{WW}^{1j} are defined for the $N_{\text{jet}} = 0$ and $N_{\text{jet}} = 1$ analyses separately. Four main sources of uncertainty have been considered: QCD renormalisation and factorisation scales, dependence on PDF model, dependence on the choice of Monte Carlo generator, and dependence on the underlying event and parton shower model. QCD scale uncertainties (computed using the MC@NLO generator) and PDF uncertainties were calculated in the same way as for the signal. The generator modelling uncertainties have been computed by comparing the MC@NLO, POWHEG, and MCFM extrapolation parameters in an inclusive jet multiplicity sample and were found to be 3.5%. The underlying event and parton shower uncertainties were evaluated comparing the POWHEG+PYTHIA8, POWHEG+PYTHIA6 and POWHEG+HERWIG predictions and yield 4.5%. The final uncertainties on the extrapolation parameters are summarised in Table 5.20, and sum to 7.2% for the $N_{\text{jet}} = 0$ and 7.5% for the $N_{\text{jet}} = 1$ analyses. An additional theoretical uncertainty is assigned to the WW background. It is evaluated on the shape of the m_{T} distribution and compares the prediction by the MCFM, SHERPA, POWHEG, and MC@NLO+HERWIG generators. As can be seen in Figure 5.23, the largest differences are observed between MCFM and MC@NLO, and they are taken as a relative shape uncertainty around the default POWHEG m_{T} distribution. The maximum differences observed are about 10% and are concentrated at low values of the m_{T} distribution. The theoretical uncertainties on the top background for the $N_{\text{jet}} = 0$ analysis include the effects of QCD scale, initial- and final-state radiation and generator/parton-shower modelling. They are the dominant uncertainties on the top background estimation derived
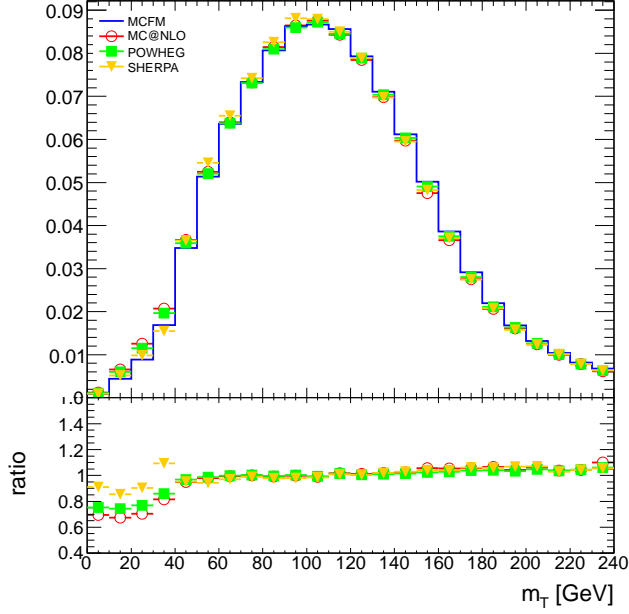
Figure 5.23: Comparison of the m_T distribution between four different WW generators. MCFM generator is taken as the reference in the ratio plot [114].

	Scale	PDFs	PS/UE	Modelling
$\alpha_{WW}^{0\mathrm{j}}$	2.5%	3.7%	4.5%	3.5%
$\alpha_{WW}^{1\mathrm{j}}$	4%	2.9%	4.5%	3.5%

Table 5.20: QCD scale, PDF, parton-shower/underlying event (PS/UE), and generator modelling uncertainties on the WW extrapolation parameters α for the NLO $qq, gg \to WW$ processes [89].

from the Monte Carlo simulation and total to 10%. The top background for the $N_\mathrm{jet} = 1$ analysis is evaluated by extrapolation from a signal-depleted control region, as is the case for WW, but the associated uncertainty is dominated by experimental uncertainties (described in the next section). The theoretical uncertainty on the extrapolation is evaluated by comparison of simulated $t\bar{t}$ and single top events with different QCD tunings for initial- and final-state radiation and is 8%. The remaining backgrounds are evaluated directly from MC simulation and the calculated cross section is used for the normalisation. This could lead to significant theoretical uncertainties. The $W\gamma$ background is normalised to the MCFM prediction as explained in Section 5.5.5. The uncertainties on the cross section and the jet bin acceptance for the $W\gamma$ process are 11% for the $N_\mathrm{jet} = 0$ analysis and 53% for the $N_\mathrm{jet} = 1$ analysis. 3% on the PDF uncertainty is also applied. The $W\gamma^*$ prediction with $m_{\ell\ell} < 7$ GeV is also scaled to match the prediction of the MCFM NLO calculation. The corresponding uncertainties on the cross section and jet bin acceptance are 19% for both $N_\mathrm{jet} = 0$ and $N_\mathrm{jet} = 1$ analyses. Additionally, the 3% PDF uncertainty applies here as well. As explained in Section 5.5.5, events with $m_{\ell\ell} < 3$ MeV have been removed because of the calculation instability. Reweighting has been applied to preserve the total cross section and

the difference between the nominal and reweighted prediction was taken as a systematic uncertainty. The theoretical uncertainties including the PDF and QCD scale uncertainties were evaluated for the remaining ZZ^* and $WZ^{(*)}$ with $m_{\ell\ell} > 7$ GeV backgrounds, and total to about 6%.

5.6.2 Experimental uncertainties

The experimental sources of systematic uncertainty include reconstruction and identification efficiencies and momentum/energy scale and resolution for the physics objects used in $H \to WW^{(*)} \to \ell\nu\ell\nu$ analysis (leptons, jets and $E_{\mathrm{T}}^{\mathrm{miss}}$). The details on their extraction are explained below and summarised in Table 5.21. Additional sources include the uncertainty on the fake factor used in the data-driven W+jets background estimation ($\sim$50%) and the uncertainty on the luminosity determination (3.6%).

The jet energy scale is determined from a combination of test beam, simulation, and *in situ* measurements [88]. Its uncertainty is split into seven independent components: baseline (calorimeter response for $|\eta| < 0.8$), topologies with close-by jets, different quark/gluon composition and response, the b-jet energy scale, impact from in-time and out-of-time event pile-up, and forward jet response ($|\eta| > 0.8$). The jet energy scale uncertainty, for jets used in this analysis, varies between 1% and 13% depending on jet p_{T} and η. The jet energy resolution varies from 5% to 25% as a function of jet p_{T} and η, and the relative uncertainty on it, as determined from *in situ* measurements, ranges from 2% to 5%. The reconstruction and identification efficiencies of the leptons used in this thesis are estimated using the T&P method described in Chapter 4. The corresponding uncertainties, including the uncertainties on the leptons' momenta scales and resolution, are smaller than 1%. The only exception is the uncertainty on the electron selection efficiency, which varies between 2% and 5% as a function of p_{T} and η of the electron. The uncertainty on the b-jet tagging efficiency varies between 5% and 18% as a function of jet p_{T}. Jet energy scale and lepton momentum scale uncertainties are propagated to the $E_{\mathrm{T}}^{\mathrm{miss}}$ computation. Additional contributions to the $E_{\mathrm{T}}^{\mathrm{miss}}$ uncertainty arise from soft jets with $p_{\mathrm{T}} < 20$ GeV as well as from low-energy calorimeter deposits not associated with reconstructed physics objects [98]; their effect on the total signal and background yields is about 3%.

As in the case of the theoretical sources, the experimental uncertainties on the backgrounds normalised to control regions are evaluated on the extrapolation parameter. Additionally one has to include the uncertainties on the other backgrounds contributing in the control regions which are then subtracted from the observed number of events. Large contamination of the top background (Table 5.18) in the WW 1-jet CR results in high "cross-talk" uncertainty. These three sources of systematic uncertainty, together with the statistical uncertainty, are summarised in Table 5.22. The uncertainty on the total expected background will be smaller since it accounts for the correlations of the backgrounds.

5.6.3 Summary

Table 5.23 lists the leading systematic uncertainties on the signal and background yields (% on the signal and total background) in the $N_{\mathrm{jet}} = 0$ and $N_{\mathrm{jet}} = 1$ signal regions. The leading theoretical uncertainties include the ggF renormalisation and factorisation scales, followed by the PDF and PS/UE modelling. The largest experimental uncertainties come from the jet energy scale and resolution, followed by the b-tagging efficiency in the $N_{\mathrm{jet}} = 1$ channel. Their impact on the signal and background m_{T} distributions is shown below.

Source of Uncertainty	Impact on the analysis
Jet Energy Resolution (JER)	MC jet resolution smeared using jet p_T, η-dependent parametrisation
Jet Energy Scale (JES)	Seven components:
	Baseline JES: 2-13% depending on the process, jet p_T, η
	Close-by jets: $<\sim 2\%$
	Flavor composition, response: 1-9% depending on the process
	b-JES: significant for $t\bar{t}$ only, 1-6%
	In-time pileup: 0.5-10% depending on the process, jet p_T, η
	Out-of-time pileup: 1-16% depending on the process, jet p_T, η
	Foward JES: 0.8-8% depending on the process and jet η
Electron Selection Efficiency	Separate systematics for electron identification,
	reconstruction and isolation, added in quadrature
	Identification: 3% for $p_\mathrm{T} \sim 15$ GeV,
	decreasing to 1% for $p_\mathrm{T} > 30$ GeV in the central region
	Reconstruction: 0.6 - 1.1% for $p_\mathrm{T} > 15$ GeV
	trigger: 1-2%
	Total uncertainty of 2-5% depending on η and E_T
Electron Energy Scale	Uncertainty smaller than 1%, depending on η and E_T
Electron Energy Resolution	Energy varied within its uncertainty,
	0.6% of the energy at most
Muon Selection Efficiency	0.3-1% as a function of η and p_T
Muon Momentum Scale and Resolution	Uncertainty smaller than 1%
b-tagging Efficiency	p_T dependent scale factor uncertainties: 4.7 - 18%
Missing Transverse Energy	Lepton and hard jet energy uncertainties propagated to $E_\mathrm{T}^\mathrm{miss}$
	Soft terms: ± 1 GeV uncertainty on energy scale; energy resolution
	uncertainty as a function of total p_T of hard objects and
	primary vertex multiplicity

Table 5.21: Experimental sources of systematic uncertainty per object or event [89].

Background	Stat. (%)	Theory (%)	Expt. (%)	Crosstalk (%)	Total (%)
WW, $N_\mathrm{jet}=0$	3.3	7.2	1.5	6.2	13
WW, $N_\mathrm{jet}=1$	9	8	12	34	54
top, $N_\mathrm{jet}=1$	2	8	29	1	37

Table 5.22: Summary of the total uncertainties on backgrounds normalised using control regions (WW for the $N_\mathrm{jet}=0$ and $N_\mathrm{jet}=1$ analyses and top in the $N_\mathrm{jet}=1$ analysis) [89].

Source (0-jet)	Signal (%)	Bkg. (%)
Inclusive ggF signal ren./fact. scale	13	-
1-jet incl. ggF signal ren./fact. scale	10	-
PDF model (signal only)	8	-
QCD scale (acceptance)	4	-
Jet energy scale and resolution	4	2
W+jets fake factor	-	5
WW theoretical model	-	5

Source (1-jet)	Signal (%)	Bkg. (%)
1-jet incl. ggF signal ren./fact. scale	26	-
2-jet incl. ggF signal ren./fact. scale	15	-
Parton shower/ U.E. model (signal only)	10	-
b-tagging efficiency	-	11
PDF model (signal only)	7	-
QCD scale (acceptance)	4	2
Jet energy scale and resolution	1	3
W+jets fake factor	-	5
WW theoretical model	-	3

Table 5.23: Leading systematic uncertainties on the signal and background yields in the $N_{\text{jet}} = 0$ and $N_{\text{jet}} = 1$ analyses [89].

Figures 5.24 and 5.25 show the impact of the baseline jet energy scale uncertainty on the m_{T} distribution for the Higgs signal, WW and top background. Additionally, Figure 5.26 shows the impact of the fake factor, electron energy scale and b-tagging efficiency on the W+jets, non-WW diboson and top backgrounds, respectively in the $N_{\text{jet}} = 0$ signal region.

5.7 Statistics treatment

This section summarises the statistical treatment of the Higgs searches in the $H \to WW^{(*)} \to \ell\nu\ell\nu$ channel. An m_{T} fitting procedure is described in detail, including the description of the likelihood and treatment of systematics in the fit. At the end, the extraction of the p-values, significances and limits is outlined.

5.7.1 Method

In the early versions of this analysis, a simple m_{T} window cut-based procedure was used to extract the limits on the Higgs production cross-section. Later on, it was substituted by a procedure that involves fitting the transverse mass spectrum. This means that Figures 5.7 and 5.9, obtained after the $\Delta\phi_{\ell\ell}$ selection, are used as an input to the statistics machinery. This treatment yields a better expected sensitivity because the shape information is now available. To avoid a degradation of performance due to low-statistics bins, the m_{T} distribution is first mapped separately in each channel such that the sum of backgrounds is uniformly distributed. The number of bins used for the remapping is five and three for $N_{\text{jet}} = 0$ and $N_{\text{jet}} = 1$ analyses, respectively.

A simple likelihood as a function of signal and background strength parameters can be written as:

$$\mathcal{L}(\mu, \mu_b) = P(N|\mu s + \mu_b b_{\text{SR}}^{\text{exp}}) \times P(M|\mu_b b_{\text{CR}}^{\text{exp}}) \qquad (5.5)$$

where the previously used background extrapolation parameter was substituted with the
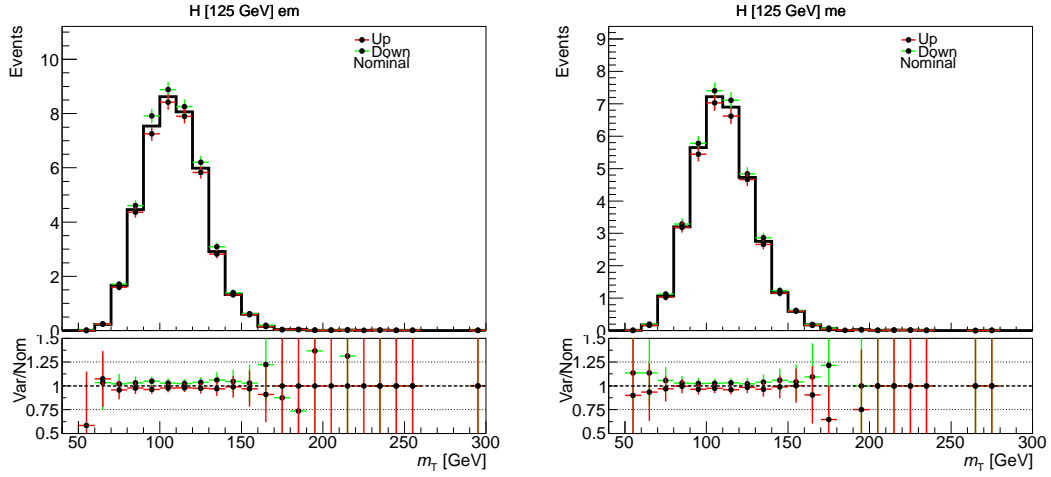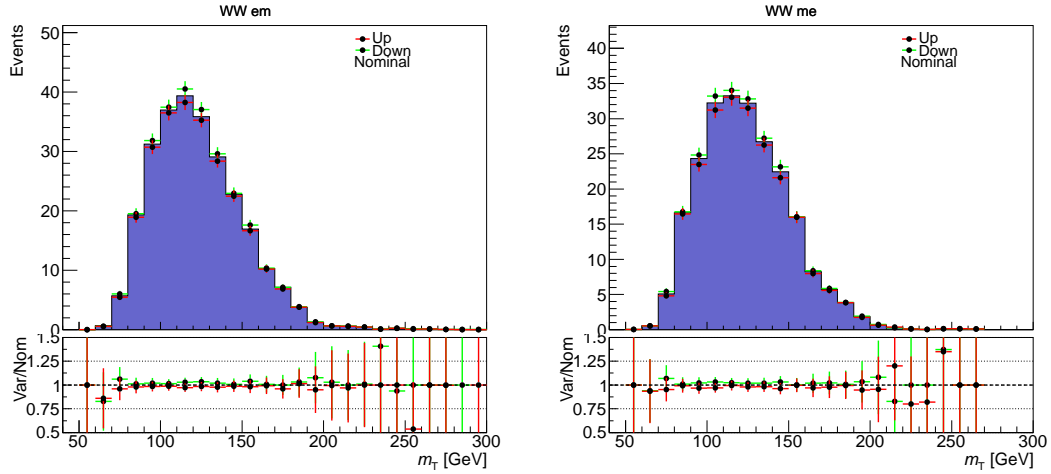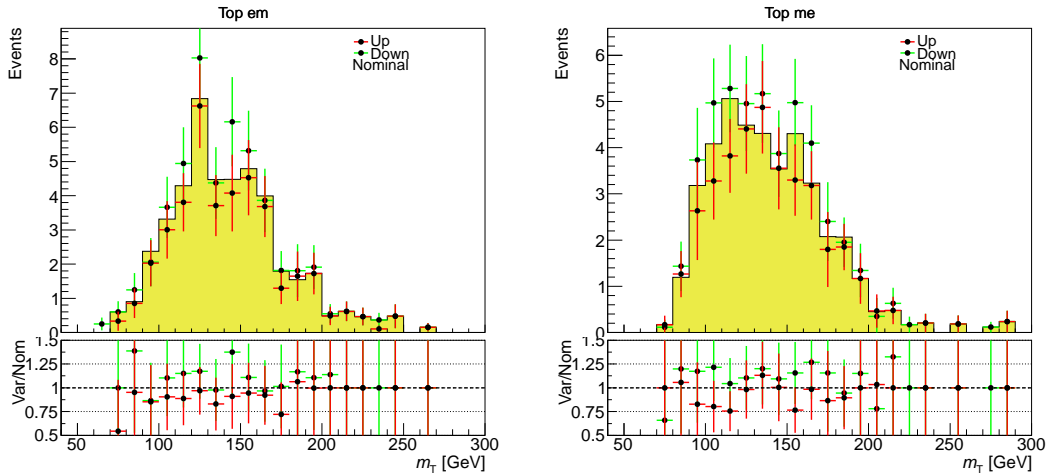
Figure 5.24: Impact of the baseline JES uncertainty in the $N_{\mathrm{jet}} = 0$ channel for the individual $e\mu$ (left) and μe (right) channels. The plots show: a) the Higgs signal, b) the WW background and c) the top background.
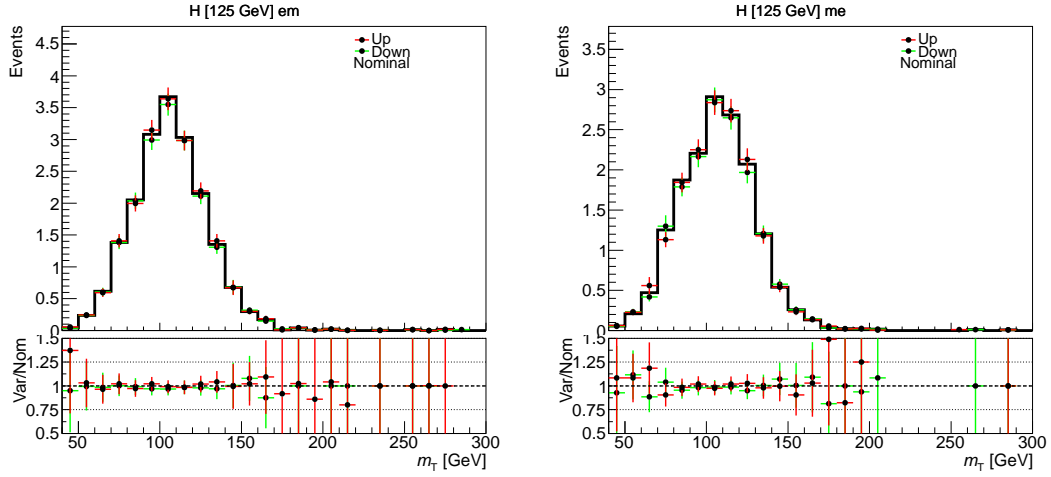
a)
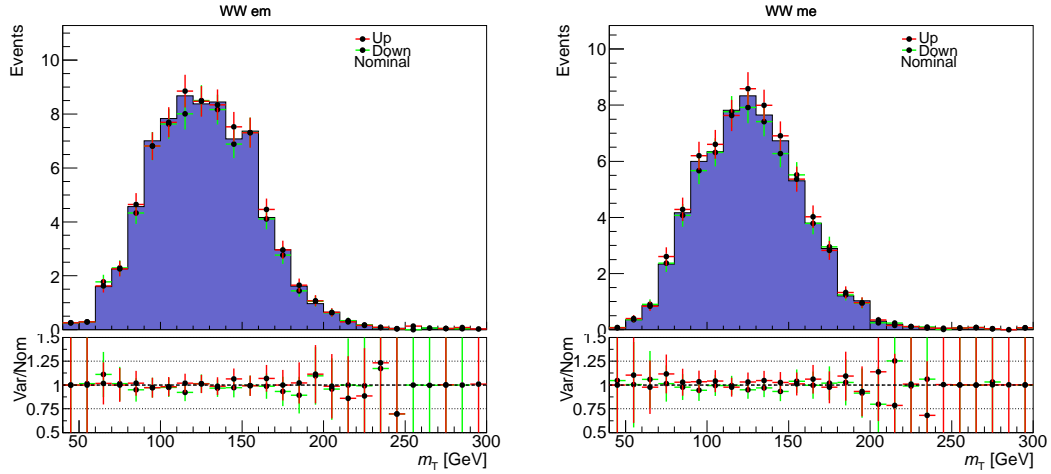
b)
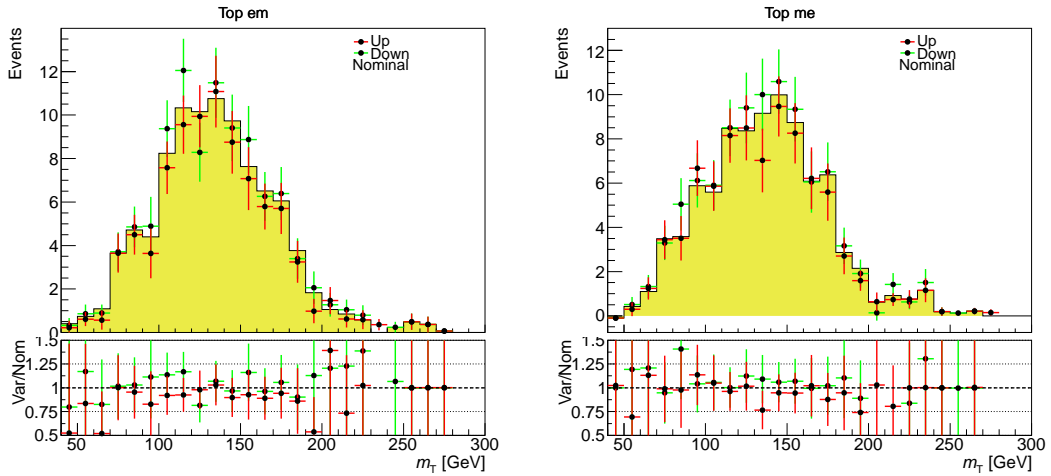
c)

Figure 5.25: Impact of the baseline JES uncertainty in the $N_{\mathrm{jet}} = 1$ channel for the individual $e\mu$ (left) and μe (right) channels. The plots show: a) the Higgs signal, b) the WW background and c) the top background.
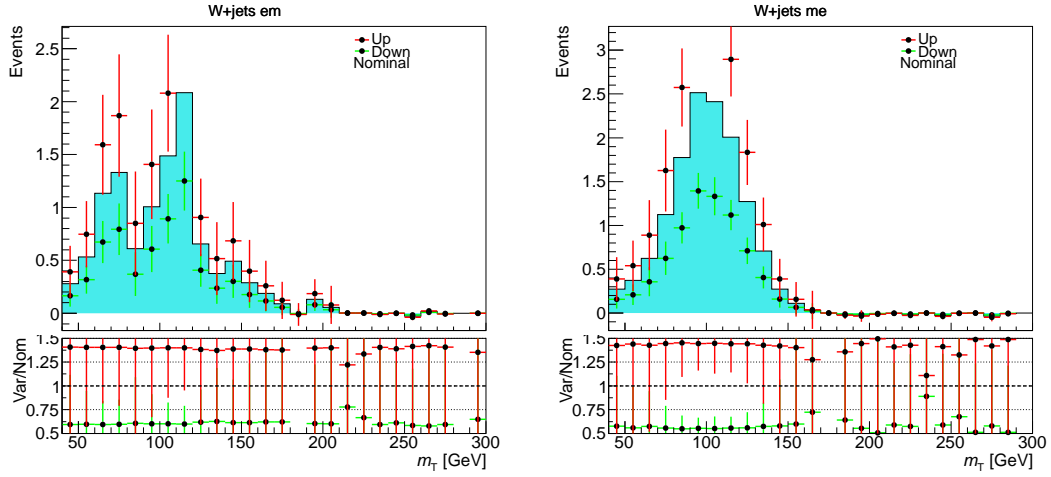
a)
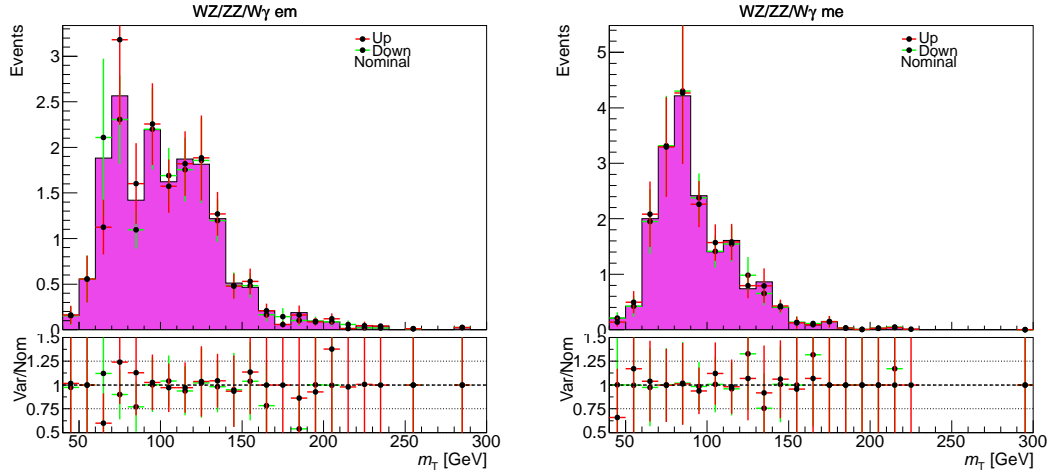
b)
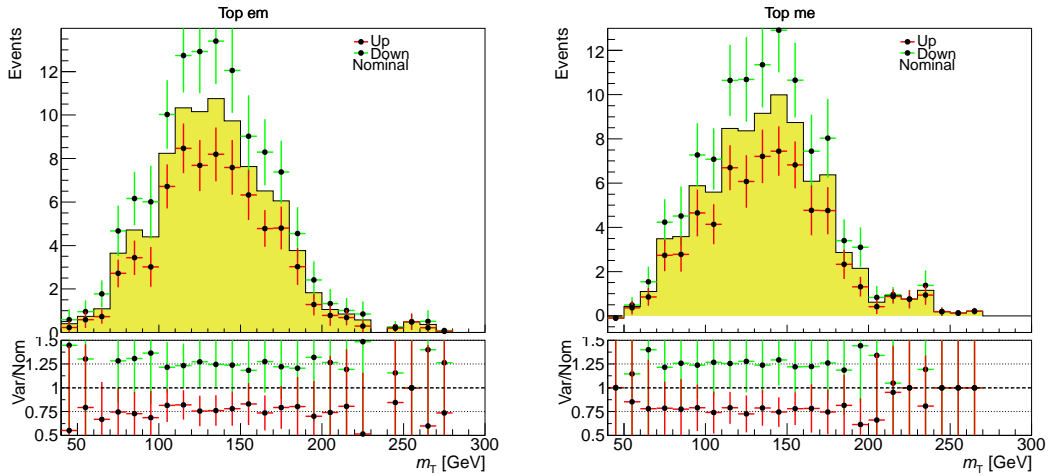
c)

Figure 5.26: Impact of the fake factor, electron energy scale and b-tagging efficiency in the $N_{\text{jet}} = 1$ channel for the individual $e\mu$ (left) and μe (right) channels. The plots show: a) the W+jets background, b) non-WW diboson background and c) top background.

strength parameter. Here $b_{\text{SR}}^{\text{exp}}$ and $b_{\text{CR}}^{\text{exp}}$ are expected background yields in the signal and control region determined by MC, μ is the signal strength parameter, μ_b is the background strength parameter and M is an auxiliary control region measurement.

Systematic uncertainties are handled by introducing nuisance parameters θ with a constraint described by the probability density functions. $N(\tilde{\theta}|\theta)$ represents an auxiliary measurement $\tilde{\theta}$ related to the nuisance parameter θ [123]. Different choices of constraints can be made (the use of these constraints will be discussed in Section 5.7.2):

- a unit Gaussian describing the uncertainty on a parameter that can be both positive and negative:

$$\frac{1}{\sqrt{2\pi}}\exp\left(\frac{(\tilde{\theta}-\theta)^2}{2}\right). \tag{5.6}$$

Then, an observable A with the best estimate $\tilde{A}$ and an associated uncertainty $\epsilon\tilde{A}$ can be written as $A = \tilde{A} \cdot (1 + \epsilon\theta)$. If an observable can yield only positive values (luminosity, cross section etc.), then the solution is to use the Gaussian constraint truncated at or slightly above zero which means that the probability distribution describes a variable with a value bounded from below;

- a log-normal distribution (in which the described variable's logarithm is normally distributed). This allows to avoid the possible difficulties of a truncated Gaussian:

$$\frac{1}{\sqrt{2\pi}\ln(\kappa)}\exp\left(-\frac{(\ln(\theta/\tilde{\theta}))^2}{2(\ln\kappa)^2}\right)\frac{1}{\theta}, \tag{5.7}$$

where κ characterises the width of the distribution. Then, a response of a variable A to the normally distributed nuisance parameter θ, can be written as $A = \tilde{A}\kappa^\theta$. For small uncertainties, the Gaussian and the log-normal distributions are asymptotically identical, whereas the log-normal is more suited for large uncertainties;

- a Poisson distribution:

$$\frac{\lambda(\theta)^{\tilde{\theta}}}{\tilde{\theta}!}\exp\left(-\lambda(\theta)\right). \tag{5.8}$$

Expanding the likelihood from Eq. 5.5 to the one used in this analysis, a product over lepton flavours and jet multiplicities is done. Because the m_{T} distribution is binned, a product over bins is also introduced. The strength parameters μ_b, introduced previously, are applied to the WW background in the $N_{\text{jet}}=0$ and $N_{\text{jet}}=1$ analyses, as well as the top background in the $N_{\text{jet}}=1$ channel. These backgrounds are constrained by the data measurements in the control regions. The minor backgrounds which do not have floating strength parameters as well as the data-driven W+jets estimates are added to the Poisson expectations. The full likelihood can be written as:

$$\mathcal{L}(\mu,\vec{\theta}) = \{\prod_{i=e\mu,\mu e}\prod_{j=0}^{N_{\text{jets}}}\prod_{k=1}^{N_{\text{bins}}}P(N_{ijk}|\mu s_{ijk} + \sum_{l}^{N_{\text{bkg}}}b_{ijkl})\} \times \tag{5.9}$$

$$\times\{\prod_{m=1}^{N_{CR}}P(M|\mu s + \mu_b b_{\text{CR}} + \sum_{n}^{N_{\text{bkg}}-1}b_n)_m\} \times \{\prod_{o=1}^{N_\theta}N(\tilde{\theta}_o|\theta_o)\},$$

where $\vec{\theta}$ is the full suite of nuisance parameters, b is the background rate, $N(\tilde{\theta}_o|\theta_o)$ expresses the constraints on the nuisance parameters, and $P(M|\mu s + \mu_b b_{\mathrm{CR}} + \sum\limits_{n}^{N_{\mathrm{bkg}}-1} b_n)$ includes the auxiliary measurements on the backgrounds constrained by data in the control regions. In the case of the top background in the $N_{\mathrm{jet}} = 0$ channel and $Z/\gamma^* \to \tau\tau$ background in both $N_{\mathrm{jet}} = 0$ and $N_{\mathrm{jet}} = 1$ channels, the rate b is multiplied by the appropriate normalisation factor. The numerical values were quoted in the previous section.

5.7.2 Systematic uncertainties

The signal and background expectations are functions of the nuisance parameters $\vec{\theta}$. These functions are parametrised such that the response of s and b to each θ is factorised from the nominal value of the expected rate. That is, $s = s_0 \times \prod \nu(\theta)$ (similarly $b = b_0 \times \prod \nu(\theta)$), where the form of $\nu(\theta)$ depends on the source of systematic uncertainty. Four different cases can be distinguished:

- Flat systematics (which do not change the m_{T} shape) take the form $\nu_{\mathrm{flat}}(\theta) = \kappa^{\theta}$, where κ is determined by measuring ν_{flat} at $\theta = \pm 1$. In this case, the constraint term on θ that is present in the likelihood is a unit Gaussian and κ^{θ} is log-normally distributed;

- In the case that a systematic affects the shape, its effect is first separated into a flat component and a pure shape component, such that varying the pure shape component of s or b has no effect on the expected rate, and the flat component is treated as described above. The pure shape component is distributed as a truncated Gaussian and is expressed as $\nu_{\mathrm{shape}}(\theta) = 1 + \epsilon\theta$, where ϵ is again determined by measuring ν_{shape} at $\theta = \pm 1$. The truncation, described previously, is imposed such that $\nu_{\mathrm{shape}}(\theta < \frac{-1}{\epsilon}) = 0$. The systematic sources can have both a normalisation and a shape component. In this case, the same θ is shared between both functions $\nu_{\mathrm{flat}}(\theta)$ and $\nu_{\mathrm{shape}}(\theta)$;

- Purely statistical uncertainties from MC statistics or data-driven methods. Here, the constraint represents an auxiliary measured number of events $\tilde{\theta}$ with an expected number $\theta\lambda$. That is, it is the Poisson probability $P(\tilde{\theta}|\theta\lambda) = \frac{(\theta\lambda)^{\tilde{\theta}}e^{-\theta\lambda}}{\tilde{\theta}!}$;

- When the normalisation of a background is constrained using a high statistics data control region, the constraint is then the Poisson probability $P(\tilde{\theta}|\lambda(\theta)) = \frac{(\theta\lambda(\theta))^{\tilde{\theta}}e^{-\lambda(\theta)}}{\tilde{\theta}!}$, where $\tilde{\theta}$ is the observed number of events in the control region. The expected number of events is $\lambda = \mu s + \theta b_{\mathrm{CR}} + \sum\limits_{i}^{N_{bg}-1} b_i$, where b_{CR} is the background targeted by the control region. This procedure properly takes into account the contamination in the control region due to both the signal and other backgrounds. In the full likelihood there are three nuisance parameters representing the strengths of two major backgrounds: WW $N_{\mathrm{jet}} = 0$, WW $N_{\mathrm{jet}} = 1$ and top $N_{\mathrm{jet}} = 1$. Further, the strength parameters multiply the expected background anywhere that background is present. In this way, the contaminations among the various control regions are treated properly.

5.7.3 Procedure

A test statistic $\tilde{q}_\mu$ is used to test for the compatibility of the data with the background-only and signal+background hypotheses. It is based on a profile likelihood ratio constructed as follows:

$$\tilde{\lambda}(\mu) = \begin{cases} \dfrac{\mathcal{L}(\mu, \hat{\hat{\theta}}(\mu))}{\mathcal{L}(\hat{\mu}, \hat{\theta})} & \hat{\mu} \geq 0, \\[2ex] \dfrac{\mathcal{L}(\mu, \hat{\hat{\theta}}(\mu))}{\mathcal{L}(0, \hat{\hat{\theta}}(0))} & \hat{\mu} < 0 \end{cases} \tag{5.10}$$

where $\hat{\hat{\theta}}(\mu)$ and $\hat{\hat{\theta}}(0)$ refer to the conditional maximum likelihood estimators (MLE) of $\vec{\theta}$, given a signal strength parameter of 0 or μ, respectively, and $\hat{\mu}$ and $\hat{\theta}$ are the global parameters that maximise the likelihood. The test statistic $\tilde{q}_\mu$ is then given as:

$$\tilde{q}_\mu = \begin{cases} -2 \ln \tilde{\lambda}(\mu) & \hat{\mu} \leq \mu \\ 0 & \hat{\mu} > \mu \end{cases} = \begin{cases} -2 \ln \dfrac{\mathcal{L}(\mu, \hat{\hat{\theta}}(\mu))}{\mathcal{L}(0, \hat{\hat{\theta}}(0))} & \hat{\mu} < 0 \,, \\[2ex] -2 \ln \dfrac{\mathcal{L}(\mu, \hat{\hat{\theta}}(\mu))}{\mathcal{L}(\hat{\mu}, \hat{\theta})} & 0 \leq \hat{\mu} \leq \mu \,, \\[2ex] 0 & \hat{\mu} > \mu \,. \end{cases} \tag{5.11}$$

The signal strength used in the limit setting is always positive. The case where $\hat{\mu} < 0$ describes a deficit in data with respect to the expected background. The upper constraint $\hat{\mu} > \mu$, when the test statistic is assigned a null value, is imposed by hand to guarantee a one-sided confidence interval. In practice it means that the fluctuations of the data with $\hat{\mu} > \mu$ do not serve as an evidence against a hypothesis of a signal with strength μ. The values of the nuisance parameters $\hat{\hat{\theta}}_0^{\text{obs}}$ and $\hat{\hat{\theta}}_\mu^{\text{obs}}$ maximising the likelihood are established for the background-only and background+signal hypotheses, respectively. Based on these, toy Monte Carlo pseudo-data are generated to construct the sampling distributions assuming a signal strength μ and 0: $f(\tilde{q}_\mu | \mu, \hat{\theta}_\mu)$ and $f(\tilde{q}_\mu | 0, \hat{\theta}_0)$. From the sampling distributions, two p-values p_μ and p_b are derived that are associated with the actual observation for the two tested hypotheses:

$$p_\mu = \int_{\tilde{q}_{\mu,\text{obs}}}^{\infty} f(\tilde{q}_\mu | \mu, \hat{\theta}_\mu) d\tilde{q}_\mu \tag{5.12}$$

$$p_b = \int_0^{\tilde{q}_{\mu,\text{obs}}} f(\tilde{q}_\mu | 0, \hat{\theta}_0) d\tilde{q}_\mu \tag{5.13}$$

The modified frequentist method CL_s [124,125] is used to compute 95% confidence intervals on the signal strength parameter μ, where CL_s is constructed as the ratio of p-values

$$CL_s = \frac{p_\mu}{1 - p_b} \tag{5.14}$$

The 95% confidence level (CL) upper limit on μ is the solution to $CL_s = 0.05$. For computing the statistical significance of the observed test statistic $\tilde{q}_\mu^{\text{obs}}$, the background-only p-value is computed from the test statistic q_0, with a different constraint $\hat{\mu} > 0$:

$$p_0 = \int_{q_{0,\text{obs}}}^{\infty} f(q_0 | 0, \hat{\theta}_0) dq_0 \tag{5.15}$$

p_0 expresses the probability that the background will fluctuate to give the observed excess in data. One can extract the statistical significance Z from p_0 by translating from the Gaussian tail probability:

$$Z = \Phi^{-1}(1 - p_0), \tag{5.16}$$

where Φ^{-1} is the quantile of the standard Gaussian.

Chapter 6

Results

The first section summarises the results of the Higgs search in the $H{\rightarrow}WW^{(*)}{\rightarrow}\ell\nu\ell\nu$ channel based on the analysis presented in the previous chapters. The second part focuses on the combination of the ATLAS Higgs searches based on the 7 TeV and 8 TeV $p-p$ collision data.

6.1 $H{\rightarrow}WW^{(*)}{\rightarrow}\ell\nu\ell\nu$ channel

Table 6.1 shows the observed and expected numbers of events at each of the cut stages explained in the previous chapter, in the $N_{\mathrm{jet}}=0$ and $N_{\mathrm{jet}}=1$ signal regions for the $e\mu+\mu e$ channels combined [89]. The W+jets prediction is based on the fake factor data-driven method. The WW, $t\bar{t}$, $tW/tb/tqb$ and $Z/\gamma^{*}{\rightarrow}\tau\tau$ backgrounds are normalised to their predictions from the corresponding control regions. The remaining backgrounds are estimated using the MC simulation. In the $N_{\mathrm{jet}}=0$ selection, WW contributes 72% of the total background prediction. The sub-dominant processes include the top background with 12% and W+jets and non-WW diboson backgrounds, each with about 8%. In the case of the $N_{\mathrm{jet}}=1$ selection, the top background contributes 50%, WW 30% and the other processes share the remaining 20% in an equal way. An excess of the observed events over the expected MC background prediction can be seen in both jet multiplicity channels. The final m_{T} distributions that are used in the statistical fit are shown in Figure 6.1 in the $N_{\mathrm{jet}}=0$ and $N_{\mathrm{jet}}=1$ channels for $e\mu$ and μe lepton flavour channels combined (see Chapter 5). A sensitive region in m_{T} for a Higgs boson with a mass $m_H = 125$ GeV can be obtained after placing a requirement of $0.75\,m_H < m_{\mathrm{T}} < m_H$. Table 6.2 shows the expected and observed numbers of events after the above mentioned selection for the $e\mu+\mu e$ channels combined. Here, both the statistical and systematic uncertainties are included. The uncertainties on the backgrounds constrained with the data control-regions (WW, top in the $N_{\mathrm{jet}}=1$ analysis) do not include the uncertainty from the subtraction of other processes to the control region. The total uncertainty on the predicted background is calculated accounting for the correlations among the predictions, so the total does not correspond exactly to the sum in quadrature of the individual contributions.

The excess can be quantified as the p_0 value which expresses how likely the background-only hypothesis is to fluctuate to give the observed excess in data. The observed p_0 value for $m_H = 125$ GeV is $4{\times}10^{-3}$, which according to Eq. 5.16 corresponds to 2.6 standard deviations. The minimum observed p_0, $3{\times}10^{-3}$, is found for $m_H = 111$ GeV and corresponds to 2.8 standard deviations. Figure 6.3a shows the observed (solid line) and the expected

Cutflow evolution in the different signal regions									
$N_{\mathrm{jet}} = 0$	Signal	WW	$WZ/ZZ/W\gamma$	$t\bar{t}$	$tW/tb/tqb$	$Z/\gamma^* + \mathrm{jets}$	$W + \mathrm{jets}$	Total Bkg.	Obs.
Jet veto	110 ± 1	3004 ± 12	242 ± 8	387 ± 8	215 ± 8	1575 ± 20	340 ± 5	5762 ± 28	5960
$\Delta\phi_{\ell\ell,MET} > \pi/2$	108 ± 1	2941 ± 12	232 ± 8	361 ± 8	206 ± 8	1201 ± 21	305 ± 5	5246 ± 28	5230
$p_{\mathrm{T},\ell\ell} > 30$ GeV	99 ± 1	2442 ± 11	188 ± 7	330 ± 7	193 ± 8	57 ± 8	222 ± 3	3433 ± 19	3630
$m_{\ell\ell} < 50$ GeV	78.6 ± 0.8	579 ± 5	69 ± 4	55 ± 3	34 ± 3	11 ± 4	65 ± 2	814 ± 9	947
$\Delta\phi_{\ell\ell} < 1.8$	75.6 ± 0.8	555 ± 5	68 ± 4	54 ± 3	34 ± 3	8 ± 4	56 ± 2	774 ± 9	917
$N_{\mathrm{jet}} = 1$	Signal	WW	$WZ/ZZ/W\gamma$	$t\bar{t}$	$tW/tb/tqb$	$Z/\gamma^* + \mathrm{jets}$	$W + \mathrm{jets}$	Total Bkg.	Obs.
One jet	59.5 ± 0.8	850 ± 5	158 ± 7	3451 ± 24	1037 ± 17	505 ± 9	155 ± 5	6155 ± 33	6264
b-jet veto	50.4 ± 0.7	728 ± 5	128 ± 5	862 ± 13	283 ± 10	429 ± 8	126 ± 4	2555 ± 20	2655
$Z \to \tau\tau$ veto	50.1 ± 0.7	708 ± 5	122 ± 5	823 ± 12	268 ± 9	368 ± 8	122 ± 4	2411 ± 19	2511
$m_{\ell\ell} < 50$ GeV	37.7 ± 0.6	130 ± 2	39 ± 2	142 ± 5	55 ± 4	99 ± 3	30 ± 2	495 ± 8	548
$\Delta\phi_{\ell\ell} < 1.8$	34.9 ± 0.6	118 ± 2	35 ± 2	134 ± 5	52 ± 4	22 ± 2	24 ± 1	386 ± 8	433

Table 6.1: Observed and expected number of events in the $N_{\mathrm{jet}} = 0$ and $= 1$ signal regions for $e\mu$ and μe channels combined. Only statistical errors are shown [89].

	Signal	WW	$WZ/ZZ/W\gamma$	$t\bar{t}$	$tW/tb/tqb$	$Z/\gamma^* + \mathrm{jets}$	$W + \mathrm{jets}$	Total Bkg.	Obs.
$N_{\mathrm{jet}} = 0$	45 ± 9	242 ± 32	26 ± 4	16 ± 2	11 ± 2	4 ± 3	34 ± 17	334 ± 28	423
$N_{\mathrm{jet}} = 1$	18 ± 6	40 ± 22	10 ± 2	37 ± 13	13 ± 7	2 ± 1	11 ± 6	114 ± 18	141

Table 6.2: The observed numbers of events compared to the expectation from signal ($m_H = 125$ GeV) and background after the full event selection, including a cut on the transverse mass of $0.75 m_H < m_{\mathrm{T}} < m_H$. The uncertainties shown include both the statistical and systematic contributions [89]

signal+background (dashed line) p_0 curves. The $N_{\mathrm{jet}} = 0$ and $N_{\mathrm{jet}} = 1$ $e\mu + \mu e$ results are combined. Figure 6.3b shows the same observed curve with the expected (dashed line) Higgs signal hypothesis at $m_H = 125$ GeV. The expected p_0 for a SM Higgs at $m_H = 125$ GeV is 3×10^{-2}, corresponding to 1.9 standard deviations. The fitted signal strength parameter μ is shown as a function of m_H in Figure 6.4a. The black line shows the best-fit observed μ and the red line corresponds to the expected best-fit μ for a $m_H = 125$ GeV Higgs signal. The numerical value for the observed best-fit μ at $m_H = 125$ GeV is:

$$\hat{\mu} = 1.48^{+0.35}_{-0.33} \, (\text{stat.})^{+0.41}_{-0.36} \, (\text{syst. theor.})^{+0.28}_{-0.27} \, (\text{syst. exp.}) \pm 0.05 \, (\text{lumi.})$$
$$= 1.5 \pm 0.6 \, (\text{total}) . \tag{6.1}$$

The dominant contribution to the total systematic uncertainty comes from the theoretical systematic uncertainty with the largest uncertainty being on the WW background normalisation. Table 6.3 shows the breakdown of the different components of the total uncertainty on the best-fit signal strength at $m_H = 125$ GeV. These uncertainties have been determined in the fit and they include all the correlations between the nuisance parameters. They represent the so-called post-fit knowledge, it is in contrast to the uncertainties on the total signal and background yield (shown in Table 6.2) that are pre-fit. Adding more integrated luminosity will make the statistical uncertainty even smaller and the analysis will be systematics dominated. Figure 6.2 shows the pulls of the nuisance parameters i.e. the compatibility of the initial values of the nuisance parameters with the fitted ones for $\mu = \hat{\mu}$. Overconstraining of the nuisance parameters by the fit would result in the pulls being far away from zero. The only parameter that is slightly overconstrained is the W+jets
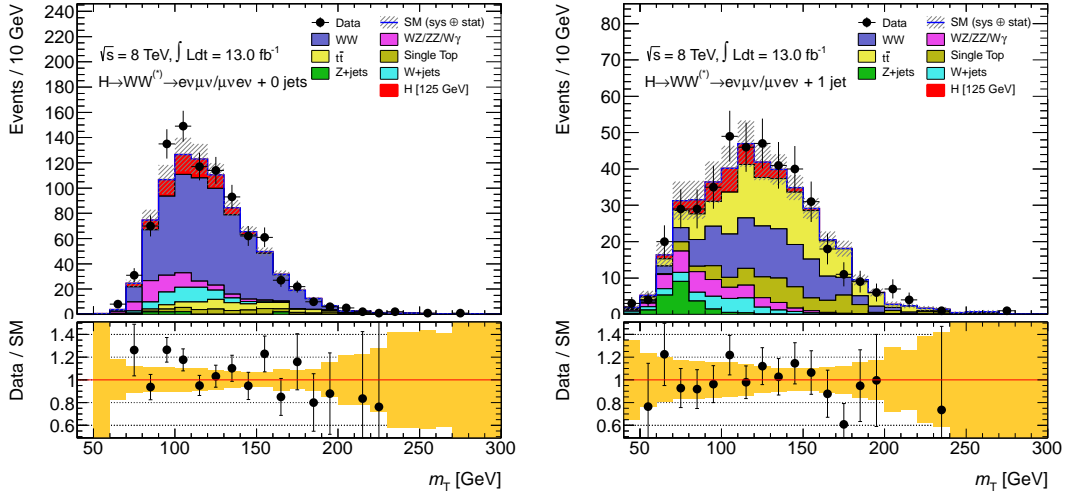
Figure 6.1: The transverse mass distribution in the $N_{\text{jet}} = 0$ (left) and $N_{\text{jet}} = 1$ (right) channels for the $e\mu$ and μe channels combined. Statistical and systematic uncertainties are included. The signal is shown for $m_H = 125$ GeV and is stacked on top of the background.

fake rate. The first three bins show the fitted values of the strength parameters of the backgrounds normalised to the data in in the control regions. They are in agreement with the normalisation factors described in Section 5.5.

The expected best-fit μ for $m_H = 125$ GeV and associated uncertainties is:

$$
\begin{aligned}
\hat{\mu}^{\text{exp}} &= 1 \pm 0.32\,(\text{stat.})^{+0.43}_{-0.41}\,(\text{syst.}) \\
&= 1^{+0.54}_{-0.52}\,(\text{total}),
\end{aligned}
\tag{6.2}
$$

which again shows that the analysis is systematics dominated. The measurement of the observed best-fit signal strength parameter can be translated into a measurement of the Higgs cross section times branching ratio. The value at $m_H = 125$ GeV is:

$$\sigma(pp \to H) \cdot \mathcal{B}(H \to WW) = 7.0^{+1.7}_{-1.6}\,(\text{stat.})^{+1.7}_{-1.6}\,(\text{syst. theor.})^{+1.3}_{-1.3}\,(\text{syst. exp.}) \pm 0.3\,(\text{lumi.})\ \text{pb},$$

which is higher than the theoretical SM Higgs boson cross section times branching ratio:

$$\sigma^{\text{SM}}(pp \to H) \cdot \mathcal{B}^{\text{SM}}(H \to WW) = 4.77^{+0.64}_{-0.64}(\text{cross section})^{+0.20}_{-0.20}(\text{branching fraction})\ \text{pb}.$$

Upper limits on the SM Higgs cross section can be derived following the CL_s method. Figure 6.4b shows the observed (dashed line) and expected (solid line) 95% CL upper limits on σ/σ_{SM} as a function of the Higgs mass. The observed data exclude a SM Higgs boson with $m_H > 139$ GeV, whereas the expected limit is at 127 GeV.

6.2   ATLAS combination

The discovery of a new particle, consistent with the SM Higgs boson, was announced by the ATLAS and CMS experiments on July 4th, 2012. The ATLAS collaboration presented results based on the combination of five individual Higgs channels: $H \to b\bar{b}$, $H \to \tau\tau$, $H \to WW^{(*)}$, $H \to \gamma\gamma$ and $H \to ZZ^{(*)}$. The combination was later updated with the $\sqrt{s} = 8$

Table 6.3: The contributions to the relative uncertainty on the measured signal strength for $m_H = 125$ GeV. The total relative uncertainty is also given [89].
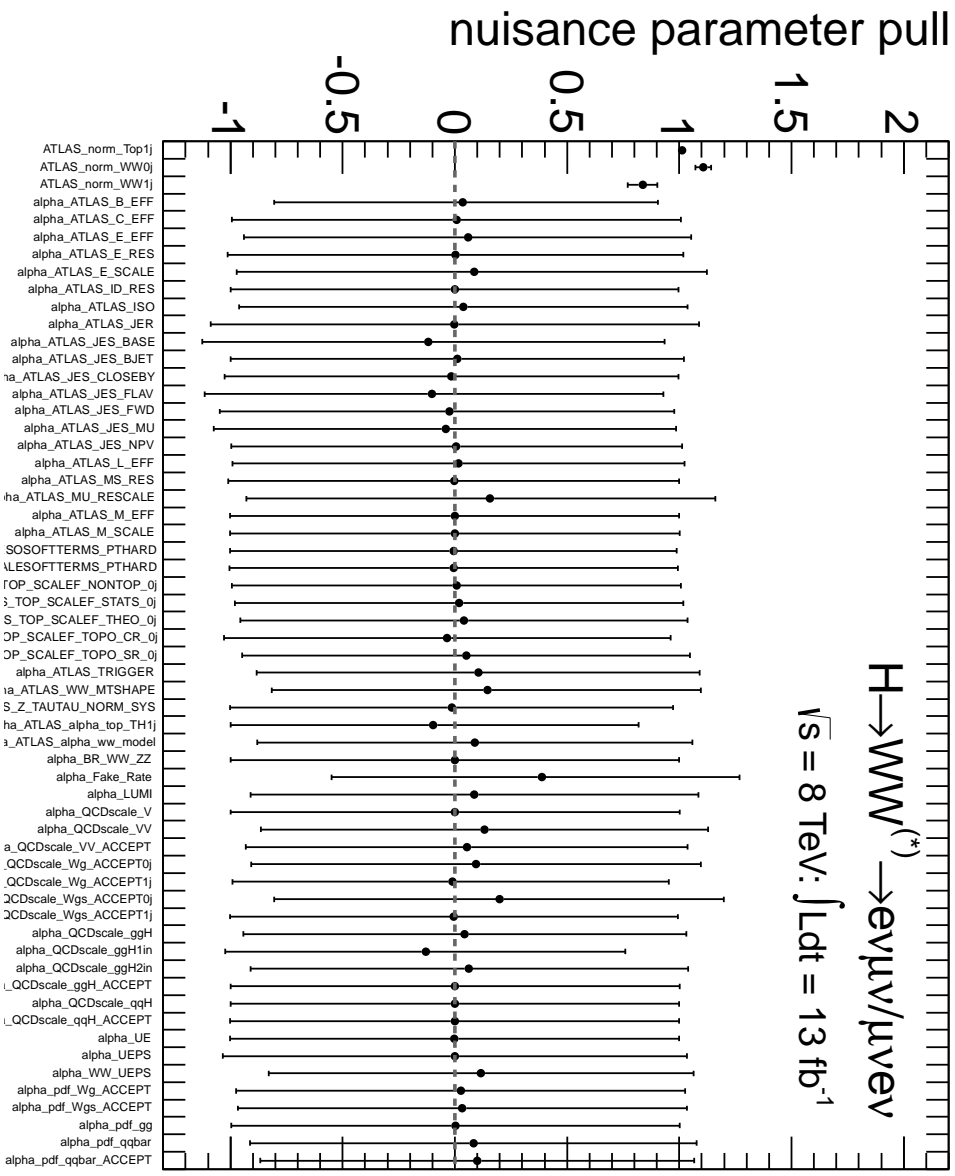
Category	Source	Uncertainty, up (%)	Uncertainty, down (%)
Statistical	Observed data	+23	−22
Theoretical	Signal yield ($\sigma \cdot \mathcal{B}$)	+14	−9
Theoretical	WW normalisation	+20	−20
Experimental	Objects	+14	−11
Theoretical	Signal acceptance	+9	−6
Experimental	MC statistics	+8	−8
Experimental	W+jets fake factor	+11	−12
Theoretical	Backgrounds, excluding WW	+9	−9
Luminosity	Integrated luminosity	+3	−3
Total		+41	−38

nuisance parameter pull

$H \rightarrow WW^{(*)} \rightarrow e\nu\mu\nu/\mu\nu e\nu$

$\sqrt{s} = 8$ TeV, $\int L\,dt = 13\ \text{fb}^{-1}$

Nuisance parameters (top to bottom):

ATLAS_norm_Top1j
ATLAS_norm_WW0j
ATLAS_norm_WW1j
alpha_ATLAS_B_EFF
alpha_ATLAS_C_EFF
alpha_ATLAS_E_EFF
alpha_ATLAS_E_RES
alpha_ATLAS_E_SCALE
alpha_ATLAS_ID_RES
alpha_ATLAS_ISO
alpha_ATLAS_JER
alpha_ATLAS_JES_BASE
alpha_ATLAS_JES_BJET
alpha_ATLAS_JES_CLOSEBY
alpha_ATLAS_JES_FLAV
alpha_ATLAS_JES_FWD
alpha_ATLAS_JES_MU
alpha_ATLAS_JES_NPV
alpha_ATLAS_L_EFF
alpha_ATLAS_MS_RES
alpha_ATLAS_MU_RESCALE
alpha_ATLAS_M_EFF
alpha_ATLAS_M_SCALE
RESOSOFTTERMS_PTHARD
SCALESOFTTERMS_PTHARD
TOP_SCALEF_NONTOP_0j
TOP_SCALEF_STATS_0j
TOP_SCALEF_THEO_0j
TOP_SCALEF_TOPO_CR_0j
TOP_SCALEF_TOPO_SR_0j
alpha_ATLAS_TRIGGER
alpha_ATLAS_WW_MTSHAPE
alpha_Z_TAUTAU_NORM_SYS
alpha_ATLAS_alpha_top_TH1j
alpha_ATLAS_alpha_ww_model
alpha_BR_WW_ZZ
alpha_Fake_Rate
alpha_LUMI
alpha_QCDscale_V
alpha_QCDscale_VV
alpha_QCDscale_VV_ACCEPT
alpha_QCDscale_Wg_ACCEPT0j
alpha_QCDscale_Wg_ACCEPT1j
alpha_QCDscale_Wgs_ACCEPT0j
alpha_QCDscale_Wgs_ACCEPT1j
alpha_QCDscale_ggH
alpha_QCDscale_ggH1in
alpha_QCDscale_ggH2in
alpha_QCDscale_ggH_ACCEPT
alpha_QCDscale_qqH
alpha_QCDscale_qqH_ACCEPT
alpha_UE
alpha_UEPS
alpha_WW_UEPS
alpha_pdf_Wg_ACCEPT
alpha_pdf_Wgs_ACCEPT
alpha_pdf_gg
alpha_pdf_qqbar
alpha_pdf_qqbar_ACCEPT

x-axis: −1, −0.5, 0, 0.5, 1, 1.5, 2

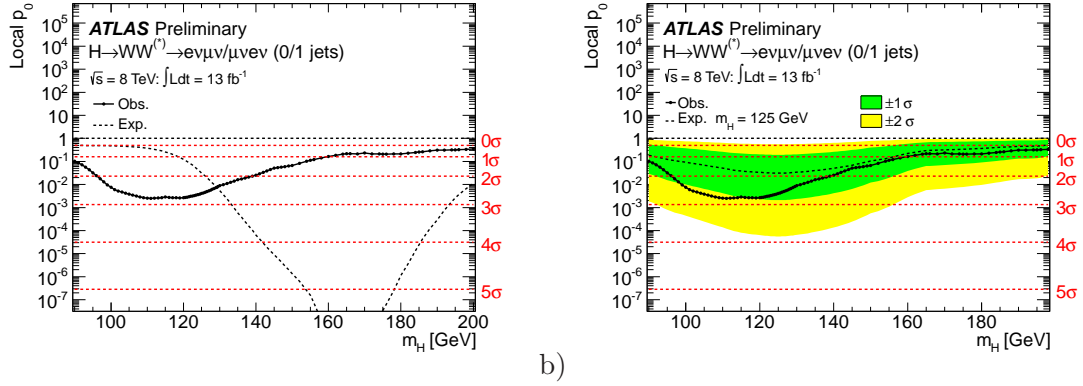Figure 6.2: Fitted values of the nuisance parameters for $\mu = \hat{\mu}$ [80].

Figure 6.3: Left: observed (solid line) and expected (dashed line) p_0 curves as a function of m_H. Right: observed (solid line) p_0 curve as a function of m_H. The dashed line shows the corresponding expectation for a $m_H = 125$ GeV signal hypothesis [89].
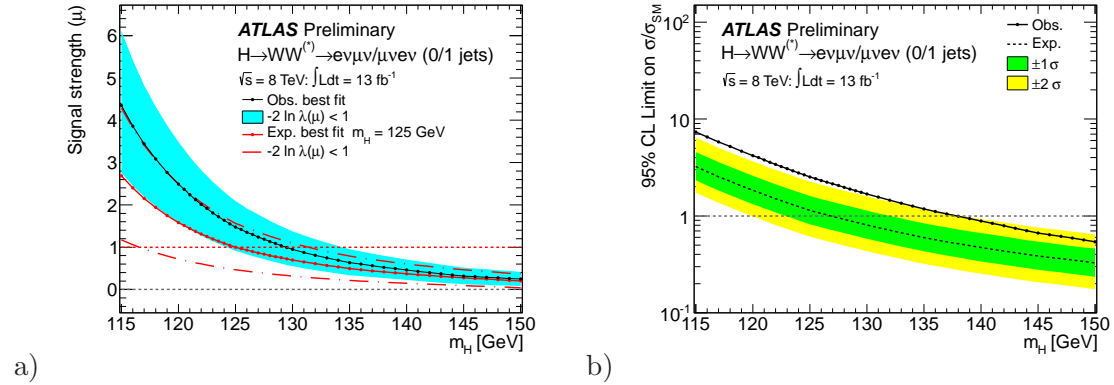

Figure 6.4: Left: fitted signal strength parameter (μ) as a function of m_H. The expected result for an injected signal with $m_H = 125$ GeV(continuous red line) is included for comparison. The uncertainty on μ corresponds to the two crossings at $-2\ln\lambda(\mu) = 1$. Right: observed (solid) and expected (dashed) 95% CL upper limits on the cross section, normalised to the SM Higgs boson production cross section and as a function of m_H [89].

TeV 5.8 fb^{-1} $H \to WW^{(*)} \to \ell\nu\ell\nu$ analysis and published in Ref. [126]. Figure 6.5a shows the observed and expected p_0 curves as a function of m_H. The minimum is found at 126.5 GeV and the associated p_0 is 1.7×10^{-9} which corresponds to 5.9 standard deviations. The 95% CL upper limit on the signal strength μ is shown in Figure 6.5b. The observed exclusion regions are 111-122 GeV and 131-559 GeV. The mass measurement using the profile likelihood ratio for the two high mass resolution channels, $H \to ZZ^{(*)}$ and $H \to \gamma\gamma$, yields $126.0 \pm 0.4(\text{stat.}) \pm 0.4(\text{syst.})$ GeV. The best-fit signal strength is shown in Figure 6.6a for the individual channels at $m_H = 126$ GeV. Their combination yields $\hat{\mu} = 1.4 \pm 0.3$ which is consistent with the SM Higgs boson hypothesis. Figure 6.6b shows the likelihood contours of μ vs. m_H in the $H \to \gamma\gamma$, $H \to ZZ^{(*)}$ and $H \to WW^{(*)} \to \ell\nu\ell\nu$ channels.
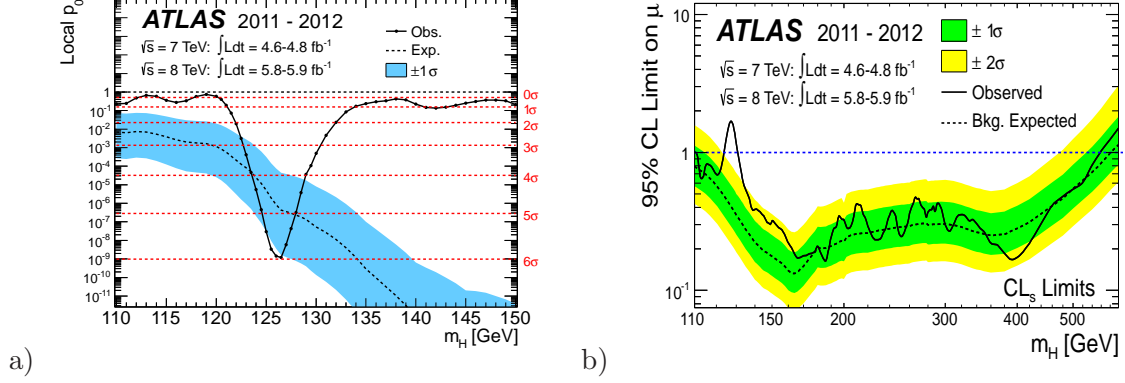
Figure 6.5: Left: The observed (solid) local p_0 as a function of m_H in the low mass range. The dashed curve shows the expected local p_0 under the hypothesis of a SM Higgs boson signal at that mass with its $\pm 1\sigma$ band. The horizontal dashed lines indicate the p-values corresponding to significances of 0 to 6 σ. Right: observed and expected 95% CL upper limits on the signal strength μ as a function of the Higgs mass [126].
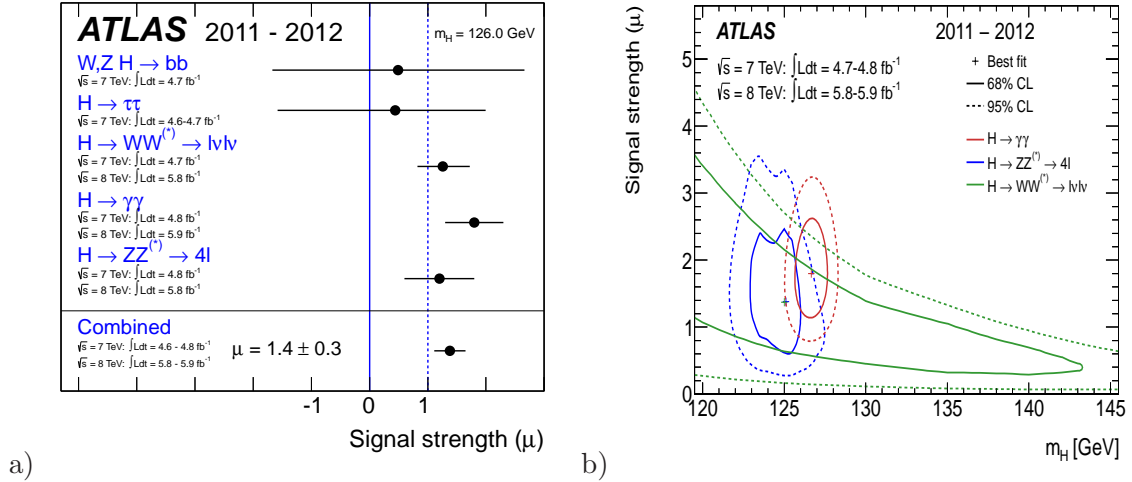

Figure 6.6: Measurement of the signal strength parameter μ (a) at $m_H = 126$ GeV and the likelihood contours (b) μ vs. m_H using $\sqrt{s} = 7$ TeV and $\sqrt{s} = 8$ TeV data collected until June [126].

Chapter 7

Conclusions

The analysis of the $H \to WW^{(*)} \to \ell\nu\ell\nu$ channel using 13 fb^{-1} of data collected at $\sqrt{s} = 8$ TeV has been presented. Only different lepton flavour channels ($e\mu + \mu e$) with zero or one accompanying jets have been used. An excess of data events over the background-only prediction has been observed. The significance of this excess at $m_H = 125$ GeV corresponds to 2.6 standard deviations. The observed best-fit signal strength parameter μ, defined as the ratio of the observed and expected number of events, is 1.5 ± 0.6 which is consistent with a Standard Model Higgs boson. This measurement can be translated into a cross section times branching ratio measurement which yields 7.0 ± 2.7 pb at $m_H = 125$ GeV and can be compared to the SM prediction, 4.8 ± 0.7 pb.

The analysis presented in this thesis has been updated with the full 2011 and 2012 dataset (so-called LHC Run I) corresponding to 25 fb^{-1} of proton-proton collision data [127]. It includes both the same flavour ($ee + \mu\mu$) and diferent flavour ($e\mu + \mu e$) channels and all the jet multiplicity bins. The results were presented in March 2013 and they confirm the existence of the newly discovered boson. The significance of the excess in the $H \to WW^{(*)} \to \ell\nu\ell\nu$ channel corresponds to 3.8σ at $m_H = 125$ GeV and the best-fit signal strength μ yields 1.01 ± 0.31. Since higher jet multiplicity channels have been added and the analysis has been optimised for the VBF production mode, several tests aiming at the direct assessment of the coupling measurements have been performed. The results yield a best-fit ggF signal strength $\mu_{\text{ggF}} = 0.82 \pm 0.36$ and a best-fit VBF signal strength $\mu_{\text{VBF}} = 1.66 \pm 0.67$.

The results of the Higgs boson searches in different decay channels in ATLAS have been recently combined and published [128]. The most sensitive and significant channels have used the full LHC Run I data. The combined mass measurement derived from the high mass-resolution channels, $H \to ZZ^{(*)}$ and $H \to \gamma\gamma$, is $m_H = 125.5 \pm 0.2\,(\text{stat.})^{+0.5}_{-0.6}\,(\text{syst.})$ GeV. The combined signal strength is determined to be $\mu = 1.33 \pm 0.14\,(\text{stat.}) \pm 0.15\,(\text{syst.})$ at $m_H = 125.5$ GeV. The cross section ratio between vector boson mediated and gluon initiated Higgs boson production processes is found to be $\mu_{\text{VBF}}/\mu_{\text{ggF}} = 1.4^{+0.4}_{-0.3}\,(\text{stat.})^{+0.6}_{-0.4}\,(\text{syst.})$. Lastly, the significance of the observed excess at $m_H = 125.5$ GeV exceeds a 10σ level which more than qualifies for a discovery of a new particle. Measurements of the spin-parity (J^P) properties of the new boson have been recently updated and tests have been performed whether the new boson is compatible with a SM hypothesis (0^+) or with alternative models ($J^P = 0^-, 1^+, 1^-, 2^+$). All these alternative hypotheses have been excluded at confidence levels above 97.8% when combining the results from three channels, $H \to \gamma\gamma$, $H \to ZZ^{(*)}$ and $H \to WW^{(*)}$ [129].

The year 2012 concluded the LHC Run I. The machine is undergoing an extensive upgrade and will start delivering data at $\sqrt{s} = 13$ TeV only in 2015. The data collected during the first two years established the discovery of a new particle consistent with the Higgs boson. So far it has been found to decay to pairs of bosons, $\gamma\gamma$, ZZ and WW. Searches for a Higgs boson in the fermionic decay channels, $\tau\tau$, $b\bar{b}$ and $\mu\mu$, are ongoing. A measurement of the Yukawa coupling between the Higgs boson and fermions is necessary to establish the true nature of the new boson. The next years' data will also test whether the newly discovered Higgs boson is indeed a Standard Model Higgs boson or if theories beyond the Standard Model are required to explain its properties.

Appendix A

$W\gamma$ background estimation in the ee channel

When designing the $W\gamma$ validation region for the ee channel a complication arises that one must separate between the electron from the W decay and the electron from the photon conversion. However, taking the b-layer and conversion signal and background efficiency into account, the fraction of events where the W electron enters the $W\gamma$ validation region (fails the b-layer or the conversion requirement) and the conversion electron passes the signal region cuts is less than 2%. The cut on $E_{\mathrm{T,rel}}^{\mathrm{miss}}$ is removed because of lack of statistics and the $p_{\mathrm{T,rel}}^{\mathrm{miss}}$ requirement is loosened to 25 GeV. The rejection of the DY and W+jets backgrounds is not diminished by relaxing the cut on $p_{\mathrm{T,rel}}^{\mathrm{miss}}$.

Despite the relaxed cuts, the ee channel VR suffers from less statistics than the $e\mu + \mu e$ channels, especially in the $N_{\mathrm{jet}} = 1$ VR. At the final cut stage, the expected purity of $W\gamma$ events in the validation region reaches 83% in the $N_{\mathrm{jet}} = 0$ bin and 76% in the $N_{\mathrm{jet}} = 1$ bin. The different background components in the $W\gamma$ ee $N_{\mathrm{jet}} = 0$ and $= 1$ validation regions can be found in Table A.1. Figure A.1 shows the *Tight Bit Electron* distribution for the ee channel and Figure A.2 shows the $E_{\mathrm{T,rel}}^{\mathrm{miss}}$ and m_{T} distributions for the $W\gamma$ ee $N_{\mathrm{jet}} = 0$ and $= 1$ validation regions.

The MC simulation models both the shape and the normalisation of the $W\gamma$ background. Since this is a sub-dominant background contribution in the ee signal region and there is not enough statistics in the validation region, no data-driven correction is applied at the moment.

	$WZ/ZZ/W\gamma$	$W\gamma$	$W\gamma^*$	$Z\gamma$	WZ	ZZ	Z+jets	W+jets	Total Bkg.	Obs	Data/MC
$W\gamma$ ee 0 jet VR	71 ± 3	69 ± 3	2.2 ± 1.8	0.0 ± 0.0	0.19 ± 0.08	0.02 ± 0.02	0.09 ± 0.09	11 ± 1	82 ± 3	79	0.96 ± 0.11
$W\gamma$ ee 1 jet VR	34 ± 2	33 ± 2	0.85 ± 0.85	0.0 ± 0.0	0.18 ± 0.09	0.01 ± 0.01	4.7 ± 4.4	4.2 ± 0.4	43 ± 5	38	0.89 ± 0.18

Table A.1: Observed and expected number events in the $W\gamma$ $N_{\mathrm{jet}} = 0$ and $= 1$ VR at the final cut stage ($\Delta\phi_{\ell\ell} < 1.8$) for 13 fb^{-1}. Only statistical errors are reported here.
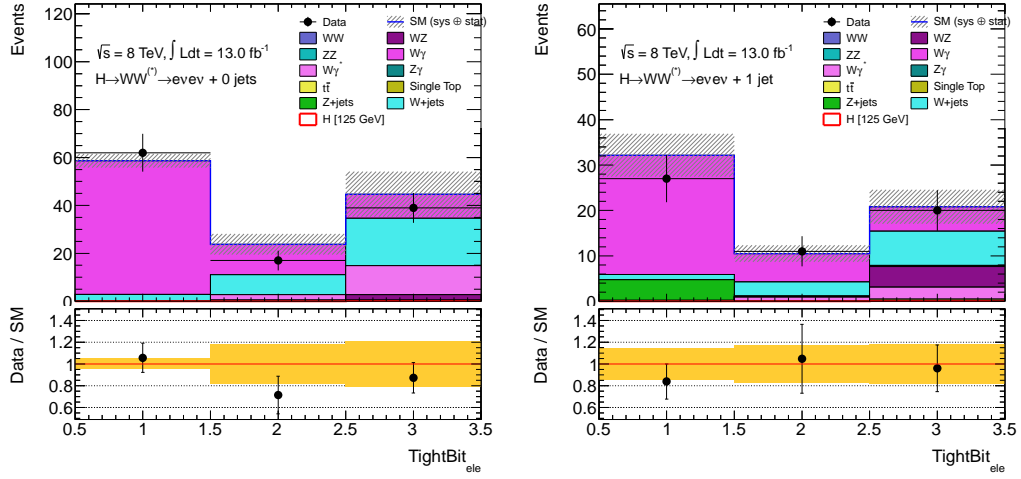
Figure A.1: The Tight Bit (conversion and b-layer electron bits), where bits 1 and 2 constitute the $W\gamma$ ee VR and bit 3 the standards same-sign ee selection, for $N_{\mathrm{jet}} = 0$ (left) and $N_{\mathrm{jet}} = 1$ (right). Statistical and systematic uncertainties are included.
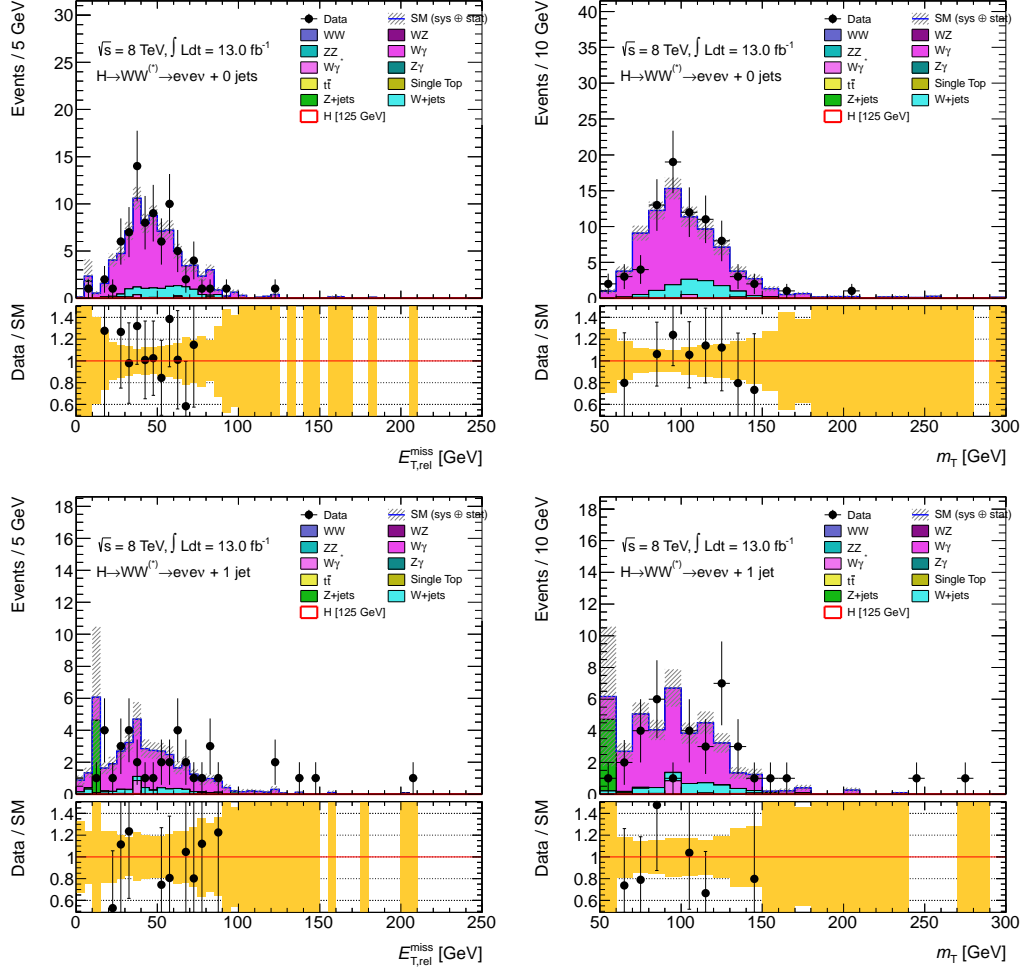
Figure A.2: The $E_{\mathrm{T,rel}}^{\mathrm{miss}}$ and m_{T} distributions in the $W\gamma$ ee VR $N_{\mathrm{jet}}=0$ (top) and $N_{\mathrm{jet}}=1$ (bottom) channels. Statistical and systematic uncertainties are included.

Bibliography

[1] J. Beringer et al. (Particle Data Group) Phys. Rev. D **86** (2012).

[2] P. W. Higgs, *Broken symmetries, massless particles and gauge fields*, Phys. Lett. **12** (1964) 132.

[3] P. W. Higgs, *Broken Symmetries and the Masses of Gauge Bosons*, Phys. Rev. Lett. **13** (1964) 508.

[4] P. W. Higgs, *Spontaneous symmetry breakdown without massless bosons*, Phys. Rev. **145** (1966) 1156.

[5] G. Guralnik, C. Hagen, and T. Kibble, *Global conservation laws and massless particles*, Phys.Rev.Lett. **13** (1964) 585–587.

[6] T. Kibble, *Symmetry breaking in non-Abelian gauge theories*, Phys.Rev. **155** (1967) 1554–1561.

[7] F. Englert and R. Brout, *Broken Symmetry and the Mass of Gauge Vector Mesons*, Phys. Rev. Lett. **13** (1964) 321.

[8] G. Guralnik, C. Hagen and T. Kibble, *Global conservation laws and massless particles*, Phys. Rev. Lett. **13** (1964) 585.

[9] S. L. Glashow, *Partial-symmetries of weak interactions*, Nuclear Physics **22** (1961) 579–588.

[10] A. Djouadi, *The anatomy of electroweak symmetry breaking: Tome I: The Higgs boson in the Standard Model*, Physics Reports **457** no. 14, (2008) 1 – 216.

[11] The ALEPH, DELPHI, L3, OPAL, SLD, CDF, and DØ Collaborations, and the LEP Tevatron SLD Electroweak Working Group, *Precision electroweak measurements and constraints on the Standard Model*, 2010.

[12] LEP Working Group for Higgs boson searches, *Search for the Standard Model Higgs boson at LEP*, **565** (2003) 61, `arXiv:0306033 [hep-ex]`.

[13] The CDF and DØ Collaborations, and the Tevatron New Phenomena and Higgs Working Group, *Combined CDF and D0 Search for Standard Model Higgs Boson Production with up to 10.0 fb^{-1} of Data*, `arXiv:1203.3774 [hep-ex]`.

[14] M. Baak, M. Goebel, J. Haller, A. Hoecker, D. Ludwig, et al., *Updated Status of the Global Electroweak Fit and Constraints on New Physics*, Eur.Phys.J. **C72** (2012) 2003, `arXiv:1107.0975 [hep-ph]`.

[15] Dobbs, M.A. and Frixione, S. and Laenen, Eric and Tollefson, K. and Baer, H. and others, *Les Houches guidebook to Monte Carlo generators for hadron collider physics*, `arXiv:hep-ph/0403045 [hep-ph]`.

[16] LHC Higgs Cross Section Working Group, S. Dittmaier, C. Mariotti, G. Passarino, and R. Tanaka (Eds.), *Handbook of LHC Higgs Cross Sections: 1. Inclusive Observables*, CERN-2011-002 (CERN, Geneva, 2011), `arXiv:1101.0593 [hep-ph]`.

[17] LHC Higgs Cross Section Working Group, S. Dittmaier, C. Mariotti, G. Passarino, and R. Tanaka (Eds.), *Handbook of LHC Higgs Cross Sections: 2. Differential Distributions*, CERN-2012-002 (CERN, Geneva, 2012), `arXiv:1201.3084 [hep-ph]`.

[18] H. Georgi, S. Glashow, M. Machacek, and D. V. Nanopoulos, *Higgs bosons from two gluon annihilation in proton proton collisions*, Phys.Rev.Lett. **40** (1978) 692694.

[19] A. Djouadi, M. Spira, and P. Zerwas, *Production of Higgs bosons in proton colliders: QCD corrections*, Phys.Lett. **B264** (1991) 440–446.

[20] S. Dawson, *Radiative corrections to Higgs boson production*, Nucl.Phys. **B359** (1991) 283–300.

[21] M. Spira, A. Djouadi, D. Graudenz, and P. Zerwas, *Higgs boson production at the LHC*, Nucl.Phys. **B453** (1995) 17–82, `arXiv:9504378 [hep-ph]`.

[22] D. Graudenz, M. Spira, and P. M. Zerwas, *QCD corrections to Higgs-boson production at proton-proton colliders*, Phys. Rev. Lett. **70** (1993) 1372–1375.

[23] R. V. Harlander and W. B. Kilgore, *Next-to-next-to-leading order Higgs production at hadron colliders*, Phys.Rev.Lett. **88** (2002) 201801, `arXiv:0201206 [hep-ph]`.

[24] C. Anastasiou and K. Melnikov, *Higgs boson production at hadron colliders in NNLO QCD*, Nucl.Phys. **B646** (2002) 220–256, `arXiv:0207004 [hep-ph]`.

[25] V. Ravindran, J. Smith, and W. L. van Neerven, *NNLO corrections to the total cross-section for Higgs boson production in hadron hadron collisions*, Nucl.Phys. **B665** (2003) 325–366, `arXiv:0302135 [hep-ph]`.

[26] S. Catani, D. de Florian, M. Grazzini, and P. Nason, *Soft gluon resummation for Higgs boson production at hadron colliders*, JHEP **0307** (2003) 028, `arXiv:0306211 [hep-ph]`.

[27] A. Martin, W. Stirling, R. Thorne, and G. Watt, *Parton distributions for the LHC*, Eur.Phys.J. **C63** (2009) 189–285, `arXiv:0901.0002 [hep-ph]`.

[28] U. Aglietti, R. Bonciani, G. Degrassi, and A. Vicini, *Two loop light fermion contribution to Higgs production and decays*, Phys.Lett. **B595** (2004) 432–441, `arXiv:0404071 [hep-ph]`.

[29] S. Actis, G. Passarino, C. Sturm, and S. Uccirati, *NLO electroweak corrections to Higgs boson production at hadron colliders*, Phys.Lett. **B670** (2008) 12–17, `arXiv:0809.1301 [hep-ph]`.

[30] D. de Florian and M. Grazzini, *Higgs production at the LHC: updated cross sections at $\sqrt{s} = 8$ TeV*, `arXiv:1206.4133 [hep-ph]`.

[31] C. Anastasiou, S. Buehler, F. Herzog, and A. Lazopoulos, *Inclusive Higgs boson cross-section for the LHC at 8 TeV*, JHEP **1204** (2012) 004, `arXiv:1202.3638 [hep-ph]`.

[32] J. Baglio and A. Djouadi, *Higgs production at the lHC*, JHEP **1103** (2011) 055, `arXiv:1012.0530 [hep-ph]`.

[33] M. Ciccolini, A. Denner, and S. Dittmaier, *Strong and electroweak corrections to the production of Higgs + 2-jets via weak interactions at the LHC*, Phys.Rev.Lett. **99** (2007) 161803, `arXiv:0707.0381 [hep-ph]`.

[34] M. Ciccolini, A. Denner, and S. Dittmaier, *Electroweak and QCD corrections to Higgs production via vector-boson fusion at the LHC*, Phys.Rev. **D77** (2008) 013002, `arXiv:0710.4749 [hep-ph]`.

[35] K. Arnold, M. Bahr, G. Bozzi, F. Campanario, C. Englert, et al., *VBFNLO: A Parton level Monte Carlo for processes with electroweak bosons*, Comput.Phys.Commun. **180** (2009) 1661–1670, `arXiv:0811.4559 [hep-ph]`.

[36] P. Bolzoni, F. Maltoni, S.-O. Moch, and M. Zaro, *Higgs production via vector-boson fusion at NNLO in QCD*, Phys.Rev.Lett. **105** (2010) 011801, `arXiv:1003.4451 [hep-ph]`.

[37] V. DelDuca, G. Klämke, M. L. Mangano, M. Moretti, F. Piccinini, R. Pittau, A. D. Polosa, and D. Zeppenfeld, *Monte Carlo studies of the jet activity in Higgs + 2 jet events*, JHEP **10** (2006) 16, `arXiv:0608158 [hep-ph]`.

[38] T. Han and S. Willenbrock, *QCD correction to the $pp \rightarrow WH$ and ZH total cross-sections*, Phys.Lett. **B273** (1991) 167–172.

[39] O. Brein, A. Djouadi, and R. Harlander, *NNLO QCD corrections to the Higgs-strahlung processes at hadron colliders*, Phys.Lett. **B579** (2004) 149–156, `arXiv:0307206 [hep-ph]`.

[40] M. Ciccolini, S. Dittmaier, and M. Krämer, *Electroweak radiative corrections to associated WH and ZH production at hadron colliders*, Phys.Rev. **D68** (2003) 073003, `arXiv:0306234 [hep-ph]`.

[41] W. Beenakker, S. Dittmaier, M. Krämer, B. Plumper, M. Spira, et al., *Higgs radiation off top quarks at the Tevatron and the LHC*, Phys.Rev.Lett. **87** (2001) 201805, `arXiv:0107081 [hep-ph]`.

[42] W. Beenakker, S. Dittmaier, M. Krämer, B. Plumper, M. Spira, et al., *NLO QCD corrections to $t\bar{t}H$ production in hadron collisions*, Nucl.Phys. **B653** (2003) 151–203, `arXiv:0211352 [hep-ph]`.

[43] S. Dawson, L. Orr, L. Reina, and D. Wackeroth, *Next-to-leading order QCD corrections to $pp \rightarrow t\bar{t}h$ at the CERN Large Hadron Collider*, Phys.Rev. **D67** (2003) 071503, `arXiv:0211438 [hep-ph]`.

[44] S. Dawson, C. Jackson, L. Orr, L. Reina, and D. Wackeroth, *Associated Higgs production with top quarks at the large hadron collider: NLO QCD corrections*, Phys.Rev. **D68** (2003) 034022, `arXiv:hep-ph/0305087 [hep-ph]`.

[45] I. W. Stewart and F. J. Tackmann, *Theory uncertainties for Higgs and other searches using jet bins*, Phys.Rev. **D85** (2012) 034011, `arXiv:1107.2117 [hep-ph]`.

[46] ATLAS and CMS Collaborations, *Procedure for the LHC Higgs boson search combination in summer 2011*, ATL-PHYS-PUB-2011-011, CMS-NOTE-2011-005 (2011). https://cdsweb.cern.ch/record/1375842.

[47] J. M. Campbell, J. W. Huston and W. J. Stirling, *Hard Interactions of Quarks and Gluons: A Primer for LHC Physics*, Rept. Prog. Phys. **70** (2007), `arXiv:0611148 [hep-ph]`.

[48] R.W. Assmann, M. Lamont and S. Meyers, *A brief history of the LEP Collider*, Nucl.Phys.B (2012).

[49] F. Marcastel, "Vue aerienne du trac LHC avec incrustation d'une vue artistique reprsentant un dipole du LHC." Mar, 2005.

[50] S. Holmes, R. S. Moore, and V. Shiltsev, *Overview of the Tevatron Collider Complex: Goals, Operations and Performance*, JINST **6** (2011) T08001, `arXiv:1106.0909 [physics.acc-ph]`.

[51] The ATLAS web page. `http://www.cern.ch/atlas/`.

[52] ATLAS Collaboration, *ATLAS detector and physics performance: Technical Design Report, 1*. Technical Design Report ATLAS. CERN, Geneva, 1999.

[53] ATLAS Collaboration, *ATLAS detector and physics performance: Technical Design Report, 2*. Technical Design Report ATLAS. CERN, Geneva, 1999.

[54] ATLAS Collaboration, *The ATLAS Experiment at the CERN Large Hadron Collider*, Journal of Instrumentation **3** no. 08, (2008) S08003.

[55] ATLAS Collaboration, *Readiness of the ATLAS Tile Calorimeter for LHC collisions.*, The European Physical Journal C - Particles and Fields **70** no. 4, (2010) 1193–1236.

[56] G. Corcella et al., *HERWIG 6: An event generator for hadron emission reactions with interfering gluons (including super-symmetric processes)* , JHEP **0101** (2001) 010.

[57] T. Sjostrand, S. Mrenna, and P. Z. Skands, *PYTHIA 6.4 physics and manual*, JHEP **0605** (2006) 026, `arXiv:0603175 [hep-ph]`.

[58] T. Sjostrand, S. Mrenna, and P. Z. Skands, *A Brief Introduction to PYTHIA 8.1*, CERN-LCGAPP **04** (2007) 1, `arXiv:0710.3820 [hep-ph]`.

[59] T. Gleisberg et al., *Event generation with SHERPA 1.1*, JHEP **0902** (2009) 007, `arXiv:0811.4622 [hep-ph]`.

[60] M. L. Mangano et al., *ALPGEN, a generator for hard multi-parton processes in hadronic collisions*, JHEP **0307** (2003) 001, `arXiv:0206293 [hep-ph]`.

[61] J. Alwall et al., *MadGraph/MadEvent v4: The new web generation*, JHEP **0709** (2007) 028, `arXiv:0706.2334 [hep-ph]`.

[62] J. Alwall, M. Herquet, F. Maltoni, O. Mattelaer, and T. Stelzer, *MadGraph 5 : Going Beyond*, JHEP **1106** (2011) 128, `arXiv:1106.0522 [hep-ph]`.

[63] S. Frixione and B. R. Webber, *Matching NLO QCD computations and parton shower simulations*, JHEP **0206** (2002) 029, `arXiv:0204244 [hep-ph]`.

[64] S. Alioli, P. Nason, C. Oleari, and E. Re, *A general framework for implementing NLO calculations in shower Monte Carlo programs: the POWHEG BOX*, JHEP **1006** (2010) 043, `arXiv:1002.2581 [hep-ph]`.

[65] ATLAS Collaboration, *The ATLAS simulation infrastructure*, Eur. Phys. J. C **70** (2010) 823, `arXiv:1005.4568 [physics.ins-det]`.

[66] S. Agostinelli et al., *GEANT 4, a simulation toolkit*, Nucl. Instrum. Meth. **A506** (2003) 250.

[67] ATLAS Collaboration, *Performance of the ATLAS silicon pattern recognition algorithm in data and simulation at $\sqrt{s} = 7$ TeV*, ATLAS-CONF-2010-072 (2010).

[68] ATLAS Collaboration, *Performance of the ATLAS Inner Detector track and vertex reconstruction in the high pile-up LHC environment*, ATLAS-CONF-2012-042 (2012).

[69] ATLAS Collaboration, *Performance of primary vertex reconstruction in proton-proton collisions at $\sqrt{s} = 7$ TeV in the ATLAS experiment*, ATLAS-CONF-2010-069 (2010).

[70] W. Waltenberger, R. Frühwirth and P. Vanlaer, *Adaptive vertex fitting*, J. Phys. G **34** no. 12, (2007) 343.

[71] ATLAS Collaboration, *Measurement of the Inelastic Proton-Proton Cross-Section at $\sqrt{s} = 7$ TeV with the ATLAS Detector*, Nature Commun. **2** (2011) 463, `arXiv:1104.0326 [hep-ex]`.

[72] ATLAS Collaboration, *Vertex reconstruction plots*, ATLAS-COM-PHYS-2012-474 (2012).

[73] ATLAS Collaboration, *Tau reconstruction and identification performance in ATLAS*, ATLAS-CONF-2010-086 (2010).

[74] ATLAS Collaboration, *Performance of the reconstruction and identification of hadronic tau decays in ATLAS with 2011 data*, ATLAS-CONF-2012-142 (2012).

[75] ATLAS Collaboration, *Calorimeter clustering algorithms: description and performance*, ATLAS-LARGE-PUB-2008-002 (2008).

[76] ATLAS Collaboration, *Electron performance measurements with the ATLAS detector using the 2010 LHC proton-proton collision data*, European Physical Journal C **72** (2012), `arXiv:1110.3174 [hep-ex]`.

[77] ATLAS Collaboration, *Improved electron reconstruction in ATLAS using the Gaussian Sum Filter-based model for bremsstrahlung*, ATLAS-CONF-2012-047 (2012).

[78] ATLAS Collaboration, *Expected performance of the ATLAS experiment: detector, physics and trigger*, CERN-OPEN-2008-20 (2008), `arXiv:0901.0512 [hep-ex]`.

[79] ATLAS Collaboration, *Electron efficiency measurements in early 2012 data*, ATL-COM-PHYS-2011-783 (2011).

[80] ATLAS Collaboration, *Nominal $H \to WW$ analysis with 13 fb^{-1} of data collected with the ATLAS detector at $\sqrt{s} = 8$ TeV*, ATL-COM-PHYS-2012-1509 (2012).

[81] S. Hassani, L. Chevalier, E. Lançon, J.-F. Laporte, R. Nicolaidou, and A. Ouraou, *A muon identification and combined reconstruction procedure for the ATLAS detector at the LHC using the (MUONBOY, STACO, MuTag) reconstruction packages*, Nucl. Instrum. Meth. **A572** no. 1, (2007) 77 – 79.

[82] T. Lagouri, *A muon identification and combined reconstruction procedure for the ATLAS detector at the LHC at CERN*, IEEE Trans. Nucl. Sci. **51** no. 6, (2004) 3030–3033.

[83] ATLAS Collaboration, *Pile-up dependence of the ATLAS muon performance.*, ATL-COM-PHYS-2011-1640 (2011).

[84] S. D. Ellis and D. E. Soper, *Successive combination jet algorithm for hadron collisions*, PRD **48** (1993) 3160–3166, `arXiv:9305266 [hep-ph]`.

[85] Y. L. Dokshitzer, G. D. Leder, S. Moretti, and B. R. Webber, *Better jet clustering algorithms*, JHEP (1997), `arXiv:9707323 [hep-ph]`.

[86] M. Cacciari, G. P. Salam, and G. Soyez, *Anti-k_t jet clustering algorithm*, JHEP **0804** (2008) 063, `arXiv:0802.1189 [hep-ph]`.

[87] ATLAS Collaboration, *Jet energy measurement with the ATLAS detector in proton-proton collisions at $\sqrt{s} = 7$ TeV*, `arXiv:1112.6426 [hep-ex]`.

[88] ATLAS Collaboration, *Jet energy scale and its systematic uncertainty in proton-proton collisions at $\sqrt{s} = 7$ TeV with ATLAS 2011 data.*, ATLAS-CONF-2013-004 (2013).

[89] The ATLAS Collaboration, *Update of the $H \to WW^{(*)} \to \ell\nu\ell\nu$ analysis with 13 fb^{-1} of $\sqrt{s} = 8$ TeV data collected with the ATLAS Detector*, ATLAS-CONF-2012-194 (2012).

[90] ATLAS Collaboration, *Commissioning of the ATLAS high-performance b-tagging algorithms in the 7 TeV collision data*, ATLAS-CONF-2011-102 (2011).

[91] ATLAS Collaboration, *Performance of impact parameter-based b-tagging algorithms with the ATLAS detector using pp collisions at $\sqrt{s} = 7$ TeV*, ATLAS-CONF-2010-091 (2010).

[92] ATLAS Collaboration, *Performance of the ATLAS secondary vertex b-tagging algorithm 7 TeV collision data*, ATLAS-CONF-2010-042 (2010).

[93] G. Piacquadio and C. Weiser, *A new inclusive secondary vertex algorithm for b-jet tagging in ATLAS*, J.Phys.Conf.Ser. **119** (2008) 032032.

[94] ATLAS Collaboration, *Measurement of the b-tag Efficiency in a Sample of Jets Containing Muons with 5 fb^{-1} of Data from the ATLAS Detector*, ATLAS-CONF-2012-043 (2012). https://cdsweb.cern.ch/record/1435197.

[95] ATLAS Collaboration, *Calibrating the b-Tag efficiency and mistag rate in 35 pb^{-1} of data with the ATLAS detector*, ATLAS-CONF-2011-089 (2011).

[96] ATLAS Collaboration, *b-tagging efficiency calibration in 35 pb^{-1} of data with the ATLAS detector using the System8 method*, ATLAS-CONF-2011-143 (2011).

[97] ATLAS Collaboration, *Measuring the b-tag efficiency in a $t\bar{t}$ sample with 4.7 fb^{-1} of data from the ATLAS detector*, ATLAS-CONF-2012-097 (2012).

[98] ATLAS Collaboration, *Performance of missing transverse momentum reconstruction in proton-proton collisions at 7 TeV with ATLAS*, Eur. Phys. J. C **72** (2012) 1844, `arXiv:1108.5602 [hep-ex]`.

[99] ATLAS Collaboration, *Reconstruction and calibration of missing transverse energy and performance in Z and W events in ATLAS proton-proton collisions at $\sqrt{s} = 7$ TeV*, ATLAS-CONF-2012-101 (2012).

[100] ATLAS Collaboration, *Combined search for the Standard Model Higgs boson using up to 4.9 fb^{-1} of pp collision data at $\sqrt{s} = 7$ TeV with the ATLAS detector at the LHC*, **710** (2012) 49, `arXiv:1202.1408 [hep-ex]`.

[101] ATLAS Collaboration, *Search for the Standard Model Higgs boson in the $H \to WW^{(*)} \to \ell\nu\ell\nu$ decay mode with 4.7 fb^{-1} of ATLAS data at $\sqrt{s} = 7$ TeV*, Phys.Lett. **B716** (2012) 62–81, `arXiv:1206.0756 [hep-ex]`.

[102] T. Binoth, M. Ciccolini, N. Kauer and M. Krämer, *Gluon-induced W-boson pair production at the LHC*, JHEP **0612** (2006) 046, `arXiv:0611170 [hep-ph]`.

[103] B. P. Kersevan and E. Richter-Was, *The Monte Carlo event generator AcerMC version 2.0 with interfaces to PYTHIA 6.2 and HERWIG 6.5*, `arXiv:hep-ph/0405247 [hep-ph]`.

[104] R. C. Gray, C. Kilic, M. Park, S. Somalwar, and S. Thomas, *Backgrounds To Higgs boson searches from $W\gamma^* \to l\nu l(l)$ asymmetric internal conversion*, `arXiv:1110.1368 [hep-ph]`.

[105] D. de Florian, G. Ferrera, M. Grazzini, and D. Tommasini, *Transverse-momentum resummation: Higgs boson production at the Tevatron and the LHC*, JHEP **1111** (2011) 064, `arXiv:1109.2109 [hep-ph]`.

[106] A. Bredenstein, A. Denner, S. Dittmaier, and M. Weber, *Precise predictions for the Higgs-boson decay $H \to WW/ZZ \to 4$ leptons*, Phys.Rev. **D74** (2006) 013004, `arXiv:hep-ph/0604011 [hep-ph]`.

[107] A. Bredenstein, A. Denner, S. Dittmaier, and M. Weber, *Radiative corrections to the semileptonic and hadronic Higgs-boson decays $H \to WW/ZZ \to 4$ fermions*, JHEP **0702** (2007) 080, `arXiv:hep-ph/0611234 [hep-ph]`.

[108] A. Djouadi, J. Kalinowski, and M. Spira, *HDECAY: A Program for Higgs boson decays in the Standard Model and its supersymmetric extension*, Comput.Phys.Commun. **108** (1998) 56–74, `arXiv:hep-ph/9704448 [hep-ph]`.

[109] J. M. Butterworth, J. R. Forshaw, and M. H. Seymour, *Multiparton interactions in photoproduction at HERA*, Z. Phys. **C72** (1996) 637, `arXiv:hep-ph/9601371 [hep-ph]`.

[110] J. Alwall et al., *Comparative study of various algorithms for the merging of parton showers and matrix elements in hadronic collisions*, Eur. Phys. J. C **53** (2008) 473, `arXiv:0706.2569 [hep-ph]`.

[111] H.-L. Lai, M. Guzzi, J. Huston, Z. Li, P. M. Nadolsky, et al., *New parton distributions for collider physics*, Phys.Rev. **D82** (2010) 074024, `arXiv:1007.2241 [hep-ph]`.

[112] P. M. Nadolsky et al., *Implications of CTEQ global analysis for collider observables*, Phys. ReV. D **78** (2008) 013004, `arXiv:0802.0007 [hep-ph]`.

[113] J. M. Campbell and R. K. Ellis, *An update on vector boson pair production at hadron colliders*, Phys. Rev. D **60** (1999) 113006, `arXiv:9905386 [hep-ph]`.

[114] ATLAS Collaboration, *Theoretical inputs to the $H \to WW$ search with the ATLAS detector at $\sqrt{s} = 8$ TeV*, ATL-COM-PHYS-2012-1515 (2012).

[115] ATLAS Collaboration, *Object selection for the $H \to WW$ search with the ATLAS detector at $\sqrt{s} = 8$ TeV, 13 fb^{-1} update*, ATLAS-COM-PHYS-2012-861 (2012).

[116] V. Barger, G. Bhattacharya, T. Han, and B. A. Kniehl, *Intermediate mass Higgs boson at hadron supercolliders*, Phys. Rev. **D43** no. 3, (1991) 779.

[117] A. J. Barr, B. Gripaios, and C. G. Lester, *Measuring the Higgs boson mass in dileptonic W-boson decays at hadron colliders*, JHEP **0907** (2009) 072, `arXiv:0902.4864 [hep-ph]`.

[118] S. Asai et al., *Prospects for the search for a Standard Model Higgs boson in ATLAS using vector boson fusion*, Eur. Phys. J. C **32S2** (2004) 19.

[119] ATLAS Collaboration, *Background estimates in the $H \to WW\ell\nu\ell\nu$ analysis with 13 fb^{-1} of data collected with the ATLAS detector at $\sqrt{s} = 8$ TeV*, ATL-COM-PHYS-2012-1516 (2012).

[120] B. Mellado, X. Ruan, and Z. Zhang, *Extraction of top backgrounds in the Higgs boson search with the $H \to WW^\star \to \ell\ell + E_{\mathrm{T}}^{\mathrm{miss}}$ decay with a full-jet veto at the LHC*, Phys. Rev. D **84** (2011) 096005, `arXiv:1101.1383 [hep-ph]`.

[121] M. Botje et al., *The PDF4LHC working group interim recommendations*,
`arXiv:1101.0538 [hep-ph]`.

[122] R. D. Ball, V. Bertone, F. Cerutti, L. Del Debbio, S. Forte, et al., *Impact of heavy
quark masses on parton distributions and LHC phenomenology*,
Nucl.Phys. **B849** (2011) 296–363, `arXiv:1101.1300 [hep-ph]`.

[123] ATLAS Collaboration, CMS Collaboration, LHC Higgs Combination Group,
Procedure for the LHC Higgs boson search combination in summer 2011,
ATL-PHYS-PUB-2011-011 (2011).

[124] A.L. Read, *Presentation of search results: the CL_s technique*,
J. Phys. G **28** (2002) 2693.

[125] G. Cowan, K. Cranmer, E. Gross, and O. Vitells, *Asymptotic formulae for
likelihood-based tests of new physics*, Eur. Phys. J. C **71** (2011) 1554.

[126] ATLAS Collaboration, *Observation of a new particle in the search for the Standard
Model Higgs boson with the ATLAS detector at the LHC*, Phys. Lett. B **716**
no. arXiv:1207.7214. CERN-PH-EP-2012-218, (2012) 1–29. 39 p.

[127] ATLAS Collaboration, *Measurements of the properties of the Higgs-like boson in
the $WW^{(*)} \to \ell\nu\ell\nu$ decay channel with the ATLAS detector using $25\,fb^{-1}$ of
proton-proton collision data*, ATLAS-CONF-2013-030 (2013).
https://cdsweb.cern.ch/record/1527126.

[128] ATLAS Collaboration, *Measurements of Higgs boson production and couplings in
diboson final states with the ATLAS detector at the LHC*,
`arXiv:1307.1427 [hep-ex]`.

[129] ATLAS Collaboration, *Evidence for the spin-0 nature of the Higgs boson using
ATLAS data*, `arXiv:1307.1432 [hep-ex]`.

Summary

The Standard Model is a very well established theory in modern particle physics. It successfully describes three of the fundamental fources of nature: electromagnetism, weak force and strong force. The gravitational interactions are on a macroscopic scale and so far they have not been unified with the other three forces. The electromagnetic force describes the interactions between charged particles, the weak force explains the β decay and the strong force binds quark together to form protons and neutrons, which in turn, together with electrons, form atoms. Those four forces describe our universe in the state as we know it.

Quantum field theories are theories that postulate that particles are the excitations of some physical fields. Each of the three above mentioned forces, and their associated force carriers, is actually a representation of a quantum field which rises from the internal gauge symmetries of nature. These symmetries are based on $U(1)$, $SU(2)$ and $SU(3)$ Lie groups and combined they form a gauge symmetry $SU(3)_C \times SU(2)_L \times U(1)_Y$ which is the basis of the Standard Model. The interactions are mediated by gauge bosons: eight massless gluons (gauge bosons of the strong interactions) g_α ($\alpha = 1, \ldots, 8$), three massive weak gauge bosons $W^\pm$ and Z, and one massless photon γ. Since the $W^\pm$ and Z bosons are massive it means that the electroweak symmetry is not a symmetry of the vacuum. The Lagrangian describing the physical system is invariant under the symmetry transformation but the vacuum is not. This mechanism is known as spontaneous symmetry breaking. A related mechanism, called the Higgs mechanism, postulates that the gauge bosons acquire masses through the interactions with the Higgs field. As a consequence, a neutral, massive, spin-0 boson appears and it is called a Higgs boson. This particle is claimed to be the last missing piece of the Standard Model and it has been long sought for. First searches have been carried out at the LEP and Tevatron experiments and the collected data have set limits on the Higgs boson's mass.

The Large Hadron Collider is a complex of accelerators and experiments designed to mainly study proton-proton collisions at high energies and high beam intensities. The last two years were very successful in terms of the operation of the machine and the collected data sample. The proton beams were collided at 7 TeV and 8 TeV centre-of-mass energy in 2011 and 2012, respectively. The total recorded luminosisty by the ATLAS detector exceeded 27 fb^{-1} which is enough to be able to exclude or confirm the existence of the Higgs boson. Searches have been carried out across many different final states with less or more success, depending on the complexity of the production and decay mode. The analysis presented in this thesis focuses on the Higgs boson being produced in the gluon-gluon fusion mechanism and decaying to a pair of W bosons, that further are allowed to decay only leptonically, $H \to WW^{(*)} \to \ell\nu\ell\nu$. The quoted results are based on an intermediate dataset obtained with 13 fb^{-1} of 8 TeV data collected until September 2012. Only different lepton flavour ($e\mu + \mu e$) channels and events with one or without any accompanying jets are

included. Nevertheless, the results obtained are sensitive to the presence of the Higgs boson and the observed significance of an excess of data above the background prediction reaches a level of 2.8σ at 125 GeV.

The $H \to WW^{(*)}$ channel is one of the most sensitive ones in the low and intermediate mass region. The branching ratio for a Higgs boson to decay to a pair of W bosons is 21.5% at m_H =125 GeV and is the second highest after $H \to b\bar{b}$ with 57.7% branching fraction. The final state considered in this thesis allows for the W bosons to decay only leptonically which results in events with two leptons (electrons or muons) and two neutrinos. The neutrinos are neutral and weakly interacting particles and they escape the detector without being detected. Their existence can be inferred from the missing transverse energy ($E_{\mathrm{T}}^{\mathrm{miss}}$) needed to balance the transverse momenta of all the particles in the final state. Precise measurements of $E_{\mathrm{T}}^{\mathrm{miss}}$ require very good knowledge of the detector (mainly the calorimeters) and the identification and reconstruction of all the objects in the event. Because of the neutrinos in the final state, the mass of a Higgs boson cannot be fully reconstructed and instead a mass of the objects in the transverse plane is used (the transverse mass, m_{T}). The main backgrounds to the $H \to WW^{(*)} \to \ell\nu\ell\nu$ channel include the Standard Model WW continuum and top processes. Other backgrounds, where the jets or photons are faking real leptons, considered include the W+jets and $W\gamma^{(*)}$ processes. The last step of the analysis includes the statistical fit of the transverse mass variable based on which the limits on the SM Higgs boson cross section and the significance of the excess, if any, can be calculated.

The full Run I (2010-2012) dataset proved to be enough to discover a new particle with a mass around 125 GeV (with approximately 10σ significance) which is compatible with the SM Higgs boson. The discovery has been made in two very clean and sensitive channels, $H \to \gamma\gamma$ and $H \to ZZ^{(*)}$. The combined mass from these two channels yields $m_H = 125.5 \pm 0.2\,(\mathrm{stat.})_{-0.6}^{+0.5}\,(\mathrm{syst.})$ GeV. The results from the $H \to WW^{(*)}$ decay channel contributed significantly to the discovery and this channel on its own reaches almost 4σ level with the full luminosity and the full analysis that additionally includes the same lepton flavour ($ee + \mu\mu$) channels and the category with two or more accompanying jets. The spin-parity measurements favour the SM Higgs boson hypothesis ($J^P = 0^+$) over alternative hypotheses ($J^P = 0^-, 1^+, 1^-, 2^+$), they have been excluded at confidence levels above 97.8%. Even though the particle has already been discovered, there are more questions than answers remaining: is it a SM particle, does it decay to fermions, is there anything beyond the SM? These are only a few of the important questions that the current experiments are trying to answer. One thing is sure, the story is not over and the journey is just beginning.

Samenvatting

Het Standaardmodel is een uitbundig geteste theorie voor de beschrijving van de moderne deeltjesfysica. Het is succesvol in het beschrijven van drie van de fundamentale krachten die voorkomen in de natuur: elektromagnetisme, de zwakke kernkracht en de sterke kernkracht. De zwaartekracht werkt alleen op macroscopische schalen en is tot nu niet gecombineerd met de andere drie krachten. Elektromagnetisme beschrijft de interacties tussen geladen deeltjes, de zwakke kernkracht verklaart radioactief β-verval en de sterke kernkracht bindt quarks tot protonen en neutronen, die samen met de elektronen gecombineerd worden tot atomen. Deze vier krachten beschrijven het universum zoals wij dat kennen.

De quantumveldentheorie zegt dat deeltjes aangeslagen toestanden zijn van fysieke velden in de ruimte-tijd. Alle bovengenoemde krachten, en hun bijbehorende krachtdragers, zijn eigenlijk representaties van deze velden, welke onstaan door bepaalde ijksymmetrieën in de natuur. Deze symmetrieën zijn gebaseerd op de $U(1)$, $SU(2)$ en $SU(3)$ Lie-groepen en gecombineerd vormen ze de $SU(3)_C \times SU(2)_L \times U(1)_Y$ groep welke het Standaardmodel representeert. De deeltjes die interacties bevorderen zijn de ijkbosonen: 8 massaloze gluonen (ijkbosonen van de sterke kernkracht) $g_\alpha (\alpha = 1, ..., 8)$, voor de zwakke kernkracht de zware ijkbosonen $W^\pm$ en Z, en het massaloze foton γ. Omdat de $W^\pm$ en de Z massa hebben, betekent dat de electro-zwakke kracht geen symmetrie van het vacuüm kan zijn. De Lagrangiaan die de fysica beschrijft is invariant onder de symmetrie-operaties, maar het vacuüm is dat niet. Dit mechanisme staat bekend als spontane symmetriebreking. Een gerelateerd mechanisme, genaamd het Higgsmechanisme, postuleert dat de ijkbosonen hun massa krijgen door interacties met het Higgsveld. De consequentie van dit mechanisme is dat er een neutraal geladen, spinloos deeltje met massa opduikt, genaamd het Higgsboson. Het deeltje wordt geclaimd als het laatste missende deeltje van het Standaardmodel en er is lange tijd naar gezocht. De eerste zoektochten werden uitgevoerd door de LEP- en Tevatron-experimenten en met de verzamelde hoeveelheid data zijn er limieten op de massa van het Higgsboson gezet.

De Large Hadron Collider is een complex van versnellers en experimenten speciaal ontworpen voor proton-proton botsingen bij hoge energieën en hoge bundelintensiteiten. De afgelopen twee jaar heeft de LHC een uitstekende prestatie geleverd qua performance en het verzamelen van data. De totale geregistreerde luminositeit van de ATLAS detector is meer dan 27 fb^{-1}, wat voldoende is om het bestaan van een Higgsboson te kunnen bevestigen of uitsluiten. Verscheidene analyses hebben met meer of minder succes gekeken naar de verschillende vervalskanalen van het Higgsboson, afhankelijk van de complexiteit die elk productieproces en vervalskanaal met zich meebracht. De analyse die is uiteengezet in dit proefschrift gaat over de productie van het Higgsboson via gluon-gluon fusie en met vervolgens het verval naar twee W-bosonen, welke op hun buurt weer vervallen naar leptonen, $H \rightarrow WW^{(*)} \rightarrow \ell\nu\ell\nu$. De in dit proefschrift genoemde resultaten zijn gebaseerd op een dataset van 13 fb^{-1} bij 8 TeV verkregen met data die is verzameld tot september

2012. Alleen kanalen waarbij de leptonen een verschillende flavor hadden ($e\mu + \mu e$) en events met één of zonder geassocieerde jets zijn meegenomen in de analyse. Desondanks zijn de behaalde resultaten gevoelig voor de aanwezigheid van het Higgsboson en het geobserveerde overschot aan data, ten opzichte van de verwachte achtergrond alleen, bereikt een significantieniveau van 2.8σ bij 125 GeV.

Het $H \rightarrow WW^{(*)}$ kanaal is een van de meest gevoelige kanalen voor lage en intermediaire massa's. De vervalsfractie van het Higgsboson naar twee W-bosonen is 21.5% bij een massa $m_H = 125$ GeV en wordt alleen overtroffen door het $H \rightarrow b\bar{b}$ kanaal met een vervalfractie van 57.7%. Dit proefschrift beschouwt alleen het vervalskanaal waarin beide W-bosonen leptonisch vervallen, wat resulteert in events met twee leptonen (muonen of electronen) en twee neutrino's. De neutrino's zijn elektrisch ongeladen deeltjes die alleen zwakke interacties aangaan en daarmee de detector verlaten zonder gedetecteerd te worden. Hun aanwezigheid kan worden afgeleid aan de hand van de missende transversale energie (E_T^{miss}), welke nodig is om de transversale impuls van de gemeten vervalsproducten te balanceren. Precieze metingen aan de E_T^{miss} vereisen een zeer goed begrip van de detector (vooral de calorimeters) en de identificatie en de reconstructie van alle objecten in een event. Omdat de neutrino's deel uitmaken van de vervalsproducten, kan de massa van het Higgsboson niet compleet gereconstrueerd worden en in plaats daarvan worden de massa's van de objecten in het tranversale vlak genomen (de transversale massa, m_T). De voornaamste achtergrondkanalen voor het $H \rightarrow WW^{(*)} \rightarrow \ell\nu\ell\nu$ kanaal zijn het Standaardmodel WW continue spectrum en top-quark processen. Andere achtergronden, waarbij fotonen of jets een leptonsignaal nabootsen, zoals W+jets en $W\gamma^{(*)}$ processen zijn ook in beschouwing genomen. De laatste stap in de analyse introduceert een statistische fit aan de transversale massa variabele, waarmee een limietwaarde op de Standaardmodel Higgs werkzame doorsnede kan worden gezet en het significantieniveau van het overschot, als dat er al is, kan worden berekend.

De volledige Run I (2010-2012) dataset bleek voldoende te zijn om de ontdekking van een nieuw deeltje met een massa rond de 125 GeV te claimen (met een significantie van ongeveer 10σ) wat in de lijn der verwachting is met het Standaardmodel. De ontdekking is gemaakt met de hulp van twee schone en gevoelige kanalen, $H \rightarrow \gamma\gamma$ en $H \rightarrow ZZ^{(*)}$. Het gecombineerde resultaat van deze twee kanalen levert een massa van $m_H = 125.5 \pm 0.2\text{(stat.)}^{+0.5}_{-0.6}\text{(syst.)}$ GeV op. Het resultaat van het $H \rightarrow WW^{(*)}$ vervalskanaal leverde een significante bijdrage aan de ontdekking en op zichzelf levert dit kanaal een significantie van bijna 4σ met de volledige dataset en de volledige analyse, die ook de ee en $\mu\mu$ kanalen en de categorie events met 2 of meer jets meeneemt. Metingen van de spin en pariteit (J^P) geven een voorkeur aan voor de Standaardmodel-hypothese ($J^P = 0^+$) boven andere alternatieven ($J^P = 0^-$, 1^+, 1^-, 2^+): deze alternativen zijn uitgesloten met een betrouwbaarheidsniveau van tenminste 97.8%. Alhoewel er een nieuw deeltje is ontdekt, blijven er vragen onbeantwoord: is het daadwerkelijk het SM Higgsboson, kan het vervallen naar fermionen, is er überhaupt iets meer dan het Standaardmodel? Dit zijn slechts enkele van vele belangrijke vragen die de hedendaagse experimenten proberen te beantwoorden. Eén ding is zeker: het verhaal is niet afgelopen, maar de zoektocht is pas net begonnen.

Curriculum Vitae

Magda Chelstowska was born on July 31$^{\text{st}}$ 1985 in Gdańsk, Poland. She attended a high-school in Gdańsk in a bilingual class with an extended programme in mathematics and physics. She then studied at the Gdańsk University of Technology (GUT) and finished with a master dergree in physics. The research that led to her master thesis was carried out in the Institute of Nuclear Physics in Kraków (IFJ PAN) and was accompanied by one year of particle physics courses at the University of Science and Technology in Kraków (AGH). During her studies she went to Grenoble for a one-year exchange programme to study nuclear and particle physics at Ecole Nationale Supérieure de Physique de Grenoble (ENSPG).

In the summer of 2009 she was accepted for the CERN Summer Student programme and she spent 10 weeks there, attending lectures and studying photon conversions in the ATLAS Inner Detector. Afterwards she got accepted as a PhD student at the Radboud University in Nijmegen and carried out her research under the supervision of prof. Nicolo de Groot and dr. Frank Filthaut. After spending one year on the service work in the muon combined performance group in ATLAS, she started a physics analysis in the Higgs working group. She spent more than two years working on the search for a Standard Model Higgs boson in the $WW^{(*)} \to \ell\nu\ell\nu$ channel. The results of the analysis led to the writing of this thesis.

Acknowledgements

This thesis wouldn't have been written without the help of my supervisor Nicolo de Groot and my co-supervisor Frank Filthaut. They have been of great help and support starting from my first days in Nijmegen, in the end of 2009. Thanks to them I managed to spend more than one year at CERN in the middle of data taking. Thank you for giving me such a great opportunity! I hope that I deserved it and that I fulfilled your expectations.

My days in Nijmegen also wouldn't have been the same if it wasn't for my amazing colleagues from the EHEF department. They made my time in the Netherlands very memorable and filled with lots of different activities. I would like to thank my office mates Geert-Jan, Marcel and Melvin who were always there for me during the working hours and afterwards as well. Also Eric, Folkert and Lucian made the time at our office very enjoyable. I cannot even begin to thank Stefan G. and Thijs for everything they did for me. Even though we weren't working with Harm on the same topic we managed to find a common language and common interests. Other colleagues from the department, Antje, Antonia, Antonio, Gijs, Guus, Ioannis, Irene, Jari, Jose, Stefan J., Valerio and Vince, were always there available for coffee breaks, discussions and after work activities. My everyday life at the department wouldn't have been the same without the three amazing ladies: Annelies, Gemma and Marjo - thank you for everything. During those three years in Nijmegen we managed to become friends with many of my colleagues and I hope those friendships will last long after my story with Nijmegen is finished.

Thanks to the multiple visits to Nikhef I managed to meet many great people there as well! Even though we haven't spent much time together you will always have a place in my memory. I would especially like to thank Lisa for showing me that girls in science can rock as well. With Rosemarie and Tatjana we worked together and shared the same office at CERN. It was great girls! Lucie is my role model: she is an amazing mother while being a very devoted physicist and a friend. Robin and Roel - thanks for making the SLAC summer school even a better experience than it already was.

After 15 months spent in Nijmegen it was time to move to CERN for a year to seriously start working on finding the Higgs - which we actually did! While still keeping in touch on a regular basis with my advisors Frank and Nicolo, I received a good dose of supervision from Jianming and Pierre who helped me establish where I am now. At CERN many people come and go during the course of time so it is rather difficult to take a step from being just colleagues to friends. I had lots of luck that I managed to meet a group of amazing people with whom I will for sure stay friends with. Teamα you know who you are but just for the record: Aaron, Corrinne, Joana, Joe, Johanna, Jonathan, Olivier, Richard and Stefan. There are simply too many people to list everyone who made an impact on my work and my life at CERN but just to name a few: Andi, Doug, Evelyn, Jonas, Lashkar, Manuela, Ralf and many others.

There is one person whom, if asked if I liked her when we first met, would without

any doubt have said no. It was too long ago to remember if it was actually true but if this question was asked now I am sure that she'd say yes. Elina, you were my post-doc at CERN and now you continue being my friend after you've left the field. Even though we don't live in the same cities I hope we will stay friends for a long time.

My family was there for me all the time during the course of working for Nijmegen and writing my thesis. They offered constant support and interest in my research whenever I talked to them on the phone or came to visit them in Poland.

There is an even more special person who was there with me and for me even before I started my PhD programme. He supported me all the way from the very first days of my research till the end of writing this thesis. I have to thank him for being so considerate and understanding when I had to work till the morning hours to provide the results and meet the conference deadlines. There is and always will be a place for you in my heart, Momchil.